

# Parsec Scale Faraday Rotation in Quasars

A Dissertation

Presented to

The Faculty of the Graduate School of Arts and Sciences

Brandeis University

Physics

David H. Roberts, Advisor

In Partial Fulfillment  
of the Requirements for the Degree  
Doctor of Philosophy

by

**Michael Ochs**

December 1994

RECEIVED  
BRANDEIS UNIVERSITY  
LIBRARY  
DEC 15 1994

BRANDEIS UNIVERSITY  
LIBRARY  
DEC 15 1994

21-001  
100-12  
1994

19980115 178


This dissertation, directed and approved by the candidate's Committee, has been accepted and approved by the Graduate Faculty of Brandeis University in partial fulfillment of the requirements for the Degree of

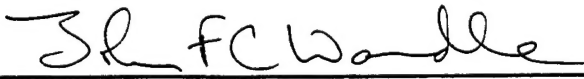
**DOCTOR OF PHILOSOPHY**

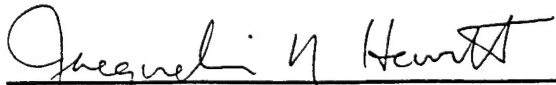
---

Dean, Arts and Sciences

**Dissertation Committee:**

  
\_\_\_\_\_  
David Roberts, Chairman

  
\_\_\_\_\_  
John F.C. Wardle

  
\_\_\_\_\_  
Jacqueline Hewitt (MIT)

REPORT DOCUMENTATION PAGE			Form Approved OMB No. 0704-0188	
Public reporting burden for this collection of information is estimated to average 1 hour per response, including the time for reviewing instructions, searching existing data sources, gathering and maintaining the data needed, and completing and reviewing the collection of information. Send comments regarding this burden estimate or any other aspect of this collection of information, including suggestions for reducing this burden, to Washington Headquarters Services, Directorate for Information Operations and Reports, 1215 Jefferson Davis Highway, Suite 1204, Arlington, VA 22202-4302, and to the Office of Management and Budget, Paperwork Reduction Project (0704-0188) Washington, DC 20503.				
1. AGENCY USE ONLY (Leave Blank)	2. REPORT DATE December 1994	3. REPORT TYPE AND DATES COVERED Final		
4. TITLE AND SUBTITLE Parsec Scale Faraday Rotation in Quasars			5. FUNDING NUMBERS  AFRL-SR-BL-TR-98-  0036	
6. AUTHORS Michael Ochs				
7. PERFORMING ORGANIZATION NAME(S) AND ADDRESS(ES) Brandeis University				
9. SPONSORING/MONITORING AGENCY NAME(S) AND ADDRESS(ES) AFOSR/NI 110 Duncan Avenue, Room B-115 Bolling Air Force Base, DC 20332-8080			10. SPONSORING/MONITORING AGENCY REPORT NUMBER	
11. SUPPLEMENTARY NOTES				
12a. DISTRIBUTION AVAILABILITY STATEMENT Approved for Public Release			12b. DISTRIBUTION CODE	
13. ABSTRACT (Maximum 200 words) See attached.				
DTIC QUALITY INSPECTED				
14. SUBJECT TERMS			15. NUMBER OF PAGES	
			16. PRICE CODE	
17. SECURITY CLASSIFICATION OF REPORT Unclassified	18. SECURITY CLASSIFICATION OF THIS PAGE Unclassified	19. SECURITY CLASSIFICATION OF ABSTRACT Unclassified	20. LIMITATION OF ABSTRACT UL	

Copyright by  
Michael Ochs

1994



To

*Erica Golemis and William Blake*

*who taught me passion*

and to

*Irene L. (Bastash) Ochs and William K. Ochs*

*who taught me honesty*

## Acknowledgements

First I would like to thank Dave Roberts and John Wardle for their great help. Not only did they develop the system used in this work, but they helped me to understand the many nuances and technical details of interferometry and, particularly, polarization VLBI. Dave always had wonderful insights on the idiosyncrasies of hybrid mapping and the many ways it could go astray. John, together with Scott Aaron, helped me to catch one major calibration error and kept me from forging ahead down the wrong path. He also helped in untangling the knots of synchrotron radiation with relativistic motion and Faraday effects.

Second, many thanks go to Jackie Hewitt for constant encouragement and her interest in this work. Also, she noted the correlation between the total intensity and the rotation measure in 3C 273--something which I overlooked, since I spent most of my time staring at complex polarization maps.

Third, thanks go to the many people who helped me during my time at Brandeis. Tim Cawthorne, during his time both at Brandeis and at Harvard, was both an inspiration and a constantly pestered source of information about relativistic jets, shocks, and VLBI. Denise Gabuzda, in addition to hints about VLBI, gave me many good pieces of advice, some of which I followed and some of which I ignored to my own loss. Leslie Brown was always willing to run off and fix some new bug in the myriad of programs which make up the Brandeis system, and she always seemed to manage to do it instantaneously. Scott Aaron provided some much needed relief by doing some AIPS calibration and sparing me further battles with that system.

Fourth, there are many telescope operators and correlator operators to thank. I cannot thank them all by name, but I wish that I could. Special thanks go to Bob Phillips at Haystack for his help in correlating these experiments. Most important to the MarkIIIa correlations, thanks go to Mike Titus, who, I believe, can work miracles all throughout his 40 hour days.

Finally, and most of all, thanks go to Erica Golemis. Nothing made my life more enjoyable than not only being happily married but also not having to constantly worry about the more mundane matters of this world. Also she is responsible for bringing a certain small chaotic system into our lives. In the end, science is a human endeavor and nothing really matters more than how we live at home.

This work was funded in part by the Air Force Office of Scientific Research.

## ABSTRACT

### Parsec Scale Faraday Rotation in Quasars

A dissertation presented to the Faculty of the  
Graduate School of Arts and Sciences of Brandeis  
University, Waltham, Massachusetts

by Michael Ochs

A system for making polarization very long baseline interferometry (VLBI) maps of extragalactic radio sources has been developed over that last decade by the radioastronomy group at Brandeis University. This work represents the first extension of these methods to multiple frequency mapping of the complex polarization of quasars on milliarcsecond scales. By observing at two wavelengths, 3.6 cm and 6 cm, maps of the parsec scale Faraday rotation measures in the quasars 3C 345 and 3C 273 have been produced. While 3C 345 shows little or no Faraday rotation, 3C 273 shows a rotation measure peak of roughly  $150 \text{ rad-m}^{-2}$  and a gradient of roughly  $90 \text{ rad-m}^{-2}$  in ten parsecs along the jet ( $H_0 = 100 \text{ km-s}^{-1}\text{-Mpc}^{-1}$ ).

The rotation measure maps in combination with the complex polarization images allow the reconstruction of the magnetic field in the parsec scale jets present in these quasars. Both quasars show reconstructed magnetic fields parallel to the jet axis, while the BL Lacertae object OJ 287, observed and mapped as a position angle calibrator, shows a reconstructed magnetic field perpendicular to the parsec scale jet axis.

In addition to substantial Faraday rotation, 3C 273 also shows depolarization in the parsec scale jet, with the fractional polarization dropping by 50% between 3.6 cm and 6 cm. These measurements allow a direct estimate of the magnetic field cell sizes in the narrow line region (NLR) of 3C 273, assuming that the NLR is responsible for the observed depolarization. The cell size is determined to be 0.3 pc, which is at least four orders of magnitude larger than the upper limits determined from VLA measurements, indicating that the NLR cannot be responsible for the depolarization.

These results indicate either that the NLR must be substantially different from present models or that our understanding of Faraday depolarization is incorrect. It is shown that the depolarization is consistent with internal Faraday effects in the jet and that the rotation measure correlates with the total intensity, but not the polarized intensity, in the jet.

**The Windhover**  
To Christ our Lord

I caught this morning morning's minion, king-  
dom of daylight's dauphin, dapple-dawn-drawn Falcon, in his riding  
Of the rolling level underneath him steady air, and striding  
High there, how he rung upon the rein of a wimpling wing  
In his ecstasy! then off, off forth on swing,  
As a skate's heel sweeps smooth on a bow-bend: the hurl and gliding  
Rebuffed the big wind. My heart in hiding  
Stirred for a bird,—the achieve of, the mastery of the thing!

Brute beauty and valour and act, oh, air, pride, plume here  
Buckle! AND the fire that breaks from thee then, a billion  
Times told lovelier, more dangerous, O my chevalier!

No wonder of it: shéer plód makes plough down sillion  
Shine, and blue-bleak embers, ah my dear,  
Fall, Gall themselves, and gash gold-vermilion.

-- Gerard Manley Hopkins

## Table of Contents

I. Introduction	16
A. The Goal of Studies of AGN	16
B. Terminology and Conventions	19
C. Radio Characteristics of AGN	21
D. Non-Radio Characteristics of AGN	33
E. Unified Schemes	39
II. Very Long Baseline Interferometry	46
A. History	46
B. Basic Equations for VLBI	49
C. Problems and Solutions in Total Intensity Mapping	53
D. Problems and Solutions in Linear Polarization Mapping	61
III. The Brandeis Polarization VLBI Package	72
A. Segmented Data and The Brandeis Format	72
B. Flux Calibration	74
C. Polarization Calibration	86
D. Mapping	93
IV. Faraday Rotation	97
A. Physical Processes of Faraday Rotation	97
B. Faraday Rotation Measurements of Unresolved Quasar Cores	102
C. Faraday Rotation Measurements on the Parsec Scale	105
V. The Quasars 3C 273 and 3C 345	113
A. 3C 273	113
B. 3C 345	119

VI. Observations	125
A. Epoch 1990.4	125
B. Epoch 1992.2	141
VII. Results for 3C 345	157
A. Epoch 1990.4	158
B. Epoch 1992.2	169
VIII. Results for 3C 273	196
A. Epoch 1990.4	197
B. Epoch 1992.2	210
IX. Analysis and Discussion	232
A. Reliability of the Maps	232
B. Quasars and BL Lac Magnetic Fields	247
C. Properties for External Faraday Screens	250
D. Internal Faraday Rotation	255
X. Conclusion	259
Appendix A: The Macintosh Modelling System	263
Appendix B: The Source Code Control System	298
Appendix C: The Brandeis Calibration Manual	299
Bibliography	315

## List of Tables

Table 1: The Observational Categories of AGN	19
Table 2: The Brandeis Data Format	73
Table 3: The Implications of Faraday Rotation Observations	100
Table 4: 3C 273 Component Characteristics in Epoch 1989.2	116
Table 5: 3C 273 10.7 GHz Component Positions	118
Table 6: 3C 273 Polarization Data in Epoch 1984.8	119
Table 7: 3C 345 Component Positions in Epoch 1990.2	121
Table 8: 3C 345 Polarization Data in Epoch 1988.1	123
Table 9: Antenna Characteristics at 6 cm in Epoch 1990.4	126
Table 10: D Terms at 6 cm in Epoch 1990.4	127
Table 11: Antenna Characteristics at 3.6 cm in Epoch 1990.4	131
Table 12: D Terms at 3.6 cm in Epoch 1990.4	133
Table 13: Antenna Characteristics at 6 cm in Epoch 1992.2	142
Table 14: D Terms at 6 cm in Epoch 1992.2	143
Table 15: Antenna Characteristics at 3.6 cm in Epoch 1992.2	147
Table 16: D Terms at 3.6 cm in Epoch 1992.2	148
Table 17: 3C 345 Component Positions at Four Epochs	187
Table 18: 3C 345 Component Fluxes at Four Epochs	188
Table 19: 3C 345 Component Polarization Properties at 6 cm	189
Table 20: 3C 345 Component Polarization Properties at 3.6 cm	190
Table 21: Residual Errors in Cross Hand Visibilities at 6 cm in Epoch 1992.2	236
Table 22: Polarization Characteristics of 3C 345 on Three Scales	241
Table 23: Polarization Characteristics of 3C 273 on Three Scales	242
Table 24: Polarization on Intermediate Scales in 3C 345	243
Table 25: Polarization on Intermediate Scales in 3C 273	244



## List of Illustrations

Figure 1: The Geometry of Superluminal Motion	28
Figure 2: Coordinate and Angle Definitions for Equation 1.8	30
Figure 3: The Standard Model for Quasars	40
Figure 4: The Coordinate System for Interferometry	50
Figure 5: A Set of Four Antennas Demonstrating Self-Calibration	56
Figure 6: The Process of Hybrid Mapping	58
Figure 7: Three Antennas Forming a Triangle for Determining Antenna Gains	67
Figure 8: Parallel Hand Visibility Plots	80
Figure 9: Parallel Hand Visibility Amplitude against UV Distance	83
Figure 10: Parallel Hand Visibility Amplitudes against Time	84
Figure 11: Plots of Closure Phases	87
Figure 12: Plots of D Term Solutions	91
Figure 13: Magnetic Field Variations within the Telescope Beam	98
Figure 14: Polarized Flux and Position Angle with Internal Faraday Rotation	100
Figure 15: Geometry of a CDQ Jet	106
Figure 16: The Magnetic Movie of 3C 345	122
Figure 17: Total Intensity Map of OJ 287 at 6 cm in Epoch 1990.4	128
Figure 18: Complex Polarization Map of OJ 287 at 6 cm in Epoch 1990.4	129
Figure 19: Total Intensity Map of OJ 287 at 3.6 cm in Epoch 1990.4	134
Figure 20: Complex Polarization Map of OJ 287 at 3.6 cm in Epoch 1990.4	135
Figure 21: 3C 345 Parallel Hand UV Coverage at 6 cm in Epoch 1990.4	137
Figure 22: 3C 345 Cross Hand UV Coverage at 6 cm in Epoch 1990.4	137
Figure 23: 3C 273 Parallel Hand UV Coverage at 6 cm in Epoch 1990.4	138

Figure 24: 3C 273 Cross Hand UV Coverage at 6 cm in Epoch 1990.4	138
Figure 25: 3C 345 Parallel Hand UV Coverage at 3.6 cm in Epoch 1990.4	139
Figure 26: 3C 345 Cross Hand UV Coverage at 3.6 cm in Epoch 1990.4	139
Figure 27: 3C 273 Parallel Hand UV Coverage at 3.6 cm in Epoch 1990.4	140
Figure 28: 3C 273 Cross Hand UV Coverage at 3.6 cm in Epoch 1990.4	140
Figure 29: Total Intensity Map of OJ 287 at 6 cm in Epoch 1992.2	145
Figure 30: Complex Polarization Map of OJ 287 at 6 cm in Epoch 1992.2	146
Figure 31: Total Intensity Map of OJ 287 at 3.6 cm in Epoch 1992.2	150
Figure 32: Complex Polarization Map of OJ 287 at 3.6 cm in Epoch 1992.2	151
Figure 33: 3C 345 Parallel Hand UV Coverage at 6 cm in Epoch 1992.2	153
Figure 34: 3C 345 Cross Hand UV Coverage at 6 cm in Epoch 1992.2	153
Figure 35: 3C 273 Parallel Hand UV Coverage at 6 cm in Epoch 1992.2	154
Figure 36: 3C 273 Cross Hand UV Coverage at 6 cm in Epoch 1992.2	154
Figure 37: 3C 345 Parallel Hand UV Coverage at 3.6 cm in Epoch 1992.2	155
Figure 38: 3C 345 Cross Hand UV Coverage at 3.6 cm in Epoch 1992.2	155
Figure 39: 3C 273 Parallel Hand UV Coverage at 3.6 cm in Epoch 1992.2	156
Figure 40: 3C 273 Cross Hand UV Coverage at 3.6 cm in Epoch 1992.2	156
Figure 41: Total Intensity Map of 3C 345 at 6 cm in Epoch 1990.4	160
Figure 42: Complex Polarization Map of 3C 345 at 6 cm in Epoch 1990.4	161
Figure 43: Total Intensity Map of 3C 345 at 3.6 cm in Epoch 1990.4	162
Figure 44: Complex Polarization Map of 3C 345 at 3.6 cm in Epoch 1990.4	163
Figure 45: Smoothed Polarization Map of 3C 345 at 3.6 cm in Epoch 1990.4	164
Figure 46: Faraday Rotation Measure Map of 3C 345 in Epoch 1990.4	166
Figure 47: Map of the Reconstructed Magnetic Field In 3C 345 in Epoch 1990.4	168
Figure 48: Total Intensity Map of 3C 345 at 6 cm in Epoch 1992.2	171
Figure 49: Complex Polarization Map of 3C 345 at 6 cm in Epoch 1992.2	172

Figure 50: Weighted Polarization Map of 3C 345 at 6 cm in Epoch 1992.2	173
Figure 51: Total Intensity Map of 3C 345 at 3.6 cm in Epoch 1992.2	175
Figure 52: Complex Polarization Map of 3C 345 at 3.6 cm in Epoch 1992.2	176
Figure 53: Smoothed Total Intensity Map of 3C 345 at 6 cm in Epoch 1992.2	178
Figure 54: Smoothed Polarization Map of 3C 345 at 6 cm in Epoch 1992.2	179
Figure 55: Smoothed Total Intensity Map of 3C 345 at 3.6 cm in Epoch 1992.2	180
Figure 56: Smoothed Polarization Map of 3C 345 at 3.6 cm in Epoch 1992.2	181
Figure 57: First Faraday Rotation Measure Map of 3C 345 in Epoch 1992.2	183
Figure 58: Second Faraday Rotation Measure Map of 3C 345 in Epoch 1992.2	184
Figure 59: Third Faraday Rotation Measure Map of 3C 345 in Epoch 1992.2	185
Figure 60: Fourth Faraday Rotation Measure Map of 3C 345 in Epoch 1992.2	186
Figure 61: First Map of the Magnetic Field In 3C 345 in Epoch 1992.2	192
Figure 62: Second Map of the Magnetic Field In 3C 345 in Epoch 1992.2	193
Figure 63: Third Map of the Magnetic Field In 3C 345 in Epoch 1992.2	194
Figure 64: Fourth Map of the Magnetic Field In 3C 345 in Epoch 1992.2	195
Figure 65: Total Intensity Map of 3C 273 at 6 cm in Epoch 1990.4	198
Figure 66: Complex Polarization Map of 3C 273 at 6 cm in Epoch 1990.4	199
Figure 67: Total Intensity Map of 3C 273 at 3.6 cm in Epoch 1990.4	201
Figure 68: Complex Polarization Map of 3C 273 at 3.6 cm in Epoch 1990.4	202
Figure 69: Smoothed Polarization Map of 3C 273 at 3.6 cm in Epoch 1990.4	203
Figure 70: Faraday Rotation Measure Map of 3C 273 in Epoch 1990.4	204
Figure 71: Strip Plot of 3C 273 at 6 cm in Epoch 1990.4	206
Figure 72: Strip Plot of 3C 273 at 3.6 cm in Epoch 1990.4	208
Figure 73: Map of the Reconstructed Magnetic Field In 3C 273 in Epoch 1990.4	209
Figure 74: Total Intensity Map of 3C 273 at 6 cm in Epoch 1992.2	211
Figure 75: Weighted Polarization Map of 3C 273 at 6 cm in Epoch 1992.2	212

Figure 76: Total Intensity Map of 3C 273 at 3.6 cm in Epoch 1992.2	214
Figure 77: Weighted Polarization Map of 3C 273 at 3.6 cm in Epoch 1992.2	215
Figure 78: Smoothed Total Intensity Map of 3C 273 at 6 cm in Epoch 1992.2	217
Figure 79: Smoothed Polarization Map of 3C 273 at 6 cm in Epoch 1992.2	218
Figure 80: Smoothed Total Intensity Map of 3C 273 at 3.6 cm in Epoch 1992.2	219
Figure 81: Smoothed Polarization Map of 3C 273 at 3.6 cm in Epoch 1992.2	220
Figure 82: First Faraday Rotation Measure Map of 3C 273 in Epoch 1992.2	221
Figure 83: Second Faraday Rotation Measure Map of 3C 273 in Epoch 1992.2	222
Figure 84: Third Faraday Rotation Measure Map of 3C 273 in Epoch 1992.2	223
Figure 85: Strip Plot of 3C 273 at 6 cm in Epoch 1992.2	225
Figure 86: Strip Plot of 3C 273 at 3.6 cm in Epoch 1992.2	226
Figure 87: First Map of the Magnetic Field In 3C 273 in Epoch 1992.2	229
Figure 88: Second Map of the Magnetic Field In 3C 273 in Epoch 1992.2	230
Figure 89: Third Map of the Magnetic Field In 3C 273 in Epoch 1992.2	231
Figure 90: Cross Hand and Parallel Hand Visibility Plots on 3C 84 at 6 cm	237
Figure 91: Cross Hand and Parallel Hand Visibility Plots on 3C 84 at 3.6 cm	239
Figure 92: Fractional Polarization along the Jet in 3C 273	252
Figure 93: The Region of the NLR Responsible for Parsec Scale Faraday Rotation	253
Figure A1: The Geometry for Beaming in a Relativistic Jet	269
Figure A2: Coordinates and Definitions Used in Equation A.3	270
Figure A3: Jet Geometry for a Bent Jet	274
Figure A4: Propagation of a Wavefront in a Relativistic Jet	276
Figure A5: Rotation of the Earth and Aperture Synthesis	281
Figure A6: The Macintosh Screen Layout for the Modelling System	289

## **I. Introduction**

### *A. The Goal of Studies of AGN*

#### *1. Discovery of AGN*

Active galactic nuclei (AGN) were first identified in the 1940's, when certain spiral galaxies, now known as Seyfert galaxies, were shown to have extremely luminous cores with high-excitation emission lines (Seyfert, 1943). A second type of AGN, quasi-stellar objects (QSOs), were identified in the 1960's by attempts to find the optical counterparts to sources of strong radio emission. The radio emission appeared to arise from odd "stars", which had indecipherable spectra. When the odd "stars" were finally identified as very distant, and therefore extremely luminous, objects, by deciphering the spectra as highly redshifted high-excitation emission lines (Schmidt, 1963), it became clear that the new wavelengths made available by radio astronomy offered a significant advance to our understanding of the universe. Since the radio emission appeared to arise from the QSO, these radio sources were labelled QSRS (or quasars), for quasi-stellar radio sources. Further observational distinctions, such as the detectability of emission lines or variability of optical emission, resulted in the creation of a number of distinct categories for the classification of powerful extragalactic objects.

High resolution optical CCD observations of QSOs showed them to be surrounded by faint nebulosity with the appearance of an underlying galaxy, showing that the QSOs probably correspond to the cores of active galaxies (Weedman, 1986), suggesting that QSOs and quasars are a form of AGN. The discovery of host galaxies for a number of QSOs, the similarity of QSO and quasar spectra at non-radio wavelengths, and the similarity of QSO and some Seyfert galaxy spectra have led many in the field to refer to all AGN as quasars (*e.g.* Weedman, 1986).

## *2. Goals of this Dissertation*

The fundamental goal of our studies of AGN is the understanding of all the various forms of active galaxies within a single framework or unified scheme, which relates their observational characteristics to their structure. The desire for such a unification comes from a belief that determining the relationships of the various AGN to each other will lead to a deeper comprehension of how AGN form and how they emit prodigious amounts of energy over such a broad range of frequencies. Such a belief is reasonable in view of the success of the Hertzsprung-Russell diagram in advancing our understanding of stars and nuclear synthesis.

This dissertation deals with questions involving the subset of QSOs known as quasars. Quasars are the roughly 10% of QSOs which appear like QSOs in the infrared to ultraviolet wavebands, but which have a strong radio component as well (Begelman, 1989). One source discussed here, 3C 345, also shows high optical polarization and extreme optical variability which places it into an overlapping but distinct subset of AGN known as blazars (Angel and Stockman, 1980). The strong core radio emission of many AGN, including all blazars, allows parsec scale mapping of their radio cores by interferometry. Such mapping is the highest resolution tool available in astronomy and offers the closest view to the central power source responsible for the tremendous energy output in these objects. By creating parsec scale maps with sensitivity to linear

polarization, the magnetic field can be mapped in the inner jets of radio-loud AGN. Such information is fundamental to our understanding of the types of AGN and plays an important role in restricting the possible unified schemes for understanding AGN.

By creating parsec-scale polarization-sensitive maps at multiple frequencies, the Faraday rotation affecting the inner jet in radio-loud AGN can be determined. Such measurements yield two significant pieces of information for our studies. First, by removing uncertainties in our knowledge of the propagation of this radiation after it has been emitted, these measurements allow us to truly reconstruct the magnetic field in the parsec-scale jet, where synchrotron emission of radio photons results in emitted photons having electric field polarization perpendicular to the magnetic field in the jet. Second, the determination of the Faraday rotation yields information on the intervening material between us and the AGN jet. Because these jets are on the order of a few tens of parsecs in projected length (probably about three to eight times that in actual length), the material responsible for Faraday rotation is likely to lie in the region known to be responsible for narrow line emission in AGN. The Faraday rotation measurements then give us information on the integrated electron density and line of sight magnetic field in this region.

The goal of this dissertation is to demonstrate the capability of making Faraday rotation measurements on the parsec scale in quasars. These measurements, made here on the quasars 3C 273 and 3C 345, restrict the possible unified schemes presently under consideration. One unified scheme presently popular is shown to be consistent with the measurements presented here, and the possibility of more definite tests of this scheme are discussed. Analysis of the Faraday rotation measurements is used to constrain some characteristics of the region responsible for narrow line emission in quasars.

<u>Type of AGN</u>	<u>Abbr</u>	<u>Characteristics</u>
Quasi-Stellar Object	QSO	An extragalactic object which appears point-like on a photographic plate but has broad emission lines and a high redshift
Broad Absorption Line QSO	BAL-QSO	A QSO which shows broad absorption features near the QSO redshift in the continuum
Quasi-Stellar Radio Source	Quasar	A QSO which has radio power roughly equivalent to the power emitted at other wavebands
Core Dominated Quasar	CDQ	A quasar where the VLA core is stronger than the extended radio emission at 5 GHz
Lobe Dominated Quasar	LDQ	A quasar where the VLA core is weaker than the extended radio emission at 5 GHz
Radio Galaxy	--	A galaxy which shows strong radio emission generally with two extended radio lobes
Faranoff-Riley Type I	FR I	A radio galaxy with a morphology where the two radio lobes have diffuse ends without a clear hot spot
Faranoff-Riley Type II	FR II	A radio galaxy with a morphology where the two radio lobes have clear hot spots
Seyfert Galaxy	--	A spiral galaxy with a bright nucleus showing strong emission lines
Seyfert Type 1	Sey 1	A Seyfert galaxy which shows both broad and narrow emission lines
Seyfert Type 2	Sey 2	A Seyfert galaxy which shows only narrow emission lines
Blazar	--	An extragalactic object which shows rapid variability and high optical polarization
Optically Violently Variable Quasar	OVV	A blazar with detectable broad emission lines with rest frame equivalent widths greater than 5 Å
High Polarization Quasar	HPQ	A blazar with high optical continuum polarization (>3%) at some epoch
BL Lacertae Object	BL Lac	A blazar which shows no emission lines or emission lines with rest frame equivalent widths less than 5 Å

Table 1: The observational categories of AGN.

## *B. Terminology and Conventions*

### *1. Terms Used for Types of AGN*

The categories of AGN, created initially from observational parameters, remain to this day. However, the usefulness of the categories has been reduced due to a



variety of attempts at unification of the phenomena. Such a unification remains elusive and an unfortunate by-product of the attempts at unification has been the creation of an amount of confusion within the study of AGN as various groups have begun to refer to observationally distinct objects by the same name. An extreme example of this has been the calling of BL Lacertae objects (BL Lacs), which show extreme optical variability but weak or no emission lines, quasars in one paper (Wills *et al.*, 1992), despite strong evidence against such unification (Roberts, Wardle and Brown, 1990; Aller, Aller and Hughes, 1992). Herein I will strictly adhere to the observational distinctions as defined in table 1 for two reasons. First, this dissertation is primarily observational in nature and the conclusions of this dissertation need to be interpreted with a clear understanding of the type of objects which have been studied. As stated above, the primary focus of this work is the study of quasars. Second, I wish to allow all possible schemes for unification of the phenomena to be considered without favoring one unified scheme at the outset.

## 2. Astrophysical Conventions and Units

Throughout this dissertation I will assume a Friedman cosmology with the Hubble constant defined as  $H_0 = 100h \text{ km s}^{-1} \text{ Mpc}^{-1}$  and  $q_0 = 0.5$ . In general results will vary with the Hubble constant as parameterized by  $h$ , but will not vary strongly with the assumption for  $q_0$ . The spectral index  $\alpha$  will be defined as  $S_\nu \propto \nu^{+\alpha}$ . The linearly polarized maps will show the observed electric field vectors unless it is specifically noted that the image is a reconstruction of the magnetic field. The position angle of the electric field or magnetic field is defined from  $+90^\circ$  (directly east) to  $-90^\circ$  (directly west) with positive values being measured north through east and negative values being measured north through west. All maps show north up and east to the left. Faraday rotation is defined in the standard way by the effect it has on the rotation of the electric field vector as it propagates toward us from the source. This means that a

positive rotation measure will swing the observed electric field position angle toward the east (more positive). For purposes of reconstruction of the magnetic field, the position angle of the magnetic field can be determined by removing the Faraday effect (swinging the electric field vector to the west for positive rotation measures) and then adding  $90^\circ$ , since for synchrotron radiation the emitted electric field is always perpendicular to the magnetic field. The Faraday rotation maps are maps of the residual rotation measure with the effects of our galaxy and any large scale rotation removed by subtraction of the VLA core Faraday rotation measurement from the data.

### *C. Radio Characteristics of AGN*

#### *1. History of Radio Observations*

In the years immediately following World War II, the greatly improved radio equipment developed for use in radar systems was converted for use in radio telescopes. Initial surveys indicated the presence of a large number of discrete sources distributed fairly isotropically around the sky. Because of the long wavelengths in the radio regime, single dish telescopes were limited to resolutions on the scale of many arcminutes even for reasonably large telescopes and the shortest wavelengths then used. As such, identification of radio objects with optical objects was hampered by the presence of many optical objects at the poorly known position of any radio source. However, it was clear that some powerful radio sources aligned with known giant elliptical galaxies, while other powerful radio sources were near positions with no clear galaxies in the field at all.

In the early 1960's the problem of identification of optical objects with these radio sources was solved by the determination that the radio source 3C 48 and a peculiar star with a strange spectrum were the same object. However it was not realized that 3C 48 was extragalactic because the spectrum was not interpreted in terms

of redshift. Later the radio source 3C 273 was identified with another star-like object with a redshift of 0.158, and 3C 273 was resolved in both the radio and the optical, showing a core-jet optical structure corresponding to a double radio structure, with the optical core component having a luminosity at least 100 times greater than that of any other known galactic nucleus (Schmidt, 1963). Although QSOs were discovered because of the interest raised by powerful radio sources, which appeared to be unassociated with extragalactic objects, further study revealed that only about 10% of all QSOs show the strong radio emission seen in the originally studied objects.

By the mid-1960's, radio observations of quasars revealed rapidly varying power outputs in the objects (Dent, 1965). Since the radio emission was already identified as synchrotron emission, the observed flux variation required that the source have a larger angular size than that expected at its cosmological distance to avoid self-absorption of the synchrotron emission. For this reason and because of the extreme luminosities calculated for QSOs, a school arose which argued for non-cosmological origins for quasar redshifts (see Chapter 2 of Weedman's *Quasar Astronomy* for a thorough discussion of this matter, Weedman, 1986). This would permit the observed flux and change in flux to correspond to a far smaller luminosity and change in output for any object. However, the presence of the numerous absorption systems lying between zero redshift and the QSO redshift, the demonstration of the continuity of the AGN phenomenon from Seyfert galaxies to QSOs, and the extended galactic fuzz visible in many QSOs using CCD imaging have shown that QSOs are indeed AGN at their cosmological redshift. The rapid variability of radio emission in quasars arises from the presence of bulk relativistic motion toward the observer, which compresses the variability time scales and beams flux toward the observer, as demonstrated in a spherically symmetric model in the 1960's (Rees, 1966).

## 2. Large Scale Radio Structure

Radio observations span a larger range of resolution than any other regime, since both single dish measurements and a variety of interferometers play a role in AGN studies. Single dish measurements primarily study the variability in total intensity and polarization noted above, while interferometers make detailed maps on scales from arcseconds using the Very Large Array (VLA) and MERLIN (Multiple Element Radio Linked Interferometer) to milliarcseconds using the U.S. Very Long Baseline Interferometry (VLBI) network, the Very Long Baseline Array (VLBA), the European VLBI Network (EVN), or a combination of these. Recently even higher resolution measurements have been made by using the VLBI network at high frequencies (Krichbaum *et al.*, 1990; Zensus *et al.*, 1990), and by using antennas in space (Levy *et al.*, 1989; Linfield *et al.*, 1989).

Single dish observations show two distinct types of extended extragalactic radio sources associated with optical galaxies. These radio galaxies are classified into two broad categories, Fanaroff-Riley Type I (FR I) and Fanaroff-Riley Type II (FR II), based on their morphology (Fanaroff and Riley, 1974). Galaxies were observed at 5 GHz and divided into two categories based on the ratio of the angular distance between the brightest points around the core to the total angular size of the source observed from the lowest contour level. FR I galaxies have this ratio less than 0.5 and also were shown to have luminosities at 178 MHz less than  $10^{25} \text{ W Hz}^{-1}$ , with double sided jets which end in diffuse extended lobes, as seen in higher resolution observations. FR II galaxies have this ratio greater than 0.5 and were shown to have higher luminosities at 178 MHz, with a single sided jet sometimes visible in deep images and two edge brightened lobes usually with clear hot spots (the brightest points in the 5 GHz maps) at the leading edges of the lobes, as seen at higher resolutions. In addition there are compact radio sources which are unresolved to single dish observations and which

generally are associated with extreme forms of AGN, such as powerful quasars and blazars.

### 3. Arcsecond Scale Radio Structure

Arcsecond resolution measurements show two distinct varieties of radio-loud quasars, albeit with intermediate cases. Sources which show a strong flat spectrum ( $\alpha \sim 0$ ) core component with a single-sided jet and very low level diffuse emission around the core-jet structure, core dominated quasars (CDQs), and sources which show a steeper spectrum core ( $\alpha \sim -1$ ) usually with a jet and generally with two lobes on opposite sides of the core, lobe dominated quasars (LDQs). The LDQs show a variety of structures on the arcsecond scale as imaged by the VLA including doubles (flux from each lobe without a clear core component), triples (flux from the core and lobes), core-jet and lobes with jets detectable on both sides of the core, and large symmetric sources which are roughly doubles but where the structure is close to continuous (Aldcroft, Elvis and Bechtold, 1993; Price *et al.*, 1993). CDQs generally show asymmetric structure with a core-jet, with either diffuse, detectable flux or with an asymmetric double, which is probably the core plus some enhanced emission from the lobe (O'Dea, Barvainis and Challis, 1988; Kollgaard, Wardle and Roberts, 1990). To quantify the core dominance in images, the ratio

$$R = \frac{S_{core}}{S_{ext}} \quad (1.1)$$

is used where  $S_{core}$  is the unresolved, VLA core flux and  $S_{ext}$  is the extended VLA flux, both measured at an emitted frequency of 5 GHz. In practise, this ratio  $R$  is continuous so that the sources range from extreme CDQ ( $R \gg 1$ ) to extreme LDQ ( $R \ll 1$ ), but also include sources with  $R \sim 1$ , which cannot be called either CDQ or LDQ.

#### 4. Milliarcsecond Scale Radio Structure

During the late 1960's and early 1970's, baselines used in interferometry were increased to intercontinental distances in order to obtain higher resolution information on the powerful radio sources in quasars. Initially only the fringe amplitudes were available and interpretation was unclear, although the most straightforward interpretation of the data was that the fringe change noted in multiple epoch observations of sources was due to the superluminal ( $v > c$ ) increase in separation between components on the milliarcsecond scale (Whitney *et al.*, 1971). With the increase in the number of baselines available in an intercontinental array and the improvements in data handling and processing, imaging of the milliarcsecond structure of the sources became possible by the mid-1970's (see chapter 2 for a discussion of the techniques used). These images showed that the sources had core-jet structures with an optically thick radio core and an optically thin jet composed of multiple components in most quasars. By 1987 superluminal motion had been detected in at least 24 objects (Porcas, 1987). Both LDQs and CDQs show superluminal motion, although CDQs seem to have higher apparent velocities overall (Hough and Readhead, 1987).

#### 5. BL Lacertae Objects

Another type of extragalactic object very similar to radio-loud quasars are BL Lacertae objects (BL Lacs). BL Lacs are identified optically by the presence of high optical variability and polarization with no or weak emission lines, *i.e.* rest frame equivalent width less than 5 Å (Stickel, Fried and Kühr, 1993). In the radio regime these objects tend to have flat spectrum radio cores with a VLBI core-jet structure showing superluminal motion, just as CDQs show, although with lower apparent speeds (Impey, 1987).

There is a striking difference between quasars and BL Lacs when they are observed by polarization-sensitive VLBI. There is a clear separation between the

milliarcsecond polarization structure in the two types of objects. BL Lacs show higher VLBI core polarizations (generally above 2%) than quasars and have observed 5 GHz electric field vectors in the jets strongly aligned with the jet axis, while quasars have electric field vectors which tend to lie perpendicular to the jet axis, although with a large scatter (Roberts, Wardle and Brown, 1990; Gabuzda *et al.*, 1992).

#### *6. Jet Models for Quasars and BL Lacs*

The radio emitting jets in quasars and radio galaxies can be seen to go from milliarcsecond to arcsecond scales (Kellermann and Owen, 1988). In all quasars, these jets appear, if at all, on only one side of the central radio core component, although the presence of lobes on both sides of the core in LDQs suggest that there are two jets. The first model for jets was created to allow for the transport of energy out to the radio lobes observed in quasars and radio galaxies by low frequency electromagnetic waves which would not be visible (Rees, 1971). When interferometry began to allow higher resolution deep images, hot spots became visible in a number of objects on the outer edge of the radio lobes, and the idea of electromagnetic waves was replaced by transport of plasma out to the lobes using supersonic jets (Blandford and Rees, 1974). With the VLA the suspected jets are seen in a number of sources with the hot spots as the endpoints of the jets (Perley, 1989). In CDQs the jets are always very bright with only faint lobes which are rarely seen to have a double structure, although there is evidence for hot spots near the end of some jets (*e.g.* O'Dea, 1989).

The bulk relativistic motion required to overcome the self-absorption in quasar synchrotron radio emission clearly arises in the jet in these objects, since the core-jet structure gives rise to the majority of the radio emission. Perhaps the first remarkable achievement of VLBI was the verification of the presence of bulk relativistic motion in the milliarcsecond jets by the detection of superluminal motion (Pearson and Zensus, 1987). Superluminal motion requires speeds approaching that of light together with

movement very close to the line of sight toward the observer. Figure 1 shows the situation for superluminal motion in a typical quasar. At time 1 the emission component in the jet emits radio waves which will be observed at time  $t_{obs}$ . At time 2 the emission component has moved down the jet an amount  $vt$  where  $t$  is the time which has passed in the quasar's frame of reference between emission of the light signals. During this time, the emission component has moved along the line of sight a distance  $vt \cos \theta$ , so that it has in effect chased its own light signal down the jet, since the observer sees the speed of light as a constant. The effective motion is observed across the line of sight (*i.e.* in the plane of the sky) and it is therefore given by  $vt \sin \theta$ . So, the observed velocity is

$$v_{obs} = \frac{vt \sin \theta}{\Delta t_{obs}} \quad (1.2)$$

where  $\Delta t_{obs}$  is the time between observations of the source and is given by

$$\Delta t_{obs} = \frac{ct - vt \cos \theta}{c} \quad (1.3)$$

since the delay is just the distance divided by the speed of the signal, which is  $c$ . Then converting to  $\beta_{obs}$  (typically called the apparent speed  $\beta_{app}$ ) by dividing by  $c$  and combining equations 1.2 and 1.3 gives

$$\beta_{app} = \frac{\beta \sin \theta}{(1 - \beta \cos \theta)} \quad (1.4)$$

where  $\beta$  is the speed of the emission component in the jet's frame. When  $\cos \theta = \beta$  this gives the maximum possible value of

$$\beta_{max} = \frac{\beta}{\sqrt{1 - \beta^2}} \quad (1.5)$$

which is easily much greater than 1 for  $\beta$  approaching 1. The detection of superluminal motion using VLBI was a dramatic verification of the theory of bulk relativistic motion in the jets of quasars.



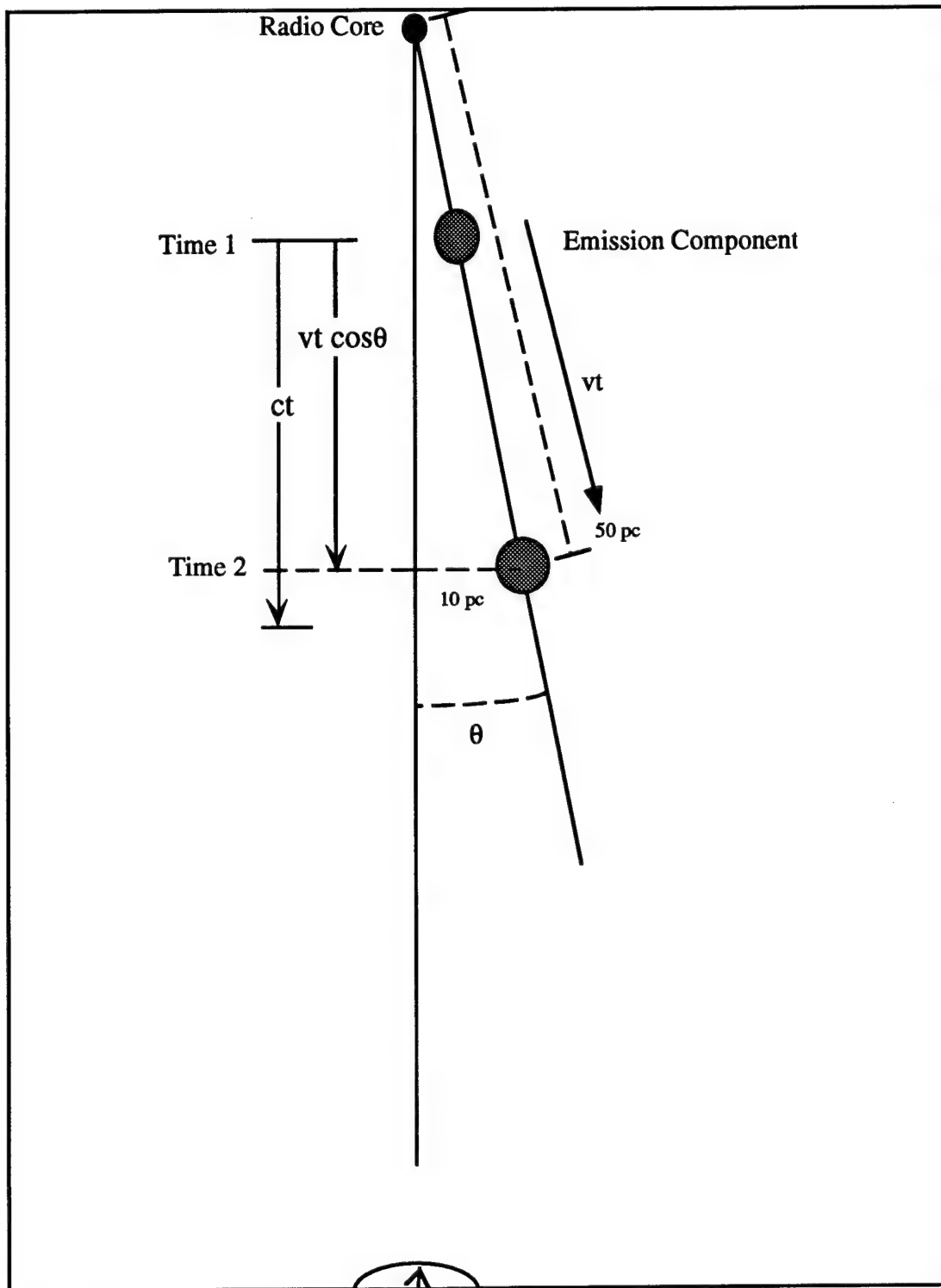


Figure 1: The conditions which give rise to the superluminal motion observed in quasars using VLBI.

The standard kinematic model for relativistic jets is a quasi-steady relativistic supersonic jet with emission from both an underlying jet and from shocks propagating down the jet either in the fluid or behind plasma blobs emitted from the core (Blandford and Königl, 1979). In VLBI maps there appears a stationary optically thick core component in all core dominated radio sources which is taken to be the point where  $\tau = 1$  in the jet, so that the core component is beamed as much as at least some of the shock components. The beaming of the core is required to avoid having the optically thin components swamp the core due to the Doppler boosting of the flux given by

$$S_{obs}(\nu) = S_{em}(\nu) D^{3-\alpha} \quad (1.6)$$

where  $S_{obs}$  is the observed flux,  $S_{em}$  is the emitted flux,  $\nu$  is the frequency, and  $D$  is the Doppler factor given by

$$D = \frac{1}{\gamma(1 - \beta \cos \theta)} \quad (1.7)$$

where  $\beta$  is the speed of the moving fluid,  $\theta$  is the angle of the jet to the line of sight, and  $\gamma$  is the standard relativistic factor. The spectral index enters equation 1.6 to account for the blueshifting of the emitted photons in a power law spectrum. Note that small bends in the jet can have a dramatic effect on the observed flux, since the flux varies with the Doppler factor to a high power.

The observed electric vector position angle,  $\xi$ , for synchrotron emission is also modified by beaming considerations to

$$\tan \xi = \frac{\gamma^{-1} \sin \theta \sin \psi' + (\cos \theta - \beta) \cos \psi'}{\tan \eta' (1 - \beta \cos \theta)} \quad (1.8)$$

where the angles are defined in figure 2 with primed values measured in the frame of the jet. Specifically  $\theta$  is the angle between the jet axis and the line of sight to the observer,  $\psi$  is the angle from the  $z$  axis to the projection of the magnetic field direction

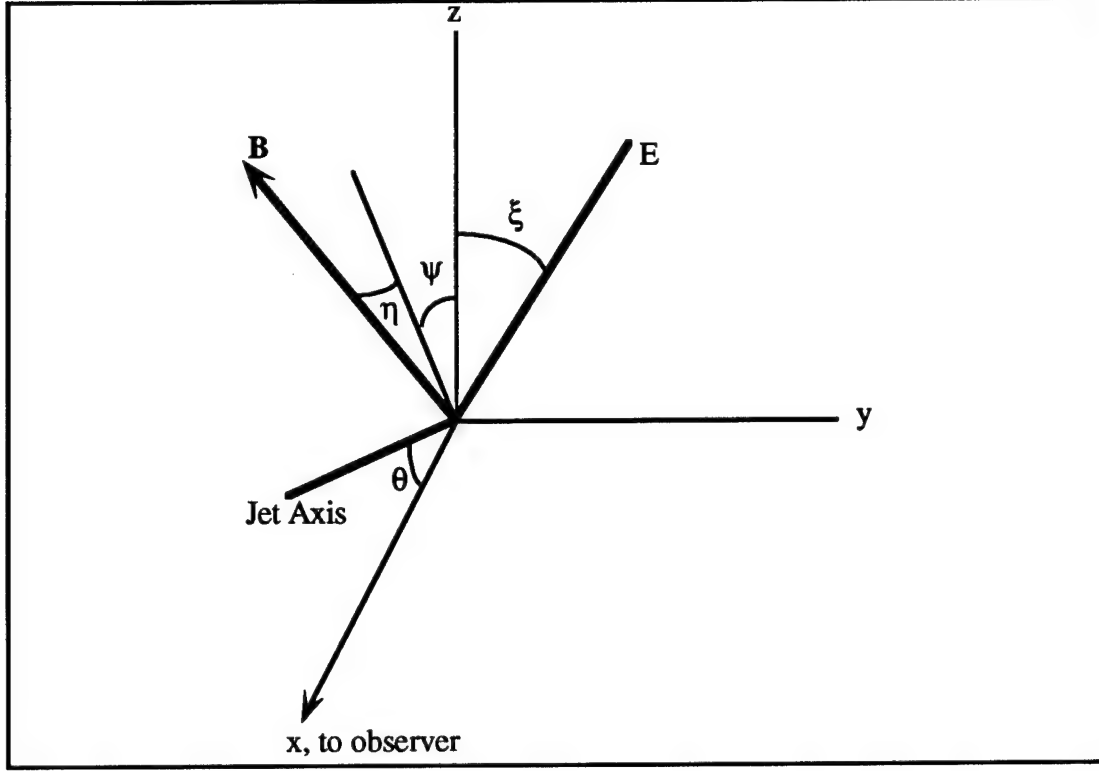


Figure 2: Coordinate and angle definitions used in equation 1.8.

onto the x-z plane, and  $\eta$  is the angle from the x-z plane to the B field vector. For a magnetic field which is parallel to the jet axis,  $\psi' = 90^\circ - \theta$  and  $\eta = 0$ , so that  $\tan \xi = \infty$  (*i.e.* the E field vector lies along the y axis here) and the observed electric field direction is perpendicular to the projected jet axis (which runs along the z axis here). For a magnetic field which is perpendicular to the jet axis,  $\psi' = -\theta$  and  $\eta$  is indeterminate, so that the numerator reduces to zero making the observed electric field lie parallel to the jet axis (both are along the z axis here). The fractional polarization in the jet will generally be less than the maximum synchrotron value as the magnetic field is tangled and ordered only to some extent by the shocks or shearing in jet.

Given the fact that VLBI polarization measurements indicate substantially different magnetic field structures in quasars and BL Lacs, it is not surprising that two

models for the ordering of magnetic fields in parsec-scale jets exist. The first is basically a handwaving shearing model in which the initially random magnetic field gathers a component parallel to the jet axis by its interaction with the external medium through which it moves. This model yields a fractional polarization  $m$  given by (Kollgaard, Wardle and Roberts, 1990)

$$m = m_0 \frac{3B_p^2 \cos^2 \epsilon}{3B_p^2 \cos^2 \epsilon + 2B_R^2} \quad (1.9)$$

where  $m_0$  is the maximum possible synchrotron polarization for a purely parallel field,  $B_p$  is the fraction of the field parallel to the jet,  $B_R$  is the fraction of the field which is random, and  $\epsilon$  is the emission angle in the frame of the fluid with  $0^\circ$  being perpendicular to the jet axis. The angle  $\epsilon$  is related to the jet axis to line of sight angle through aberration by

$$\sin \epsilon = \frac{\cos \theta - \beta}{1 - \beta \cos \theta} \quad (1.10)$$

with the definitions as above. The maximum polarization for synchrotron emission in a totally ordered field depends on the electron energy distribution and is given by (Rybicki and Lightman, 1979)

$$m_o = \frac{p+1}{p+\frac{7}{3}} = \frac{\alpha-1}{\alpha-\frac{5}{3}} \quad (1.11)$$

where  $p$  is given by  $N(E) \propto E^{-p}$  dp, with  $N(E)$  being the number of electrons at the energy  $E$ , and  $\alpha$  is the spectral index, which is related to  $p$  by  $\alpha = (1 - p)/2$ . In this model the observed electric field vector is always perpendicular to the jet direction.

The second model of magnetic fields in jets was developed to explain single dish observations of BL Lacs (Aller, Aller and Hughes, 1985; Hughes, Aller and Aller, 1985). This model is extremely detailed and considers a piston-driven shock which

compresses a region of the jet perpendicular to the jet axis, causing a tangled magnetic field to compress in a plane and become partially ordered (*i.e.* a Laing sheet) (Laing, 1980). VLBI polarization observations of the BL Lac OJ 287 (Roberts, Gabuzda and Wardle, 1987) could only be explained by modifying the shock model to allow the fluid speed (the velocity of the fluid which is emitting the radiation) to differ from the pattern speed (the speed of the shock in the jet which is observed as the component movement) (Cawthorne and Wardle, 1988). In this case the beamed flux goes as

$$S_{obs}(\nu) = S_{em}(\nu) D_s^{3-\alpha} D_{fs}^{2-\alpha} \quad (1.12)$$

with  $D_s$  being the Doppler shift of the shock

$$D_s = \frac{1}{\gamma(1 - \beta \cos \theta)} \quad (1.13)$$

with  $\beta$  and  $\theta$  measured in observer's frame, and  $D_{fs}$  being the Doppler shift of the fluid

$$D_{fs} = \frac{1}{\gamma_f(1 + \beta_f \cos \theta_f)} \quad (1.14)$$

where  $\beta_f$  and  $\theta_f$  are values for the fluid measured in the shock's frame of reference with  $\beta_f$  positive for flow from the shock towards the core. For the simple piston-driven shock, the  $D_{fs}$  term is dropped and the standard formula for beaming is recovered. The apparent velocity goes as in equation 1.4 with the  $\beta$  and  $\theta$  of the shock used. In this model the fractional polarization depends on both the apparent viewing angle of the jet,  $\epsilon$ , and the strength of the shock, measured by the factor  $k$ , which is the length of a unit length of the jet after compression (*i.e.*  $0 < k < 1$ ). The fractional polarization is then

$$m = m_0 \frac{(1 - k^2) \cos^2 \epsilon}{2 - (1 - k^2) \cos^2 \epsilon} \quad (1.15)$$

where  $\epsilon$  is given in equation 1.10. In this case the electric field vector lies parallel to the jet axis. Appendix A presents an interactive program for the Macintosh computer

system which allows exploration of the parameter space of the jet models presented above.

A further observational complication to the study of the parsec-scale polarization properties of blazars is the possibility of Faraday rotation in the intervening medium. The observed electric field vectors can be rotated after they leave the jet by free electrons coupled with magnetic fields along the line of sight to the jet. This effect is important for our interpretation of the observed electric field vectors in terms of magnetic field directions in the jets. The electric field vector position angles noted in the model descriptions above assume that any Faraday rotation effect has been removed from the observation. The causes of Faraday rotation and the implications of its presence are discussed in chapter 4, however the importance of Faraday rotation measurements in the construction and testing of unified schemes is dealt with in section E below.

#### *D. Non-Radio Characteristics of AGN*

In interpreting the radio observations presented in this work, it is useful to have a simple picture of the behavior of quasars and other AGN in all wavebands. Here a very brief, and naturally incomplete, overview of some important observational characteristics of AGN is given.

##### *1. Emission Lines*

In general, the most reliable characteristic for defining an AGN is the presence of emission lines from the nuclear region of an extragalactic object, *i.e.* either from a QSO which does not show extended structure or from the nucleus of a resolved galaxy. One exception is a BL Lac, where the emission lines are often very weak and sometimes are not detected. For QSOs and Sey I galaxies, the defining characteristic is

the presence of broad emission lines. From the lack of forbidden and semi-forbidden lines in the observed broad emission lines and from their widths, the regions emitting the broad lines are known to have densities on the order of  $10^8 - 10^9 \text{ cm}^{-3}$  and velocities of  $10^4 \text{ km s}^{-1}$  (Weedman, 1986). The size scale of the region emitting broad lines, known as the Broad Line Region (BLR), can be deduced from measurements of nearby variable Sey I galaxies (Clavel *et al.*, 1991; Peterson *et al.*, 1991; Peterson and Gaskell, 1991; Dietrich *et al.*, 1993; Peterson *et al.*, 1993). By noting the delay between the change in the continuum flux and the broad emission lines and by assuming that the continuum photoionizes the broad line emitting gas, the size scale for the clouds emitting each broad line can be determined. Delays in the well studied active galaxy NGC 5548 indicate that the BLR is stratified with the more highly ionized emission lines lying closer to the continuum source (Clavel *et al.*, 1991). The typical size scale for the BLR in Sey I galaxies is less than 0.1 pc in radius.

All AGN (except BL Lacs) show emission line features which are not highly Doppler broadened (widths of  $\sim 1000 \text{ km s}^{-1}$ ) and which have luminosity in forbidden lines. The line ratios indicate that the densities of the emitting gas are on the order of  $10^4 \text{ cm}^{-3}$  at a temperature of  $10^4 \text{ K}$ , indicative of photoionized clouds (Netzer, 1989). Since these lines are narrower and have lower ionization states than the broad lines, it is assumed that the emitting material lies farther from the central source than the broad line emitting material in a region known as the Narrow Line Region (NLR). Observations using CCD cameras in seeing conditions under 1 arcsecond have resolved the NLR in low redshift objects in O[III] and in high redshift objects in O[II] (Hutchings, 1992). The gas is not isotropically distributed but aligns with the extended radio emission on two sides of the central source. The radius of the NLR is typically on the order of 100 pc.

## 2. Absorption Lines

In addition to emission lines, many high redshift AGN show intervening absorption systems. The bulk of the systems form the Ly- $\alpha$  forest, so named because of the vast numbers of lines seen in many objects (and perhaps because you cannot always see the line for the forest). The Ly- $\alpha$  forest appears to be made of  $\sim 10^7$  solar mass clouds showing column densities of  $10^{15} \text{ cm}^{-2}$  for neutral hydrogen (Carswell, 1988). A second group of intervening absorbers are believed to be galactic disks because of the presence of heavy elements and the much higher column densities of  $3 \times 10^{18} \text{ cm}^{-2}$  (Sargent, 1988).

Some AGN also show associated absorption systems at or near the redshift of the AGN. Roughly 10% of all QSOs are broad absorption line QSOs (BAL-QSOs) which show broad absorption troughs in the continuum arising from absorption blueward of the QSO core. The absorbing material is assumed to be clouds blown outward from the QSO and moving toward us to introduce the observed blue shifting of the absorption (Weymann, Morris and Anderson, 1988). It is unclear whether the material responsible for broad absorption lines is anisotropically distributed, isotropically distributed with a low covering factor, or simply absent in some QSOs, although for low ionization BAL-QSOs the lack of O[III] emission might indicate covering factors near 100% (Boroson and Meyers, 1992). However studies of QSO spectra seem to indicate the presence of high velocity (0.03 to 0.1 c) ionized gas in all radio quiet QSOs, which may indicate that BAL-QSOs are merely those with this gas along our line of sight to the core (Stoche *et al.*, 1992).

BAL-QSOs are significant to our understanding of quasars, since broad absorption lines anti-correlate strongly with radio loudness in QSOs (Barthel, Tytler and Thomson, 1990). Although it is tempting to consider that the QSO is driving the



material responsible for the broad absorption lines outward and that this material is blocking the formation of a radio jet, the low covering factors suggested in spectroscopic studies of most QSOs suggest that if all QSOs had the potential to be radio loud, then 80% of QSOs would have strong radio emission. It may simply be that there are objects which will not emit radio radiation and those that will, and then it would not be clear to which group BAL-QSOs belong.

Some QSOs show narrow absorption line systems with redshifts close to the QSO redshift. Unlike the associated broad absorption systems, such systems correlate with radio loudness and are always at or slightly redder than the QSO redshift, so that these clouds are either stationary with respect to the core or are infalling (Foltz *et al.*, 1988). These systems may be related to the Ly- $\alpha$  emission systems seen near the QSO redshift in some radio loud quasars (Hu *et al.*, 1991), which stand out amid the general lack of Ly- $\alpha$  systems near the QSO redshift for QSOs in general (Sargent, 1988).

The significance of the correlation of narrow absorption line systems with radio emission in QSOs and the anticorrelation of broad absorption line systems with radio emission is not yet understood. The correlations do appear quite strong and so are worthy of note when considering larger questions concerning the origins and mechanisms of radio emission in AGN.

### *3. Infrared, Optical, and Ultraviolet Continuum*

The overall spectrum of any QSO approximates a power law of spectral index  $\alpha = -1$  from the infrared through the ultraviolet, so that the power in every regime is roughly equal to that at all other regimes (*i.e.* a graph of  $\log(vf_v)$  vs.  $\log v$  is flat). However the power law over many orders of magnitude is not indicative of a single cause for the emission in all wavelength regimes, but rather appears to be a superposition of a number of components. Finer details present in QSO spectra indicate the presence of multiple components of emission and four main types of QSO

spectra can be recognized (Impey, 1989). Observationally these "corrections" to the  $\alpha = -1$  power law are small, however they are important as they give clues to the actual emission processes. Some QSOs show enhanced emission in the IR which could come either from reprocessing of radiation by dust or from synchrotron emission. Others show breaks in the optical to UV power law, one type of object showing a sharp break and the other showing a weak break. These are likely to arise from enhanced thermal UV emission from a hot accretion disk around the central power source, with the steepness of the break determined by other factors such as the enhancement of the underlying optical power law emission by beaming or obscuration of the accretion disk. Finally some quasars show only slight deviations and keep the power law through the UV. Although this could arise from the chance matching of the many components, the fact that most QSOs showing only slight deviations from the power law are blazars (Impey and Tapia, 1990) suggests that it is the beamed emission from the relativistic jet which is observed through the optical regime. The minor deviations from the power law, which indicate the presence of many components of emission, make it clear that QSOs have substantial structure which must be understood in order to form a coherent picture of the objects. The approximately 10% of QSOs showing a power law which extends roughly into the radio regime are the quasars.

The small subset of AGN known as blazars show variability in their continuum power output on time scales  $\Delta t$  short enough that the light travel time across the region of the variability,  $c\Delta t$ , suggests a size where the Eddington limit is exceeded by the variable component of the emission. The Eddington limit arises from the radiation pressure, which pushes outward from the central source on any infalling matter and forces it outward if the luminosity is high enough. Effectively, the radiation density is so high in a region of size  $c\Delta t$  that all matter should be forced out of the region, even if a black hole of Schwarzschild radius  $c\Delta t$  is present, thus removing any possible fuel to

power the luminosity. To overcome the Eddington limit and keep the blazar shining, it is necessary for the observed optical flux to be beamed, so that the isotropic luminosity of the source is lower than that calculated from the flux.

QSOs with such variability are called optically violently variable quasars (OVVs). Observationally there is also a class of QSOs which at times show high optical polarization (greater than 3%) which are called highly polarized quasars (HPQs), but it is now recognized that these two sets of objects are the same (Moore and Stockman, 1984). BL Lacs also show optically violently variable behavior and high optical polarization, but OVV/HPQs have equivalent widths greater than  $5\text{\AA}$  in the emission lines. By selecting VLA radio images which have flat spectrum VLA cores stronger than the extended radio flux at 5 GHz (*i.e.* CDQs), objects are chosen which are also OVV/HPQs roughly 60-70% of the time. Once the duty cycle for high polarization (HPQs do not show their maximum polarization at all times) is considered, CDQs may all show high optical polarization (Impey and Tapia, 1990). There is some redshift dependence in these measurements with high redshift objects showing a smaller probability of having high optical polarization, which could result from the redshifting of the peak of emission from a hot accretion disk from the UV into the optical regime (Wills *et al.*, 1989). The variability in the optical is linked to variability observed in the radio as well, with the optical variability leading radio variability by one to two years in all blazars (Bregman and Hufnagel, 1989; Hufnagel and Bregman, 1992).

#### *4. High Energy Emission*

At higher energies, AGN continue to emit energy at rates equivalent to the optical emission. For blazars, the observed variability in X-ray flux appears to be tied in some objects to the radio variations, while in others it is tied to the infrared to ultraviolet variation (Begelman, 1989). Therefore it is likely that in some objects

substantial X-ray emission arises from inverse Compton scattering of either radio or infrared synchrotron emission, the synchrotron self-Compton (SSC) process. But actual synchrotron emission of X-rays directly is also possible (Bregman, 1988). The overall spectral shape of the X-ray region follows a power law with spectral index between -0.5 and -1.0 (Mushotzky, 1988; Worrall and Wilkes, 1989), with BL Lacs appearing generally as stronger X-ray sources than quasars with mostly steep spectra ( $\alpha = -1$ ) (Garilli and Maccagni, 1990). Recent work has confirmed the correlation of radio properties with X-ray properties in that radio-loud quasars are shown to have flatter X-ray spectra than radio-quiet QSOs, with CDQs having flatter spectra than LDQs (Shastri *et al.*, 1993). This is consistent with some X-ray flux arising from the radio jet by the SSC process. Although gamma ray observations are just beginning, it appears that the overall power law continues into the gamma ray regime, so that at least the most powerful AGN have significant flux in gamma rays (Hartman *et al.*, 1993).

#### *5. The Standard Model*

From the considerable mass of published observations over the last few decades, a model of AGN structure has been developed. Figure 3 shows this model (Osterbrock, 1993) with the addition of radio jets as needed for any VLBI observation to be useful. The size scales for the BLR and NLR come from observations of relatively low power and nearby Sey I galaxies, so that the size scales could be considerably different in quasars.

#### *E. Unified Schemes*

As seen above, QSOs, quasars, BL Lacs, blazars, Seyfert galaxies, and even radio galaxies all share a number of observational features. The presence of superluminal motion in CDQs, LDQs, and BL Lacs (as well as some radio galaxies) show that orientation effects such as Doppler boosting of flux play a role in how

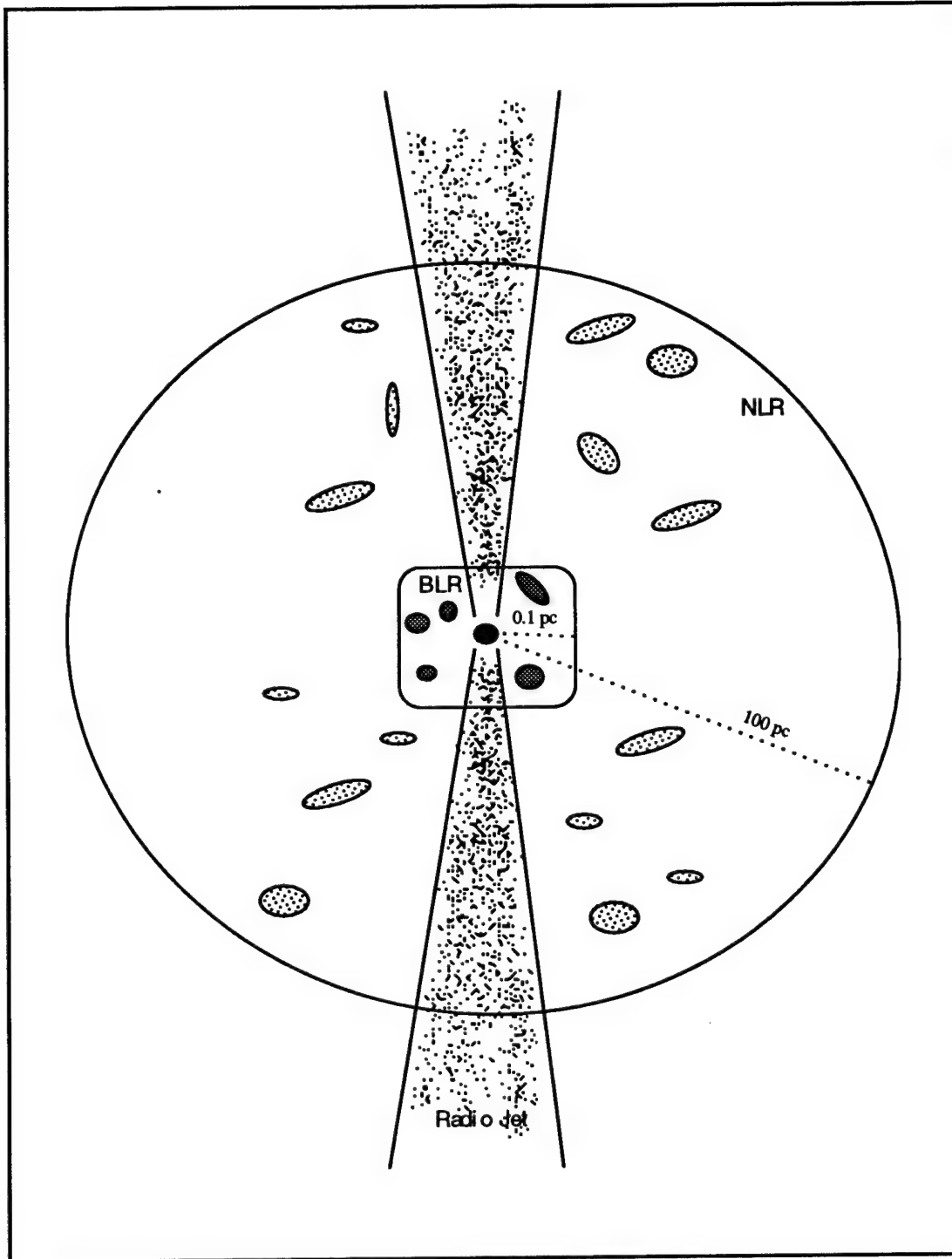


Figure 3: The standard model for quasars, showing the BLR, NLR, and radio jets.

objects appear to us. It is desirable to try to remove this observational bias, which arises from our preferred viewing angle of these objects, and to find what they look like from the side. Models which attempt to discover the appearance of objects from other viewing angles are known as unified schemes.

### *1. Radio-Quiet and CDQ Unification*

The first proposed unification was an attempt to relate the radio-quiet QSOs with CDQs (Scheuer and Readhead, 1979). In this unified scheme, CDQs are sources with weak radio emission (*i.e.* radio-quiet QSOs), which is strongly beamed. LDQs and classic double radio galaxies are different types of objects, and the detection of superluminal motion in an LDQ is given by the authors as a method to disprove this unification. Such superluminal motion has been detected and this unification cannot be correct (Hough and Readhead, 1987). There are further arguments against such a unification as well, such as the presence of faint radio emission in a halo around the CDQs but not around the radio-quiet QSOs (Kollgaard, Wardle and Roberts, 1990).

### *2. CDQ and LDQ Unification*

A more restricted unification is the combining of CDQs and LDQs as intrinsically identical sources whose radio jets are oriented within some critical angle to the line of sight or outside that critical angle respectively (Orr and Browne, 1982). This unification used the numbers of flat spectrum and steep spectrum quasars to determine the mean value for the beaming parameter in the cores and determined that  $\gamma \sim 5$ , which was in agreement with values determined from studies of superluminal motions on VLBI scales (Cohen and Unwin, 1982). This scheme is clearly correct in some way, as CDQs and LDQs form a continuous distribution as noted above. What is not yet clear is if together CDQs and LDQs form the complete range of sources with angles to the line of sight from  $0^\circ$  to  $90^\circ$ , or whether they cover only part of that range. One

problem which has not yet adequately been addressed is whether observational bias removes the LDQs lying closest to the plane of the sky from our data sets.

### 3. CDQ, LDQ, and FR II Unification

The detection of superluminal motion in the largest (*i.e.* most extended in radio emission) LDQ inspired a further unified scheme (Barthel *et al.*, 1989). Since the LDQs appear to be beamed and must therefore not lie in the plane of the sky, they cannot be the parent (unbeamed) population for CDQs but instead must have some parent population. In order to provide a parent population, powerful FR II radio galaxies were added to the quasar unification, so that FR II galaxies are the sources closest to the plane of the sky, with LDQs have jets oriented toward us but not as close to the line of sight as CDQs (Barthel, 1989). Studies of the radio luminosity functions and number densities of CDQs, LDQs, and FR IIs appear consistent with this unification if CDQs lie within  $\sim 14^\circ$  to the line of sight, LDQs lie from  $\sim 14^\circ$  to  $\sim 40^\circ$  to the line of sight, and FR II galaxies lie within  $\sim 50^\circ$  of the plane of the sky (Padovani and Urry, 1992). Furthermore, recent studies of the infrared emission of radio galaxies suggest that the lower IR emission seen in radio galaxies may represent the lack of a beamed IR component dependent on the core radio flux, consistent with radio galaxies being unbeamed quasars (Impey and Gregorini, 1993). The primary problem with this unification scheme is that radio galaxies do not show the optical characteristics of QSOs, particularly the strong broad emission lines. However, some well-studied Sey II galaxies, which by definition lack broad emission lines, have detectable broad emission lines in polarized flux, presumably due to reflection off a region illuminated by a hidden BLR (Miller, 1988; Tran, Miller and Kay, 1992). This suggests that radio galaxies may have a hidden BLR which would make them similar to QSOs (except, naturally, for the stellar appearance on a photographic plate). The sizes of quasar BLRs is unknown, but they are suspected to be much larger than what could be obscured by

an accretion disk or dusty torus. However Sey I BLR sizes determined by reverberation mapping appear to be much smaller (by roughly an order of magnitude) than predicted from photoionization models which are used to predict quasar BLR sizes (Eracleous and Halpern, 1993). If quasar BLR regions are similarly smaller than expected, it is possible that radio galaxies are quasars with obscured BLRs. The anticorrelation seen between radio core dominance and the width of broad emission lines is consistent with the BLR being constrained in a circular orbit perpendicular to the radio axis around the central power source, which suggests further that the BLR may be hidden in sources close to the plane of the sky (Wills and Browne, 1986). One problem remains in the fact that the O[III] emission, believed to come from the extended NLR, is weaker in FR II galaxies than in quasars (Browne, 1989), and any unified scheme must find a way of explaining this difference.

#### *4. BL Lac and FR I Unification*

In a like manner to the quasar-radio galaxy unification, a BL Lac-FR I unification has been proposed in which FR I galaxies are the parent population of BL Lacs (Wardle, Moore and Angel, 1984; Padovani and Urry, 1991; Padovani and Urry, 1992). These models taken together form a complete picture of the powerful extragalactic radio sources as two distinct types, relatively low power FR I sources, which when the core is beamed are BL Lacs, and relatively high power FR II sources, which when the core is beamed are quasars. Unfortunately deep VLA images of BL Lacs do seem to indicate that a substantial number have extended structure typical of FR II galaxies and not the FR I structure predicted to be seen in all BL Lacs (Kollgaard *et al.*, 1992). It appears therefore that FR I and FR II galaxies together form the parent population for BL Lacs. FR II galaxies may still form the parent population of quasars, but the strong division between FR I/BL Lacs on one hand and FR II/quasars on the other hand is clearly incorrect.



### 5. Unified Schemes and Polarization VLBI

The application of polarization VLBI as a test of unified schemes is extremely powerful. As noted earlier there is a clear distinction in the milliarcsecond linear polarized structure between quasars and BL Lacs, which brings into question any of the unified schemes linking quasars and BL Lacs (*e.g.* Wills *et al.*, 1992).

Faraday rotation measurements and improved dynamic range VLBI polarization imaging will help determine the validity of the quasar-FR II unification scheme as well. FR II galaxies show parallel magnetic fields on the smallest VLA scales, so that the magnetic fields seen by many milliarcseconds out from the VLBI core should be well aligned with the jets if this unified scheme is valid. If measurements of quasars show that magnetic fields are aligned in milliarcsecond quasar jets, either throughout their length or near the arcsecond scale, the quasar-FR II unified scheme will have passed an important test. As more sensitive measurements can be made using the VLBA, it may be possible to check FR II milliarcsecond polarized structure as well to check that it shows the same features as seen in quasars, although the weak cores of FR II galaxies present problems in making these measurements.

A further test of the quasar-FR II unification would be possible if FR II cores are detected in polarized flux. Under this unification scheme, quasars and FR II galaxies should have similar NLRs. Since the Faraday rotation seen on parsec scales probably arises in the NLR, FR II galaxies and quasars should show the same statistical variation in Faraday rotation on the parsec scale. Any significant differences would require an anisotropic model of the NLR.

Evidence which is consistent with the quasar-FR II unified scheme is presented here. The milliarcsecond structure of two quasars is shown to have FR II style magnetic fields even down very near the VLBI core. The Faraday rotation measurements on these two quasars also provide the first measurements of the NLR

integrated electron density-magnetic field along the line of sight to a quasar core. These measurements, when augmented by future measurements, will provide the basis for comparison of FR II and quasar NLR properties. Determination of the characteristics of the NLR from VLBI measurements presented here will help in the interpretation of optical observations of emission lines from this region.

## **II. Very Long Baseline Interferometry**

### *A. History*

The primary purpose of radio interferometry is to create an effective aperture equivalent to that of a single antenna too large to build as a single structure, either due to cost or structural limitations (in the case of VLBI this is the desire not to hollow out the earth). Because the effective aperture is not filled, the measurements which are obtained (the Fourier transforms of the sky brightness distribution) are incomplete and do not fill the Fourier transform space (the uv plane) of the sky brightness, as the measurements from a single mirror do. Due to this sparse coverage in the uv plane, reconstructing the sky brightness from the incompletely sampled Fourier components cannot be done simply by performing the inverse Fourier transform, and a number of methods, discussed below, for handling such interferometric data have been developed.

The first successful radio interferometry was done using a radio telescope that overlooked the sea in Australia (McCready, Pawsey and Payne-Scott, 1947). As the sun rose over the sea, the antenna picked up radiation directly from the sun and from its reflection off the water. The resulting interference pattern showed that the radio radiation from the sun originated in areas much smaller than the solar disk and was related to sunspots. In general, both a lack of sensitivity and the failure to recover phase information limited early interferometry to strong sources, such as the brightest

of the extragalactic radio sources (then called 'radio stars') and the sun. These limitations were overcome by the development of the phase-switching interferometer, in which an amplifier was built in at the antenna to boost the signal before it was transmitted for correlation, and in which a half-wave delay line was added that was switched in and out during observations (Ryle, 1952). The amplification of the signal and the ability to determine phase information gave the phase-switching interferometer increased sensitivity and the ability to determine, far more accurately than had been previously possible, the position of sources of radio radiation. The development of phase sensitivity also led to the determination that some sources were asymmetric (Jennison and Das Gupta, 1953).

The measurement of a single interference fringe often took the work of a number of groups making observations over an extended period, because of the difficulty of maintaining the calibration of the electronics. A method to overcome this limitation was developed by using phase closure relations which remove instrumental (and atmospheric) terms when a triangle of baselines is available (Jennison, 1958). From these measurements, requiring three or more antennas, true astronomical phases and amplitudes could be measured without the tedious, intensive calibration which had been required throughout any observation. As electronics improved, the calibration became easier, and the closure relations remained unexploited until their rediscovery for VLBI mapping.

From the fringes measured in early interferometry, it was possible to determine whether a source is pointlike or has a roughly double structure, and a rough size estimate of the separation of components in complex sources could be obtained. However, any detailed imaging or mapping of the structure was impossible because of insufficient coverage in the uv plane (*i.e.* the Fourier transform of the sky brightness was too poorly sampled to allow any attempt at the inverse transformation since each

baseline gave only a single uv point). By using both moveable antennas and the rotation of the earth to change the baselines, reasonable coverage in the uv plane was obtained (Ryle and Hewish, 1960). The technique, called aperture synthesis since the aperture is effectively constructed fringe by fringe, allowed the first images of the detailed structure of radio sources to be made. Both a moveable antenna and the use of the earth's rotation were incorporated in the design of the Cambridge radio telescope, which was the first dedicated interferometer built for high resolution studies of weaker radio sources (Ryle, 1962).

The successes of the the Cambridge telescope and other interferometers in the 1960's created interest in extending the baselines to the maximum distances possible, roughly the diameter of the earth. Early interferometric measurements were made using linked elements with the correlation done in real time. However, for VLBI observations such links were impossible, and they are still not cost effective. Instead the signals from the radio sources were mixed down to lower frequencies using separate, stable local oscillators and recorded on magnetic tape. The signals were later correlated from the recorded data. The first successful detection of fringes in VLBI was done between antennas of the Algonquin Radio Observatory, the Dominion Radio Astrophysical Observatory, and Defense Research Communications Establishment near Ottawa, Canada, using rubidium frequency standards and magnetic tape recorders (Brotten *et al.*, 1967). This experiment determined minimum sizes for a number of quasars but did not resolve any structure. A second VLBI experiment using different antennas obtained the first detection of milliarcsecond structure in a source, when 3C 237 was resolved at 21 cm (Bare *et al.*, 1967).

Within two years of the first fringes being detected, changes in the milliarcsecond structure of 3C 273 seen in the fringes appeared to require superluminal motion in the form of the expansion of a radio component (Gubbay *et al.*, 1969).

Observations using the Haystack radio telescope in Massachusetts and the Goldstone antenna in California showed changes in the fringes for 3C 279 which seemed to require a double structure with superluminal separation speeds for the two components (Whitney *et al.*, 1971). A number of possible models for these observations were proposed including relativistic jets (note that this paper is a model of how to extend the length of a *Science* publication through judicious use of lengthy and frequent endnotes). Later observations confirmed the required superluminal changes in 3C 273 (and also in 3C 279), and now it appeared that there was direct evidence for superluminal separation of components in 3C 273 (Cohen *et al.*, 1971). However, until mapping of these sources with milliarcsecond resolution became possible in the mid-1970's, the presence of superluminal expansion was doubted because of other possible interpretations of fringe changes involving flux density changes in components (Pearson and Zensus, 1987).

### *B. Basic Equations for VLBI*

This section draws on the work of Roberts, Wardle, and Brown (Roberts, Wardle and Brown, 1994, hereafter RWB) and Thompson, Moran, and Swenson (Thompson, Moran and Swenson, 1986, hereafter TMS) for derivations and presentation.

#### *1. The Fourier Transform Relationships in Interferometry*

As noted above, an interferometer measures the Fourier components (called visibilities) of the brightness distribution on each baseline. For the coordinate system defined in figure 4 (TMS figure 4.1), it is clear that the baseline coordinates  $u$  and  $v$  correspond to the plane of the sky coordinates  $\xi$  and  $\eta$  respectively. Assuming an ideal system with no noise, the Fourier transform relationship then ties the visibilities,  $V(u,v)$ , to the sky brightness distribution,  $B(\xi,\eta)$ , by

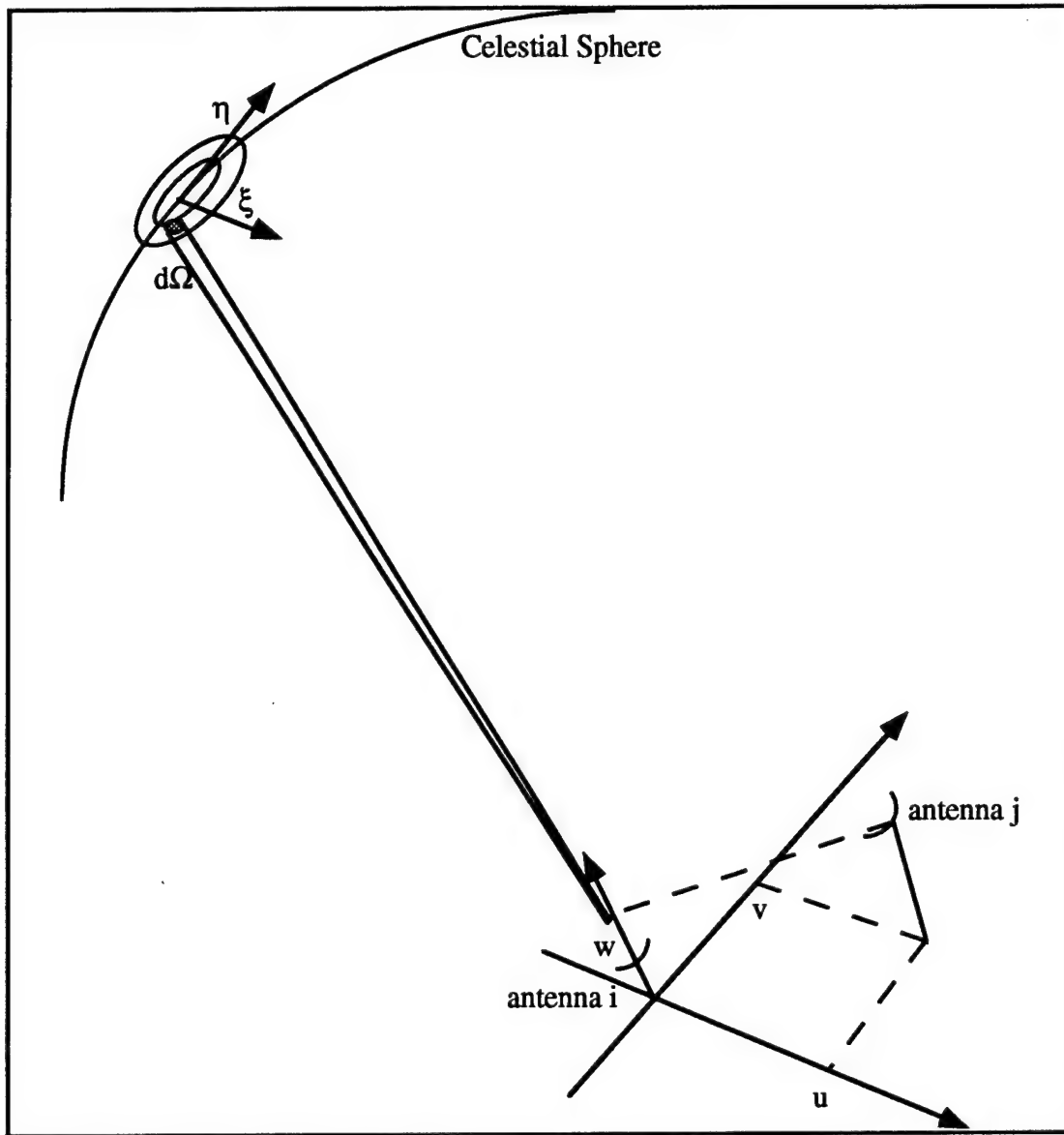


Figure 4: The coordinate system used in interferometric observations.

$$V(u, v) = \int_{-\infty}^{\infty} \int_{-\infty}^{\infty} B(\xi, \eta) e^{+i2\pi(u\xi + v\eta)} d\xi d\eta \quad (2.1)$$

$$B(\xi, \eta) = \int_{-\infty}^{\infty} \int_{-\infty}^{\infty} V(u, v) e^{-i2\pi(u\xi + v\eta)} du dv \quad (2.2)$$

so that the goal of interferometry is to measure  $V$  well enough to recover  $B$ . The sky brightness distribution can be either the total intensity or the complex polarization, so that  $V$  can involve a number of terms for each baseline. In practice these integrals are not done, and instead the discrete Fourier transforms,

$$V(u, v) = \sum_{\xi} \sum_{\eta} B(\xi, \eta) e^{+i2\pi(u\xi + v\eta)} \quad (2.3)$$

$$B(\xi, \eta) = \sum_u \sum_v V(u, v) e^{-i2\pi(u\xi + v\eta)} \quad (2.4)$$

are used, which are now manageable for modern computers handling the data from VLBI arrays. In practice the problem of determining the brightness distribution is far from solved even for an idealized system, since the visibilities are measured at only a few points in the  $uv$  plane. The result is that the estimated brightness distribution derived from equation 2.4 could contain false features, which result from the fact that many spatial frequencies are left unmeasured by the interferometer. The methods of handling these problems are dealt with in the next section.

## 2. The Stokes Parameters in Interferometry

For antennas equipped with two circularly polarized feeds, right-circular polarization (R or RCP) and left-circular polarization (L or LCP), four cross-correlations can be formed. These cross-correlations are related to the Stokes parameters (I, Q, U, and V) describing the radiation field by (RWB)

$$\begin{aligned} R_i R_j^* &= \tilde{I}_{ij} + \tilde{V}_{ij} \\ L_i L_j^* &= \tilde{I}_{ij} - \tilde{V}_{ij} \\ R_i L_j^* &= \tilde{Q}_{ij} + i\tilde{U}_{ij} \\ L_i R_j^* &= \tilde{Q}_{ij} - i\tilde{U}_{ij} \end{aligned} \quad (2.5)$$

where the subscripts  $i$  and  $j$  refer to the  $i$ th and  $j$ th antennas in a baseline, the  $\sim$  indicates values in the Fourier transform plane (the  $uv$  plane) of the sky brightness, and the  $*$



indicates the complex conjugate which arises naturally in the cross-correlation (see Gabuzda, 1988, for a discussion of this). These equations assume ideal antennas and feeds along with perfect calibration, so that the measured correlations have no instrumental or atmospheric contributions. Since circular polarization is very small in synchrotron sources,  $V$  is roughly zero. Then the  $RR^*$  and  $LL^*$  cross correlations each measure the Fourier transform of the total intensity,  $I$ , of the sky brightness distribution. Total intensity VLBI is concerned only with these correlations, and generally uses only one of the feeds on each telescope in order to increase the bandwidth recorded on tape. However, when both correlations are present the exact total intensity can be recovered by adding them together and dividing by two, which eliminates  $V$ .

The linear polarization information resides in the  $Q$  and  $U$  terms of the Stokes parameters. These are handled most conveniently with a complex term (RWB)

$$P = Q + iU = pe^{+2i\chi} \quad (2.6)$$

where  $P$  is the complex polarization,  $p$  is the linearly polarized flux, and  $\chi$  is the position angle of the electric vector on the sky. All the terms on the left hand side of equations 2.5 depend both on the baseline ( $uv$  spacing) and time, while the terms on the right hand side depend on the position on the sky ( $\xi\eta$  spacing) and time.

Equation 2.4, in conjunction with equations 2.5 and 2.6, can be used to determine the sky distribution of total intensity and complex polarization. Then

$$I(\xi, \eta) = \sum_u \sum_v \tilde{I}(u, v) e^{-i2\pi(u\xi + v\eta)} \quad (2.7)$$

gives the total intensity on the sky, while

$$P(\xi, \eta) = \sum_u \sum_v \tilde{P}(u, v) e^{-i2\pi(u\xi + v\eta)} \quad (2.8)$$

gives the linear polarization on the sky. Equations 2.5 give the correlations needed for insertion into equations 2.7 and 2.8. Since the total intensity  $I(\xi, \eta)$  is real,

$$\tilde{I}(-u, -v) = \tilde{I}(u, v)^* \quad (2.9)$$

so that the  $uv$  plane can be filled in from a single  $RR^*$  or  $LL^*$  series of correlations.

For polarization mapping however, the quantity  $P(\xi, \eta)$  is complex, so that (RWB)

$$\tilde{P}(-u, -v) = (L_1 R_2^*)^* \quad (2.10)$$

which indicates that both cross-hand correlations are needed to fill the  $uv$  plane.

Obviously no interferometer is the ideal system described above. The calibration and handling of problems in the data is discussed below, together with methods of solving the problem of the incompleteness of the coverage in the Fourier transform space.

### *C. Problems and Solutions in Total Intensity Mapping*

#### *1. Flux Calibration*

The first problem which needs to be dealt with in VLBI data results from the fact that the correlation of the signals from the antennas is done digitally and involves clipping. This results in the loss of information about the flux density of the source. The best way to calibrate the visibilities in interferometry, which converts the correlation coefficients to flux densities, is to observe a point source of known flux density and determine the scaling factor for each antenna in the array. This works since the response of an ideal interferometer on each baseline to a point source is a signal of constant amplitude, equal to the total flux of the source, with zero phase. However, at VLBI resolution there are no sources which are point-like to all baselines, so another method of calibration must be used.

It can be shown (TMS equation 9.2), that the calibrated visibility (*i.e.* in flux units) in a correlation between two antennas (labelled  $i$  and  $j$ ) is given by

$$V_{ij}(u, v) = S_T \cdot b \cdot \rho_{ij}(u, v) \left\{ \sqrt{\frac{(T_{Si} + T_{Ai})(T_{Sj} + T_{Aj})}{T_{Ai}T_{Aj}}} \right\} \quad (2.11)$$

where  $S_T$  is the total source flux,  $\rho(u, v)$  is the correlation coefficient from the digital correlator,  $b$  is a correction term (applied at the correlator) accounting for the clipping, and  $T_S$  and  $T_A$  give the system temperature and antenna temperature respectively for each antenna. The system temperature is a measure of the response of the antenna while on blank sky, measured as the equivalent temperature of a resistive load of equal power, and includes a contribution from the noise. It is clear that the way to measure the antenna temperature, which is the contribution to the response of the receiver due to the source alone, thus representing the actual signal, is to measure the received power on source and then off source pointed at a section of blank sky. In practice  $T_A$  is often so small that such a measurement is unreliable except on the strongest sources with the largest antennas. Rather than use these unreliable numbers,  $T_A$  is calculated from the known flux of the source and the antenna gain curve (*i.e.* known response of the antenna).

Once the  $T_S$  numbers have been measured and the  $T_A$  numbers calculated, the visibilities can be calibrated. However, the response of the interferometer is generally not solved adequately by this method. The calibration can be improved by looking at sources which are small in extent, so that the shortest baselines do not resolve any of the structure. Then the visibility amplitudes should be flat with time (*i.e.* with changes in location in the  $uv$  plane) and should equal the total source flux. From these measurements the  $T_S$  values can be scaled to give a better estimate of the true calibrated visibility. Unfortunately as VLBI measurements are made at higher and higher frequencies, fewer sources offer sufficiently compact structure for this correction to be useful.

## 2. Phase Instability

In VLBI the amplitudes of the visibilities can be found by straightforward calculations using information taken at the telescopes during the observations (*i.e.*  $T_S$  measurements and gain curves). However the phases of the time averaged visibilities cannot be determined by any appropriate measurement at the present time. Unlike the VLA, where all antennas look through roughly the same patch of sky, VLBI antennas look through very different parts of the atmosphere, which introduce random phase delays that are not correlated between antennas. The phase delays effectively make the phases of the visibilities random with time, but the delays are antenna-based so that the true visibility phases can be recovered by antenna-based calibration.

Since the phase errors can be treated as being antenna based, there is a quantity which is easily recoverable and which contains only phases arising from the source structure, the closure phase (Jennison, 1958). Looking at the visibilities around a triangle of baselines gives

$$\begin{aligned}\angle V_{ij} &= \phi_{ij} + \phi_{Ai} - \phi_{Aj} \\ \angle V_{jk} &= \phi_{jk} + \phi_{Aj} - \phi_{Ak} \\ \angle V_{ik} &= \phi_{ik} + \phi_{Ai} - \phi_{Ak}\end{aligned}\tag{2.12}$$

where  $\angle V_{ij}$  is the phase of the measured visibility and  $\phi_{ij}$  is the true (source) visibility phase on the baseline between the  $i$ th and  $j$ th antennas, and  $\phi_{Ai}$  is the phase contribution from the  $i$ th antenna, including electronic delays and atmospheric delays. The opposite signs of the two antenna phases on each baseline enter from the fact that the correlation is complex (see below for a more thorough analysis of the correlations). From equations 2.12, a phase relation which is independent of the antenna-based phases can be formed by summing the phases around a triangle of baselines giving

$$\phi_{closure} = \angle V_{ij} + \angle V_{jk} - \angle V_{ik} = \phi_{ij} + \phi_{jk} - \phi_{ik}\tag{2.13}$$

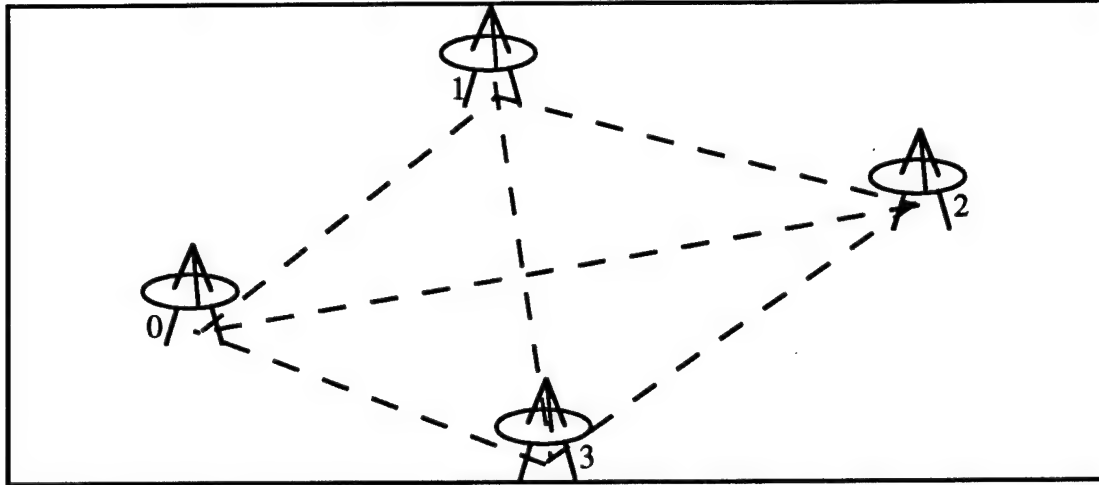


Figure 5: A set of four antennas with their baselines which are used in equation 2.14 to demonstrate self-calibration of the antenna phases.

since the antenna-based phases enter with opposite signs in the complex correlation. The closure phase contains uncontaminated information on the source structure which can be used to constrain images.

An improvement in the handling of closure phases for VLBI data arises when it is realized that the closure information is the only phase information available, and the random nature of the visibility phases arise from random antenna phases. This justifies the use of self-calibration, where the antenna phase contributions are changed by comparing the measured visibility phases to the phase of a model distribution of the source, with the constraint that such changes in antenna phases do not change the closure phases (Cornwell and Wilkinson, 1981). In figure 5, the baselines formed by a set of 4 antennas are shown. Given a model of the source, model visibilities with phases  $\phi'$  are calculated for each baseline. These are compared with the phases of the visibilities,  $\phi$ , and an estimate of the phase delay at the antenna is calculated for each baseline by

$$\begin{aligned}
\phi_{A1} &= (\phi_{10} - \phi'_{10}) \\
\phi_{A1} &= (\phi_{12} - \phi'_{12}) + \phi_{A2} = (\phi_{12} - \phi'_{12}) + (\phi_{02} - \phi'_{02}) \\
\phi_{A1} &= (\phi_{13} - \phi'_{13}) + \phi_{A3} = (\phi_{13} - \phi'_{13}) + (\phi_{03} - \phi'_{03})
\end{aligned} \tag{2.14}$$

where antenna 0 is taken as a reference antenna with zero phase delay. The correction is made to the antenna phase delay by averaging the estimates available from each baseline, either with or without weighting by the noise. These antenna phases are then used to adjust the visibility phase. A similar though somewhat more complicated adjustment can be made for the amplitude of the visibilities as well. Since VLBI sources usually show strong optically thick cores with weaker extended structure, self-calibration starting with a point source for a model recovers some of the antenna phases, and therefore, the visibility phases quite well. However, in practice the presence of strong extended ( $> 1$  milliarcsecond) VLBI emission results in poor recovery of the visibility phases by self-calibration. Generally this means that self-calibration maps the less extended BL Lacs better than quasars.

### 3. Hybrid Mapping

The basic problem for self-calibration is the determination of a model on which to perform the calibration. A point source provides a good initial model for bright core dominated blazars, but it is insufficient for determination of any structure beyond a rudimentary asymmetric double. In order to improve the determination of the source structure, hybrid mapping is used (Readhead and Wilkinson, 1978). In hybrid mapping, the results of calibration on an initial model are used to calculate new visibilities which are then Fourier transformed to give a new map, known as the dirty map. The structure of this map, as determined in a deconvolution described below, is used as a new model and the visibilities are again modified. The process is repeated until the map converges, *i.e.* until the visibilities cease to change upon calibration. In

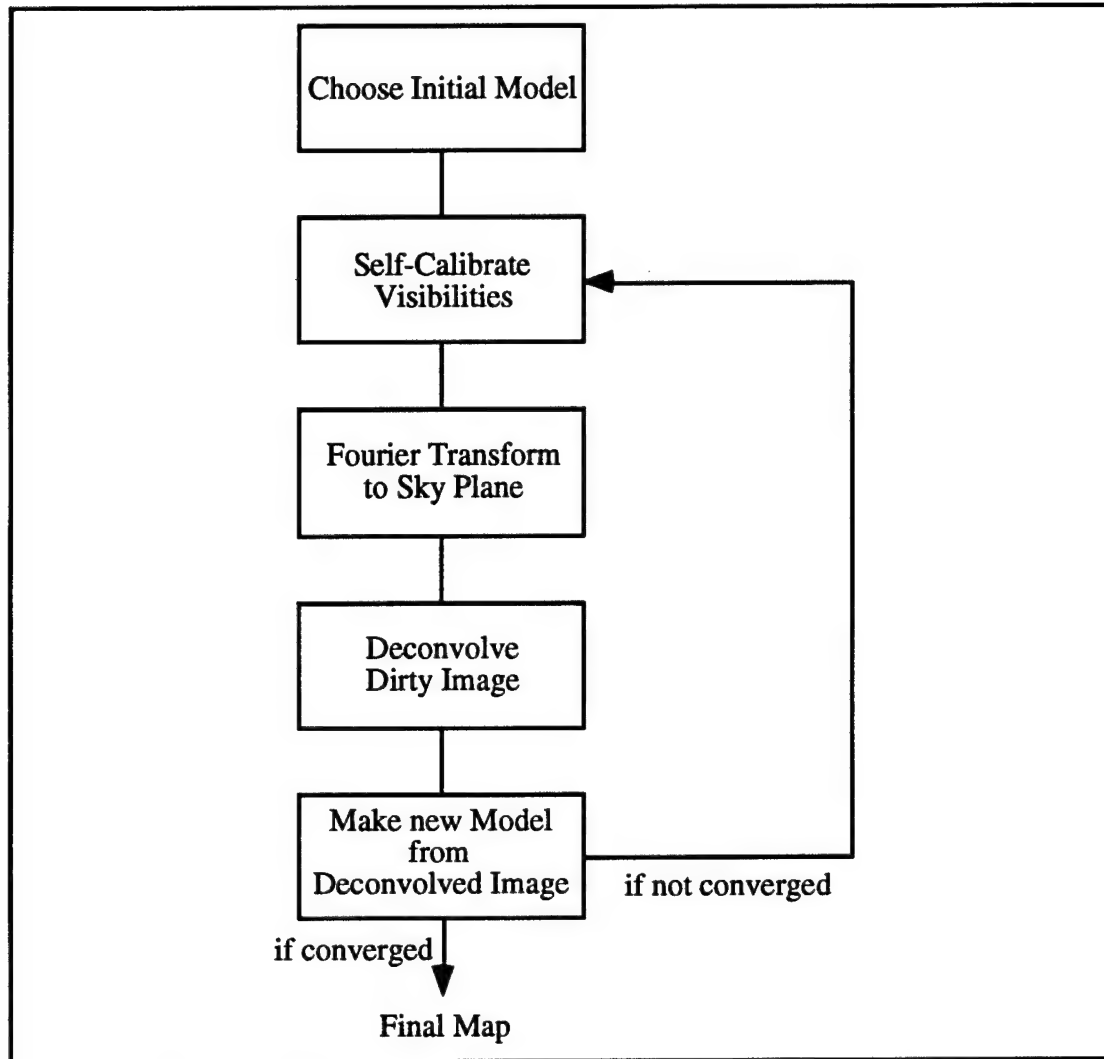


Figure 6: The process of hybrid mapping which is used to make VLBI maps.

figure 6 a flow chart for hybrid mapping including modification of the visibilities by self-calibration is shown.

#### *4. The Inverse Problem*

Since the visibilities always fail to completely sample the uv plane in VLBI, the Fourier transformation gives a sky brightness distribution with false features, due to the presence of sidelobes in the beam of the interferometer. These sidelobes have the effect

of spreading the measured flux density into a widely varying brightness distribution. The beam is defined as the response of the interferometer to a point source of unit flux density, which effectively means that each visibility measured is set to an amplitude of one and a phase of zero, and then these visibilities are transformed according to equation 2.4. The effect is to form a dirty map of a point source, known as the dirty beam in hybrid mapping.

In order to recover the true sky brightness distribution, the false features produced in the dirty map by the sidelobes of the beam must be removed. The process in effect is a deconvolution, since the dirty map can be viewed as a convolution of the true map with the dirty beam, as given by

$$I_{dirty} = \int I_{true} * P_{dirty} d\xi d\eta \quad (2.15)$$

where  $I$  is the image or map and  $P$  is the beam or point spread function of the interferometer. Effectively this is equivalent to treating the true map as a series of point sources, each of which gives a response in the dirty map equivalent to the dirty beam. The most widely used process in VLBI for performing the deconvolution is the CLEAN algorithm.

CLEAN relies on the straightforward procedure of taking the dirty map, finding its peak, and subtracting some percentage of the peak convolved with the dirty beam from the map (Högbom, 1974). This process is repeated until some preset limit is reached, either in the number of CLEAN iterations, each of which produces a CLEAN component, or in the flux level remaining in the map. CLEAN therefore treats the source as a sum of point sources, which in practice works well on the powerful sources studied by VLBI, which show a strong core with a series of components forming a jet. However, as these components move down the jet away from the core, they become more diffuse and CLEAN has difficulty successfully fitting them, since they no longer



resemble point sources. In practice this results in diffuse emission being mapped as a conglomeration of weak CLEAN components which tend to shift position randomly on successive iterations within a range determined by the scale of the diffuse emission.

The CLEAN algorithm has been mathematically analyzed for a one dimensional case, but only without the effects of noise in the data (Schwarz, 1978). It is shown that CLEAN is a least-squares fit of sine functions to the data. A problem in the analysis for VLBI is that the results of CLEAN are used to self-calibrate the visibilities for the next iteration of hybrid mapping. Since deconvolution is non-linear, the propagation effects of this process are not known.

A second method for performing the required deconvolution is the Maximum Entropy Method (MEM), which was adapted to radio astronomy from mathematical inverse theory (Gull and Daniell, 1978). In MEM the visibilities are compared to some previous desirable model, the bias image, and a measure of the entropy (a mathematical measure of the fit between the bias image and the data) in the visibilities is used to determine the best model. MEM is extremely computer intensive and became widely used only after an improved algorithm was developed in AIPS (Astronomical Image Processing System) at the NRAO, which allowed MEM maps to be made within a few hours (Cornwell and Evans, 1985). A variety of entropies are possible and the AIPS task VM maximizes the function

$$J = H - \alpha\chi^2 - \beta F \quad (2.16)$$

where  $\alpha$  and  $\beta$  are adjustable parameters which are fit during the MEM procedure.  $F$  is the total flux in the image and  $\chi^2$  is the usual chi-squared fit between model and visibilities given by

$$\chi^2 = \frac{\sum_k w_k |V_k - V'_k|^2}{\sum_k w_k} \quad (2.17)$$

where  $w_k$  is the weight for the  $k$ th visibility, and  $V_k$  and  $V_k'$  are the  $k$ th measured and model visibilities respectively.  $H$  is the entropy defined as

$$H = -\sum_i b_i \ln \left( \frac{b_i}{m_i} \right) \quad (2.18)$$

where  $b_i$  is the flux in the  $i$ th pixel of the dirty map and  $m_i$  is the flux in the  $i$ th pixel of the bias image. From equations 2.16 and 2.18 it is clear that both the image and visibility spaces come into the maximization of  $J$  and a number of Fourier transforms are done during the MEM process. Surprisingly MEM has not been very successful in application to VLBI data. It appears that the desire of MEM to make a smooth map (bias images are generally smooth distributions covering the area known to contain flux) is incompatible with the inner regions of VLBI sources which show structures of knots which are very point-like. As such, MEM requires an initial bias image made by CLEAN, which adequately shows the structure of the inner region of the VLBI jet. Once this is provided, MEM does appear to map the diffuse emission in the jet far from the core (>20 milliarcseconds) better than CLEAN can (Holdaway, 1990).

#### *D. Problems and Solutions in Linear Polarization Mapping*

In polarization VLBI the desired images are the flux distributions of the  $Q$  and  $U$  Stokes parameters since (Rybicki and Lightman, 1979)

$$\begin{aligned} p &= \sqrt{Q^2 + U^2} \\ \chi &= \frac{1}{2} \tan^{-1} \left( \frac{U}{Q} \right) \end{aligned} \quad (2.19)$$

where  $p$  is the polarized flux and  $\chi$  is the position angle of the electric field vector. As noted above, the full Stokes parameters are recovered by full correlation of two orthogonal polarizations, for linear polarization these are preferentially right circular

polarization (RCP) and left circular polarization (LCP). Then the quantities of interest can be recovered from the visibilities in equation 2.5 by (RWB)

$$\begin{aligned}\tilde{I}_{ij} &= \frac{1}{2} \left( \langle E_{Ri} E_{Rj}^* \rangle - \langle E_{Li} E_{Lj}^* \rangle \right) \\ \tilde{Q}_{ij} &= \frac{1}{2} \left( \langle E_{Li} E_{Rj}^* \rangle + \langle E_{Ri} E_{Lj}^* \rangle \right) \\ \tilde{U}_{ij} &= \frac{1}{2} \left( \langle E_{Li} E_{Rj}^* \rangle - \langle E_{Ri} E_{Lj}^* \rangle \right)\end{aligned}\tag{2.20}$$

where the angle brackets denote time averages and the notation  $E_{Ri}$  is to denote the true, or more accurately calibrated, values, since the interferometer is no longer ideal.  $I$ ,  $Q$ , and  $U$  are recovered by Fourier transformation of equations 2.20 using equation 2.4 and are functions of  $\xi$  and  $\eta$ . The correlation of the same polarization between two antennas is called a "parallel hand", while the correlation of orthogonal polarizations is a "cross hand".

### 1. Basic Theory for Polarization VLBI

A real antenna and receiving system unfortunately do not actually detect only RCP or LCP radiation. In practice there is contamination of the RCP signal by some amount of LCP waves, and *vice versa*. The response of the antenna to the radiation field can then be written as

$$\begin{aligned}R &= G_R [E_R e^{-i\phi_p} + D_R E_L e^{i\phi_p}] \\ L &= G_L [E_L e^{i\phi_p} + D_L E_R e^{-i\phi_p}]\end{aligned}\tag{2.21}$$

where  $R$  and  $L$  represent the measured voltage output of the system in RCP and LCP respectively,  $G_R$  and  $G_L$  are the antenna gains in RCP and LCP respectively,  $E_R$  and  $E_L$  are the RCP and LCP electric fields from the source respectively,  $D_R$  and  $D_L$  are dimensionless complex terms measuring how much of the orthogonal polarization is picked up by the RCP and LCP receivers respectively, and  $\phi_p$  is the parallactic angle of

the feed, which measures its orientation with respect to the source. For an altitude-azimuth mounted antenna this angle changes with the hour angle,  $H$ , of the source by

$$\tan \phi_p = \frac{\cos b \sin H}{\sin b \cos \delta - \cos b \sin \delta \cos H} \quad (2.22)$$

where  $b$  is the latitude of the telescope and  $\delta$  is the declination of the source. An equatorial mounted telescope has a parallactic angle of zero at all times, as it effectively rotates with the source. The terms  $R$ ,  $L$ ,  $G$ ,  $E$ , and  $D$  are all complex having both amplitude and phase. Our convention is that  $D_R$  measures the contamination of LCP in the RCP receiver, and  $D_L$  measures the contamination of RCP in the LCP receiver.

The correlator effectively performs a cross-multiplication and summation of the two signals given in equations 2.21, so that the four correlations between the  $i$ th and  $j$ th antennas are

$$\begin{aligned} R_i R_j^* &= G_{Ri} [E_{Ri} e^{-i\phi_{Ri}} + D_{Ri} E_{Li} e^{i\phi_{Ri}}] G_{Rj}^* [E_{Rj}^* e^{i\phi_{Rj}} + D_{Rj}^* E_{Lj}^* e^{-i\phi_{Rj}}] \\ L_i L_j^* &= G_{Li} [E_{Li} e^{i\phi_{Li}} + D_{Li} E_{Ri} e^{-i\phi_{Li}}] G_{Lj}^* [E_{Lj}^* e^{-i\phi_{Lj}} + D_{Lj}^* E_{Rj}^* e^{i\phi_{Lj}}] \\ R_i L_j^* &= G_{Ri} [E_{Ri} e^{-i\phi_{Ri}} + D_{Ri} E_{Li} e^{i\phi_{Ri}}] G_{Lj}^* [E_{Lj}^* e^{-i\phi_{Lj}} + D_{Lj}^* E_{Rj}^* e^{i\phi_{Lj}}] \\ L_i R_j^* &= G_{Li} [E_{Li} e^{i\phi_{Li}} + D_{Li} E_{Ri} e^{-i\phi_{Li}}] G_{Rj}^* [E_{Rj}^* e^{i\phi_{Rj}} + D_{Rj}^* E_{Lj}^* e^{-i\phi_{Rj}}] \end{aligned} \quad (2.23)$$

(see Gabuzda, 1988, for a derivation of the complex correlation). Each equation in 2.23 involves four terms, however the  $D$  terms tend to be of the order of a few percent of the parallel hand fringe amplitudes, as do the cross hand terms (e.g.  $E_{Li} E_{Rj}^*$ ), so that equations 2.23 can be approximated as

$$\begin{aligned} R_i R_j^* &= G_{Ri} G_{Rj}^* E_{Ri} E_{Rj}^* e^{-i(\phi_{Ri} - \phi_{Rj})} \\ L_i L_j^* &= G_{Li} G_{Lj}^* E_{Li} E_{Lj}^* e^{i(\phi_{Li} - \phi_{Lj})} \\ R_i L_j^* &= G_{Ri} G_{Lj}^* \left[ E_{Ri} E_{Lj}^* e^{-i(\phi_{Ri} + \phi_{Lj})} + D_{Ri} E_{Li} E_{Lj}^* e^{i(\phi_{Ri} - \phi_{Lj})} + D_{Lj}^* E_{Ri} E_{Rj}^* e^{-i(\phi_{Ri} - \phi_{Rj})} \right] \\ L_i R_j^* &= G_{Li} G_{Rj}^* \left[ E_{Li} E_{Rj}^* e^{i(\phi_{Li} + \phi_{Rj})} + D_{Li} E_{Ri} E_{Rj}^* e^{-i(\phi_{Li} - \phi_{Rj})} + D_{Rj}^* E_{Li} E_{Lj}^* e^{i(\phi_{Li} - \phi_{Lj})} \right] \end{aligned} \quad (2.24)$$

with the understanding that the correlator actually takes the time averages of these quantities. Equations 2.24 are valid to the order of  $D\langle E_{Ri}E_{Lj}^* \rangle$  and  $D^2$ , which are generally under 1% of the parallel hand amplitude.

In order to make total intensity maps, equations 2.20 show that only the parallel hands are needed. These terms in equations 2.24 include the parallactic angle differences between the two antennas and the phases in the antenna gains as additional phase terms, however, since in VLBI the phases of the visibilities need to be recovered by self-calibration, these terms can be ignored, and it is merely necessary to determine the amplitude of the antenna gain terms. In polarization VLBI the situation is much more complicated. The primary goal is to recover the  $D$  terms since all three terms in the cross hand correlations in equations 2.24 can be of comparable order, which means that simple inversion of the measured cross hand data would give erroneous polarization images. In order to make the images, the source quantities from equations 2.20 must be determined.

## 2. Determining the $D$ Terms

In order to remove the contamination due to the  $D$  terms, a totally unpolarized (*i.e.* unpolarized on every baseline) source is observed. Then ratios of the cross hand to parallel hand fringes on each baseline at each time are formed. From equations 2.24 four such ratios can be formed. For simplicity of discussion only one will be shown here, as all four have the same form:

$$\begin{aligned} \frac{R_i L_j^*}{L_i L_j^*} &= \frac{G_{Ri} G_{Lj}^*}{G_{Li} G_{Lj}^*} \left\{ \frac{\langle E_{Ri} E_{Lj}^* \rangle}{\langle E_{Li} E_{Lj}^* \rangle} \frac{e^{-i(\phi_{pi} + \phi_{pj})}}{e^{i(\phi_{pi} - \phi_{pj})}} + D_{Ri} \frac{\langle E_{Li} E_{Lj}^* \rangle}{\langle E_{Li} E_{Lj}^* \rangle} + D_{Lj}^* \frac{\langle E_{Ri} E_{Rj}^* \rangle}{\langle E_{Li} E_{Lj}^* \rangle} \frac{e^{-i(\phi_{pi} - \phi_{pj})}}{e^{i(\phi_{pi} - \phi_{pj})}} \right\} \\ &= \frac{G_{Ri}}{G_{Li}} \left\{ \frac{\langle E_{Ri} E_{Lj}^* \rangle}{\langle E_{Li} E_{Lj}^* \rangle} e^{-2i\phi_{pi}} + D_{Ri} + D_{Lj}^* e^{-2i(\phi_{pi} - \phi_{pj})} \right\} \end{aligned} \quad (2.25)$$

where the fact that the circular polarization is close to zero has been used to cancel  $\langle E_{Ri}E_{Rj}^* \rangle / \langle E_{Li}E_{Lj}^* \rangle$ , which is then unity. The first term in brackets in equation 2.25 is a ratio of the polarized flux to the total flux, and for a totally unpolarized source this term is zero. Then the four ratios which can be formed from equations 2.24 are

$$\begin{aligned}
 \frac{R_i L_j^*}{L_i L_j^*} &= \frac{G_{Ri}}{G_{Li}} \left\{ D_{Ri} + D_{Lj}^* e^{-2i(\phi_{Ri} - \phi_{Lj})} \right\} \\
 \frac{L_i R_j^*}{L_i L_j^*} &= \frac{G_{Rj}^*}{G_{Lj}^*} \left\{ D_{Li} e^{-2i(\phi_{Ri} - \phi_{Lj})} + D_{Rj}^* \right\} \\
 \frac{R_i L_j^*}{R_i R_j^*} &= \frac{G_{Lj}}{G_{Rj}^*} \left\{ D_{Ri} e^{2i(\phi_{Ri} - \phi_{Lj})} + D_{Lj}^* \right\} \\
 \frac{L_i R_j^*}{L_i L_j^*} &= \frac{G_{Li}}{G_{Ri}} \left\{ D_{Li} + D_{Rj}^* e^{2i(\phi_{Ri} - \phi_{Lj})} \right\}
 \end{aligned} \tag{2.26}$$

so that each set of four correlations yields four equations which determine the D terms. The ratios of the observed cross hand to parallel hand visibilities of an unpolarized source give a direct measurement of the D terms as circles in the complex plane, with one stationary vector and one vector rotating with twice the parallactic angle difference between the antennas. However, there is one complication still, since the antenna gains have not been removed.

### 3. Aligning the Antenna Gains

The antenna gains are complex and introduce both amplitude and phase changes in the measured signals. Looking at the antenna gains in terms of both amplitude,  $\Gamma$ , and phase,  $\alpha$ , so that the gain ratios in equations 2.26 are of the form

$$\frac{G_{Ri}}{G_{Li}} = \frac{\Gamma_{Ri} e^{i\alpha_{Ri}}}{\Gamma_{Li} e^{i\alpha_{Li}}} = \frac{\Gamma_{Ri}}{\Gamma_{Li}} e^{i(\alpha_{Ri} - \alpha_{Li})} \tag{2.27}$$

shows that the relative gain of the RCP versus LCP receivers and electronics must be determined at each antenna in order to recover the D terms. Although it should be possible to determine the antenna gain amplitude ratios for each antenna at each time

from the calibration data, in practice it is not possible to get a great enough degree of accuracy from the present systems.

In figure 7 a triangle of baselines is shown formed between three antennas. In order to calibrate the amplitude of the antenna gains, the ratio

$$\left| \frac{R_i R_j^*}{L_i L_j^*} \right| = \frac{\Gamma_{Ri} \Gamma_{Rj}^* \langle E_{Ri} E_{Rj}^* \rangle}{\Gamma_{Li} \Gamma_{Lj}^* \langle E_{Li} E_{Lj}^* \rangle} = \frac{\Gamma_{Ri} \Gamma_{Rj}}{\Gamma_{Li} \Gamma_{Lj}} \quad (2.28)$$

is formed on each baseline and the final ratio on the right follows from the lack of circular polarization and from the fact that the  $\Gamma$ 's are the amplitudes of the complex antenna gains. Note that the structure of the source does not enter into this equation, so that this calibration can be performed at each time point regardless of which source is being observed. Then around the triangle of baselines, the ratio

$$\frac{\left| \frac{R_1 R_2^*}{L_1 L_2^*} \right| \left| \frac{R_1 R_3^*}{L_1 L_3^*} \right|}{\left| \frac{R_2 R_3^*}{L_2 L_3^*} \right|} = \frac{\frac{\Gamma_{R1} \Gamma_{R2} \Gamma_{R1} \Gamma_{R3}}{\Gamma_{L1} \Gamma_{L2} \Gamma_{L1} \Gamma_{L3}}}{\frac{\Gamma_{R2} \Gamma_{R3}}{\Gamma_{L2} \Gamma_{L3}}} = \left( \frac{\Gamma_{R1}}{\Gamma_{L1}} \right)^2 \quad (2.29)$$

gives the necessary correction to align the right and left hand data. If there is more than one triangle available to perform the calibration, then the values determined on each triangle can be averaged to determine the best correction. In practice correlation or limitations at the telescopes sometimes cause there to be missing correlations making it impossible to form the ratio of equation 2.29, then the missing alignments can be interpolated from nearby data points.

A similar trick using the triangle of baselines in figure 7 permits the determination of the phase offset ( $\alpha_R - \alpha_L$ ) at each antenna. Forming the ratio in equation 2.28 for the phases however results in exact cancellation as the phases shift sign with the complex conjugation (this is equivalent to forming the closure phase). Instead a reasonably phase stable antenna (*i.e.*  $\alpha_R - \alpha_L$  approximately constant) must

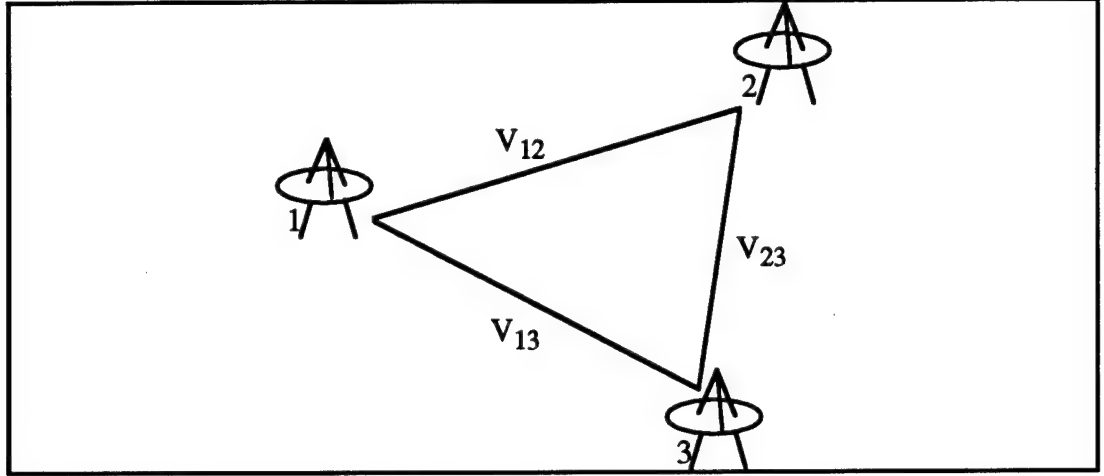


Figure 7: Three antennas which form a triangle allow the antenna gains to be determined on each antenna as in equation 2.28.

be chosen as the reference antenna for the experiment. Then the ratio

$$\begin{aligned} \angle \left( \frac{R_i R_j^*}{L_i L_j^*} \right) &= \frac{e^{i(\alpha_{Ri} - \alpha_{Rj})} e^{-i(\phi_{Ri} - \phi_{Rj})}}{e^{i(\alpha_{Li} - \alpha_{Lj})} e^{i(\phi_{Li} - \phi_{Lj})}} \left\{ \angle \left( \frac{E_{Ri} E_{Rj}^*}{E_{Li} E_{Lj}^*} \right) \right\} \\ &= e^{i(\alpha_{Ri} - \alpha_{Li})} e^{-i(\alpha_{Rj} - \alpha_{Lj})} e^{-2i(\phi_{Ri} - \phi_{Lj})} \end{aligned} \quad (2.30)$$

is formed between the  $i$ th and  $j$ th antennas, where the second line follows from the lack of circular polarization. The parallactic angles are known and can be accounted for simply, however there is no way to set an absolute phase and a reference antenna must be chosen and given zero phase offset between the RCP and LCP feeds. In equation 2.30, if the  $i$ th antenna is the reference antenna, then the first factor in the second line is unity and the measurement of the phase of the visibility ratio yields the phase offset at the  $j$ th antenna. In practice, the first reference antenna is set to zero phase difference and all other antennas are calibrated relative to that antenna. Since in VLBI all antennas are not always on source, a second antenna is then chosen as reference and its undetermined antenna phase differences are interpolated from the previous values calculated from the first reference antenna. Any further calculations which can be made



are filled in and then a new reference antenna is chosen. The importance of phase stability in the reference antenna (and in at least a few additional antennas) is clear, as the need to interpolate values rules out using an antenna with rapidly changing phase differences.

The setting of a zero offset in the reference antenna effectively introduces a phase offset in the data set. This will need to be determined later, however the D terms can now be determined as equations 2.26 do not require the true visibility phases to be known for the calibration. If the first term in equation 2.25 had not dropped out (*i.e.* if the source were polarized), it would be necessary to simultaneously solve for the source polarization including the phase offset still present. This is another advantage to using an unpolarized source for the calibration of the D terms.

Since the gain terms in equations 2.26 are known, they can be accounted for before fitting the vectors on the right hand sides of equations 2.26 to the circles formed by the visibilities (see chapter 3 for figures of actual fits by the Brandeis package). The data for each possible ratio over the experiment (*i.e.* over a range of uv points) form a circle centered on its origin in the complex plane. The non-rotating D term vector points from the origin of the plane to the center of the circle, while the rotating D term vector revolves with the parallactic angle terms to trace out the circle formed by the visibility ratios.

#### *4. Summary of Calibration for Polarization VLBI*

At this point it is worth reviewing the terms that the calibration for polarization VLBI determine. First the rough amplitude gains for each polarization at each antenna are determined from the system temperature measurements (or VLA correlation coefficients) and the gain curve information according to equation 2.11

$$V_{ij}(u, v) = S_T b \rho_{ij}(u, v) \left\{ \sqrt{\frac{(T_{Si} + T_{Ai})(T_{Sj} + T_{Aj})}{T_{Ai}T_{Aj}}} \right\} \quad (2.11)$$

so that the visibilities are in units of flux density. Next the amplitude gain difference between the RCP and LCP gains are removed for each antenna by forming the ratios of parallel hand visibilities as in equation 2.29

$$\frac{\left| \frac{R_1 R_2^*}{L_1 L_2^*} \right| \left| \frac{R_1 R_3^*}{L_1 L_3^*} \right|}{\left| \frac{R_2 R_3^*}{L_2 L_3^*} \right|} = \frac{\frac{\Gamma_{R1} \Gamma_{R2}}{\Gamma_{L1} \Gamma_{L2}} \frac{\Gamma_{R1} \Gamma_{R3}}{\Gamma_{L1} \Gamma_{L3}}}{\frac{\Gamma_{R2} \Gamma_{R3}}{\Gamma_{L2} \Gamma_{L3}}} = \left( \frac{\Gamma_{R1}}{\Gamma_{L1}} \right)^2 \quad (2.29)$$

which makes the calibrated flux density on each baseline as equal as possible in the two parallel hand correlations. A reference antenna is then picked on the basis of its phase stability, and the phase differences between the RCP and LCP feeds of all other antennas are determined by comparison to the reference antenna, using the analog of equation 2.30 given by

$$\angle \left( \frac{R_{ref} R_2^*}{L_{ref} L_2^*} \right) = e^{-i(\alpha_{R2} - \alpha_{L2})} e^{-2i(\phi_{R1} - \phi_{R2})} \quad (2.31)$$

which aligns all antenna gain phase differences within an offset set by the true phase difference of the reference antenna which was set arbitrarily to zero. By observing an unpolarized source and using equations 2.26

$$\begin{aligned} \frac{R_1 L_2^*}{L_1 L_2^*} &= \frac{G_{R1}}{G_{L1}} \left\{ D_{R1} + D_{L2}^* e^{-2i(\phi_{R1} - \phi_{R2})} \right\} \\ \frac{L_1 R_2^*}{L_1 L_2^*} &= \frac{G_{R2}^*}{G_{L2}^*} \left\{ D_{L1} e^{-2i(\phi_{R1} - \phi_{R2})} + D_{R2}^* \right\} \\ \frac{R_1 L_2^*}{R_1 R_2^*} &= \frac{G_{L2}^*}{G_{R2}^*} \left\{ D_{R1} e^{2i(\phi_{R1} - \phi_{R2})} + D_{L2}^* \right\} \\ \frac{L_1 R_2^*}{L_1 L_2^*} &= \frac{G_{L1}}{G_{R1}} \left\{ D_{L1} + D_{R2}^* e^{2i(\phi_{R1} - \phi_{R2})} \right\} \end{aligned} \quad (2.26)$$

the D terms for both polarizations on all antennas are determined from the ratios of the observed cross hands to the observed parallel hands. At the end of this process, the antenna gains, G terms, and polarization cross talk coefficients, D terms, have been determined.

The visibilities on the right hand side of equations 2.20 are the desired quantities for mapping. These are determined by rewriting equations 2.23 as

$$\begin{aligned}
 E_{Ri}E_{Rj}^* &= \frac{1}{G_{Ri}G_{Rj}^*} R_i R_j^* e^{i(\phi_{Ri} - \phi_{Rj})} \\
 E_{Li}E_{Lj}^* &= \frac{1}{G_{Li}G_{Lj}^*} L_i L_j^* e^{-i(\phi_{Li} - \phi_{Lj})} \\
 E_{Ri}E_{Lj}^* &= \frac{1}{G_{Ri}G_{Lj}^*} R_i L_j^* e^{i(\phi_{Ri} - \phi_{Lj})} - D_{Ri} E_{Li} E_{Lj}^* e^{2i(\phi_{Ri} - \phi_{Lj})} - D_{Lj}^* E_{Ri} E_{Rj}^* \\
 E_{Li}E_{Rj}^* &= \frac{1}{G_{Li}G_{Rj}^*} L_i R_j^* e^{-i(\phi_{Li} - \phi_{Rj})} - D_{Li} E_{Ri} E_{Rj}^* e^{-2i(\phi_{Li} - \phi_{Rj})} - D_{Rj}^* E_{Li} E_{Lj}^*
 \end{aligned} \tag{2.32}$$

where time averaging is assumed and the first two equations are still approximations good to about 1%, as the D terms and cross hand visibilities are down about an order of magnitude from the parallel hand visibilities. Note that the true parallel hand visibilities are needed to correct the cross hand visibilities in the third and fourth equations of 2.32. In practice, the first order true parallel hand visibilities are determined from equations 2.32, then the true cross hand visibilities are determined. These true cross hand visibilities are used to correct the parallel hand visibilities (the terms with a D term multiplied by a true cross hand visibility in equations 2.23) in order to get an error of the order of 0.1%, especially on antennas with poor D terms. The first order parallel hands are good to about the order of 1%, and these enter the true cross hand visibilities multiplied by a D term, so that the errors in the cross hand visibilities are of the order of 0.1%. So after calibration all visibilities are corrected to within 0.1%. In actuality, variations in the antennas and receivers used and the available calibration information

introduce errors which are larger than this. A good estimate of these errors comes from very strong signals from powerful radio sources, such as 3C 84 and 3C 273, where the signal-to-noise ratio is large. In these cases, minute by minute variation in the final calibrated signal indicates that the parallel hand flux calibration varies up to 1%, while the cross hand flux calibration varies up to roughly 5%. The phase of the cross hand correlation appears to be quite stable however.

All visibilities are fully calibrated with the terms determined by this process, except for a phase delay offset between the orthogonal polarizations at the reference antenna. This offset effectively enters into the cross hand visibilities through the  $G$  terms. In order to determine  $\alpha_{\text{Rref}} - \alpha_{\text{Lref}}$ , which was set to zero initially, a compact, polarized calibrator source is mapped by hybrid mapping. The polarization determined by the hybrid mapping process is compared to the polarization measured at the VLA, and the phase delay of the reference antenna is adjusted so that the position angles of the two measurements agree (with the full polarized flux recovered in the VLBI map). The data set is then fully calibrated and hybrid mapping of other sources can be done. Since there remains the randomness of the visibility phases in the VLBI data set, self-calibration of the parallel hand data is necessary. However, since this calibration effectively adjusts the antenna gain phases for each polarization at each antenna, it automatically adjusts the cross hand data, since that has been fully linked to the parallel hand data by the calibration.

### III. The Brandeis Polarization VLBI Package

The Brandeis package of programs comprise a set of main executables and subroutines which solve the equations in chapter 2 in order to produce polarized images of radio sources. The primary supported package resides on a Digital Equipment Corporation DecStation 5000/200 workstation and is divided into two main sets, programs for calibration of the visibilities (CALIB), and programs for producing images by the method of hybrid mapping (HMAP). Each set of programs is stored within Digital's Source Code Control System (SCCS) which maintains code integrity and recoverability, while allowing multiple programmers to access and change source codes. The SCCS is linked to the UNIX *make* utility to provide for automatic updating of executables when changes are made in subroutine source code, main program source code, or include files. A discussion of the SCCS and the *make* utility is given in Appendix B.

#### A. Segmented Data and The Brandeis Format

The Brandeis group traditionally has received data in the form of one minute integrations of the visibilities in all four correlations (as in equations 2.5) from the Haystack Mark IIIA correlator (see Brown, 1992, for a discussion of the process of

<u>Rec #</u>	<u>Name</u>	<u>Contents</u>
1	Header	segment time (A8), source (A8), year (INT), day (INT), hour (INT), minute (INT), decimal second (REAL), Greenwich siderial time (REAL), units of amplitude (A4), central observing frequency (REAL), source flux (REAL) of the visibilities is written. Then N <sub>S</sub> copies of index (INT), station ID (A1), U (REAL), V(REAL), W (REAL) geodetic station coordinates, hour angle (REAL), elevation (REAL), and parallactic angle (REAL) of the source as seen from the station are written, where N <sub>S</sub> is the number of antennas in the experiment.
2	Baseline Number	Number of Baselines (N <sub>BL</sub> ) (INT)
3	Visibilities	N <sub>BL</sub> copies of the following: the baseline ID (A2), four copies (one for each correlator) of the correlator ID (A2), amplitude (REAL), phase (REAL), signal to noise ratio (REAL), duration (REAL) of the correlated visibilities, the u (REAL), v(REAL), w (REAL) coordinates of the baseline, and finally the quality codes of the four correlations RR (A1), LL (A1), RL (A1), LR (A1)

Table 2: The format for data stored in visibility and calibrated database files in the Brandeis package. Data is written by unformatted FORTRAN write statements.

correlation and segmenting into the one minute integrations). This procedure will be replaced in the future by FITS format output from the VLBA correlator and a new procedure will need to be created to transfer this data into the Brandeis package.

Presently the data arrives by ftp from Haystack in a text file with the values of the one minute integrations, called segments. This file includes the segment amplitude, phase, epoch and duration of the datum, signal-to-noise ratio, and quality code from the fringe fitting program in addition to a number of other details. The data comes unsorted and must be transformed into a sorted data set before it can be processed. The data set is sorted according to source in right ascension order, observation epoch, baseline in east to west order, and correlation, in that order. The correlations are sorted into RCP⊗RCP (RR), LCP⊗LCP (LL), RCP⊗LCP (RL), and LCP⊗RCP (LR), respectively.

The sorted data set is then ready to be transformed into the Brandeis data format, an unformatted filing system which reduces the file size for storage on the computer. The Brandeis format consists of a series of unformatted records written with unformatted FORTRAN write commands as shown in table 2. Each segment of data is written into the file with the format of table 2 in order from the sorted data file, so that the Brandeis format file is in the same order as the text file. Three data files have this format in the Brandeis package, the visibility (VIS) file which contains uncalibrated visibilities with  $10^4$  x correlation coefficients for amplitudes, the calibrated database (CDB) file which has flux calibration completed, and the polarization-calibrated database (PDB) which is fully calibrated.

### *B. Flux Calibration*

The first series of programs in the CALIB set handle the conversion of the amplitudes of the correlated visibilities from correlation coefficients to flux units (mJy) according to equation 2.11.

### *1. Auxillary Files*

In order to keep track of the necessary factors a number of separate files are created. Primary to each experiment is the experiment (EXP) file, which includes the antennas present in the observations with their geocentric and geodetic coordinates, type of mount, and receivers present (*i.e.* LCP and RCP, LCP only, *etc.*), the sources and their positions at a standard epoch and on the day of the observation, and their fluxes, and the scans with the time of the start of the scan, the source observed, the duration of the scan, and the antennas which actually reported having observed the source successfully. Each scan contains a number of segments depending on the scan duration. The EXP file is used by all programs in the CALIB set.

The EXP file is created from the correlator control file used at Haystack by the CALIB routine WRTEXP. From the EXP file two further files are immediately created using the routine WRTPARCAL. These are the calibration (CAL) file, which is an unformatted file that contains the system temperature and antenna temperature data and is initialized with all zeroes, and the parameter (PAR) file, which contains information on the source position relative to each antenna including the elevation, hour angle, and parallactic angle.

### *2. The Antenna and System Temperature Files and Equivalents*

From equation 2.11 it is clear that, in addition to the total source flux in the EXP file, the system and antenna temperatures at each antenna at each time are needed for calibration (except for the VLA, see below). Using the Mark IIIA recording system, these measurements are generally done separately by the antenna personnel and logged either on paper or electronically. Typically the system temperature is measured within five minutes of the beginning of a scan and the antenna temperature is done at the same time (although most antennas do not perform the antenna temperature measurement and, as noted in chapter 2, it tends to be unreliable anyway). The system



temperatures are written into the system temperature (TS) files using a series of programs which handle the various formats used by the observing stations:

A) The original Mark III log format consists of an ASCII file with time stamps and automatically recorded information which includes lines containing the system temperatures. These log files are converted to an extracted log (LE) format by the CALIB routine EXTRACT, and then a TS file is created using the routine WRTTS, which interactively leads the user through the data in the LE file.

B) For antennas which send the data using paper logs, the routine HANDTSTA allows the user to create a TS file interactively. The program prompts for the TS data points on each scan reported to involve the antenna in the EXP file. If no calibration data are available, the HANDTSTA routine allows the use of a simple model which includes a baseline temperature and an elevation dependent temperature to create the TS file for an antenna.

C) For the VLA, the calibration data is not in the form of system and antenna temperatures but is instead in terms of the real part of the correlation coefficients for the phased array. The data is contained in minute by minute records of these values for each receiver (RCP and LCP), and the CALIB routine WRTYCAL determines which measurements were made while the VLBI data was recorded and averages these data to create the calibration (YRR, YLL) files. The routine WRTYCAL keeps track of the number of antennas on source at each time. Only the values which involve the maximum number of VLA baselines in the scan are used in the average. Typically the number of baselines is constant over the scan, but sometimes an antenna will drop out reducing the correlation coefficient. For calibration of the VLBI data, the correlation coefficients are converted to the ratio

$$\frac{T_A}{T_s} = \frac{d \times N \times (\text{correlation coefficient})}{256 \times (\text{scaling factor})} \quad (3.1)$$

where  $d$  is the VLA waveguide duty cycle of 0.969, 256 represents unity correlation,  $N$  is the number of baselines present, and the scaling factor reflects the adjustment of the correlation coefficient to fit the output field (Brown, 1992).

D) For VLBA antennas the system temperatures are reported in minute by minute records on each baseband converter, giving four values for each receiver at each station. The CALIB routine VLACAL averages these measurements for the times when the VLBA recorder was writing the data, keeping track of the assignment of baseband converters to RCP and LCP receivers.

### *3. Producing the Antenna Gain Data*

Once all the antennas have TS files present (or YRR and YLL files for the VLA), the system temperature measurements are written into the CAL file. The CALIB routine EDTCAL reads the TS (or YRR and YLL) files one by one, prompting for which file to read, and inserts the values from these files into the CAL file at the appropriate points. After EDTCAL has been run, the system temperature information is complete for the experiment.

Since the antenna temperature measurements are generally unreliable, antenna temperatures are generated from antenna gain curves, the known elevation of the antenna while on source as coded in the PAR file, and the known flux of the source determined in the simultaneous VLA interferometer mode experiment. The antenna gain curves for each telescope in each experiment are kept in the ANTGAINS.MST file in one of four formats, chosen to match the typical reported gain curve from the stations used in VLBI observations. Most common is the gain curve with the form

$$g(K / Jy) = C_1(1 + C_3Y + C_4Y^2 + C_5Y^3 + C_6Y^4) \quad (3.2)$$

*where*  $Y = ZA - C_2$

with ZA being the zenith angle and the C's the reported or derived coefficients. The gain curve shows the antenna response in degrees for a source measured in Janskys. Equatorially mounted antennas sometimes use this equation with

$$Y = HA - C_2 \quad (3.3)$$

where HA is the hour angle. The Green Bank antenna, which will no longer be used in VLBI experiments, uses a special system of spherical harmonics which is approximated in the Brandeis package by dropping the odd terms, which were always extremely small, giving

$$g(K / Jy) = C_1 (C_2 Y_{00} + C_3 Y_{10} + C_4 Y_{11E} + C_5 Y_{20} + C_6 Y_{21E} + C_7 Y_{22E}) \quad (3.4)$$

where  $C_1$  converts from the Greenbank cgs units to Janskys, and the Y's are a set of spherical harmonics. The Haystack antenna uses another gain curve formula given by

$$g(K / Jy) = C_1 e^{\{-c_2 [(Y - c_3) c_4]^2\}} \quad (3.5)$$

*where Y = elevation*

but this antenna will no longer be used in VLBI observations. The gain curve coefficients are entered into the ANTGAINS.MST file by hand and are either given directly in the log files or are calculated from the pictorial antenna gain curve sent in the log. For antennas which fail to give gain curves, previous gain curves can be used. For more modern antennas (*e.g.* VLBA antennas and Deep Space Network antennas), flat gain curves often fit the data at typical observing frequencies.

Once the gain curves have been entered into the ANTGAINS.MST file, the CALIB routine WRTGAI is used to determine the gain factor for each visibility in the experiment using equation 2.11 and equations 3.2 to 3.5. This routine creates the gain (GAI) file which is used by the routine WRTCDB.

#### *4. Creating and Checking the CDB File*

WRTCDB applies the gains to the amplitudes of the visibilities measured in correlation coefficients in the VIS files and converts them into mJy, writing the data out into the CDB file. The CDB file created in this first pass needs to be checked for the quality of the calibration, since the system temperature and gain curve system is not highly accurate, and since some stations fail to send any calibration data.

First the alignment of the right and left hand data on each baseline is checked. The CALIB routine PLTVIS plots the visibilities from any database in the Brandeis format. PLTVIS is used to plot all the CDB data as a function of epoch on each baseline. The LL and RR correlations are plotted, as in figure 8. Figure 8(a) shows the visibilities on the baseline between the Efflsberg antenna and the North Liberty VLBA antenna in the epoch 1992.4 8.4 GHz experiment. The plus symbols show the amplitudes of the LL visibilities while the circles show the amplitudes of the RR visibilities. It is clear that the LL visibilities are slightly higher systematically than the RR visibilities. Figure 8(b) shows the same plot for the baseline between the VLBA North Liberty stations and the VLBA Fort Davis station. Here the LL and RR visibilities are very well aligned which suggests that the Efflsberg antenna has a slight misalignment in the calibration between the RCP and LCP system temperature measurements. Figures 8(c) and 8(d) show the corresponding data for the VLBA North Liberty to VLA visibilities and the VLBA Fort Davis to VLA visibilities. While it appears that Bonn is slightly misaligned, it is not clear if either Fort Davis or the VLA might be slightly misaligned. In all these cases, the misalignments of the data are quite small and will be handled later in the calibration. For large systematic misalignments it is better to handle a rough overall correction at this stage by scaling the TS file for any antennas which show strong misalignments using the routine SCALETSTA. Equation 2.11 shows that the system temperature enters the calibration as a square root, so that,

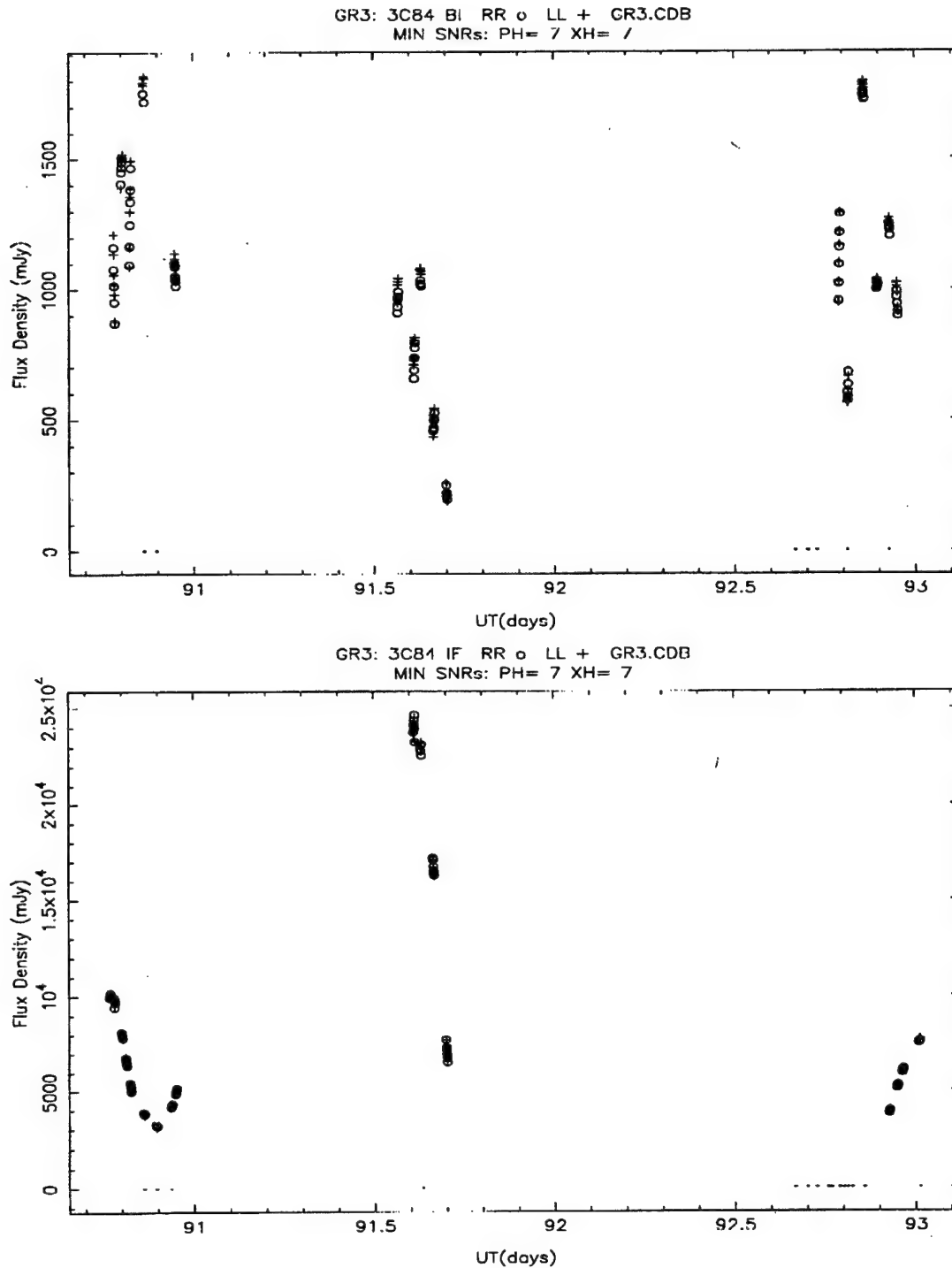


Figure 8: Parallel hand visibility plots: (a) at top shows a baseline where the LL and RR correlations give slightly different fluxes, (b) at bottom shows a baseline with well aligned LL and RR fluxes.

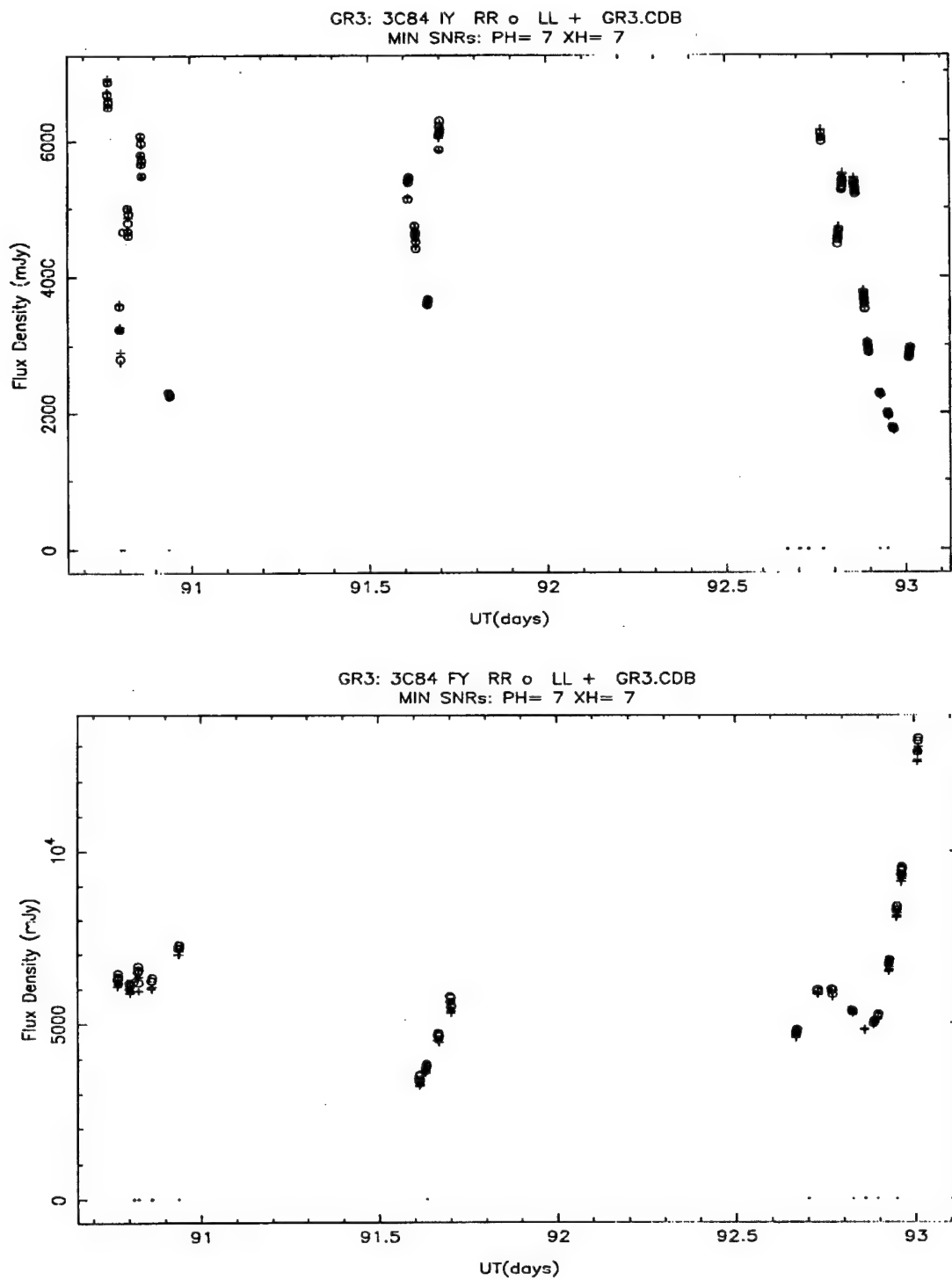


Figure 8: Parallel hand visibility plots: (c) at top and (d) at bottom show additional baselines containing the antennas in (a) and (b).

using the LCP receiver as the standard, the scaling factor for the TS file is

$$T_{CAL}^{RCP}(new) = \left( \frac{Amp_{LL}}{Amp_{RR}} \right)^2 T_{CAL}^{RCP}(old) \quad (3.6)$$

where the new RCP calibration temperature is entered as prompted. Note that this adjusts the antenna calibration globally throughout the experiment, so the misalignment should be systematic and not merely on a single baseline. Because of the danger inherent in adjusting VLBI data baseline by baseline, the Brandeis package does not allow baseline dependent corrections.

After the adjustment of the TS file a new CAL file is created by using the routine EDTCAL. Then a new GAI file is created using WRTGAI and finally a new CDB file is created using WRTCDB. Next the overall alignment of each antenna within the experiment should be checked by using the CALIB routine PLTVIS to plot the entire RR and LL data set against UV distance. Figure 9 shows such a plot for 3C84 at 8.4 GHz, where not all antennas have LCP receivers as indicated by the larger number of RR correlations. Note that the visibilities drop smoothly as the UV distance (baseline length) increases and that the source is resolved. The large scatter of data at short spacings indicates the presence of complex structure in the source. If some data deviated sharply from the smooth distribution in such a plot, the CALIB routine PLTVIS should be used to plot out specific baselines to find which data are inconsistent. If a given antenna is systematically misaligned with the rest of the experiment, its TS file should be adjusted to bring its calibration into line with the experiment. Again the system temperature enters into the calibration as a square root so that

$$T_{CAL}(new) = \left( \frac{Amp_{aligned}}{Amp_{CDB}} \right)^2 T_{CAL}(old) \quad (3.7)$$

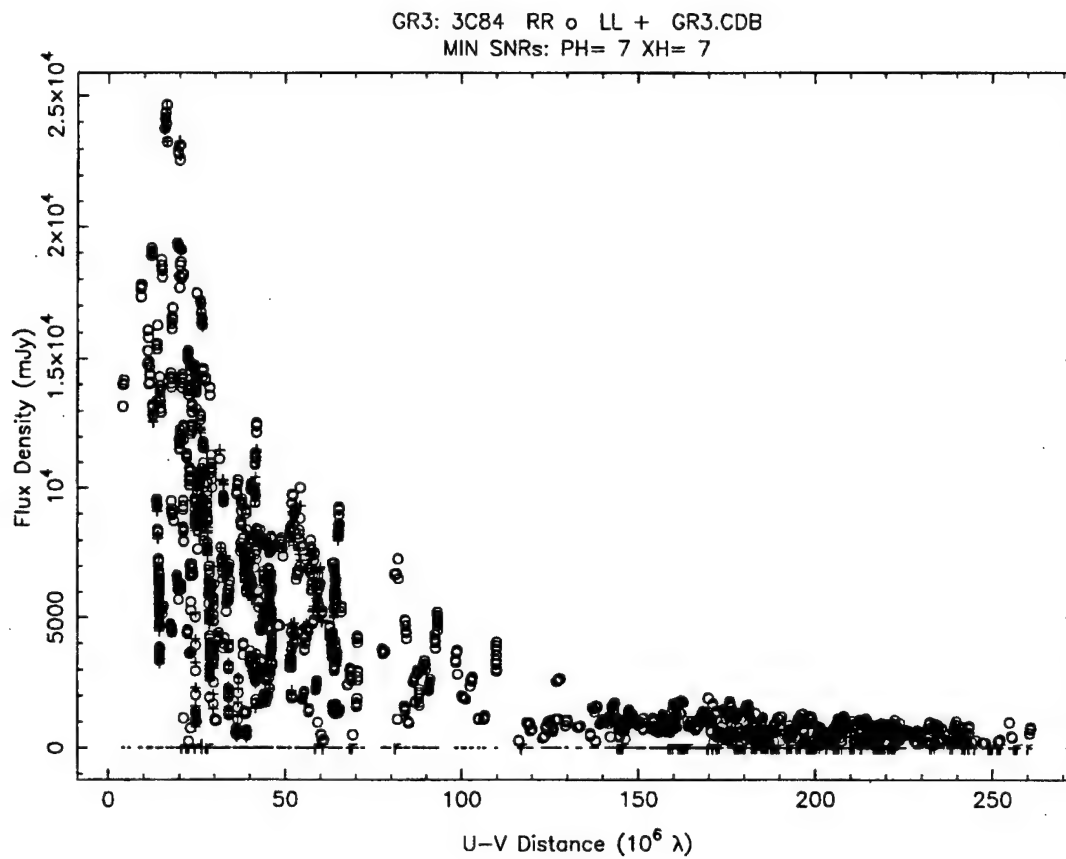


Figure 9: A plot of parallel hand visibility amplitude against UV distance. The plot indicates a resolved source as the amplitude drops with increasing UV distance. The source is also complex in structure as shown by the scatter in the amplitudes at short UV spacings.

where  $Amp_{aligned}$  is the expected amplitude and  $Amp_{CDB}$  is the amplitude in the CDB file. In this case both the RCP and LCP calibration temperatures are scaled using the CALIB routine SCALETSTA. Again the CAL file, GAI file, and CDB file must be regenerated.

Although there are apparently no point sources in VLBI, there are some very compact sources which appear point-like on the shortest baselines. These sources can be used to check the calibration further. Since OJ 287 is routinely observed for determination of the reference antenna RCP - LCP phase difference (as in equation



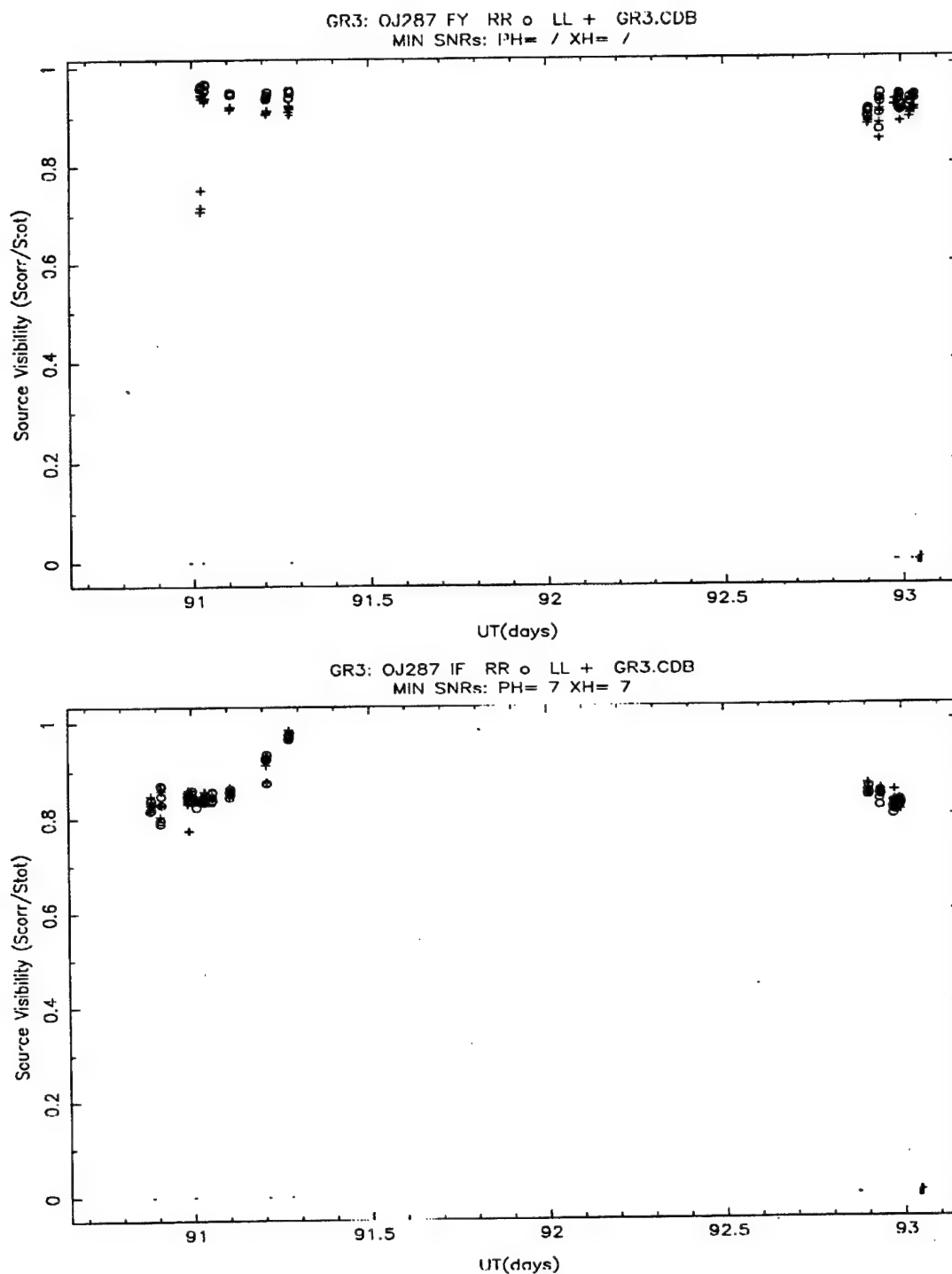


Figure 10: Plots of the parallel hand visibility against time on a number of baselines: (a) at top is a short baseline showing the visibility amplitude is roughly constant, (b) at bottom is a longer baselines and variation in the amplitude is beginning to be seen.

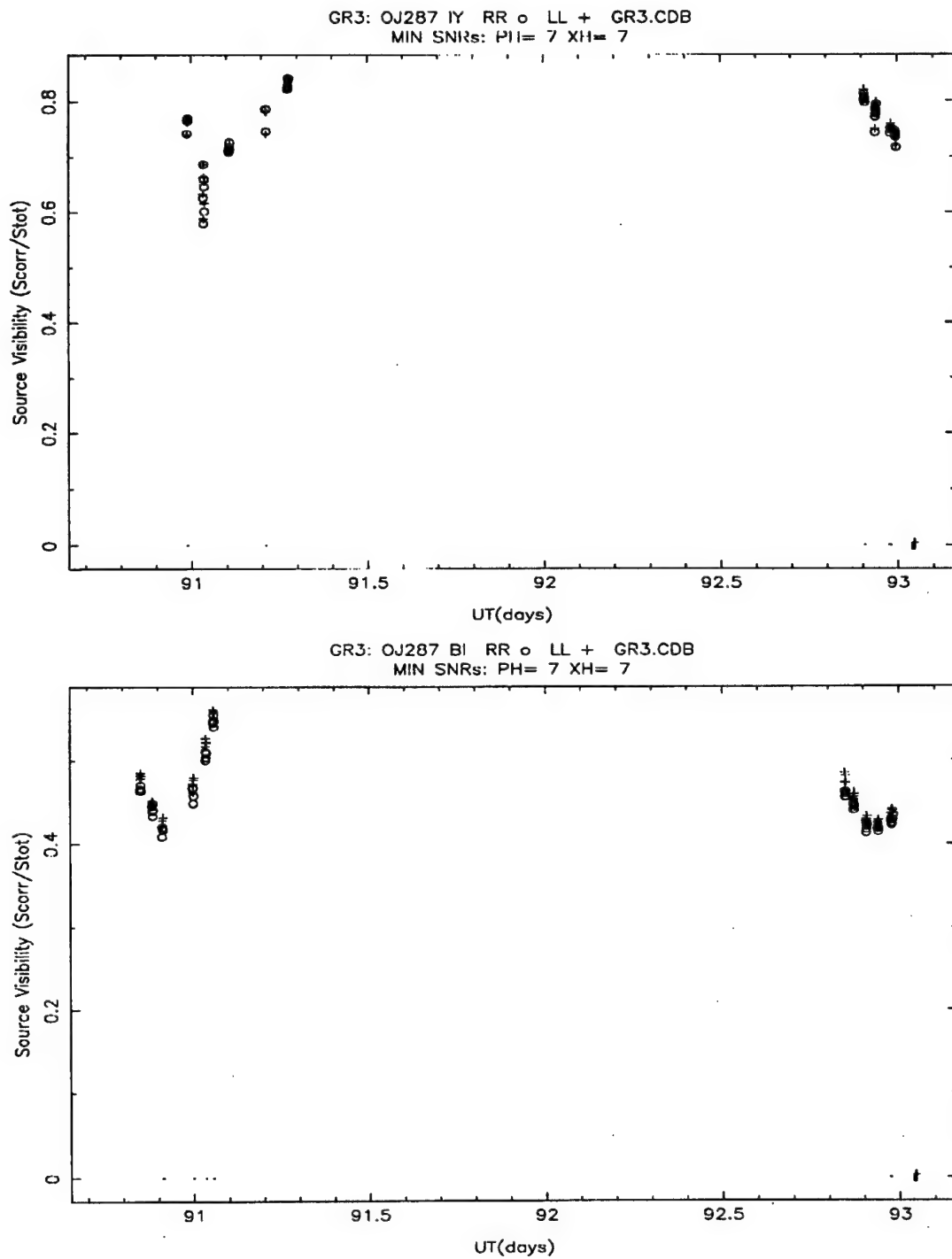


Figure 10: Plots of the parallel hand visibility against time on a number of baselines: (c) at top is a moderately long baseline showing amplitude variation, (d) at bottom is a long baseline showing a large amplitude variation.

2.31), this source is available for checking the calibration. By plotting the RR and LL visibilities on the shortest baselines, as in figure 10, and comparing the recovered flux to the total flux as measured by the VLA, the calibration can be adjusted to align the data using equation 3.7. The series from 10(a) to 10(d) is in terms of increasing baseline length, which shows that the usefulness of this method is clearly limited to the very shortest baselines, since less than half of the total flux is recovered on transatlantic baselines.

A final check of the quality of the data is permitted by the PLTVIS routine. The closure phases can be plotted, as in figure 11, which checks that the RR and LL closure phases agree, and that the closure phases are smoothly varying. The large number of symbols along the bottom in figures 11(a) and 11(b) indicate missing closure phases. These arise from the flagging of data, the failure of antennas, or the failure of correlation, all of which may eliminate one baseline in the triangle, thus eliminating the closure phase information. The closure phases are not dependent on instrumental factors (as noted in equation 2.13), so that nothing but flagging of the data can be done if problems are discovered. At this point the data is fully calibrated for total intensity mapping.

### *C. Polarization Calibration*

As noted in chapter 2, in order to make polarized images the cross hand data must be corrected to remove instrumental effects. The Brandeis package does this using a series of programs which first align the RCP and LCP antenna phases, then determine the D terms, and finally apply the corrections to the data set.

#### *1. Flagging the Data Set*

The first step in determining the instrumental terms is to remove any poor data. In VLBI there are often substantial problems in the data set due to a number of factors,

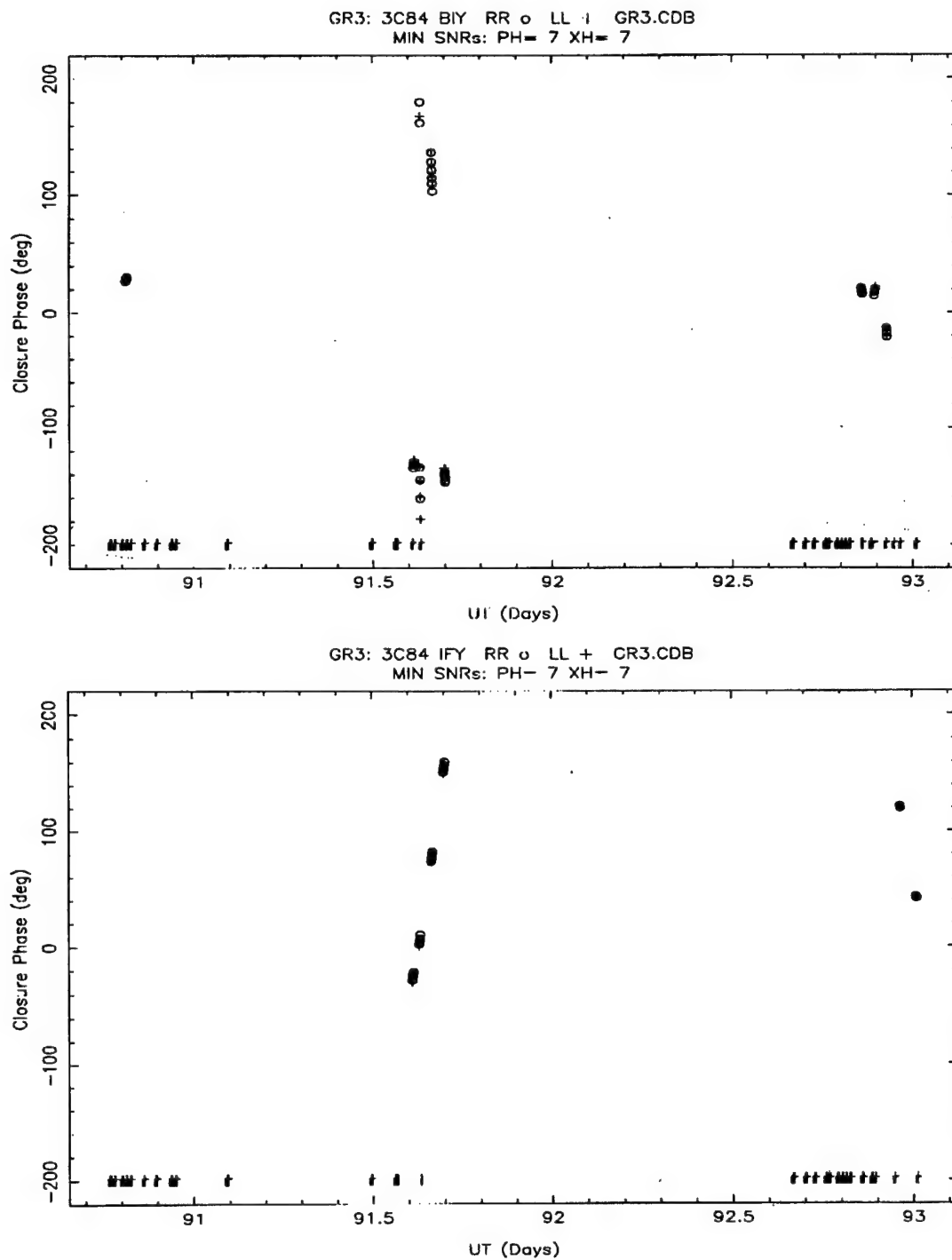


Figure 11: Plots of closure phases: (a) at top and (b) at bottom give two sets of closure phases around triangles of baselines.

including problems at the correlator and antenna-based losses of data either due to the electronics or recording systems. In order to identify poor data the CALIB routine IPCAL has an option to perform "block checks" on the data. The block check method analyzes each scan, which is made up of from five to thirteen segments. For parallel hand data (RR and LL visibilities), where the phases are subject to atmospheric and clock-based variations, a scalar average of the amplitudes is performed. If the variation within the scan is greater than that expected from the known signal-to-noise ratios, the data is marked for the user to investigate. Bad data points can then be flagged by entering the segment information into a flag file by hand. Cross hand data (RL and LR visibilities) are divided by parallel hand data segment by segment, which removes many instrumental phase factors from the data. A vector average is performed, and the scans which exceed the variation expected from the signal-to-noise ratio are marked for the user to inspect and possibly flag out. Because of the sparseness of VLBI data, the Brandeis VLBI package does not allow automatic flagging of data, so that the maximum number of visibilities can be retained.

## *2. Aligning the RCP and LCP Gains*

After the flagging has been performed, the CALIB routine RLCAL is used to view and adjust the RCP and LCP gains. Amplitude adjustments to the data are calculated according to equation 2.29. These are printed out so that the user can look for sudden jumps in the calibration indicative of problems. Sudden changes in the required factor applied to an antenna to align the RR and LL visibilities should result in flagging of the problem data. After the poor data have been removed, the amplitude gains have been solved.

It is next necessary to choose a reference antenna which has stable phase behavior, *i.e.* at most a slowly varying RCP - LCP phase difference with a maximum of about  $10^\circ$  spread over the experiment. RLCAL allows the user to plot the antenna

phases determined on each baseline or to print out the phases for investigation. Stable antennas generally show stable behavior with a number of good antennas, so that it is easy to spot the most stable antenna. After choosing the best antenna, the phase difference at each antenna should be determined in order to create a list of all the antennas, from the most phase stable to the least.

Next equation 2.31 is solved for all antennas, during the times when they are linked to the reference antenna by a visibility, by setting the reference antenna to have zero RCP - LCP phase difference. Since in VLBI not all antennas can look at a source at a given time, this will leave undetermined antenna phases. This is why a series of stable antennas is needed. The next most stable antenna is chosen and the values of its phase difference are interpolated from the values determined from the visibilities including it and the reference antenna. Then equation 2.30 is solved for all baselines to this second antenna. This process is repeated until all antenna phases are determined in the experiment. With the completion of the CALIB routine RLCAL, the antenna gains, labelled G terms in chapter 2, are fully calibrated and this calibration information is written into a file (the RLCAL file) for later use.

### *3. Determining the Instrumental Polarization*

The CALIB routine IPCAL determines the D terms of the antennas. The data set (CDB file) is first corrected by applying the calibration file created by the routine RLCAL, then the totally unpolarized source 3C 84 is used with cross to parallel hand ratios being formed according to equations 2.26. Since the G terms have been accounted for, these ratios give circles in the complex plane as noted in chapter 2. The D terms are determined by fitting the circles with two vectors, which give the amplitudes and phases of the D terms.

In practice there are antennas with poor D terms and baselines with extremely poor coverage in the complex plane. In attempting to fit a constant and a rotating (with

parallactic angle difference) vector to sparse data, the circle is not well defined and so the D terms become somewhat random. As a result, the first iteration for solving the D terms in the routine IPCAL must be carefully checked to get a good first estimate of the D terms. Once an initial reliable estimate of the D terms is obtained, iteration on the D terms can begin. After the first iteration, the data should be checked to see that there is no poor data. The output from IPCAL iterations includes each data point in the ratios formed, and bad data is noted by its inconsistency with nearby points. After flagging, iterations continue until the D terms settle and do not continue to change significantly.

After the D terms have been determined, they should be checked by plotting out the data using option 10 in the routine IPCAL and the CALIB routine IP\_DPLOT. These produce plots in the complex plane of the ratios formed in equations 2.26, together with the vectors which are fit to the data. Figure 12 shows typical fits obtained in the epoch 1992.4 8.4 GHz experiment. Figure 12(a) shows the fit obtained with an antenna with a poor D term (Medicina). Note the scale which indicates that the cross hand to parallel hand ratio is as high as 20% on the unpolarized source. Figure 12(b) shows the fit obtained when both antennas have very low D terms. The lines from the data points, indicated by the plus symbols, to the circle indicates where the actual data lies in comparison to its calculated point. Although the fit initially looks much poorer than for Medicina, the scale here is now under 1% and the noise in the data is now significant. The figure shown is only one of many for these antennas, and the final D term fit must be compared on all baselines. Figures 12(c) and 12(d) show that two ratios can be formed (by referencing the cross hand to either the LL or RR parallel hand), which changes which vector is rotating with the parallactic angle difference and which is stationary.

After the antenna gains have been fully determined and the D terms have been determined, the visibilities can be corrected using equations 2.32. This is done by the

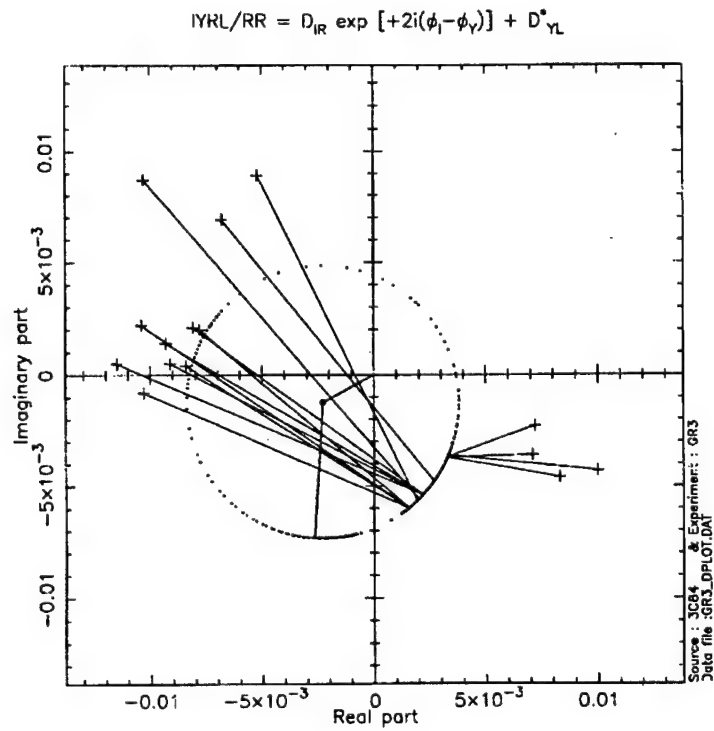
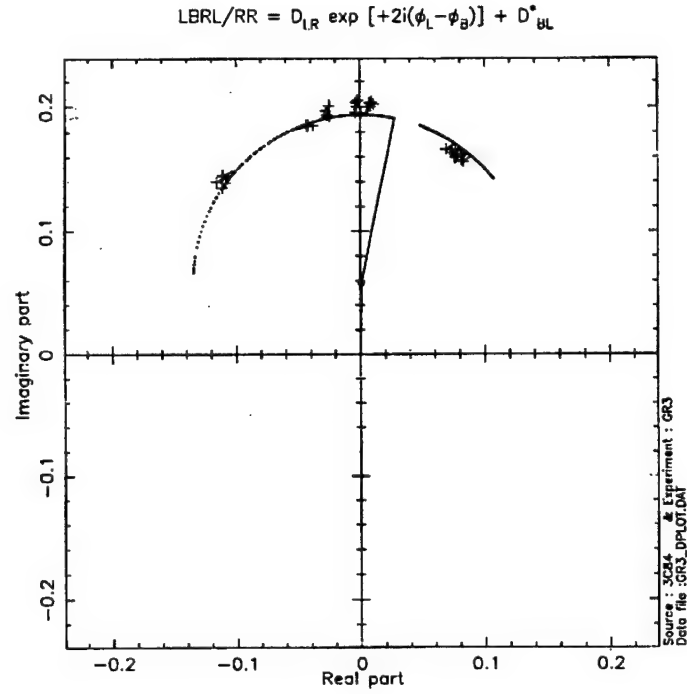


Figure 12: Plots of D term solutions in the complex plane: (a) at top is for a baseline involving a large D term, (b) at bottom is for a baseline with two antennas with small D terms.



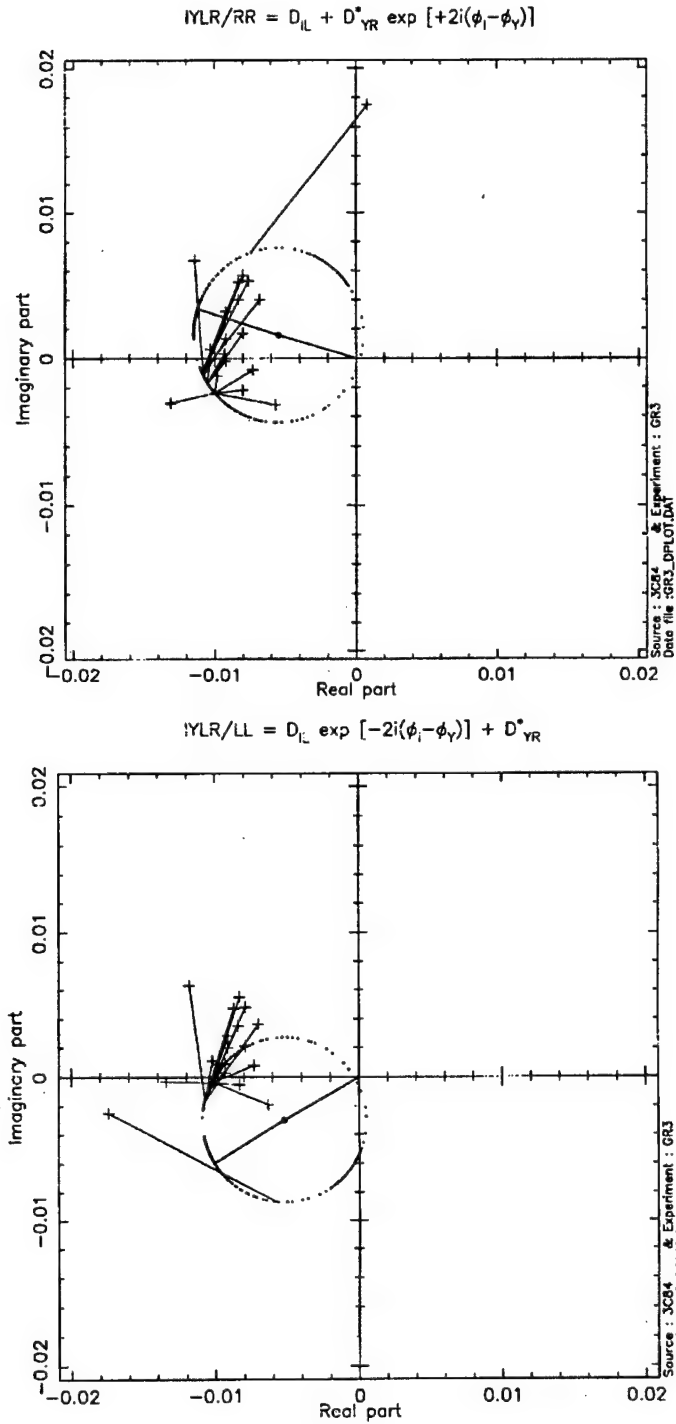


Figure 12: Plots of D term solutions in the complex plane: (c) at top and (d) at bottom show that the rotating and stationary vectors exchange when the parallel hand visibility is switched from RR to LL in the calculation.

CALIB routine WRTpdb2 which reads the CDB file, adjusts the data using the RLCAL output and the D terms file, and writes out the corrected data into the PDB file. The data are now fully calibrated and ready for hybrid mapping, except for the unknown RCP - LCP phase difference of the reference antenna. This is determined by hybrid mapping of the BL Lac object OJ 287 or other compact highly polarized object. The recovered VLBI polarized flux and position angle are determined and these are compared to the arcsecond core polarized flux and position angle measured using the VLA interferometer mode scans. The VLBI and VLA data are aligned by inserting the required phase difference of the reference antenna in the D terms file and reconstruction of the PDB file. A manual which provides step-by-step instructions for calibration of polarization VLBI data is given in Appendix C.

#### *D. Mapping*

The Brandeis package includes the set of programs referred to as HMAP, which permits hybrid mapping of the VLBI data in both total intensity and linear polarization. The HMAP routines permit data flagging, self-calibration of the visibilities both in phase and amplitude (equations 2.14), Fourier transformation of the data (equation 2.4), and deconvolution by both the CLEAN algorithm and the MEM algorithm (for a thorough discussion of the original VAX version of HMAP see Holdaway, 1990).

The hybrid mapping is performed in a definite series of steps. The data is first flagged using the HMAP routine FLAG\_VIS, which reads the flag file created previously during data handling using the CALIB routines RLCAL and IPCAL. This creates a hybrid mapping database (HDB) file. An initial estimate of the visibility phases are determined using the HMAP routine SELF\_CAL by self-calibration on a point source, which works reasonably well, since all observed VLBI sources show strong cores with varying amounts of extended structure. The HMAP routine

DIRTY\_MAP performs a Fourier transform of the visibilities to produce a dirty map and a dirty beam as indicated in equations 2.4 and 2.15. This dirty map is deconvolved using the dirty beam by the HMAP routine CLEAN\_MAP using the CLEAN algorithm. The results of the CLEAN process, the CLEAN components (CC's), are used as a model to perform another round of self-calibration. The process of SELF\_CAL, DIRTY\_MAP, and CLEAN\_MAP is repeated iteratively until convergence of the data in the form of a stable map.

In practice, four iterations are performed and the data is then printed out so that bad data points can be flagged by adding them to the flag file. The process is then started over. How the data is handled varies with the individual sources, the quality of the data, the number of visibilities and a number of other factors. Generally, for poorer quality or limited data, CLEAN boxes which constrain the placement of CLEAN components may be necessary. Limits on baselines to use for self-calibration may also be desirable since the shorter baselines measure unmappable flux in larger quasars. Finally, if only a limited number of visibilities are available, constraints on the map may be necessary in order to obtain convergence. Generally, for simpler sources (*e.g.* BL Lac objects), fewer constraints are needed and the map converges both faster and with a better fit between the Fourier transform of the map and the data.

With the porting of the HMAP system to the DecStation, a number of new routines were introduced to allow analysis of the data and mapping of the parsec scale Faraday rotation. Comparison of the final map to the data is accomplished with the HMAP routine MAPFIT. MAPFIT permits the user to compare the final HDB file, with self-calibration applied, to the final map. The map is Fourier transformed according to equation 2.3, and the resulting model visibilities are compared to the HDB visibilities. The options of using just the CLEAN components, using the full final map, which includes residuals left over in the dirty map after cleaning, or using a MEM

map are available. In general, the use of a full map with residuals gives a poor fit as the known instability in CLEAN, which introduces striping in images, appears to cause the short baseline visibilities to be grossly overestimated, although there is good agreement on the longer baselines. This may be a result of the shorter baselines measuring flux which is not mappable onto the small VLBI field. The routine MAPFIT outputs a comparison of the model and HDB visibilities, as well as the mean of the HDB versus model visibility differences, in a variety of forms for both the total intensity and complex polarization maps and data.

The parsec scale Faraday rotation measure is mapped from complex polarization maps at two frequencies using the HMAP routine ROT\_MEAS. This routine aligns the two maps at a user specified point and calculates the minimum rotation measure which would explain the observed differences at each point in the linearly polarized images. Large scale (VLA) Faraday rotation measures of the VLA cores of the objects can be accounted for in the mapping, so that effects from our own galaxy or from the kiloparsec scale and larger environment of the source can be removed prior to making the measurement of the Faraday rotation.

The maps made either by the HMAP iterations or by the Faraday rotation measure routines are viewed using a series of programs, which allow screen displays on a number of systems or produce PostScript output. Total intensity images are viewed using the HMAP routine CONTOUR\_I, while polarization images are viewed using the routine CONTOUR\_P. The rotation measure maps are produced, in gray scale only, using the HMAP routine RM\_GRAY.

In general, the HMAP package is highly flexible and offers many possible sequences of actions to produce images. It is impossible to anticipate every method which might prove fruitful in mapping the bright radio sources studied by polarization VLBI. Instead the basics of the use of the package are given here, with the hope that

users will feel free to attempt to change all parameters available in HMAP to determine the best method for their individual data sets.

## IV. Faraday Rotation

### A. Physical Processes of Faraday Rotation

Faraday rotation is the process whereby linearly polarized radiation traveling through an ionized plasma containing a magnetic field has its position angle changed. This occurs because the circularly polarized components of the radiation propagate at different speeds, due to their different refractive indices.

#### 1. The Standard Formula

The position angle of the observed electric field vector is changed through Faraday rotation by (Burn, 1966)

$$\chi_{obs} = \chi_0 + RM\lambda^2 \quad (4.1)$$

where  $\chi_{obs}$  is the observed position angle,  $\chi_0$  would be the position angle observed if no rotation occurred,  $\lambda$  is the wavelength, and RM is the rotation measure given by

$$RM = 8.1 \times 10^5 \int_0^d n_e B_{\parallel} ds \quad (4.2)$$

where  $B_{\parallel}$  is the component of the magnetic field parallel to the line of sight measured in Gauss,  $n_e$  is the electron density measured in  $m^{-3}$ , and the integral is over the pathlength from the observer to the source at a distance  $d$  away, measured in pc. Using this value in equation 4.1 requires measurement of  $\lambda$  in meters.

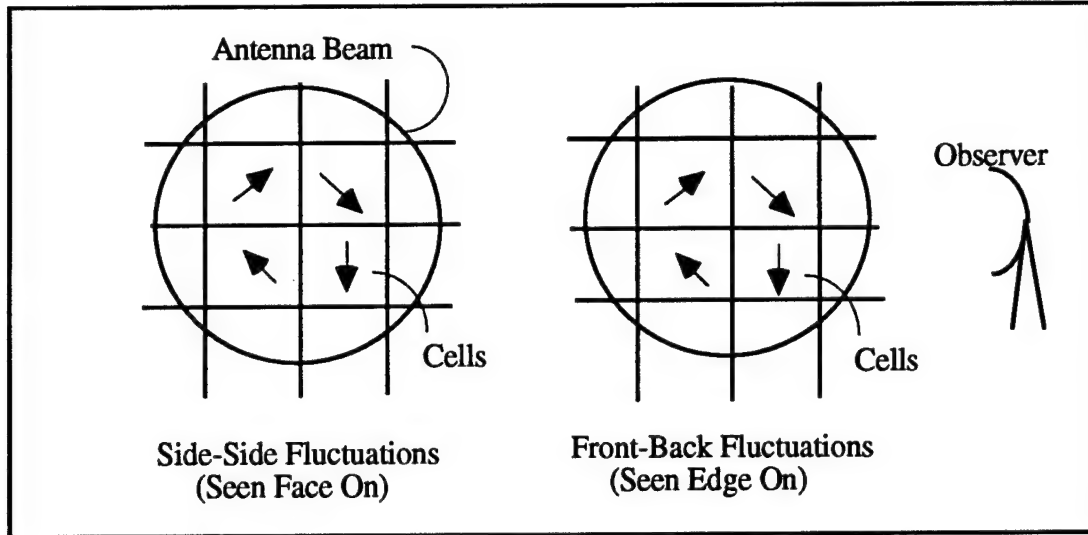


Figure 13: Magnetic field variations seen within the beam of a telescope. The direction of the arrows indicate magnetic field direction.

## 2. External Faraday Rotation

For a resolved Faraday screen between the observer and the source, equation 4.1 completely describes the necessary adjustments to recover the intrinsic complex polarization of the source. Then measurements at three wavelengths will verify a linear fit of  $\chi_{\text{obs}}$  to  $\lambda^2$ , and  $\chi_0$  can be reconstructed.

For an unresolved Faraday screen with a distribution of magnetic field fluctuations within the beam of the observing telescope (which can include both side-side and front-back fluctuations, see figure 13), the  $\lambda^2$  variation in  $\chi_{\text{obs}}$  will not necessarily hold at all observing wavelengths. Even for a background source emitting a uniform position angle, the telescope will see a spread in position angles across the source, since the radiation emerges from different cells in the screen and each cell rotates the position angle differently. Since linear polarization is a complex quantity, the telescope effectively does a vector average of the polarizations from each cell. For a Gaussian distribution of fluctuations, the observed polarized intensity,  $P(\lambda)$ , is given by (Burn, 1966)

$$P(\lambda) = P_0 e^{-2K^2 (n_e B_{\parallel})^2 d_f L \lambda^4} \quad (4.3)$$

where  $P_0$  is the polarized intensity that would be observed if there were no Faraday rotation,  $n_e$  is the electron density,  $B_{\parallel}$  is the parallel component of the magnetic field,  $K$  is the constant in equation 4.1,  $d_f$  is the scale size of the fluctuations, and  $L$  is the pathlength. While equation 4.3 is valid only for a Gaussian distribution of fluctuations, the behavior of the loss of polarized flux with wavelength is valid for all unresolved screens with fluctuations. If there is no net preferred magnetic field direction in the screen, then there is no possible preferred rotation, and the observed change in the position angle with wavelength should be roughly zero. However, the observed polarized flux should drop with increasing wavelength, giving an indication of an unresolved Faraday screen. This simple picture is complicated however by the possibility of Faraday rotation within the emitting medium, which can also show such depolarization.

### *3. Internal Faraday Rotation*

Faraday rotation can arise in any ionized plasma where a magnetic field is present. Since the radio radiation observed in quasars is emitted by the synchrotron process, both free electrons and magnetic fields are present. Synchrotron emission requires relativistic electrons, which do not give rise to significant Faraday rotation, but does not preclude thermal (*i.e.* cold) electrons. If cold electrons are also present, then in realistic geometries the polarized flux drops off with increasing wavelength, while the observed position angle varies with  $\lambda^2$  at small wavelengths but becomes random at longer wavelengths (Laing, 1984, and the discussion following). The behavior of the complex polarization for internal Faraday rotation, where the emitting volume also



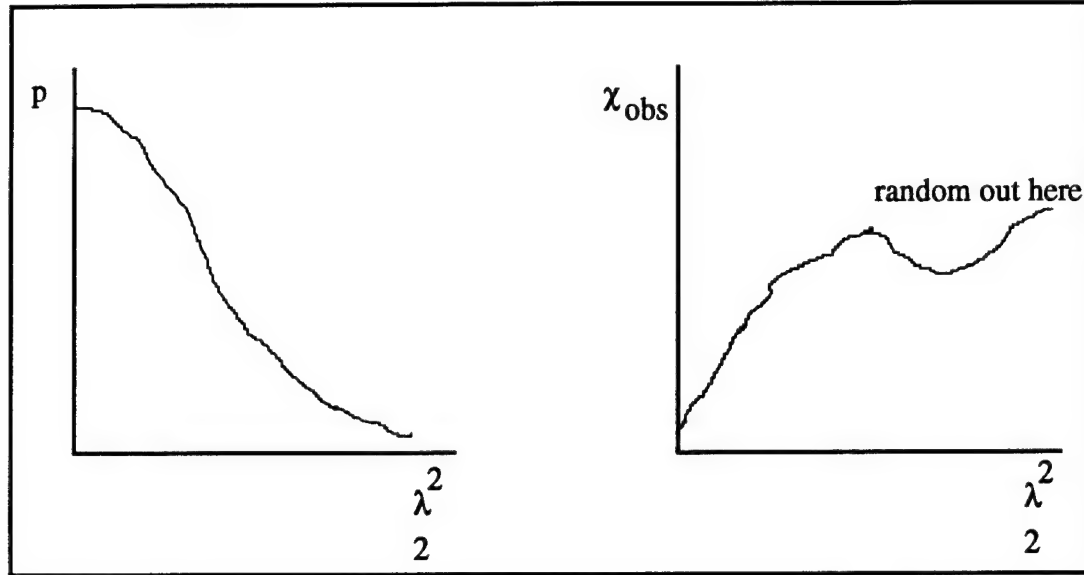


Figure 14: The changes in observed polarized flux and position angle for a source showing internal Faraday rotation, see text for reference.

<u>Rotation</u>	<u>Depol.</u>	<u>Other Behavior</u>	<u>Likely Cause of Faraday Effect</u>
$\propto \lambda^2$	None		Foreground Screen
$\propto \lambda^2$	Present	$\delta\chi < \pi/2$	Internal Rotation or Unresolved Screen If internal $\delta\chi \propto \lambda^2$ should fail at large $\lambda$
$\propto \lambda^2$	Present	$\delta\chi > \pi/2$	Probably a Foreground Screen but with additional complications
not $\propto \lambda^2$	Present		Mixed geometries inside source or Resolved Foreground Screen
None	Present		Unresolved Foreground Screen or Internal Faraday Rotation

Table 3: The implications of Faraday rotation observations, see text for reference.

gives rise to the rotation, is shown in figure 14. Table 3 summarizes the implications of various observed Faraday rotation behaviors given by Laing (Laing, 1984).

#### *4. The Location of Faraday Rotation*

Faraday rotation can occur wherever free electrons couple to magnetic fields. As such, Faraday rotation may occur anywhere along the line of sight to the source being observed, or in the source itself. One of the first uses of Faraday rotation measurements of extragalactic objects was to map out the magnetic field of our own galaxy (Seymour, 1984, and references therein). Faraday rotation also occurs in our own ionosphere, since there are free electrons together with the earth's magnetic field. Our own galaxy has been well studied and Faraday rotation measures (galactic rotation measures, GRMs) of roughly 0 to absolute magnitudes of a many tens of radians per meter squared have been mapped out. These can be removed from complex polarization images. The ionospheric contribution is usually small, and it is only necessary to consider it at wavelengths above 10 cm or so under typical conditions.

In addition to these local rotation measures, Faraday rotation can occur in the clouds, observed in absorption (see chapter 1), along our line of sight to the quasar (cloud rotation measures, CRMs). From studies of the correlation of the presence of absorption line systems in quasar optical spectra with the rotation measures determined from radio observations, it appears that rotation does occur in at least some of these intervening systems (Welter, Perry and Kronberg, 1984).

Faraday rotation can also occur in the environment of the quasar (intrinsic rotation measures, IRMs). The Faraday rotation medium could be the galactic halo of the host galaxy of the quasar or various of the structures described in chapter 1, such as the NLR or BLR. Because the BLR and NLR are known to have highly ionized gas, these regions are expected to show Faraday effects (depolarization and rotation), if magnetic fields are present.

## *B. Faraday Rotation Measurements of Unresolved Quasar Cores*

### *1. Single Dish Polarization Measurements*

Early in the study of Faraday rotation, it was realized that the observation of linearly polarized radiation coming from quasars placed extreme limits on the emitting plasma (Wardle, 1977; Jones and O'Dell, 1977). The limits result from the fact that if the Faraday rotation arises within the emitting volume, the emitted radiation from the back of the source and the radiation from the front of the source pass through different pathlengths and therefore are rotated by different amounts. This is the case of internal Faraday rotation discussed above, so the observed polarized flux should drop with wavelength, while the position angle may undergo some rotation. Observations by single dish antennas indicated that the synchrotron radiating plasmas must contain large numbers of relativistic electrons to generate the observed luminosities, but there was little or no rotation of the position angle, and the polarized flux was roughly independent of frequency for some sources (Wardle, 1977). The effectiveness of electrons in causing Faraday rotation varies with  $\gamma_e^{-2}$  (because the effective mass determines the response to the electromagnetic wave), so that relativistic electrons give rise to very little Faraday rotation. The observed polarization indicated that there must be virtually no electrons with  $\gamma_e < 100$  in the sources observed.

### *2. VLA Faraday Rotation Measurements*

With the advent of the VLA and its high resolution capabilities, the arcsecond cores of quasars could be resolved apart from the jets and lobes in rotation measure structure. Observations using the VLA at wavelengths from 1.3 cm to 6 cm indicated that some quasar cores show significant IRMs, on the order of  $200 \text{ rad m}^{-2}$  (O'Dea, 1989, hereafter O89), even though earlier, lower frequency (and therefore lower resolution) observations indicated that IRMs were at most a few tens of radians per meter squared (Rudnick and Jones, 1983, hereafter RJ).

### 3. Implications for the NLR Confining Medium

The first striking fact in these IRMs is that they seem impossibly low given the structure of the NLR, which is known to intervene between us and a substantial amount of the polarized flux, so that it should form an external Faraday screen. The NLR clouds have densities of roughly  $10^4 \text{ cm}^{-3}$  with temperatures of about  $10^4 \text{ K}$  (see chapter 1), and they appear to be confined, since they do not evaporate on short time scales. Such confinement requires (RJ)

$$n_e T \approx 10^8 \text{ K cm}^{-3} \quad (4.4)$$

in the intercloud medium to match the pressure of the clouds. If there is equipartition of the magnetic and thermal energy in the NLR intercloud medium, the magnetic field must have

$$\frac{B^2}{8\pi} = 3nkT \quad (4.5)$$

so that B is roughly a milli-Gauss. Using equation 4.2 then gives a RM of  $8.1 \times 10^4 n_e \text{ rad m}^{-2}$  for a relatively short pathlength of 100 pc. Even if the confining medium had a temperature as high as  $10^8 \text{ K}$ , the expected RM would be 81,000  $\text{rad m}^{-2}$ , far in excess of the measured value. Further, early results from spectroscopy using the Hubble Space Telescope (HST) indicate that NLRs in quasars are on the order of a few kpc (Wills *et al.*, 1993). The solution to this contradiction may lie in field reversals in the NLR, which would have the effect of rotating the position angle back and forth around the original position angle. Of course, it is also possible that the intercloud medium is not confining the clouds or that equipartition of thermal and magnetic energy is not valid.

If the magnetic field undergoes a number of reversals, then it is in essence quite tangled. A tangled magnetic field should lead to substantial Faraday depolarization as

given in equation 4.3. For a source at some redshift  $z$ , the RM for each cell in the tangled field is (O89)

$$RM_f = 8.1 \times 10^5 (n_e B)_f d_f (1+z)^{-2} \quad (4.6)$$

where the redshift of the source enters because the radiation is bluer than that observed when it passes through the NLR (Kronberg and Perry, 1982). In order for there to be only limited depolarization, the exponential term in equation 4.3 must be small, which constrains the scale size of the fluctuations. Since quasars appear to have VLA core polarizations which do not drop off as the exponential of the fourth power of the wavelength (or in fact at all with wavelength), the fluctuation scale size,  $d_f$ , must obey

$$d_f < 6.25 \times 10^{-6} \left( \frac{n_e}{10} \right)^{-2} \left( \frac{B}{10^3} \right)^{-2} \left( \frac{L}{100} \right)^{-1} (1+z)^4 \left( \frac{\lambda}{0.06} \right)^{-4} \quad (4.7)$$

where as usual  $n_e$  is in  $\text{cm}^{-3}$ ,  $B$  is in  $\mu\text{G}$ ,  $L$  is in pc, and  $d_f$  is in pc, and  $\lambda$  is in meters, with minimal depolarization between  $\lambda$  and 6 cm.. For a nearby quasar (3C 273,  $z = 0.158$ ) this gives  $d_f < 0.00001$  pc, while for a more distant quasar (3C 345,  $z = 0.595$ ) it gives  $d_f < 0.00003$  pc, for  $n_e$  of  $1 \text{ cm}^{-3}$ ,  $B$  of 1 mG, and  $L$  of 100 pc, with detectable polarization at 20 cm wavelength (observations in RJ). If the NLR is truly over a kpc in size, the fluctuations must be at least an order of magnitude smaller.

#### *4. Implications for the NLR Clouds*

If the NLR emission line clouds are actually responsible for the observed Faraday rotation, and if the intercloud medium does not cause any Faraday effect, the same arguments apply only the factors are quite different. Equation 4.7 then requires values which are mostly unknown, since we do not know the scale size of the NLR clouds or the magnetic fields which might be present. However, for the sake of argument we can use equation 4.7 and  $n_e = 10^4 \text{ cm}^{-3}$  to determine  $B\Delta L = 2.5 \times 10^{-8} \text{ G}\cdot\text{pc}$ , where  $\Delta L$  is the pathlength. If we take  $\Delta L$  to be roughly 10 pc, then  $B$  is about a

0.1  $\mu\text{G}$ . This gives a fluctuation scale size of less than 0.01 pc (for  $z = 0$ ). Note that this choice of size does not lead to equipartition but keeps the thermal energy larger than the magnetic energy in the cloud. Requiring equipartition gives a method to determine the NLR cloud size from the RM (O89)

$$L_{\text{cloud}} = 2 \times 10^{-4} \left( \frac{RM}{200} \right) \left( \frac{n_e}{10^4} \right)^{-3/2} \left( \frac{T}{10^4} \right)^{-1/2} N^{1/2} \text{ pc} \quad (4.8)$$

where  $N$  is the number of cells of magnetic field intercepted by the telescope beam and enters since the RM measures  $B_{\parallel}$ , which is  $B(3N)^{-1/2}$  for a completely tangled field, and  $z$  is taken to be 1 (a factor of 16 different from  $z = 0$ ). Typical values of  $N$  (roughly  $3 \times 10^5$  as in O89) give cloud sizes of only 0.1 pc.

The results of low rotation measures ( $\sim 200 \text{ rad m}^{-2}$ ) for quasar cores as measured by the VLA leaves open the question of where the rotation is occurring. It appears that the rotation is unlikely to occur in the intercloud medium of the NLR, which has a large pathlength, unless the cell size of the magnetic field is quite small, so that depolarization is avoided. The NLR clouds may be responsible for the Faraday rotation, but it is still unknown what the covering factor of the NLR clouds around the core of the quasar is, so that it is unclear how many quasars should be expected to show Faraday rotation, an important statistic for testing where the Faraday rotation arises.

### *C. Faraday Rotation Measurements on the Parsec Scale*

#### *1. Scales in VLBI Measurements*

Faraday rotation measurements on VLA core emission are not easy to analyze. In order to determine whether the Faraday rotation is intrinsic to the quasar or occurs in intervening systems between the observer and the quasar, statistical analysis must be

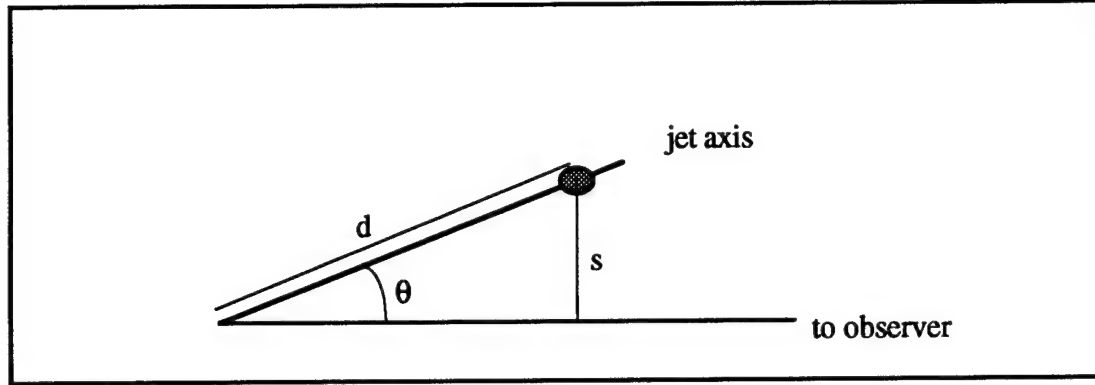


Figure 15: The geometry of a CDQ jet making an angle  $\theta$  to the line of sight, giving a transverse distance  $s$  on the plane of the sky for a jet distance  $d$ .

used. However such analyses are fraught with problems and limited data sets create difficulties (Perry, Watson and Kronberg, 1993). Further, since it is known that there is variation of the VLBI structure of quasar cores with frequency, it is not clear that Faraday rotation measurements done on VLA scales actually measure Faraday rotation rather than opacity effects in the core (O'Dea, 1989). In order to overcome these limitations, Faraday rotation measurements on VLBI scales must be made.

Faraday rotation measured by VLBI is likely to occur internally or in the NLR of quasars, because of an argument from simple geometry. Figure 15 shows the case for a CDQ showing superluminal motion. The measurement of superluminal motion requires that the angle to the line of sight made by the jet,  $\theta$ , be  $\leq 15^\circ$  in CDQs. To make the estimate of the pathlength through the quasar environment more conservative, a value of  $10^\circ$  will be used. VLBI resolution is typically better than 5 pc, so that  $s$  is taken as 10 pc conservatively. This gives the scale of the resolved jet structure,  $d$ , as

$$d = \frac{s}{\sin \theta} = 58 pc \quad (4.9)$$

which is a conservative, although some sources could clearly have larger deprojected lengths. The NLR is clearly larger than this, and is likely to be at least an order of

magnitude larger in light of the recent HST results noted above. This indicates that the VLBI jet is imbedded in the NLR, with the core likely to be imbedded either in the transition between the NLR and BLR, or perhaps in the BLR itself. For LDQs there is a much larger angle  $\theta$ , so that the distance  $d$  is even smaller.

Since Faraday rotation occurs along the line of sight, the NLR cannot be assumed to be the sole source of Faraday rotation. The rotation due to the galaxy (and when necessary the ionosphere) can be removed, however rotation from intervening systems and from the host galaxies of quasars is more difficult to handle. VLA measurements include the intervening systems and the quasar host galaxy, however the larger scale polarization from the intermediate scale jet ( $\sim 20 - 1000$  milliarcseconds) is included in the measurement. The VLBI scale measurements therefore must be interpreted in light of all other Faraday rotation measurements and care must be taken in analyzing them. However, gradients in Faraday rotation in VLBI measurements or changes between VLBI observations at different epochs must be due to the material in the NLR or the emitting volume.

## *2. Difficulties in VLBI Faraday Rotation Measurements*

There are serious difficulties to be overcome in order to make Faraday rotation measurements by VLBI. First, as noted in chapter 3, position angle calibration is dependent on a calibrator source where the full polarized flux of the VLA is recovered in the VLBI map. Faraday rotation measurements have required performing VLBI polarization experiments at a new frequency. The experience of previous observations at other frequencies must be used to choose a calibrator source. However, it is not guaranteed that a suitable calibrator will be chosen the first time at a new frequency as VLBI polarization measurements are extended to new frequencies.

Second, the limitations of the VLBI network introduce two problems for Faraday rotation mapping. First there is the problem of non-simultaneity of



observations. Since the sources observed are highly variable, at least in some of the radio components, the time gap between the observations at the two frequencies, required for the changing of receivers on the network antennas, introduces an uncertainty of whether or not the same features are measured in the two observations. Here VLBI has an advantage over VLA core measurements, since the resolved VLBI jet generally does not change within a week significantly, although the core may. This means that the Faraday rotation measurements determined from jet features are reliable, although care must be taken in interpreting features of the optically thick VLBI core. The VLBI network also determines the baselines used in the observations, so that the two different frequencies have inherently different resolutions. In practice this is handled by forcing the higher frequency to mimic the resolution of the lower frequency, but in reality the data points lie on fundamentally different size scales. The effects of this should be greatest for the edges of features, while the cores of the VLBI knots should be relatively unaffected, since both frequencies have adequate coverage in the Fourier transform space to determine the placement of knots in the jet.

Third, present VLBI linear polarization observations are limited to two frequencies. This introduces the well-known  $n\pi$  ambiguity into the Faraday rotation measurement. The ambiguity results from the fact that rotating the electric field vector by an extra  $\pi$  radians results in exactly the same observed position angle as if no extra rotation occurred. For these observations made at 6 cm and 3.6 cm, the  $n\pi$  ambiguity amounts to an uncertainty of  $\pm 1300 \text{ n rad m}^{-2}$ . This value is extremely large, and, as noted above, it is unlikely that such high rotation measures are present.

### *3. Faraday Rotation in the Optically Thin Jet*

Within the constraints on interpretation of VLBI Faraday rotation results discussed above, VLBI Faraday rotation measurements can provide significant information about the VLBI jet. There is the ability to reconstruct the true magnetic

field direction within the VLBI jet, if the Faraday rotation arises in external screens between the observer and the VLBI jet. Then equation 4.1 can be used directly to rotate the electric field vector of the observed radiation to the case where no Faraday rotation is present. Although the reconstruction of the magnetic field direction from a single frequency by using the fact that the emitted electric field of the wave is perpendicular to the magnetic field is unreliable, determination of the Faraday rotation at each position in the VLBI jet permits an unambiguous reconstruction of the magnetic field in the VLBI jet. This yields important information for testing unified schemes and for creating models of quasar jets. To truly know, however, that the Faraday rotation is external and that equation 4.1 can be applied, a third frequency should be observed to verify the  $\lambda^2$  law is linear over three points.

The question of where the Faraday rotation measured from VLA core polarizations arises becomes the question of whether the NLR clouds or NLR intercloud medium is responsible for external Faraday rotation in VLBI jets. As noted from figure 15, all quasars have substantial NLR intervening between the observer and the jet. If the NLR intercloud medium causes Faraday rotation then all quasars should (statistically) show similar Faraday rotation structure on VLBI scales. A distribution in Faraday rotation not representing a random walk would require either a wide range of magnetic field cell sizes in quasar NLRs or the Faraday rotation to arise in a different area of the NLR, *i.e.* the NLR clouds. Since the covering factor and sizes of the NLR clouds are unknown, it is possible that some quasar VLBI jets would be obscured by NLR clouds while others would not. This method of addressing the question of where the Faraday rotation arises must await the determination of the parsec scale Faraday rotation in a statistically significant sample of sources.

For Faraday rotation measurements of the resolved jets, two cases can be considered. First, the Faraday screen might be resolved on the scale of the individual

knots. Then parts of the observed individual polarized knots sample different cells in the screen, so that the magnetic fields in the cells might be directly measured. Second, the Faraday screen might be unresolved on the scale of the individual knots. Then the measured Faraday rotation arises, as with equation 4.3, from a number of individual cells. Unlike VLA measurements, the whole NLR is not sampled in this case. Instead a cylinder of the NLR is sampled (roughly the resolution of the interferometer in width and the size of the NLR in depth), so that front-back depolarization can be considered to play a larger role than side-side depolarization. The same arguments as in equations 4.3 and 4.7 can be applied, only now the number of cells is not isotropic in all three dimensions. This can place more stringent limits on the cell size in the NLR confining medium.

If the Faraday rotation arises in the NLR clouds and if the clouds are large ( $>5$  pc), then VLBI can give an extremely reliable measurement of the cloud size simply by noting where rotation begins and ends along the jet. Since rotation would be zero from the intercloud medium, the actual endpoints of a cloud would be seen as points of zero rotation measure around a region of measurable rotation. This requires maximum cloud sizes of a few tens of parsecs with present capabilities, although the VLBA should improve the dynamic range and mapping ability, so that longer jets can be mapped, and larger clouds could be measured.

A further important feature of VLBI observations to the measurement of the magnetic field cell size is the change in Faraday rotation along a jet. The primary argument for the size scale of the magnetic field being small is that depolarization of the linearly polarized radiation does not occur on VLA scales. The integrated measures of Faraday rotation from VLA core measurements assume a random walk process to generate the observed Faraday rotation. However, if two well separated points (*i.e.* more than a beamwidth apart) in a VLBI scale Faraday rotation map show the same

Faraday rotation, it is unlikely to be due to a random process. Instead, an ordered field must exist on a scale which encompasses both points. Since very small cell sizes were suggested by VLA measurements, an ordered Faraday rotation measurement along a VLBI jet would rule out a totally random field in the NLR.

VLBI observations of Faraday rotation can also be used to constrain the NLR properties. Simply applying equation 4.2 to observations to recover the integrated line of sight magnetic field and electron density allows the determination of this quantity through the NLR to the VLBI jet. It has already been realized that, given the long pathlength through the NLR, there cannot be an ordered field on the scale of the NLR. However, direct measurements of the value of the integral in equation 4.2 for any quasar are only now possible.

#### *4. Faraday Rotation in the Optically Thick Core*

As noted above, special care must be taken in any interpretation of Faraday rotation in the optically thick core. Since this feature is unresolved, it can change significantly within a one week time frame, so that the same features may not be measured during the observations at the two different frequencies. Also the core position is slightly different for the two frequencies giving a point on the Faraday rotation map where the Faraday rotation measurement mixes the optically thick emission from the lower frequency with the optically thin emission from the higher frequency. The resolution of the observations may smear this detail out over other features in the map, so that special care must be taken in interpreting features near the core of the source.

Faraday rotation measurements on the core may probe either the BLR or NLR. Since absolute position information is not available from standard interferometry, and since the scale size and shape of the BLR is still uncertain, it is not clear whether the radio core observed in VLBI lies behind the BLR or not. However, substantial

differences in core Faraday rotation and jet Faraday rotation could be taken as indicating a crossing of the transition between the BLR and NLR along the line of sight, so long as other causes can be ruled out.

#### *5. Time Evolution of Faraday Rotation on VLBI Scales*

The detection of superluminal motion in the VLBI components of quasars showed that VLBI measurements are capable of measuring the changes in quasars directly. Over the course of years, the changes in the NLR could be observable by Faraday rotation measurements on the milliarcsecond scales. If the NLR confining medium is responsible for Faraday rotation, and if the cells are unresolved on the scale of the individual knots, then as the knot moves behind the cells sudden shifts in Faraday rotation should occur. This would give a direct measure of the cell size in the NLR confining medium. Of course, unresolved (*i.e.* small) NLR clouds would also explain this result.

If large clouds are responsible for Faraday rotation, then over time it is possible to use Faraday rotation measurements to map out the NLR clouds. This would give a direct measurement of the NLR cloud size and the covering factor. With the advent of the completed VLBA and its correlator, such measurements should be possible as there will be sufficient observing time to make long term measurements of a number of quasars. The multiple frequency capability of the VLBA will also allow the linear polarization observations to be done much more simultaneously and at more wavelengths than is presently possible, which should help remove uncertainties about how changes in the quasar are effecting the measurements.

## V. The Quasars 3C 273 and 3C 345

### A. 3C 273

#### *1. General Characteristics*

The quasar 3C 273 was the first QSO identified as an extragalactic, high redshift object (Schmidt, 1963). Since it is relatively nearby,  $z = 0.158$ , and very luminous, it has been extensively observed in all wavebands. The visual magnitude is roughly 12.8, however 3C 273 shows variations of roughly half a magnitude in periods of about one month (Moore and Stockman, 1984). An optical jet, which appears to be composed of a continuous underlying jet with four bright knots, extends roughly 20 arcseconds from the core at a position angle of  $-138^\circ$  (Evans, Ford and Hui, 1989). The jet appears polarized in the R band, with a fractional polarization varying from 10% to 20% along its length and a position angle of the electric field vector perpendicular to the jet axis (Scarrott and Rolph, 1989). The optical jet is aligned with the arcsecond radio jet which extends for the same distance and ends in a lobe (Davis, Muxlow and Conway, 1985).

3C 273 is generally identified as a LPQ, with typical optical polarization of less than 1%, although in radio bands it is a powerful CDQ. However, intensive optical observations have revealed a variable component of optical continuum emission, that accounts for roughly 10% of the total optical flux and shows high

polarization with variations in total flux, polarized flux, and polarization position angle within periods of roughly a day, which has led to 3C 273 being called a "miniblazar" (Impey, Malkan and Tapia, 1989). A polarized optical outburst in 1990 was observed to coincide with an outburst in the 90 GHz mm band, further suggesting that 3C 273 harbors a blazar-like core component linked to the strong radio emission (Valtaoja *et al.*, 1991).

## 2. Behavior Before 1986

During the late 1970's and 1980's, long term monitoring programs began to study 3C 273 in many wavebands. During the period from 1983 to 1986, variations of up to ~20% of the total optical and IR flux were observed, while soft X-rays varied 20 to 40% and hard X-rays varied by a factor of 2 (Courvoisier *et al.*, 1987). Overall the luminosity of 3C 273 is roughly equal in all wavebands, with  $10^{46}$  erg s<sup>-1</sup> emitted in each decade from the IR to visible. Radio luminosity is down roughly an order of magnitude, and there is a UV bump (the big blue bump) which boosts the luminosity to  $10^{47}$  erg s<sup>-1</sup> in the ultraviolet. During this period the sub-millimeter flux reached an all time low in 1986.

The low flux in the sub-millimeter to IR bands in 1986 allowed the identification of an apparently unvarying IR component, which is generally hidden by the stronger continuum extending from the radio and mm bands (Robson *et al.*, 1986). Observations extending the IR and sub-mm observations determined that there was a break in the power law at about 5 mm, with an  $\alpha = -0.1$  power law holding for the longer wavelength radiation and an  $\alpha = -0.7$  powerlaw holding for shorter wavelengths (Clegg *et al.*, 1983). These components, together with the thermal component responsible for the big blue bump and the component responsible for enhanced X-ray emission, make a total of at least five separate emission components in 3C 273.

In February 1983, 3C 273 underwent a flare in the mm to far IR regime, which increased its flux density by roughly 25% and flattened its spectrum away from the  $\alpha = -0.7$  spectral index noted above (Robson *et al.*, 1983). This flare died out at shorter wavelengths in a period of roughly one to two months, but it was delayed in its propagation at the longer wavelengths observed (up to 3 mm).

### 3. Behavior since 1986

In early 1988, there was a dramatic flare in 3C 273 which occurred in all wavebands. Optical observations showed 5 distinct maxima, roughly 15 days apart but with 2 peaks only 3 days apart (Courvoisier *et al.*, 1988). The overall change in optical flux was roughly 20% - 25% with the IR flux changing by a factor of 2 within 1 day. As with previous flares, the spectrum became flatter during the outburst. UV observations were not made during the period of the outburst, however the UV flux had increased by the time observations were made 3 months later (Courvoisier *et al.*, 1990). The 1.1 mm flux showed the most dramatic change, increasing five fold, which extended with lower amplitude and with a delay of 5 weeks to several months into the radio regime, with longer wavelengths having lower amplitudes and longer delays.

More recently there have been further flares in 3C 273, however they did not extend into the shorter wavebands, but were limited to the far-IR to radio regimes. From the large 1988 flare until April 1990, 3C 273 was reasonably quiet without significant flaring activity. There was then a large flare, but it was much stronger at wavelengths longer than 800 mm, where it involved an increase of roughly a factor of 4 over the quiescent level of 1989 (Robson *et al.*, 1993). As with previous flares it propagated into the radio regime with wavelength dependent delays. 3C 273 flared once again in 1991, however this flare was of lower magnitude than that in 1990 at wavelengths shortward of 2 mm, while being stronger at longer wavelengths.



**3C 273 Epoch 1989.2 Positions**

<u>Component</u>	<u>Date of Birth</u>	<u>Separation Speed</u>	<u>Separation - Core</u>
C4	1976	1.0	(13.2)
C5	1978.6	1.2	(12.7)
C6	--	--	--
C7	1982.0	0.6	4.4
C8	1984.6	0.8	3.6
C9	1988.2	0.8	0.8

Table 4: 3C 273 component characteristics in epoch 1989.2. Separation speed is in milliarcseconds per year and the separation is in milliarcseconds. See text for references.

In general X-ray observations are not yet made with the time resolution necessary to follow the flaring behavior observed at other wavelengths. However, observations by Ginga in December of 1987 showed an  $\alpha = -0.53$  powerlaw spectrum for the 2 to 35 keV band, while a year later after the large flare, this had flattened to  $\alpha = -0.42$  (Turner *et al.*, 1990). In the higher energy band (35 - 500 keV), measured using the SIGMA detector aboard GRANAT, 3C 273 underwent a two fold change in flux in 41 days (Bassani *et al.*, 1992). It is unclear if X-ray variations are related to the flaring behavior observed at lower frequencies, but it is clear that X-ray variability is present even to high energies in 3C 273.

#### *4. Previous VLBI Observations*

As noted in chapter 2, 3C 273 was one of the first quasars to show superluminal motion, and it has been intensively studied since the initial development of VLBI. Shortly after the dramatic 1988 flare noted above, VLBI observations were made at 43 GHz, and table 4 summarizes the components observed and includes

components seen at earlier epochs and lower frequencies (from Krichbaum *et al.*, 1990; and including data from Unwin *et al.*, 1985; Cohen *et al.*, 1987; Zensus *et al.*, 1990, numbers in parantheses are added here for completeness). The date of birth is calculated simply by taking the component position and moving it backwards with its separation speed until it merges with the core. At the 0.1 mas resolution offered by 43 GHz VLBI, further components are seen nearer the core at roughly 0.3 and 0.6 mas (epoch 1989.2). These components appear to follow a curved trajectory out from the core in the first milliarcsecond.

Measurements at 22 GHz over a period of 5 years from 1982 to 1987 followed the evolution of components C7 and C8 over the first 2.5 mas of the jet (Zensus *et al.*, 1990). These components were seen to emerge from the core and follow a roughly straight path from about 0.5 to 2.5 mas, so that curvature on these scales is probably small in 3C 273. The calculation of the birth of these components gives times which appear to correspond to millimeter band flux density outbursts.

At 10.7 GHz, improved uv coverage and lower resolution begin to permit mapping of components farther from the core. On the scale of tens of milliarcseconds, the jet appears to emerge along a trajectory roughly matching the one seen at higher resolution at a position angle of  $-117^\circ$  and then undergoes a bend within the region between 8 and 15 mas to  $-138^\circ$  (relative to the last component before the bend) (Unwin *et al.*, 1985). Lower frequency observations (2.3 GHz) find that this position angle remains out to roughly 35 mas (Cohen *et al.*, 1983), and it is also the position angle of the larger scale optical and radio jets.

VLBI observations made at 6 cm over a number of years, once including southern hemisphere antennas to improve the North-South resolution, have mapped the jet evolution to  $\sim 30$  mas at 5 GHz (Zensus *et al.*, 1988). By watching the components change position over time, the jet is seen to emerge from the core and

**3C 273 10.7 GHz Positions**

<u>Epoch</u>	<u>C10</u>	<u>C9</u>	<u>C8</u>	<u>C7</u>	<u>C5</u>
1990.17	0.3	1.2	4.4	5.0	~12
1991.15	0.8	2.2	4.5	5.7	~12

Table 5: 3C 273 component locations in milliarcseconds for two epochs from 10.7 GHz observations. See text for reference.

follow a roughly S shaped trajectory, which deviates from a straight line by about 1 mas over its 20 mas length. The jet then appears straight at a position angle of  $-138^\circ$  out to the limit of the map at about 70 mas.

Recent Mark II VLBI observations at 10.7 GHz provide component positions out to approximately 12 milliarcseconds along the jet and indicate the birth of a new component between 1988 and 1990 (Abraham *et al.*, 1994). The components detected in these observations and their positions are shown in table 5.

By comparing VLBI maps made at multiple frequencies, rough measurements of the spectral indices of jet components can be made. The VLBI maps are generally not simultaneous, and often have gaps of roughly 3 months between them, so that the indices are somewhat model dependent. The spectra show that the core component is optically thick up to at least 10.7 GHz, while jet components are optically thin (Unwin *et al.*, 1985). Two components in the jet were measured from epoch 1981 observations at 2.3 to 10.7 GHz and spectral indices of  $-0.7$  and  $-1.0$  were determined. Extrapolation of the core component from its spectral index of  $+0.65$  to higher frequencies suggests a turnover at 40 to 70 GHz in order to not exceed the total source flux from single dish measurements. The fact that the core is optically thick and the

### 3C 273 Epoch 1984.8 Polarization Data

<u>Comp.</u>	<u>Separation</u>	<u>Pos Angle</u>	<u>I (Jy)</u>	<u>p (mJy)</u>	<u><math>\chi</math> (deg)</u>	<u>m (%)</u>
P4	--	--	15.7	84	-37	0.5
P3	5.4	-116	6.63	46	+34	0.7
P2	9.4	-121	1.60	152	-13	9.5
P1	19.6	-130	1.13	294	-36	26.0

Table 6: 3C 273 component characteristics including polarization. Separation is in milliarcseconds. See text for reference.

jet optically thin makes the core more dominant at higher frequencies, and limits how far out along the jet the components can be seen at higher frequencies.

Polarization VLBI measurements of 3C 273 show a complex structure in the jet. The results are summarized in table 6 for the epoch 1984.8 observations (Roberts *et al.*, 1990). The components are identified from the total intensity image, and the polarized image shows region P3/P2 divided into three distinct components, which show rotation of the electric field vector from  $\sim 90^\circ$  to  $\sim 0^\circ$  over 6 mas. As noted in table 6, the fractional polarization increases along the jet. There is also a tendency for the total intensity to drop faster at the edges of components than the polarized flux, so that the fractional polarization tends to increase at component boundaries.

### B. 3C 345

#### 1. General Characteristics

The quasar 3C 345 is an OVV/HPQ at redshift 0.595. It has been studied extensively since its discovery in the 1960's, including longterm monitoring of its light curve. The range in visual magntiude over the 23 years studied to 1988 is from

14.7 to 17.7, with both broad peaks and quite narrow peaks and no periodic behavior (Kidger, 1989). 3C 345 also shows rapid flaring of up to a magnitude in time periods as short as ten days. 3C 345 is a strong CDQ with an arcsecond scale jet, which runs quite straight for two arcseconds from the core along a position angle of  $-51^{\circ}$ , after which it bends to  $-43^{\circ}$  and ends with two knots (Kollgaard, Wardle and Roberts, 1989).

## *2. Behavior of 3C 345*

The quasar reached an all time low in its light curve in 1990 with a sudden 10 day decline accompanied by strong color variations across the visual band (Kidger and Takalo, 1990). Then in 1991, 3C 345 began a new outburst, which was followed in 1992 by a second peak with an overall change of 3 magnitudes in the flux density from the low in 1990 to the peak in 1992, and which included high polarization and rapid changes in electric field position angle (Kidger *et al.*, 1993). Overall this behavior is similar to the 1967 - 1969 outburst behavior. The polarization in 3C 345 appears to decline at shorter wavelengths in the optical regime, perhaps due to dilution of the polarized component by blackbody emission (Mead *et al.*, 1988). Interestingly, at least in the infrared, 3C 345 behaves differently during outbursts than other OVV/HPQs, as its spectrum gets steeper rather than flatter (Takalo *et al.*, 1992).

Multifrequency monitoring of 3C 345 has indicated substantial structure in the source. There is not a direct link from all observed optical outbursts into the radio regime, however the three largest optical/IR outbursts prior to 1986 eventually appeared in the radio with delays from 1 - 2 years (Bregman *et al.*, 1986). It appears therefore that there is a common mechanism for some of the emission observed at widely different wavelengths. However, this study also showed that at least four separate emission components are needed to explain the multifrequency observations. There appears to be a break in the power law describing the infrared to optical

### 3C 345 Epoch 1990.2 Positions

<u>Component</u>	<u>Separation from Core</u>	<u>Comments</u>
C5	1.6 mas	at $-102^\circ$
C4	2.5 mas	
C3	5.0 mas	
C2	8.5 mas	
C1	$\sim 18$ mas	at $-54^\circ$

Table 7: 3C 345 component positions for epoch 1990.2. Component separation is in milliarcseconds. See text for reference.

behavior at roughly  $20\ \mu\text{m}$ , so that from  $350$  to  $20\ \mu\text{m}$  a spectral index of  $-0.9$  is needed, while from  $20\ \mu\text{m}$  to  $1200\ \text{\AA}$  an index of  $-1.4$  is needed. A superposed blue bump is needed to explain the spectrum from about  $4000\ \text{\AA}$  to  $1500\ \text{\AA}$ , and extending the powerlaw into the X-ray regime underestimates the X-ray flux considerably.

### 3. Previous VLBI Observations

As with 3C 273, superluminal motion was discovered early in 3C 345. VLBI observations have been ongoing and have extended up to  $22.2\ \text{GHz}$ . At this frequency, 3C 345 shows a strong core with a short jet. The epoch 1981.3 map showed the component C4, associated with an outburst in 1979, within roughly a milliarcsecond of the core with a position angle of roughly  $-130^\circ$  (Readhead *et al.*, 1983). In later  $22.2\ \text{GHz}$  maps the separation became progressively larger and the position angle progressively less negative, until in epoch 1984.1 the emission component was roughly  $2\ \text{mas}$  from the core at  $-85^\circ$  (Biretta, Moore and Cohen, 1986).

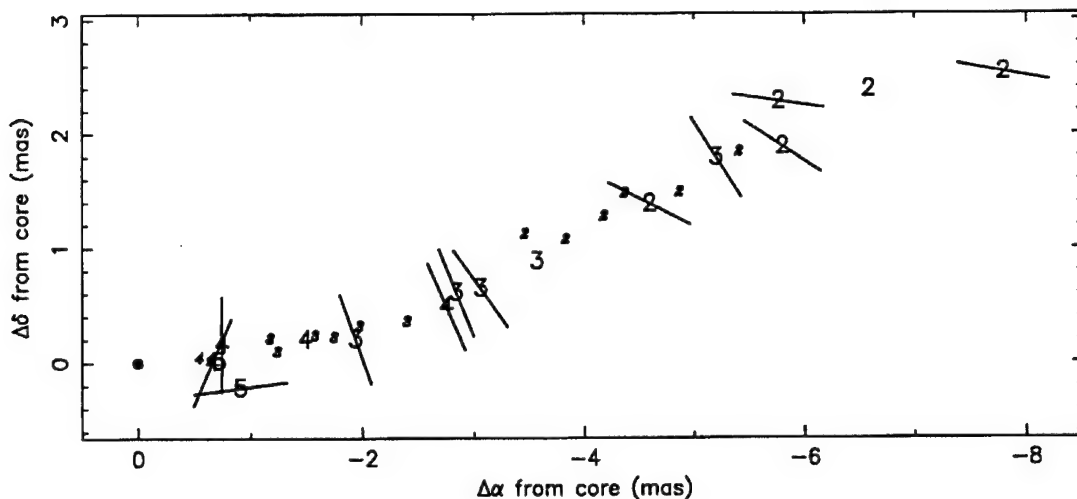


Figure 16: The magnetic movie showing the progression of components out along the jet in 3C 345 with their electric field vector position angle. See text for reference.

At observing frequencies of 5 and 10.7 GHz, components in the jet farther from the core can be seen. At 10.7 GHz, the components appear out to roughly 2 mas in early maps (epoch 1981), emerging from the core at a position angle of  $-83^\circ$  and showing a turn to the north at about 2 mas (Unwin *et al.*, 1983). In 5 GHz maps from the same epoch, the jet extends out to roughly 8 mas, with the same structure as the 10.7 GHz maps but now extending to the northwest at a position angle of  $-75^\circ$ . These maps over a two year period demonstrated clearly the superluminal motion in the jet of 3C 345, with proper motions of roughly 0.3 to 0.4 mas/yr corresponding to  $\sim 7h^{-1}c$ .

At longer wavelengths, and often with adequate dynamic range at 6 cm, an outer component can be seen in the jet at roughly 15 to 18 mas from the core (Rantakyrö *et al.*, 1992). At 18 cm this feature appears as a diffuse and extended component with the main jet (ending at roughly 12 mas) quite distinct with a sharp, edge-brightened appearance. The edge brightening of the jet as it extends to the northwest has been noted in 6 cm observations as well (Unwin and Wehrle, 1992),

**3C 345 Epoch 1988.1 Polarization Data**

<u>Comp.</u>	<u>Separation</u>	<u>Pos Angle</u>	<u>I (Jy)</u>	<u>p (mJy)</u>	<u><math>\chi</math> (deg)</u>	<u>m (%)</u>
D	--	--	1.44	55	+70	3.9
C5	0.9	-104	4.28	49	-79	1.1
C4	2.8	-80	0.67	51	+29	7.7
C3	5.5	-71	0.31	34	+38	10.9
C2	8.2	-72	0.20	16	+85	8.1

Table 8: 3C 345 component characteristics for epoch 1988.1 including polarization. Separation is in milliarcseconds. See text for reference.

and has been seen in the clean components in the many epochs of mapping at Brandeis (Brown, 1992).

From the multiple frequency VLBI maps, the spectral indices of the components can be measured. Measurements in 1981 indicated spectral indices of roughly 2.8 for the core, -0.2 and -0.1 for two jet components between 2.3 and 5 GHz (Cohen *et al.*, 1983). The core measurement is near that expected for an optically thick, single component synchrotron source, while the jet components appear to have much flatter spectra than components in the jet of 3C 273. A summary of the VLBI components and their positions relative the core taken from high dynamic range observations from 1990 are given in table 7 (Unwin and Wehrle, 1992).

3C 345 has been observed for a number of years using polarization VLBI. The course of components out along the jet together with their polarization position angles have been mapped in detail (see figure 16) (Brown, 1992). These measurements show that knots C2 to C4 have followed the same trajectory as they



have moved along the jet away from the core. Their polarization properties have also been remarkably consistent, with C4 emerging into the main jet extending to the northwest simultaneous with its rotation of electric field position angle to lie perpendicular to the local jet direction. However, C5 did not seem to follow this behavior in the epoch 1988.1 observations, as it overtook a position formerly occupied by C4 without undergoing a substantial rotation of its electric field position angle as expected. A summary of the polarization properties of the core and jet components in epoch 1988.1 is given in table 8.

## **VI. Observations**

### *A. Epoch 1990.4*

#### *1. 5 GHz Observations*

The epoch 1990.4 6 cm observations took place in early June, 1990, using the global VLBI network with 10 scheduled antennas. Three antennas failed: Hatcreek in California did not have an observer to run the telescope, Owens Valley data was not recoverable from the Mark III tape, and Pietown (VLBA) failed to record proper timing signals. The seven antennas which were successfully correlated are listed in table 9, together with their characteristics.

The observations covered 24 hours of time on the network from 01 00 UT on June 10th to 01 00 UT on June 11th. Correlation was done on the Mark IIIA correlator at Haystack Observatory in Westford, Massachusetts, in the Fall of 1990. Two passes through the correlator were performed to produce both parallel hand and cross hand visibilities. The data were segmented into one minute integrations using mode 701 of FRNGX at Haystack.

The data were reduced using the Brandeis calibration routines, CALIB routines, as described in chapter 3. System temperature measurements and gain curve information were applied routinely to produce a gain file. The gain file was used to

### EPOCH 1990.4 ANTENNAS (6 cm)

<u>Antenna</u>	<u>Code</u>	<u>Diameter</u>	<u>Rec.</u>	<u>Comments</u>
Medicina (Italy)	L	32 m	R L	Large D terms
Bonn (Germany)	B	100 m	R L	Reference Antenna
Westerbork (Netherlands)	W	14 x 25 m	R L	Phased Array
Haystack (Massachusetts)	K	37 m	R L	
Green Bank (W. Virginia)	G	43 m	R L	
Fort Davis (Texas)	F	26 m	R L	
VLA (New Mexico)	Y	27 x 25 m	R L	Phased Array

Table 9: Antenna characteristics for stations correlated in the 6 cm, epoch 1990.4 experiment.

produce a calibrated data base. The calibration on the database appeared correct when checked by analysis of the visibilities.

Because of the loss of data due to the limited number of antennas, resulting from the unexpected failure of three antennas, the number of baselines containing 3C 84 for polarization calibration was smaller than desired. Visibilities from the source OQ 208, also unpolarized but weaker, were added to the data set to improve parallactic angle coverage for the fitting of D terms and to increase the overall number of data points. OQ 208 is generally used as a check on the calibration, but here it was used as a second calibrator.

Alignment of the RCP - LCP antenna gains was completed routinely using Effelsberg (B) as the reference antenna. The D terms were determined, and the fits obtained were checked by plotting the cross-hand to parallel-hand ratios in the

### EPOCH 1990.4 6 cm D TERMS

<u>Antenna</u>	<u>RCP Amp</u>	<u>RCP Phase</u>	<u>LCP Amp</u>	<u>LCP Phase</u>
L	15.81	20.5	16.68	161.4
B	2.99	138.7	8.72	15.5
W	6.98	-176.9	7.87	-73.7
K	2.54	-179.5	1.48	-89.1
G	1.44	6.1	2.35	138.5
F	0.83	-112.3	0.71	-97.0
Y	2.46	-11.0	1.88	102.1

Table 10: D terms for antennas correlated in the 6 cm, epoch 1990.4 experiment.

complex plane. The solutions appeared good, and the final D terms obtained are given in table 10.

The polarized data base was written without final position angle calibration, and the position angle calibrator source OJ 287 was imaged by hybrid mapping. A clean box, which constrains the placement of clean components, was placed around the jet direction to obtain convergence of the map. The resulting 6 cm total intensity and complex polarization maps of OJ 287, epoch 1990.4, are shown in figures 17 and 18 respectively. The sum of the clean components resulting from hybrid mapping was compared to the complex polarization measured at the VLA, using interferometer mode scans taken between VLBI observations. The VLBI observations gave 56 mJy of polarized flux at a position angle of  $73^\circ$  compared to 63 mJy of polarized flux at  $-69^\circ$  for the VLA. The position angle of the VLBI data set was adjusted by  $38^\circ$  to align the VLBI clean components and VLA interferometer mode data (since  $73^\circ = -117^\circ$  for polarized radiation).

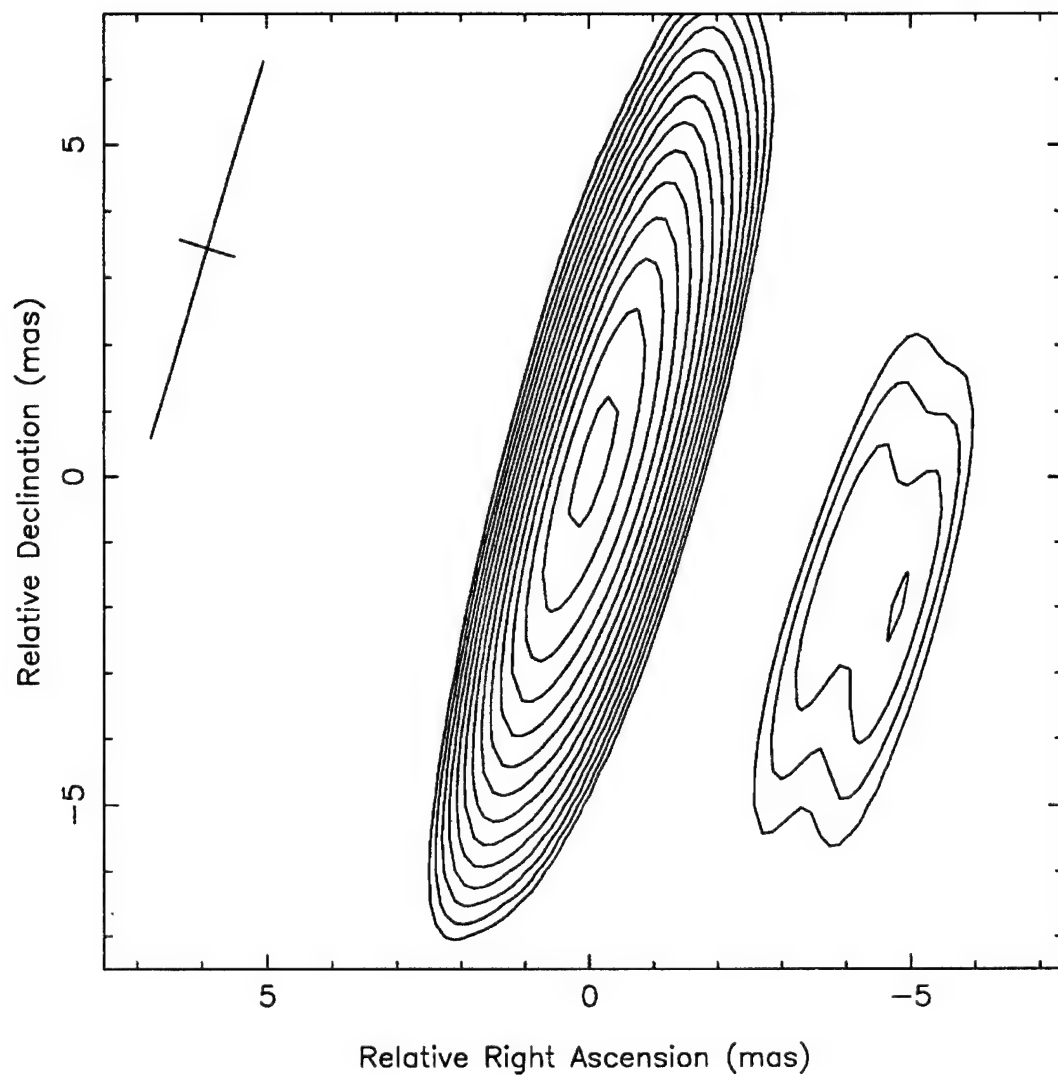


Figure 17: Total Intensity Map of OJ 287 at 6 cm, Epoch 1990.4, made with natural weighting of the visibilities. Contours are at 1, 1.4, 2, 2.8, 4, 5.7, 8, 11.3, 16, 22.6, 32, 45.3, 64, and 90.5% of peak flux of 1870 mJy/beam. The beam is 5.93 by 0.87 milliarcseconds at a position angle of  $-16.9^\circ$ .

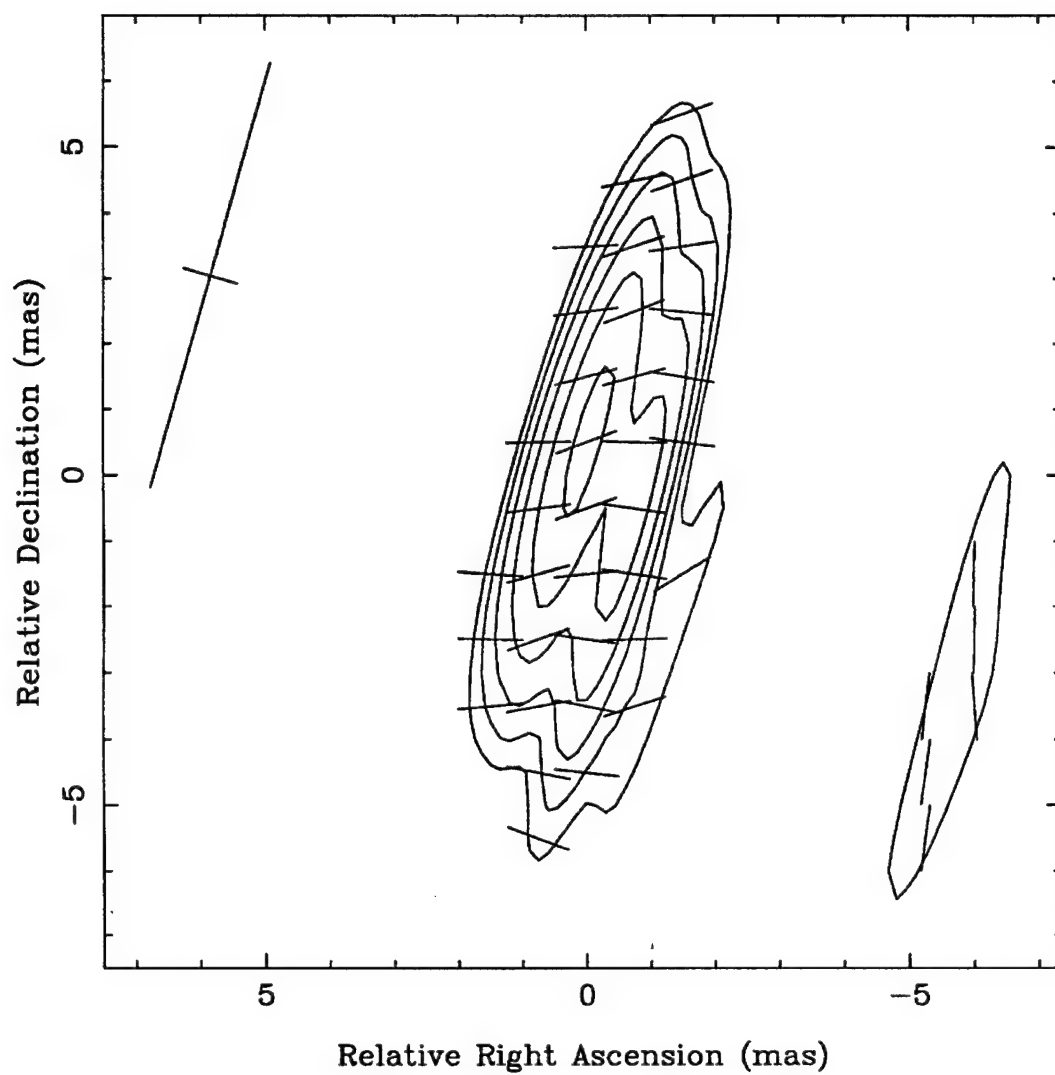


Figure 18: Complex Polarization Map of OJ 287 at 6 cm, Epoch 1990.4, made with natural weighting of the visibilities. Contours are at 16, 22.6, 32, 45.3, 64, 90.5% of the peak flux of 40.1 mJy/beam. The beam is 6.73 by 0.87 milliarcseconds at a position angle of  $-16.1^\circ$ .

#### *2. 8.4 GHz Observations*

The epoch 1990.4 3.6 cm observations took place in the middle of June using the global VLBI network. The observations ran for 24 hours from 06 30 UT on June 16th to 06 30 UT on June 17th, although not all antennas were available for the full run. Of the 12 antennas originally scheduled, only 9 returned useful data and one of these (Onsala) observed for only a few hours and had no significant data on the program sources. The antennas which failed were Haystack, which recorded at the wrong frequency due to a mistake during the setting of the local oscillator, Pietown (VLBA), which also set the wrong local oscillator, and Hatcreek, where no observer was present during the network session. The loss of Pietown was particularly damaging to this experiment, since it was one of only three dual polarization antennas available for the full 24 hours. The NASA Deep Space Network (DSN) provided two antennas, one in Madrid which observed for ~7 hours from 14 20 UT to 21 35 UT on June 16th, and one in Goldstone, California, which observed for ~12 hours from 11 35 UT to 24 00 UT on June 16th. Unfortunately these times did not provide good viewing for 3C 273. The antennas which were correlated are listed in table 11.

Correlation was done on the Mark IIIA correlator at the Haystack Observatory in Westford, Massachusetts, in the Fall of 1990. Two passes through the correlator were used to produce both the parallel hand and cross hand correlations. The data were segmented using mode 701 of FRNGX at Haystack.

The amplitude calibration was performed using the Brandeis CALIB package. System temperature measurements and gain curves were provided by most antennas, however the DSN antennas provided no observing logs. Estimates of the DSN antenna system temperatures were made by assuming a base temperature of 21 K and

### EPOCH 1990.4 ANTENNAS (3.6 cm)

<u>Antenna</u>	<u>Code</u>	<u>Diameter</u>	<u>Rec.</u>	<u>Comments</u>
Onsala (Sweden)	S	26 m	R	Stowed after 3 hrs.
Medicina (Italy)	L	32 m	R	Large D term
Bonn (Germany)	B	100 m	R L	Reference Antenna
DSN (Madrid)	M	34 m	R L	Only 7 hrs. of time
Green Bank (W. Virginia)	G	43 m	R	Large D term
Fort Davis (Texas)	F	26 m	L	
VLA (New Mexico)	Y	27 x 25 m	R L	Phased Array
DSN (Goldstone)	D	34 m	R L	Only 12 hrs. of time
Owens Valley (California)	O	40 m	R	

Table 11: Antenna characteristics for stations correlated in the 3.6 cm, epoch 1990.4 experiment.

adding a source component of 0.25 K/Jy. The gain file was created and a calibrated database produced. When this database was checked, it was clear that there was substantial misalignment between the two feeds at the DSN antennas, and the gains were adjusted accordingly. A final calibrated database was then written and checked.

Because of the loss of antennas and the limited observing time of the DSN antennas, D terms were determined using both 3C 84 and OQ 208 simultaneously. The alignment of RCP - LCP phases at the antennas proved difficult. The lack of dual polarization antennas left only Bonn and the VLA with dual polarization through much of the experiment. The loss of Pietown, with its stable offset, proved disastrous near the end of the observation, when Bonn and the VLA did not observe the same source for a period of several hours. During this time the VLA phase jumped, and



alignment was not possible. The cross hand data from these periods to the VLA could not be used.

Aside from that problem, the alignment of the two receivers was completed. The D terms were determined as usual, and plots of the cross hand to parallel hand ratios showed the solutions to be correct. Table 12 gives the final solutions for the D terms at 3.6 cm.

The polarized database was written without position angle calibration. OJ 287 was imaged by hybrid mapping and convergence could not be obtained. Because of the antennas which failed, the spread of points in the Fourier transform space clumped into three sets, short spacings from the western U.S. and Europe separately, intermediate spacings from baselines to Green Bank, and extremely long baselines from the western U.S. to Europe. To make matters worse for polarization imaging, Green Bank had only a single polarization and an extremely large D term. Difficulties in self-calibration have been noted in data sets with substantial holes in their uv coverage, such as often occurs in 3C 273 (Krichbaum *et al.*, 1990).

In order to recover the position angle calibration, OJ 287 was imaged in a number of ways. First only the antennas in the western U.S. were used. Data was flagged aggressively and an unresolved image was obtained as expected. Next only Europe was used, data was again flagged and again an unresolved image was obtained. Finally Green Bank was added independently to each data set. The source was now partially resolved, but editing of data from Green Bank baselines allowed convergence to be obtained. At all times the recovered fluxes and polarization features were compared and found to be consistent. Finally the whole data set was combined and convergence was now obtained, apparently due to the removal of a number of erroneous data by the previous flagging.

# EPOCH 1990.4 3.6 cm D TERMS

<u>Antenna</u>	<u>RCP Amp</u>	<u>RCP Phase</u>	<u>LCP Amp</u>	<u>LCP Phase</u>
S	1.17	21.1	---	---
L	13.73	-134.1	---	---
B	6.97	74.3	5.61	137.5
M	2.78	-154.1	2.56	-90.5
G	40.63	-90.5	---	---
F	---	---	3.69	50.2
Y	1.56	-6.3	0.32	-173.7
D	3.88	-97.5	3.77	-81.6
O	7.80	123.9	---	---

Table 12: D terms for antennas correlated in the 3.6 cm, epoch 1990.4 experiment.

Two separate images were obtained with equally good fit to the data using different parameters in the hybrid mapping. The solutions gave  $10^\circ$  of difference in electric field position angle from the sum of the polarized clean components. However, comparing the final maps with one of higher quality made by Gabuzda from data at roughly the same epoch (Gabuzda, private communication) showed one solution to be preferable, as it exactly matched the higher quality map. This solution also resulted in a low Faraday rotation (virtually zero) in both OJ 287 and 3C 345 when their 3.6 cm images were compared to the 6 cm images. For these reasons the calibration is assumed to be correct, despite the apparent uncertainty due to the quality of the data. The final total intensity and complex polarization maps are shown in figures 19 and 20 respectively.

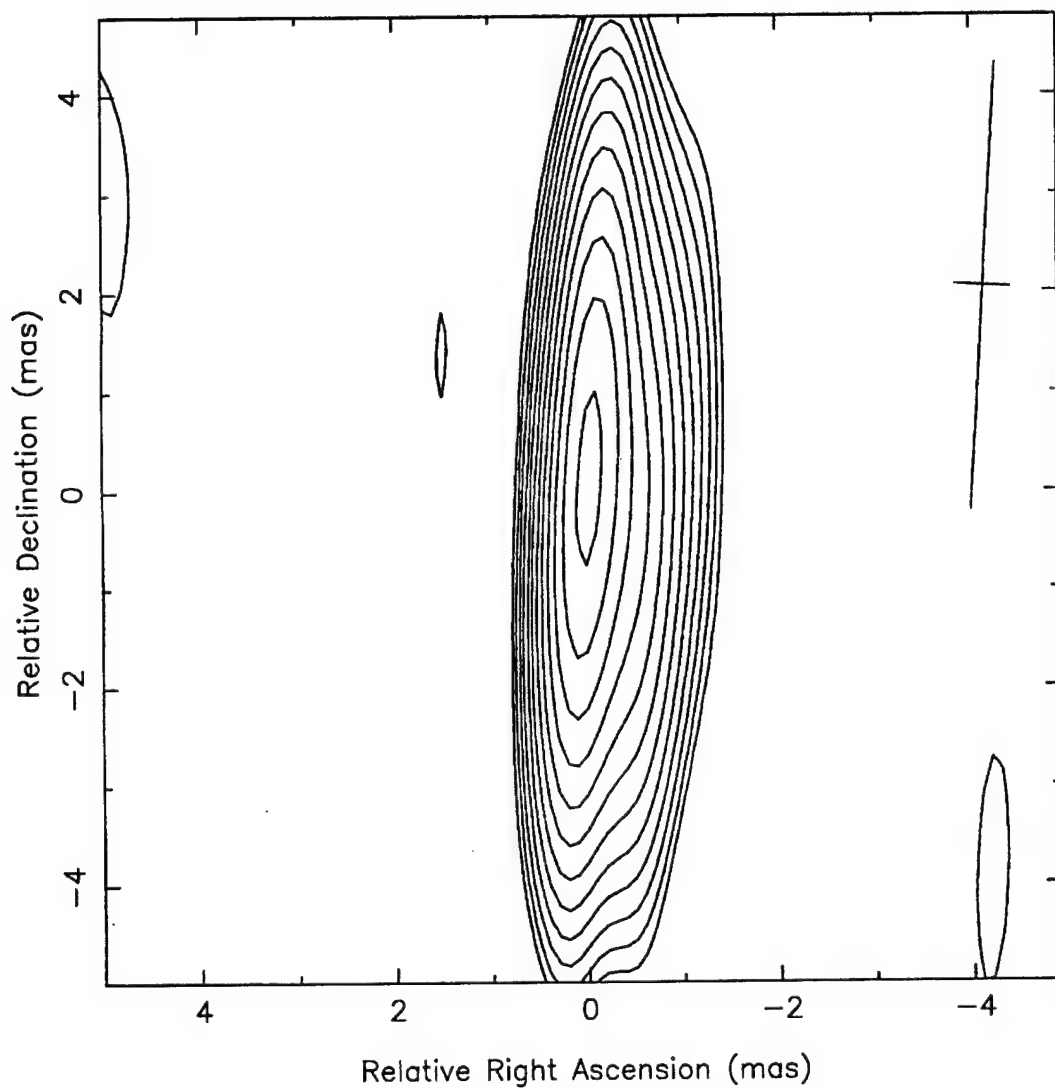


Figure 19: Total Intensity Map of OJ 287 at 3.6 cm, Epoch 1990.4, made with natural weighting of the visibilities. Contours are at -2, 2, 2.8, 4, 5.7, 8, 11.3, 16, 22.6, 32, 45.3, 64, and 90.5% of the peak flux of 2540 mJy/beam. The beam is 4.52 by 0.57 milliarcseconds at a position angle of  $-3.5^\circ$ .

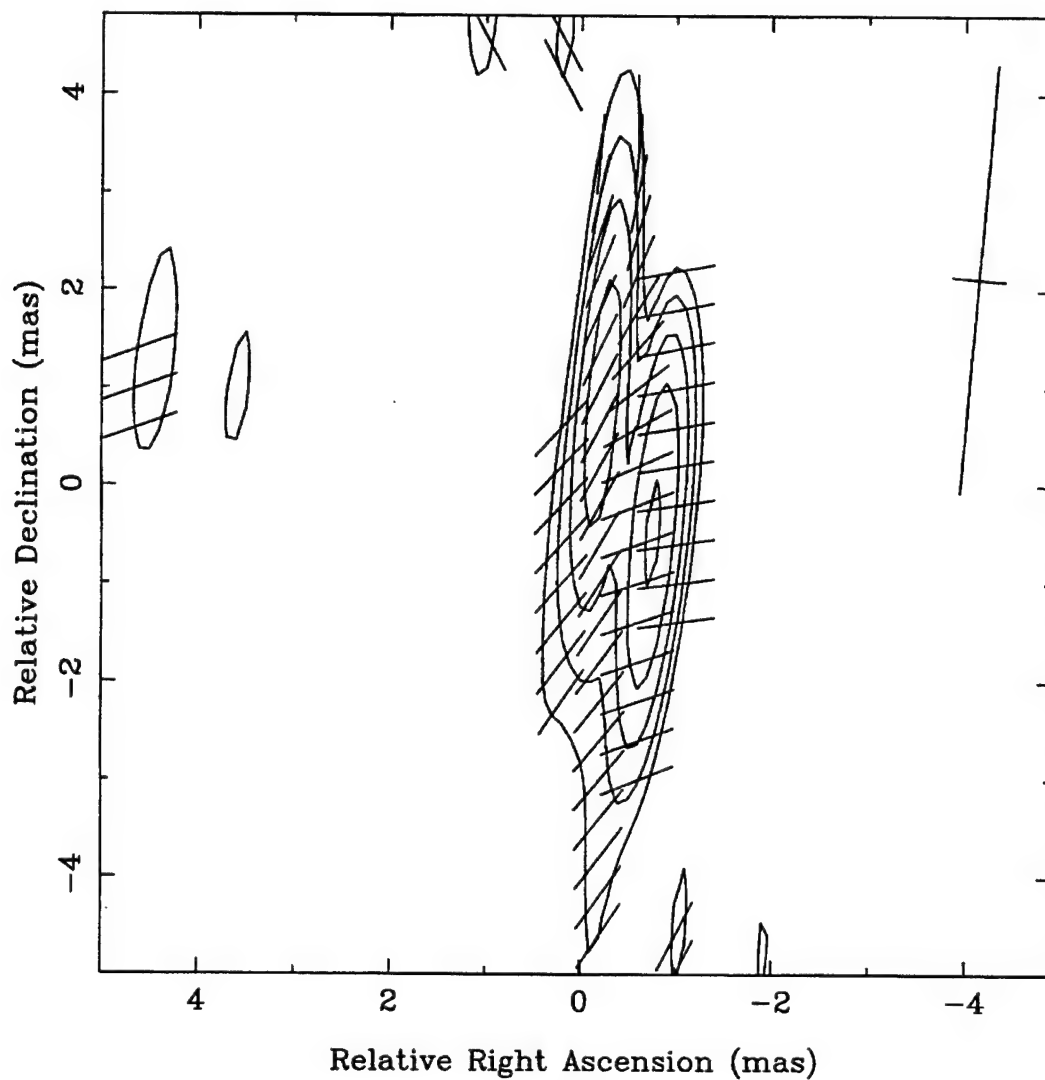


Figure 20: Complex Polarization Map of OJ 287 at 3.6 cm, Epoch 1990.4, made with natural weighting of the visibilities. Contours are at 24, 33.9, 48, 67.9, and 96% of the peak flux of 66.3 mJy/beam. The beam is 4.38 by 0.54 milliarcseconds at a position angle of  $-5.1^\circ$ .

From the final map, the sum of the polarized clean components gave 88 mJy of polarized flux at a position angle of  $-84^\circ$ , compared with 86 mJy and  $-70^\circ$  for the VLA. The data set was adjusted by  $14^\circ$  to account for the difference.

### *3. UV Coverage of Program Sources in Epoch 1990.4*

After editing of the data set, the coverage of the program sources, 3C 345 and 3C 273, was rather poor for the epoch 1990.4 observations. Figures 21 and 22 show the UV coverage for 3C 345 in total intensity (1068 parallel hand visibilities) and complex polarization (500 cross hand visibilities). In all UV coverage plots the parallel hand visibilities are plotted both at  $u,v$  and at  $-u,-v$ , which reflects the real true coverage used for the transform to the sky plane, since the total intensity on the sky is a real quantity (see chapter 2). Figures 23 and 24 give the same plots for 3C 273 with 780 parallel hand visibilities and 341 cross hand visibilities.

In the 3.6 cm experiment, the substantial number of antenna failures and, for complex polarization mapping, the low number of antennas with both RCP and LCP receivers reduced the number of visibilities dramatically. Figures 25 and 26 show the UV coverage plots for 3C 345 at 3.6 cm in total intensity (455 parallel hand visibilities) and complex polarization (255 cross hand visibilities). The situation for 3C 273 is somewhat worse with only 343 parallel hand visibilities and 167 cross hand visibilities as shown in figures 27 and 28. Also note the large gap in coverage in figure 28 for the cross hand data.

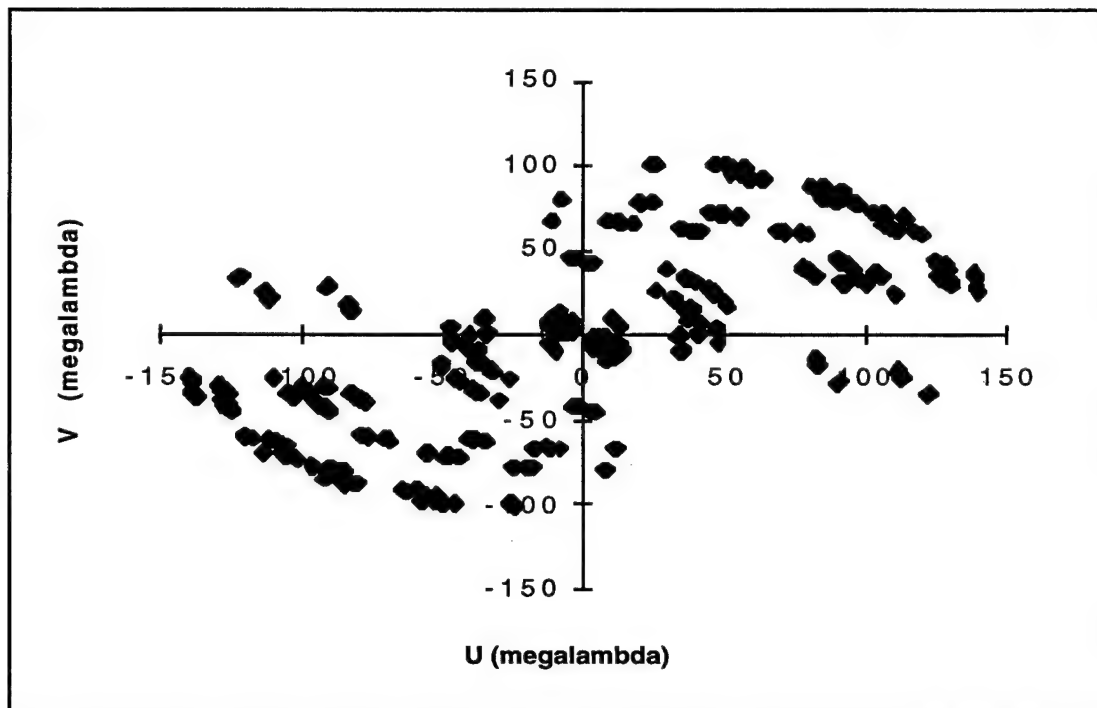


Figure 21: 3C 345 Parallel hand UV coverage in epoch 1990.4 at 6 cm.

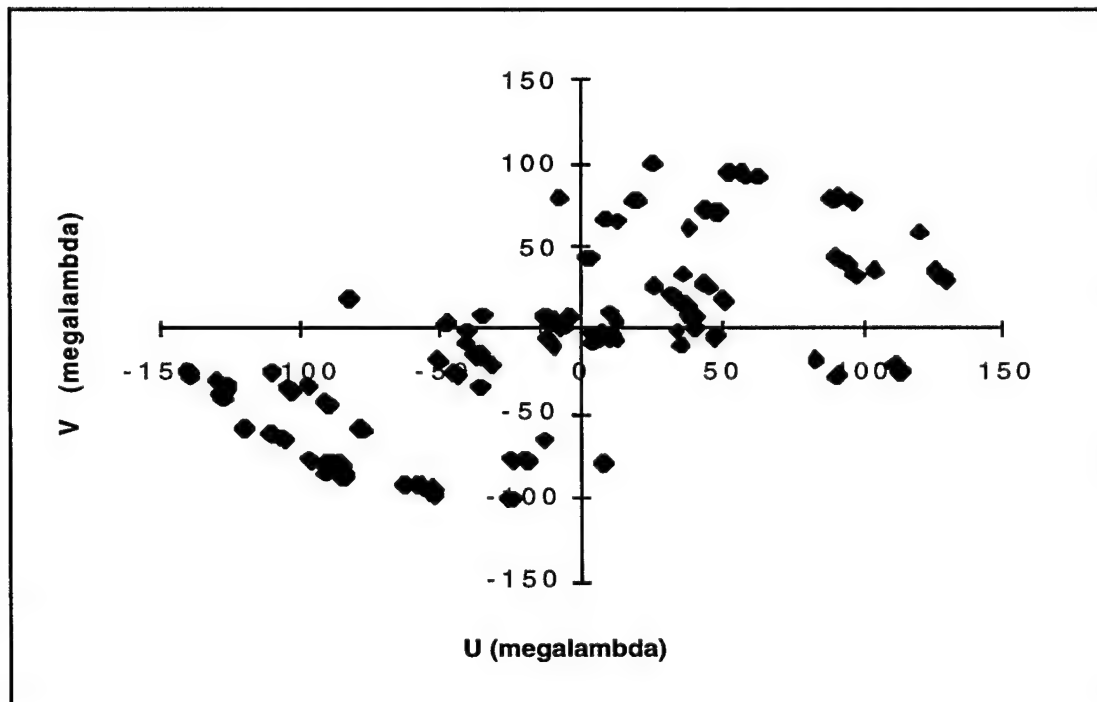


Figure 22: 3C 345 Cross hand UV coverage in epoch 1990.4 at 6 cm.

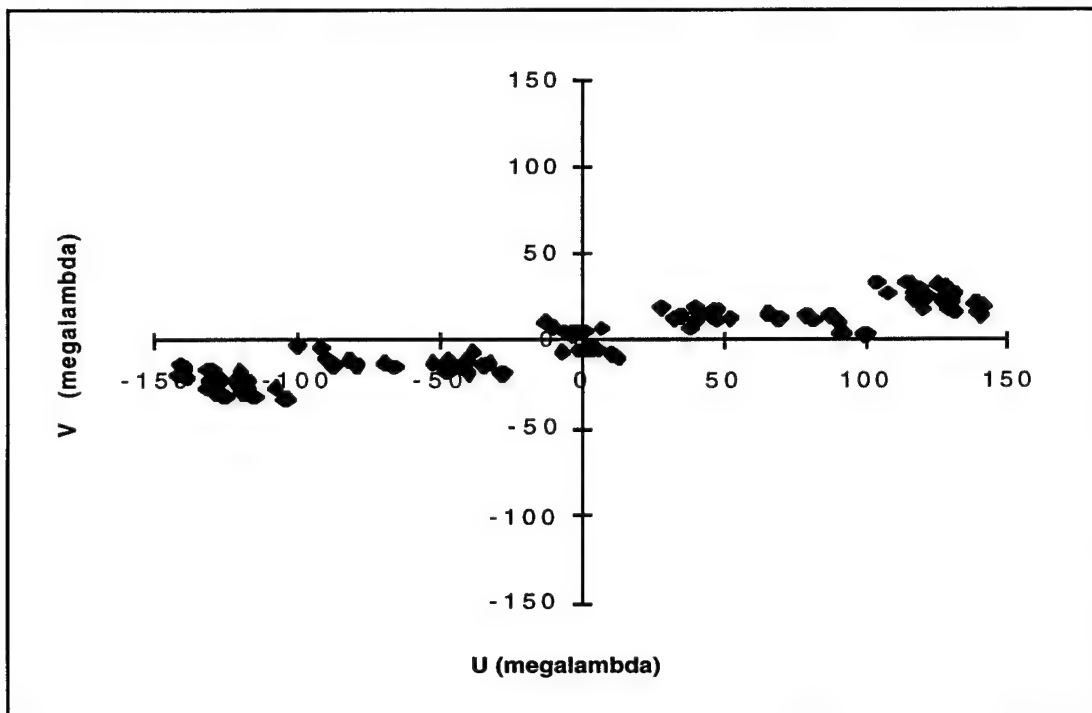


Figure 23: 3C 273 Parallel hand UV coverage in epoch 1990.4 at 6 cm.

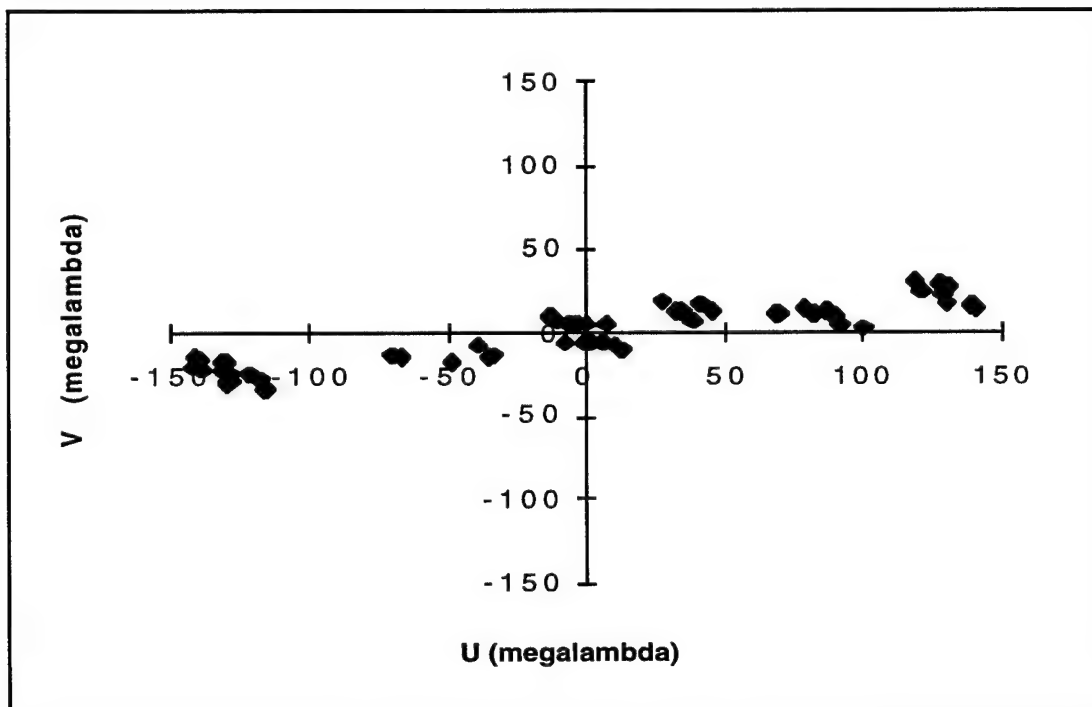


Figure 24: 3C 273 Cross hand UV coverage in epoch 1990.4 at 6 cm.

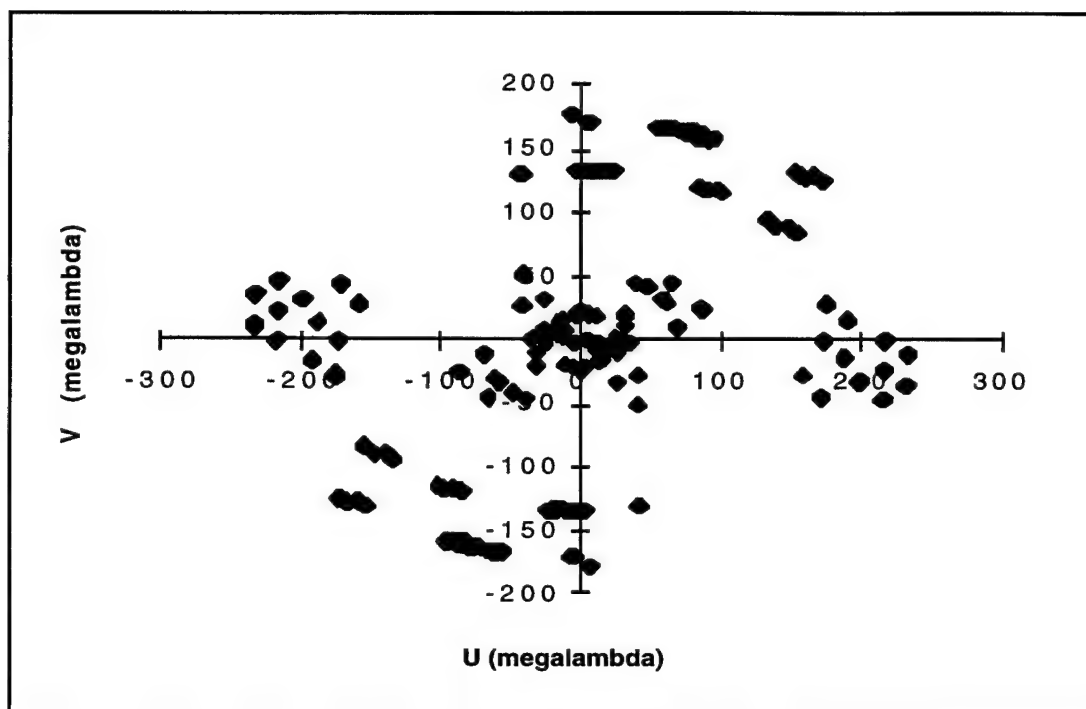


Figure 25: 3C 345 Parallel hand UV coverage in epoch 1990.4 at 3.6 cm.

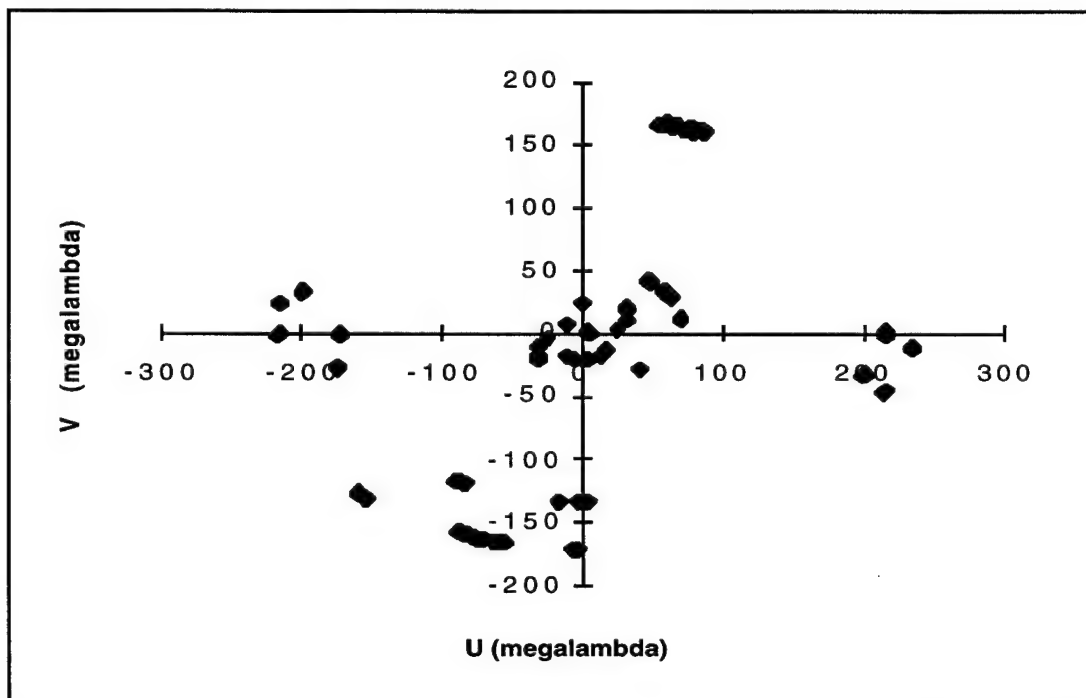


Figure 26: 3C 345 Cross hand UV coverage in epoch 1990.4 at 3.6 cm.



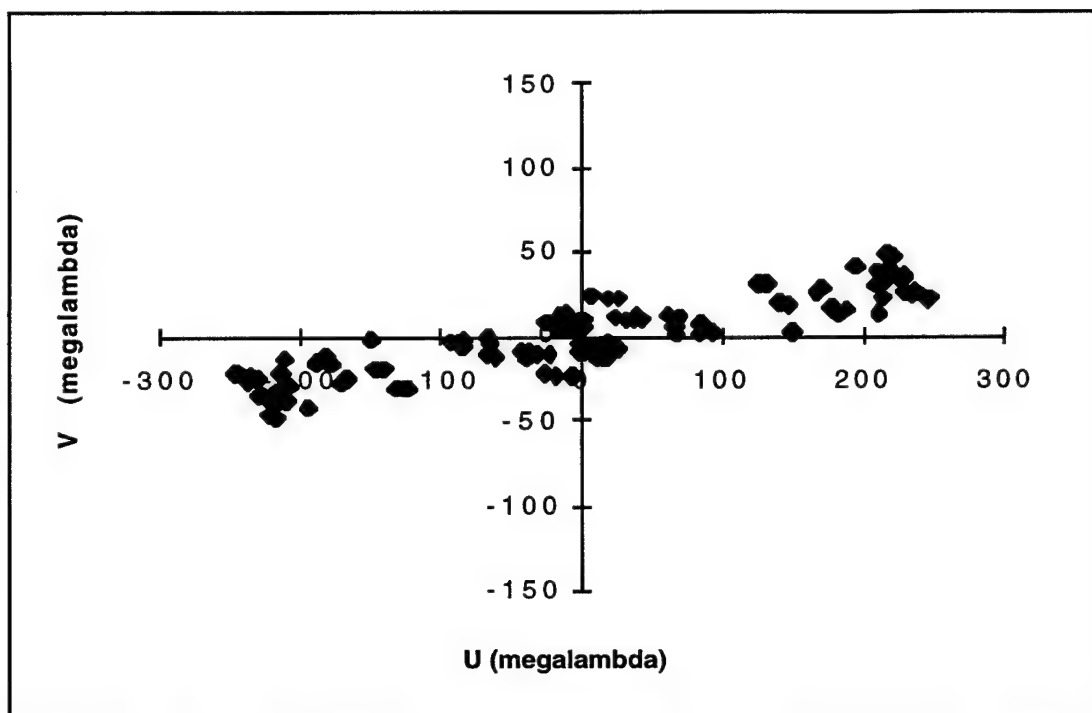


Figure 27: 3C 273 Parallel hand UV coverage in epoch 1990.4 at 3.6 cm.

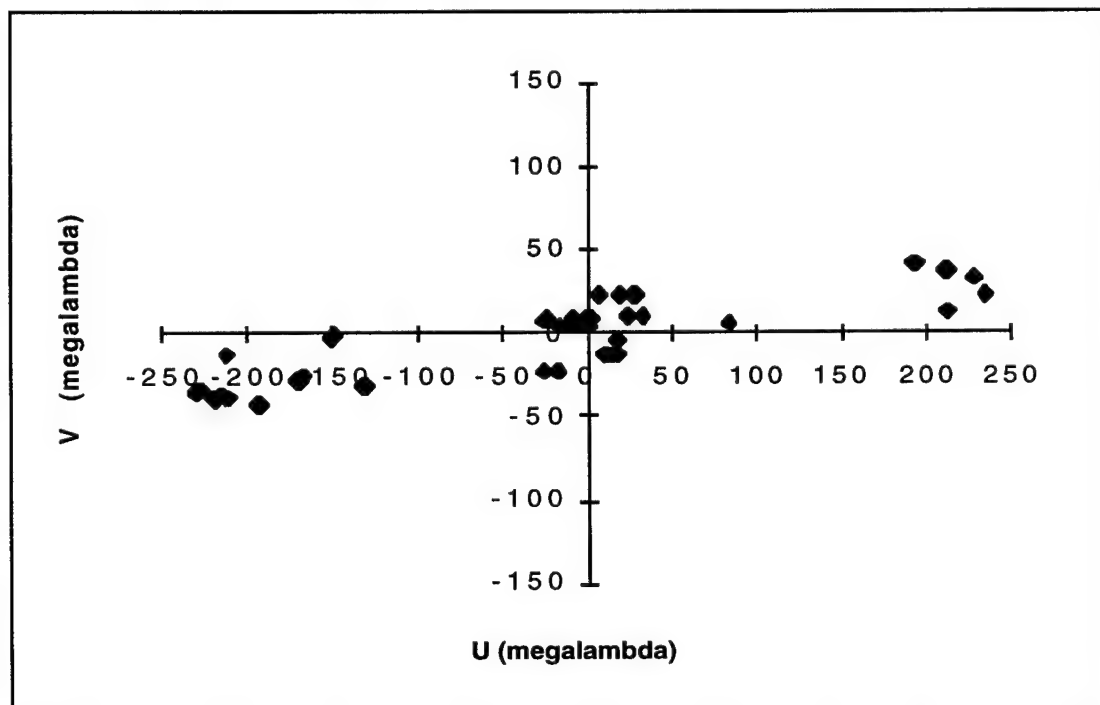


Figure 28: 3C 273 Cross hand UV coverage in epoch 1990.4 at 3.6 cm.

## *B. Epoch 1992.2*

### *1. 5 GHz Observations*

The epoch 1992.2 6 cm observations were a remarkable improvement over the earlier observations. The observations took place over a 26 hour period from 04 00 UT on March 26th to 06 00 UT on March 27th using the global VLBI network. In this experiment 15 antennas were scheduled with the understanding that a maximum of 12 would be correlated. This was done in order to avoid the problem of massive observing failures reducing the utility of the experiment as occurred in the 3.6 cm half of the epoch 1990.4 observations. Only the Brewster VLBA antenna did not observe, so two antennas were chosen to be left out of correlation. Noto (Italy) was dropped because it was known to have very large D terms, and Fort Davis (VLBA) was dropped because of minor problems with the tape. The antennas which were correlated are summarized in table 13.

Correlation was begun at the Haystack Observatory on the Mark IIIA correlator in the middle of 1992, shortly after the completion of the experiment. However, a number of intervening events at the correlator, primarily work on the Crustal Dynamics Project, delayed completion of the processing until late 1992. Two passes through the correlator were used to produce both parallel hand and cross hand visibilities. Segmenting was done using mode 701 of FRNGX at Haystack. Unfortunately a problem with the Westerbork correlation resulted in only parallel hand data being recovered. A further problem in the correlation was the much poorer recovery of RR correlations when compared to LL correlations. This problem remained despite attempts to recover the RR correlations.

The flux calibration was done using the log files containing system temperatures. Gain curves were recovered from previous observations at the same telescopes for a number of antennas, from log files for Bonn, and from the manual on

### EPOCH 1992.2 ANTENNAS (6 cm)

<u>Antenna</u>	<u>Code</u>	<u>Diameter</u>	<u>Rec.</u>	<u>Comments</u>
Medicina (Italy)	L	32 m	R L	Large D terms
Bonn (Germany)	B	100 m	R L	Reference Antenna
Westerbork (Netherlands)	W	14 x 25 m	R L	Phased Array
Jodrell Bank (England)	J		R L	
Haystack (Massachusetts)	K	37 m	R L	
Green Bank (W. Virginia)	G	43 m	R L	
VLBA-NL (Iowa)	I	25 m	R L	
VLBA-LA (New Mexico)	X	25 m	R L	
VLA (New Mexico)	Y	27 x 25 m	R L	Phased Array
VLBA-PT (New Mexico)	P	25 m	R L	
VLBA-KP (Arizona)	T	25 m	R L	
VLBA-OV (California)	O	25 m	R L	

Table 13: Antenna characteristics for stations correlated in the 6 cm, epoch 1992.2 experiment.

uVAX1 at the NRAO in Socorro for the VLBA antennas. Green Bank provided no calibration information and system temperatures were estimated from previous experiments. The gain file was created and used to produce the calibrated database. Checks of the calibrated database showed severe problems.

The plots of visibilities with uv distance for sources showed extreme scatter. Analysis led to the conclusion that the western antennas in the VLBA had erroneous calibration information and were systematically offset, some high and some low, from the visibilities expected. Adjustment of the system temperatures of these antennas,

### EPOCH 1992.2 6 cm D TERMS

<u>Antenna</u>	<u>RCP Amp</u>	<u>RCP Phase</u>	<u>LCP Amp</u>	<u>LCP Phase</u>
L	15.04	176.1	15.87	-0.4
B	3.73	-54.9	5.46	-139.1
W	---	---	---	---
J	1.38	84.2	2.16	-22.2
K	2.18	-30.6	1.25	-22.6
G	1.49	170.6	1.30	-28.8
I	1.20	-18.5	0.96	-139.2
X	1.10	127.6	0.77	67.9
Y	2.22	145.8	2.07	-64.3
P	1.57	123.0	1.24	77.6
T	0.88	118.7	0.24	45.0
O	1.39	103.7	1.25	19.0

Table 14: D terms for antennas correlated in the 6 cm, epoch 1992.2 experiment.

and of Green Bank, corrected the problem. A new calibrated database was created and checked, and it appeared to be correctly calibrated.

Polarization calibration was completed with a minimum of problems. The alignment of RCP and LCP antenna gains was done using Bonn as a reference antenna, and most VLBA antennas also appeared extremely stable. The D terms were calculated using only 3C 84, and plots of cross hand to parallel hand visibility ratios in the complex plane indicated good fits. The D terms determined are shown in table 14. The polarized database was created using the calibration data.

Hybrid mapping of OJ 287 was accomplished with very little trouble. Mapping converged with no requirement of a clean box or self-calibration restrictions. Final total intensity and complex polarization maps are shown in figures 29 and 30 respectively. A total of 119 mJy of polarized flux was recovered in the clean components with a position angle of  $-28^\circ$  for the electric field vector, compared with values of 117 mJy and  $-76^\circ$  from the VLA. The use of a tight clean box around the center of the map resulted in a shift of  $2^\circ$  in the sum of the VLBI polarized clean components to  $-29^\circ$ . A correction of  $-48^\circ$  was applied to the electric field vector position angle.

### *2. 8.4 GHz Observations*

The 8.4 GHz observations took place in late March and early April in two separate sessions, totalling 29 hours. The observations occurred from 18 00 UT on March 30th to 17 00 on March 31st and from 15 30 UT on April 1st to 01 30 UT on April 2nd. The data was pooled for all subsequent processing and treated as a single data set. Originally 14 antennas were scheduled, with the understanding that 12 would be correlated. However, three VLBA antennas failed to record proper timing signals on the VLBI tape, making it impossible to correlate these antennas. These stations were Los Alamos, Pietown, and Kitt Peak. Despite the loss of these three dual polarization antennas, the experiment still represents a substantial improvement over the previous epoch, with 6 dual polarization antennas and 11 antennas over all. Characteristics of the antennas correlated are summarized in table 15.

The flux calibration was done using system temperature measurements from the antennas. As with the 6 cm observations, Green Bank sent no calibration data, and estimates were made from previous experiments. Gain curves were recovered from the log file for Effelsberg, previous experiments for other non-VLBA antennas, and uVAX1 at NRAO for the VLBA antennas. The gain file was created and used in

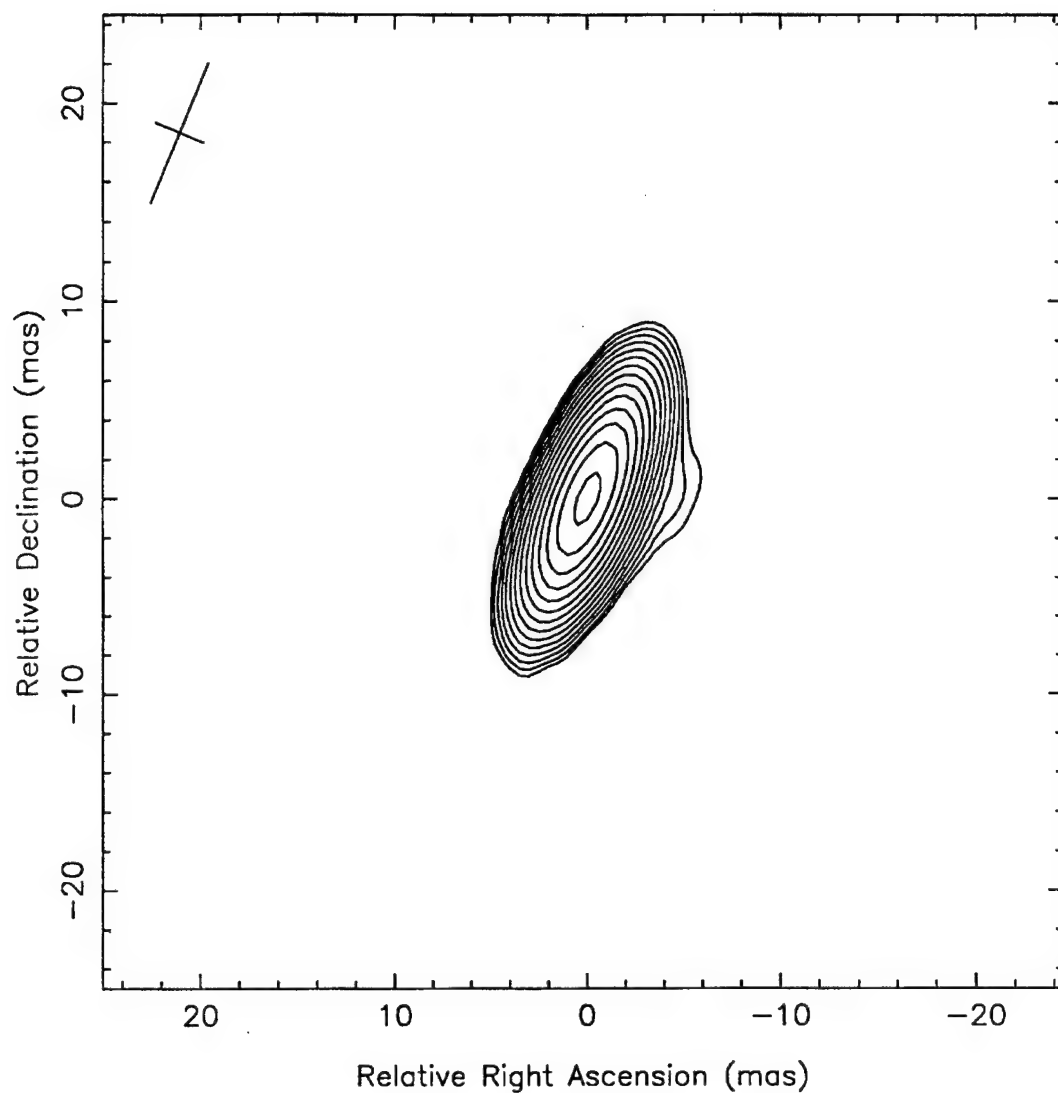


Figure 29: Total Intensity Map of OJ 287 at 6 cm, Epoch 1992.2, made with natural weighting of the visibilities. Contours are at -1, 1, 1.4, 2, 2.8, 4, 5.7, 8, 11.3, 16, 22.6, 32, 45.3, 64, 90.5% of the peak flux of 2540 mJy/beam. The beam is 7.66 by 2.65 milliarcseconds at a position angle of  $-22.5^\circ$ .

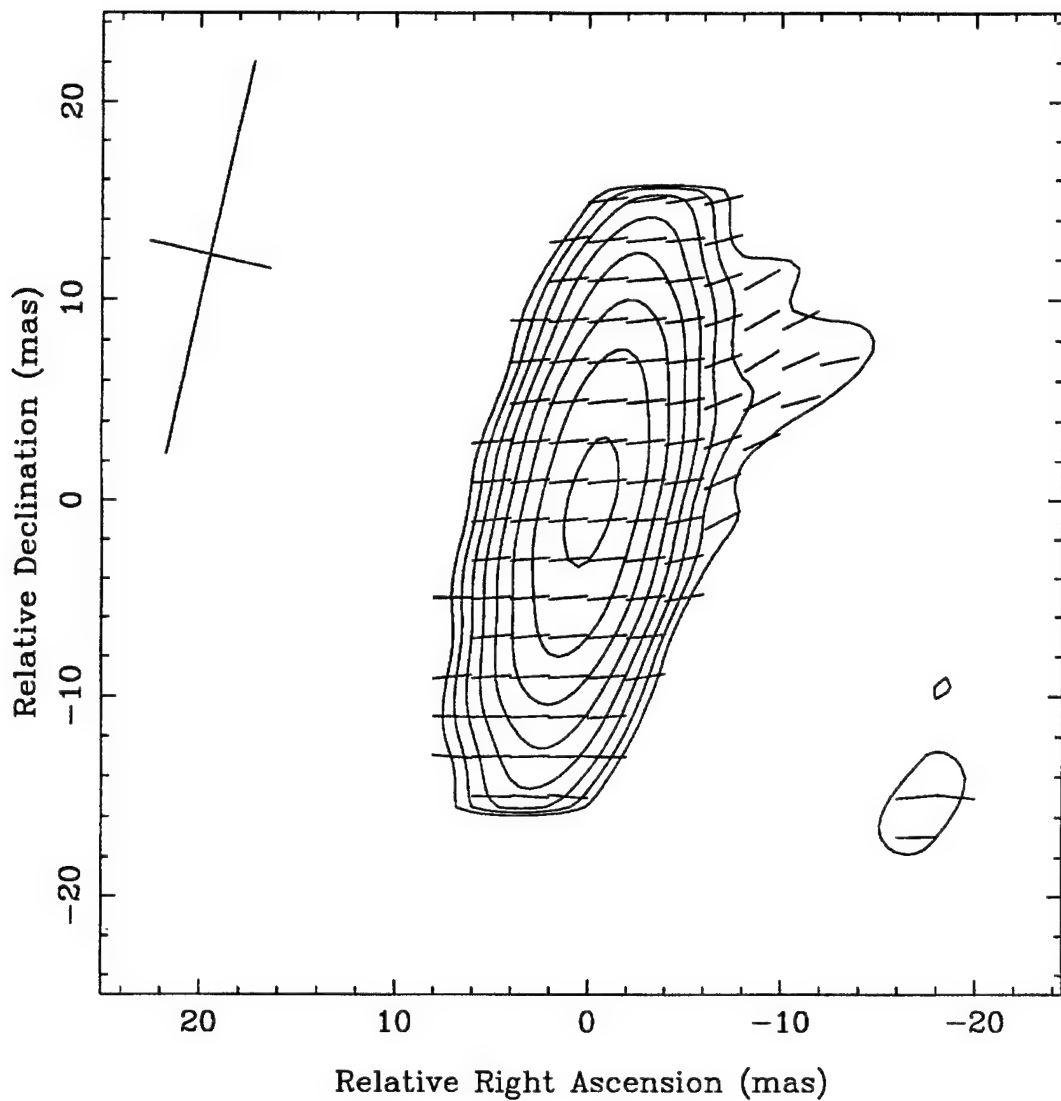


Figure 30: Complex Polarization Map of OJ 287 at 6 cm, Epoch 1992.2, made with natural weighting of the visibilities. Contours are at 8, 11, 16, 22.6, 32, 45.3, 64, 90.5% of the peak flux of 117 mJy/beam. The beam is 20.11 by 6.27 milliarcseconds at a position angle of  $-12.8^\circ$ .

### EPOCH 1992.2 ANTENNAS (3.6 cm)

<u>Antenna</u>	<u>Code</u>	<u>Diameter</u>	<u>Rec.</u>	<u>Comments</u>
Noto (Italy)	N	32 m	R	Large D term
Onsala (Sweden)	S	26 m	R	Large D term
Medicina (Italy)	L	32 m	R	Large D term
Bonn (Germany)	B	100 m	R L	Reference Antenna
Haystack (Massachusetts)	K	37 m	R	
Green Bank (W. Virginia)	G	43 m	R	Large D term
VLBA-NL (Iowa)	I	25 m	R L	
VLBA-FD (Texas)	F	25 m	R L	
VLA (New Mexico)	Y	27 x 25 m	R L	Phased Array
VLBA-OV (California)	O	25 m	R L	
VLBA-BR (Washington)	R	25 m	R L	Only last 6 hours

Table 15: Antenna characteristics for stations correlated in the 3.6 cm, epoch 1992.2 experiment.

making the calibrated database file. Checks on the database indicated the need for an adjustment to the Green Bank calibration, however all other antennas appeared well calibrated. After correcting the Green Bank calibration, a new calibrated database file was created.

Polarization calibration went very smoothly. Efflsberg was used as the reference antenna, and the RCP - LCP offsets at the antennas were established without difficulty as a number of VLBA antennas looked very stable as well. The D



### EPOCH 1992.2 3.6 cm D TERMS

<u>Antenna</u>	<u>RCP Amp</u>	<u>RCP Phase</u>	<u>LCP Amp</u>	<u>LCP Phase</u>
N	12.73	83.9	---	---
S	11.38	160.7	---	---
L	13.57	79.7	---	---
B	7.51	-84.1	5.80	-89.2
K	1.41	-43.8	---	---
G	12.11	-57.6	---	---
I	0.61	-46.4	0.57	164.0
F	1.31	-93.6	0.72	-67.5
Y	0.60	150.0	0.26	151.3
O	0.94	39.4	2.75	120.0
R	1.07	167.0	1.76	78.9

Table 16: D terms for antennas correlated in the 3.6 cm, epoch 1992.2 experiment.

terms were determined by using 3C 84 as the calibrator. Fits were plotted in the complex plane using the cross hand to parallel hand ratios, and these fits appeared good. The D terms determined are shown in table 16. The polarized database was created using this calibration data.

Hybrid mapping of OJ 287 was straightforward with no requirements for clean boxes or self-calibration limitations. The final total intensity and complex polarization maps are shown in figures 31 and 32 respectively. The sum of the polarized clean components was 147 mJy of polarized flux at a position angle of  $15^\circ$  in the electric field vector, compared to values of 159 mJy and  $-73^\circ$  at the VLA (the

calibrated VLA data set was provided by Scott Aaron of Brandeis University). In order to investigate whether this was reliable, all single polarization antennas were removed from the data set leaving only dual polarization antennas with small D terms. The same complex polarization was recovered. Applying a clean box around the core of the map from the full data set resulted in a shift in the position angle to  $12^\circ$ . An average of the values determined from the sum of the VLBI clean components was used, so that a position angle correction of  $-87^\circ$  was applied to the data set.

A problem with the position angle calibration at 3.6 cm was that the total polarized flux of OJ 287 was not recovered. This introduces an uncertainty into the calibration, since it is not known if the unrecovered polarized flux has the same position angle as the flux recovered. As such, aligning the sum of VLBI clean components with the VLA unresolved complex polarization may give the wrong result. Even on the shortest baselines available in the VLBI data set, the source appears to be partially resolved with visibilities between Iowa and the VLA (baselines of roughly  $40 \text{ M}\lambda$ ) giving as low as 90 mJy of flux or as high as 160 mJy of flux. On the shorter baselines between Fort Davis and the VLA (roughly  $14 \text{ M}\lambda$ ), the visibilities give fluxes from 125 to 150 mJy, although the corrected position angle is fairly consistent at roughly  $-72^\circ$  (with a few outliers). The calibration appears to be correct, although the failure to recover the full polarized flux seen by the VLA should be kept in mind.

### *3. UV Coverage of Program Sources in Epoch 1992.2*

The observations in 1992 were far more successful than those in 1990, and this is reflected in the UV coverage obtained for the program sources. Figures 33 and

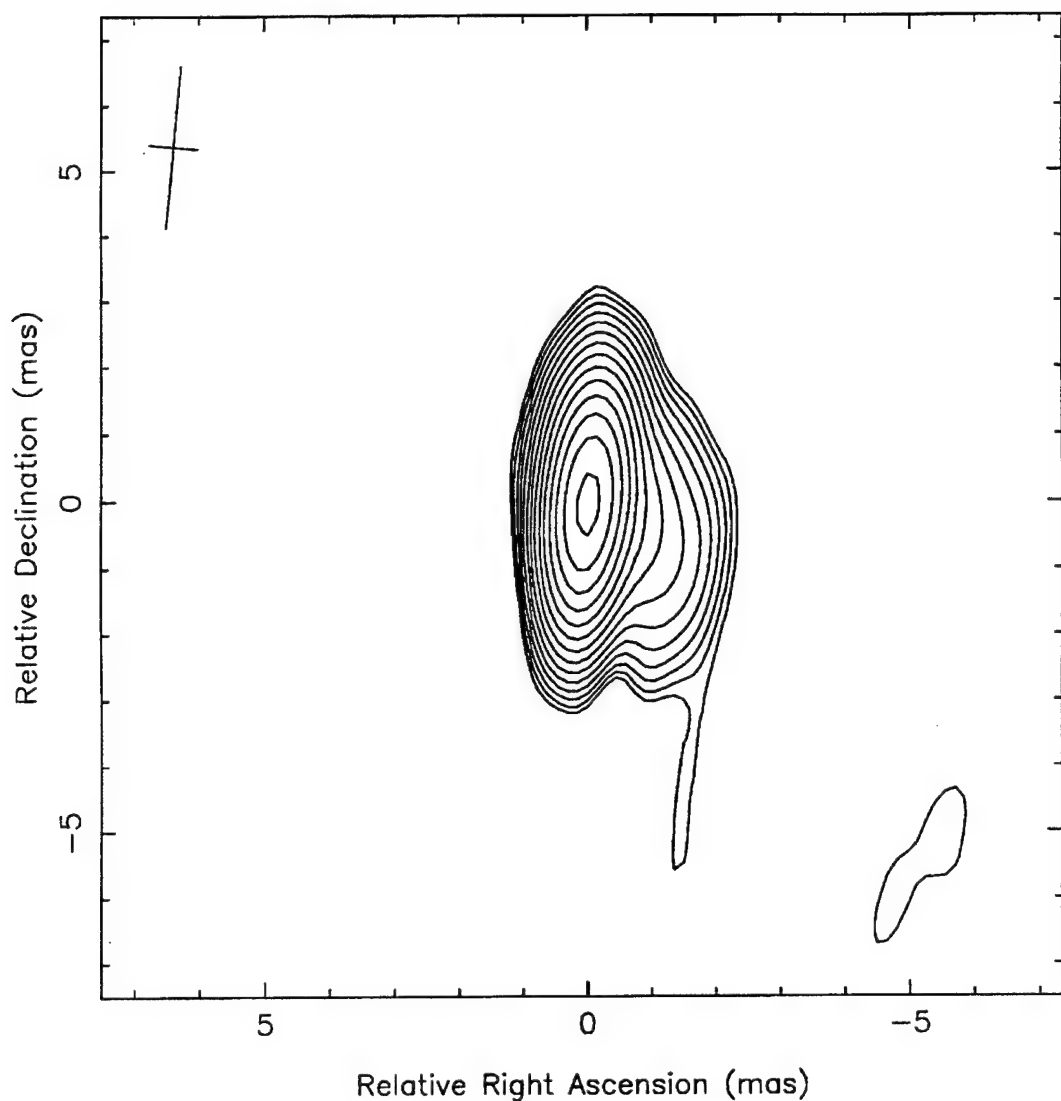


Figure 31: Total Intensity Map of OJ 287 at 3.6 cm, Epoch 1992.2, made with natural weighting of the visibilities. Contours are at 1, 1.4, 2, 2.8, 4, 5.7, 8, 11.3, 16, 22.6, 32, 45.3, 64, and 90.5% of the peak flux of 1870 mJy/beam. The beam is 2.49 by 0.74 milliarcseconds at a position angle of  $-5.2^\circ$ .

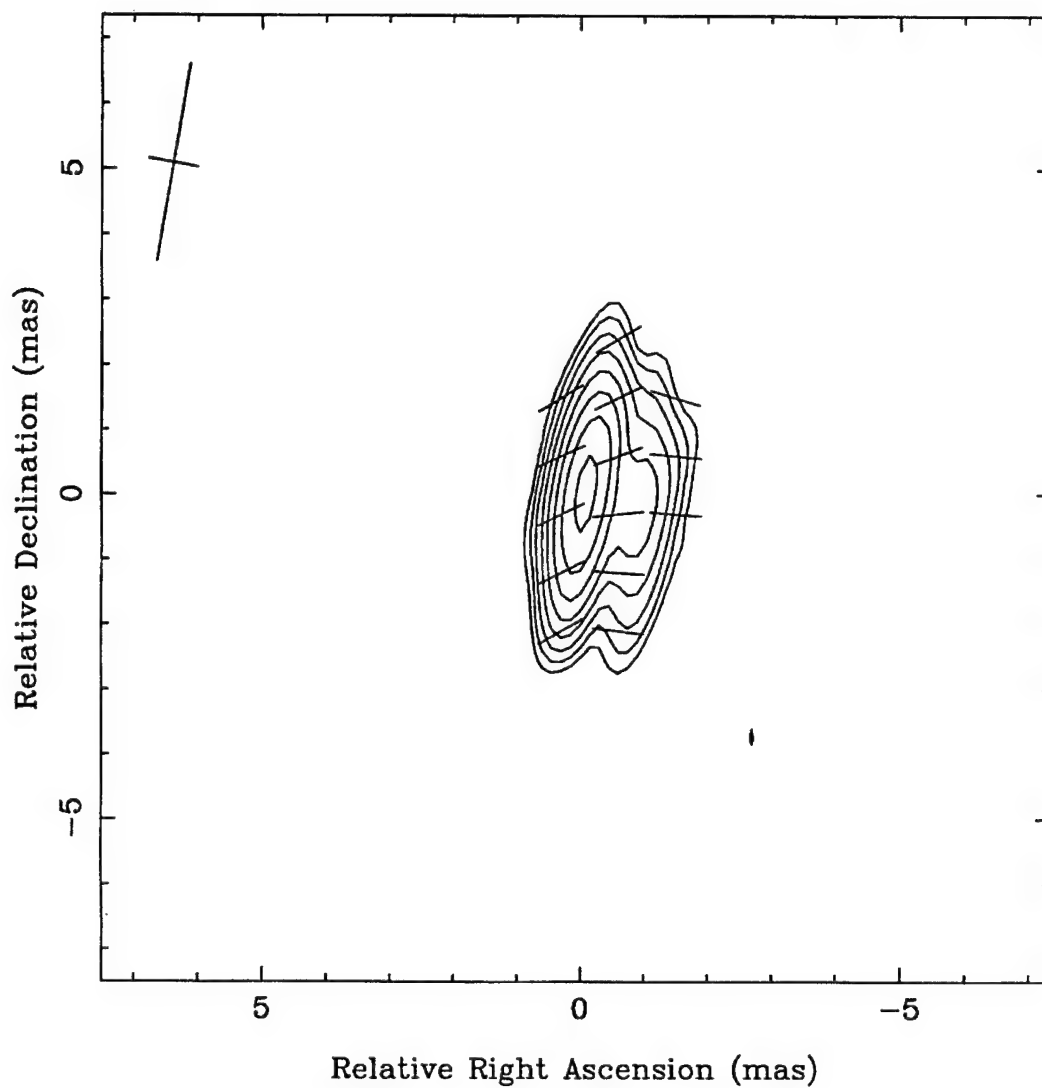


Figure 32: Complex Polarization Map of OJ 287 at 3.6 cm, Epoch 1992.2, made with natural weighting of the visibilities. Contours are at 8, 11.3, 16, 22.6, 32, 45.3, 64, and 90.5% of the peak flux of 110 mJy/beam. The beam is 3.07 by 0.76 milliarcseconds at a position angle of  $-9.8^\circ$ .

34 show the total intensity (3990 parallel hand visibilities) and complex polarization (1124 visibilities) obtained for 3C 345 at 6 cm. Figures 35 and 36 give the UV coverage plots for 3C 273 at 6 cm (2373 parallel hand visibilities and 1306 cross hand visibilities).

Observations at 3.6 cm were even more dramatically improved than those at 6 cm, since the number of dual polarization stations increased sharply with the addition of several VLBA stations. Figures 37 and 38 give UV coverage plots for 3C 345 in total intensity (1836 parallel hand visibilities) and complex polarization (559 cross hand visibilities) at 3.6 cm. Figures 39 and 40 give the corresponding plots for 3C 273 at 3.6 cm (1114 parallel hand visibilities and 419 cross hand visibilities). Note that there is still a significant gap in the complex polarization coverage for 3C 273, which arises from the lack of dual polarization antennas in both Europe and especially the eastern United States.

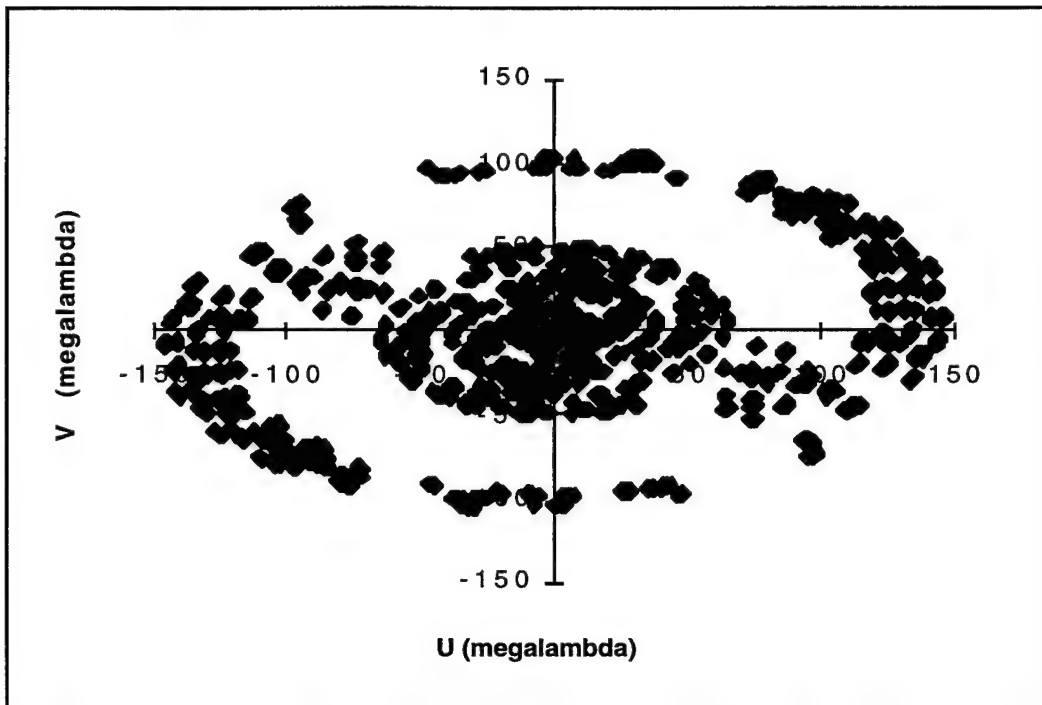


Figure 33: 3C 345 Parallel hand UV coverage in epoch 1992.2 at 6 cm.

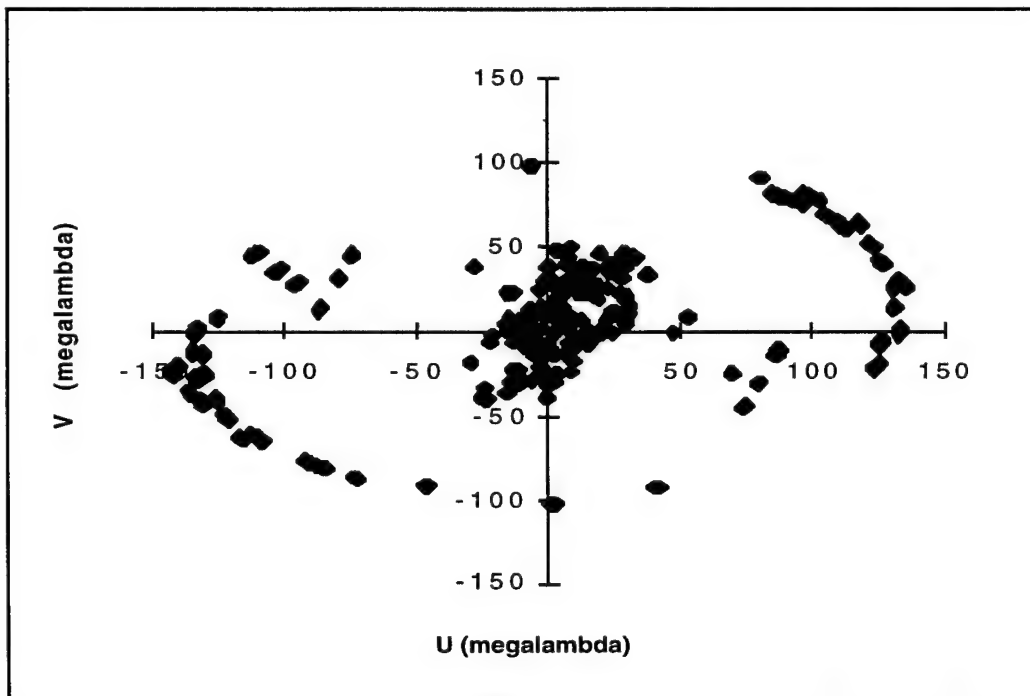


Figure 34: 3C 345 Cross hand UV coverage in epoch 1992.2 at 6 cm.

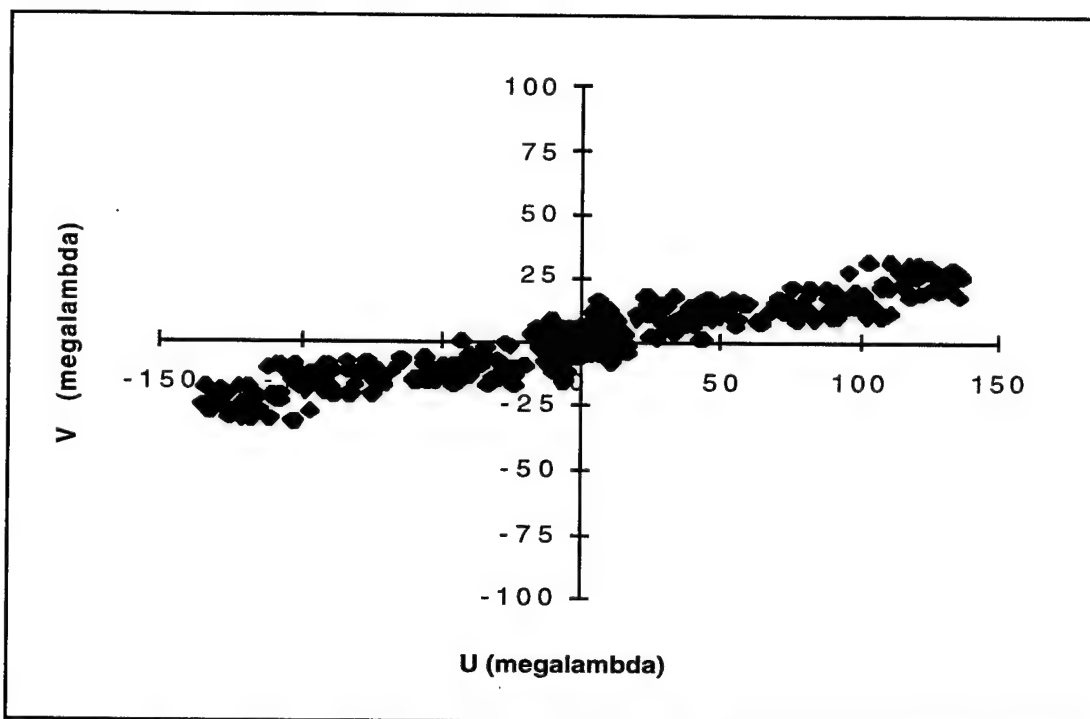


Figure 35: 3C 273 Parallel hand UV coverage in epoch 1992.2 at 6 cm.

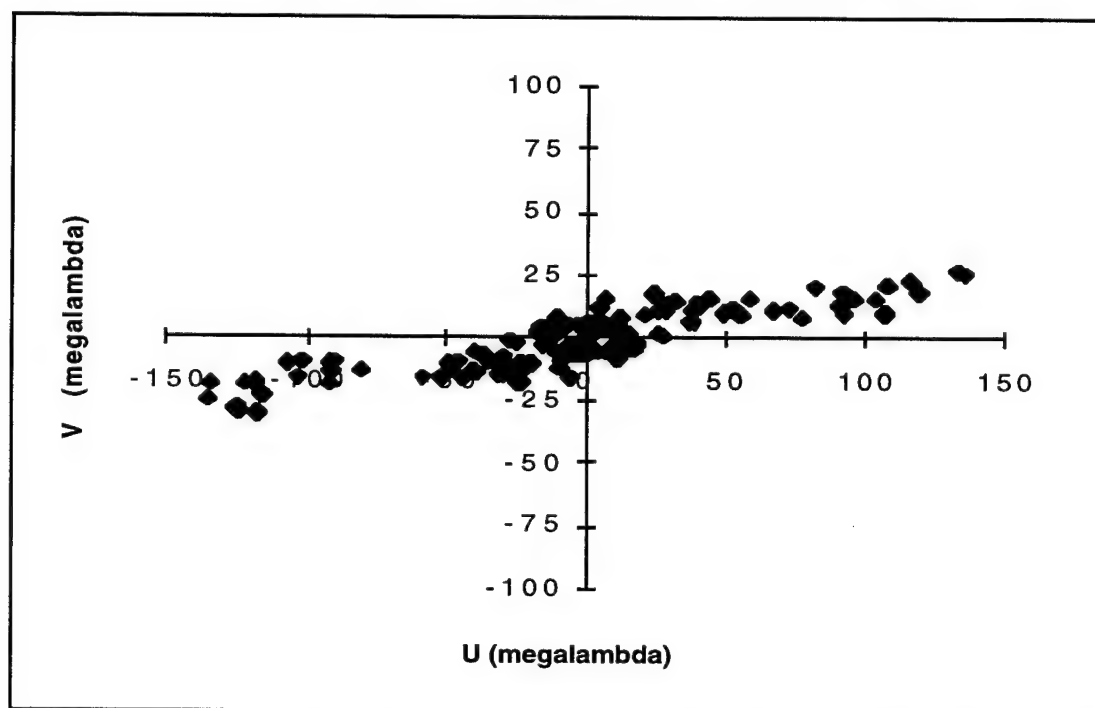


Figure 36: 3C 273 Cross hand UV coverage in epoch 1992.2 at 6 cm.

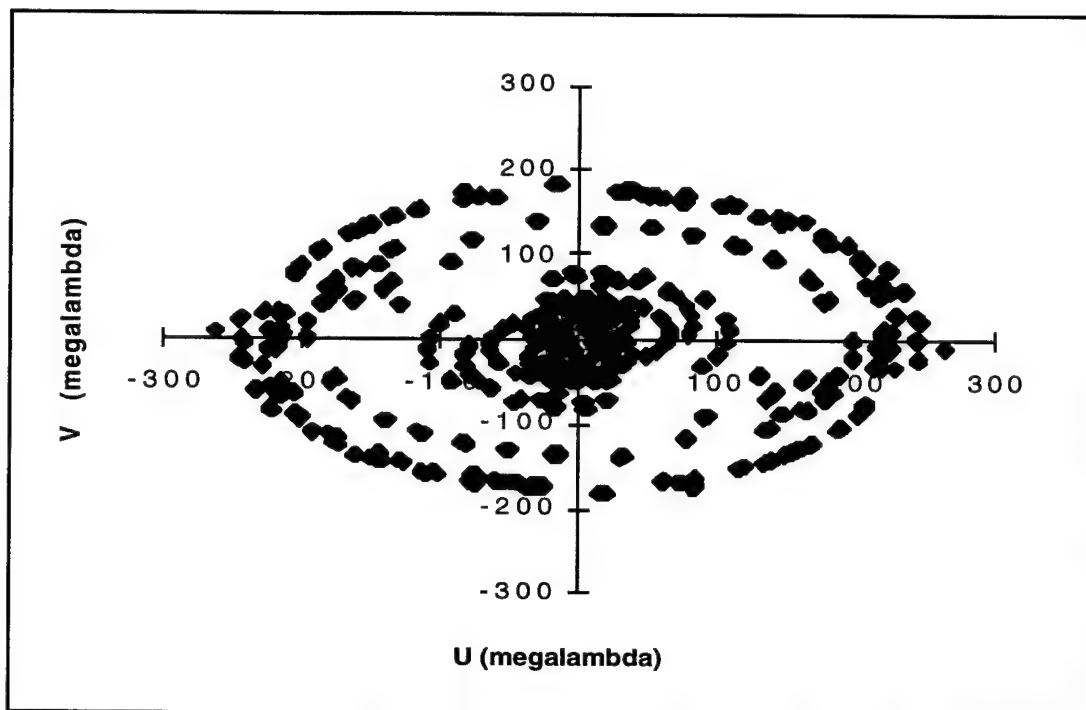


Figure 37: 3C 345 Parallel hand UV coverage in epoch 1992.2 at 3.6 cm.

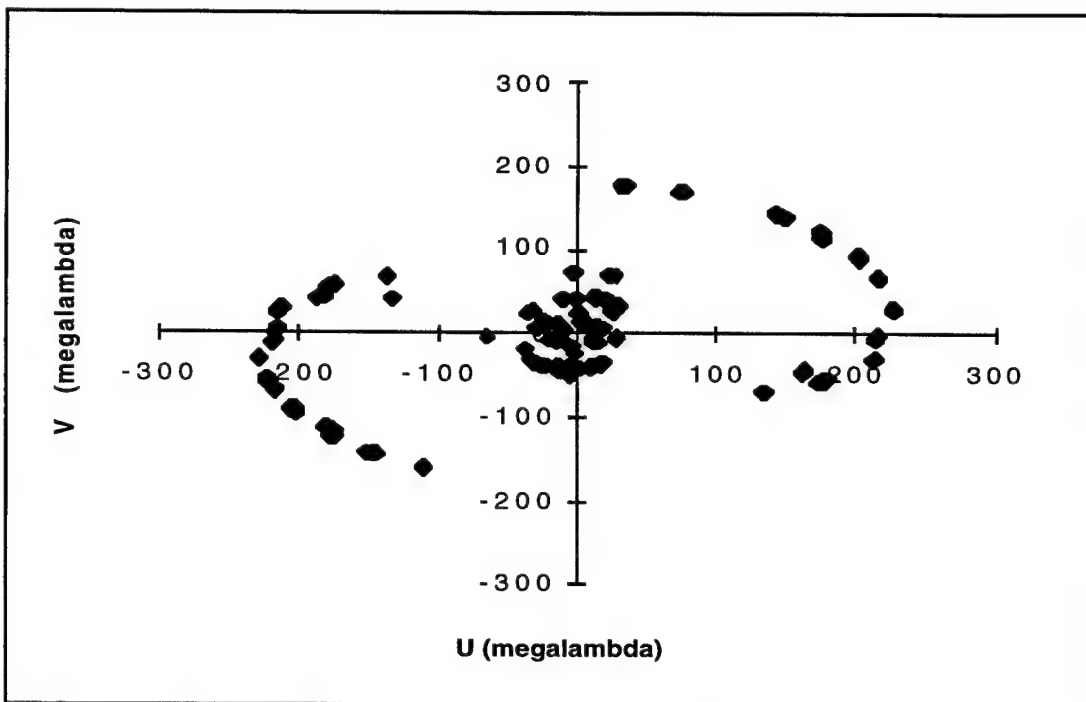


Figure 38: 3C 345 Cross hand UV coverage in epoch 1992.2 at 3.6 cm.



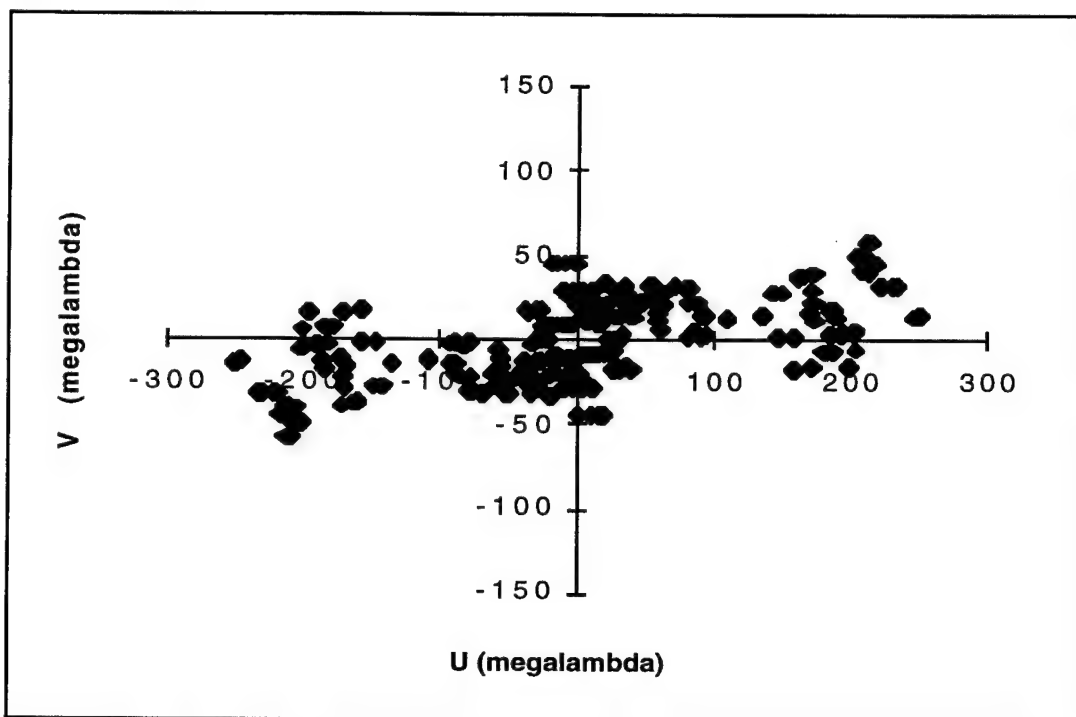


Figure 39: 3C 273 Parallel hand UV coverage in epoch 1992.2 at 3.6 cm.

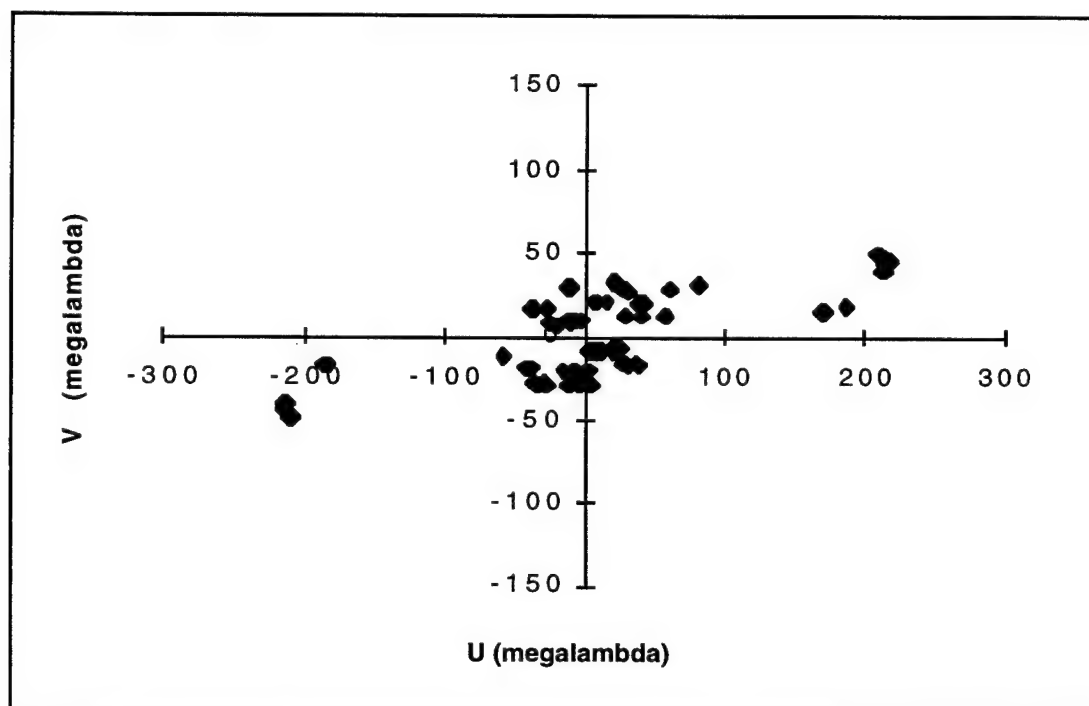


Figure 40: 3C 273 Cross hand UV coverage in epoch 1992.2 at 3.6 cm.

## **VII. Results for 3C 345**

In this chapter the results of the two epochs of dual frequency polarization VLBI observations of 3C 345 are presented. As noted in chapter 6, there were a variety of problems, primarily in the epoch 1990.4 observations, which effect the interpretation of the maps. The earlier epoch maps are used primarily to help confirm features seen in epoch 1992.2, since there are clear problems in the epoch 1990.4 maps indicating calibration errors. While the higher quality epoch 1992.2 maps have been heavily processed to exactly match resolutions and other features between the two frequencies, such detailed work has not been done on the epoch 1990.4 maps. Detailed comparison of the maps, including discussion of the differences which are apparent between 3C 345 and 3C 273, occurs in chapter 9.

It is often typical to give the component positions along the jet in reporting VLBI results. At least some parts of the maps below show virtually continuous clean components along the jets, and attempts to choose where to place the center of a component have proven to give erratic results, probably because of the edge brightening, which results in there being no strong center to the components. Therefore extrapolation from previous maps made with greater UV coverage using Mark II VLBI (see chapter 5) was used to determine a center position for difficult components in cases where a clear center was not determinable. The clean

components were then summed around these positions, either dividing the components on a line halfway between centers or dividing along a narrow gap in the clean components if one existed. Component properties summarized in tables in this chapter were determined in this way.

The images presented here were produced by hybrid mapping as described in chapter 2, using phase self-calibration and deconvolution with the CLEAN algorithm. In all cases, one global amplitude self-calibration, in which each antenna gain was adjusted by a single multiplier, was applied. Maps are shown with roughly logarithmic contour levels.

Polarization images show polarized flux as contours with electric field direction superimposed using tick marks. All polarization images are adjusted for large scale Faraday rotation measured using previous results from arcsecond core measurements, so that the Faraday rotation maps presented are maps of the residual, milliarcsecond-scale rotation measure.

3C 345 is well-positioned for VLBI studies with the present northern hemisphere arrays. Its high declination makes it visible to most antennas for a long period each day and allows many telescopes to see it simultaneously. This means that data sets tend to be quite large, since the number of visibilities goes up with the square of the number of telescopes observing the source.

#### *A . Epoch 1990.4*

##### *1. Maps and Reduced Data*

As noted in chapter 6, the 1990.4 epoch observations were plagued with a number of failures. After calibration and editing there were 1068 I visibilities and 500 P visibilities from the June, 1990, 6 cm observations on 3C 345. Convergence of the model to the data was improved by the use of a minimal CLEAN box, which

required CCs to lie north of 0.2 mas south from the brightest component (C5).

Convergence was obtained in 19 iterations of hybrid mapping.

Figure 41 shows the final map with the restoring beam in the upper left. The core-jet morphology is clear, with the brightest component being the first knot in the jet lying to the southwest of the core. The jet then curves toward the northwest. This map aligns well with the epoch 1990.18 map, made using 15 antennas in a Mark II experiment, which shows the same features, although in much better detail and with much greater dynamic range (Unwin and Wehrle, 1992).

Figure 42 shows the corresponding complex polarization image of the same size with the restoring beam shown in the upper left. The first false features are at roughly 16% of the peak. The position angle shows a sharp rotation between the core polarization and the jet, and the electric field vectors in the jet are almost perpendicular to the jet axis as the jet extends away from the bright component C5.

At 3.6 cm, the data set is quite limited. The calibration and editing reduced the data to 455 I visibilities and 255 P visibilities. A CLEAN box restricting components to lie within a 3.5 mas tall box from -0.3 mas to +3.2 mas relative to C5 was required to obtain convergence in the map. The map converged in 19 iterations of hybrid mapping.

The 3.6 cm total intensity map is shown in figure 43. There are negative features apparent at the -4.0% level. The core-jet structure is clear, but the separation between the core and the knot C5 is somewhat higher than expected. The jet follows the usual behavior with the outer knots becoming progressively weaker at the higher observing frequency, until the outer components are reached. Here the jet brightens (at RA  $\sim$  5 mas) unexpectedly. This is probably due to the same type of self-calibration problem which caused a brightening in the outer jet in 3C 273 in the 3.6

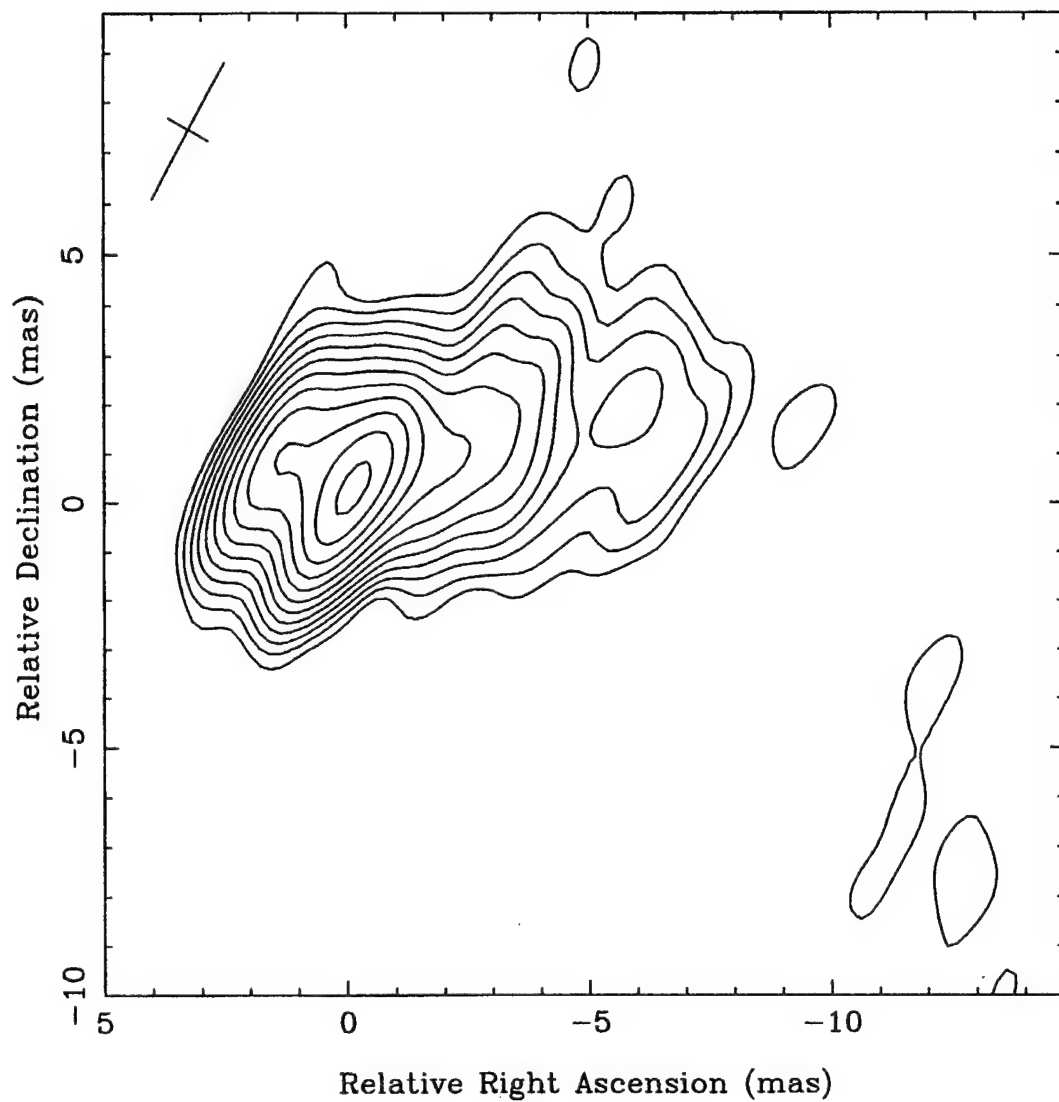


Figure 41: Total Intensity Map of 3C 345 at 6 cm, Epoch 1990.4, made with natural weighting of the visibilities. Contours are at 2, 2.8, 4, 5.7, 8, 11.3, 16, 22.6, 32, 45.3, 64, and 90.5% of the peak flux of 1570 mJy/beam. The beam is 3.1 by 0.9 milliarcseconds at a position angle of  $-28.8^\circ$ .

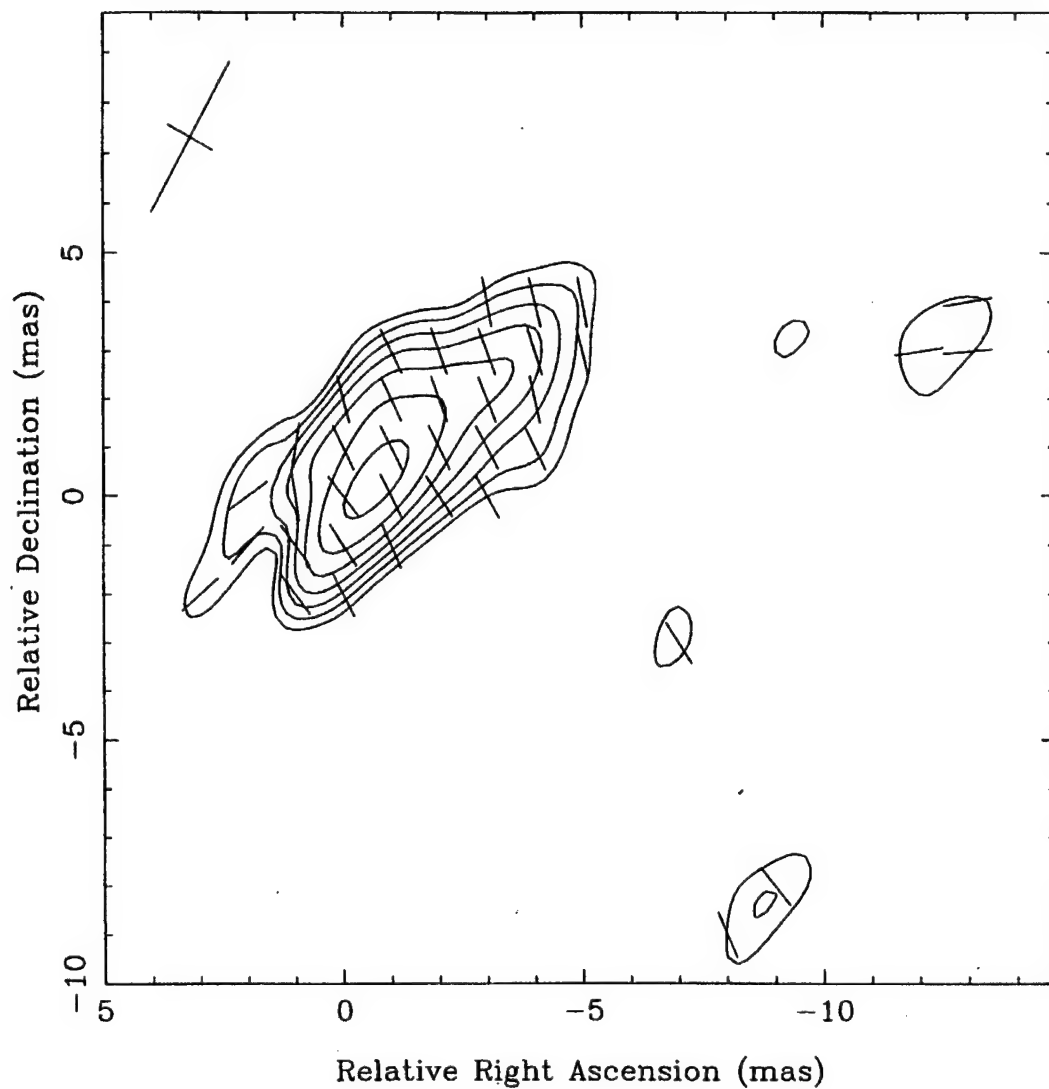


Figure 42: Complex Polarization Map of 3C 345 at 6 cm, Epoch 1990.4, made with natural weighting of the visibilities. Contours are at 11, 15.6, 22, 31.1, 44, 62.2, and 88% of the peak flux of 70.8 mJy/beam. The beam is 3.4 by 1.1 milliarcseconds at a position angle of  $-28.8^\circ$ .

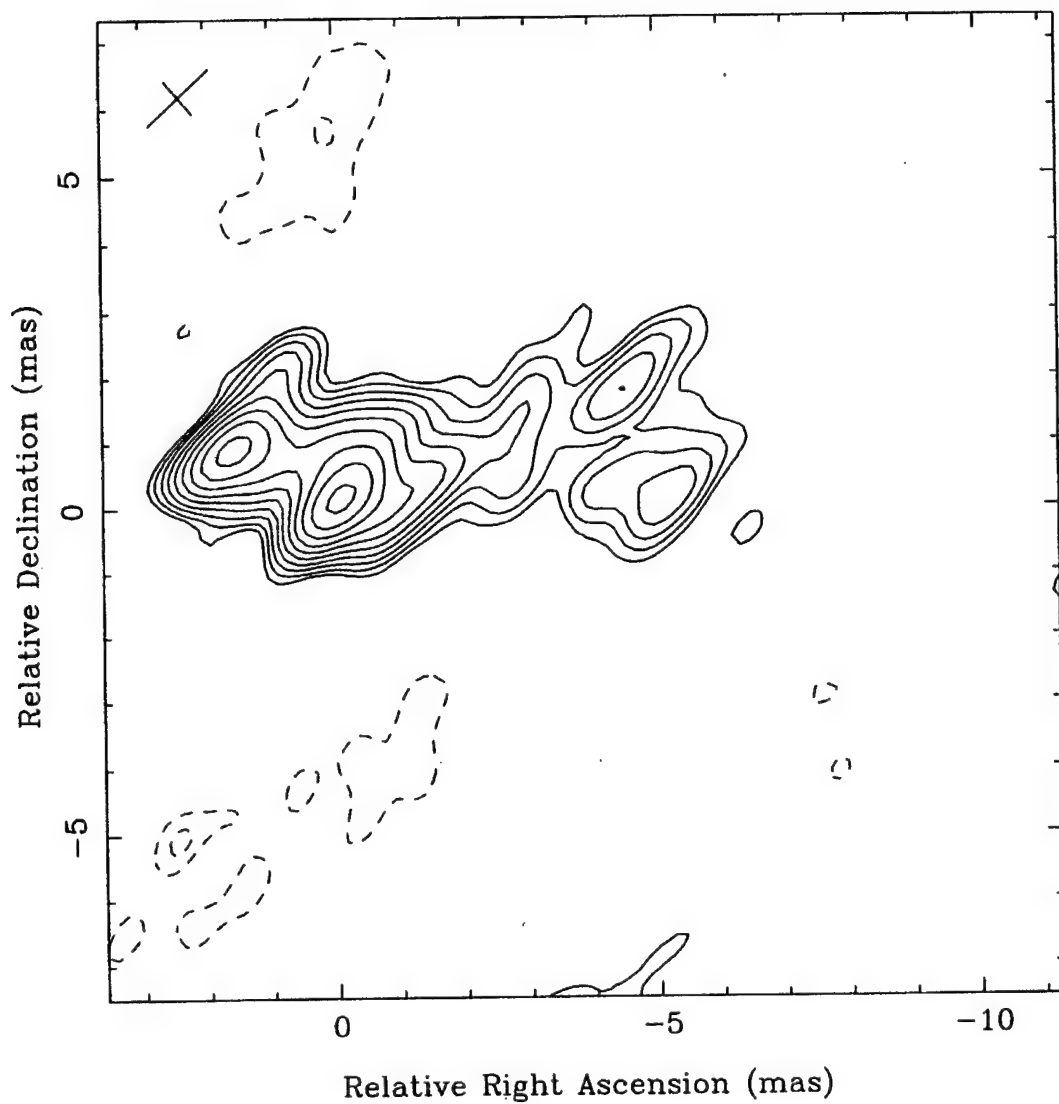


Figure 43: Total Intensity Map of 3C 345 at 3.6 cm, Epoch 1990.4, made with natural weighting of the visibilities. Contours are at  $-4$ ,  $-2.8$ ,  $2.8$ ,  $4$ ,  $5.7$ ,  $8$ ,  $11.3$ ,  $16$ ,  $22.6$ ,  $32$ ,  $45.3$ ,  $64$ , and  $90.5\%$  of the peak flux of  $878$  mJy/beam. The beam is  $1.3$  by  $0.7$  milliarcseconds at a position angle of  $-48.1^\circ$ .

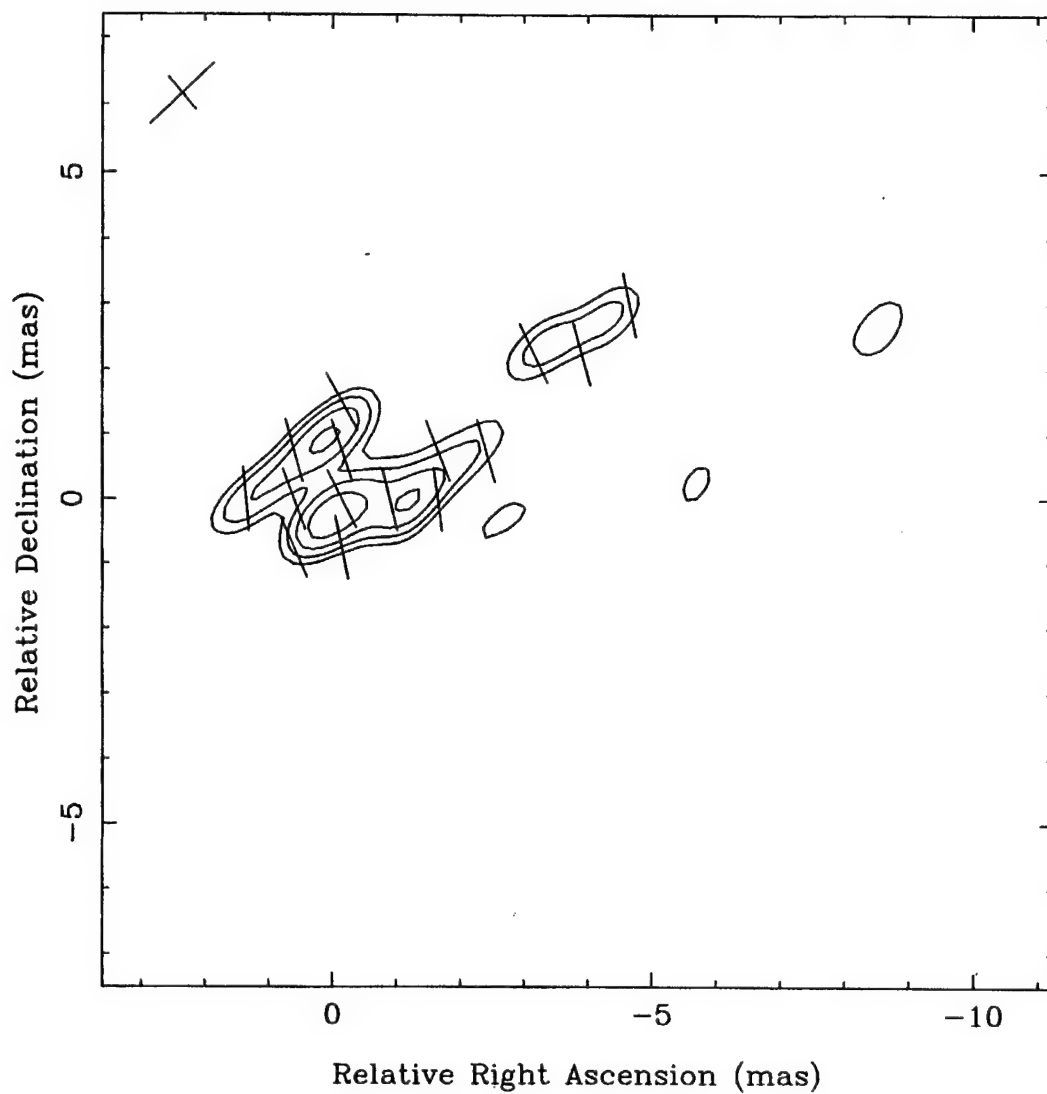


Figure 44: Complex Polarization Map of 3C 345 at 3.6 cm, Epoch 1990.4, made with natural weighting of the visibilities. Contours are at 26, 36.8, 52, and 73.4% of the peak flux of 43.5 mJy/beam. The beam is 1.3 by 0.7 milliarcseconds at a position angle of  $-48.0^\circ$ .



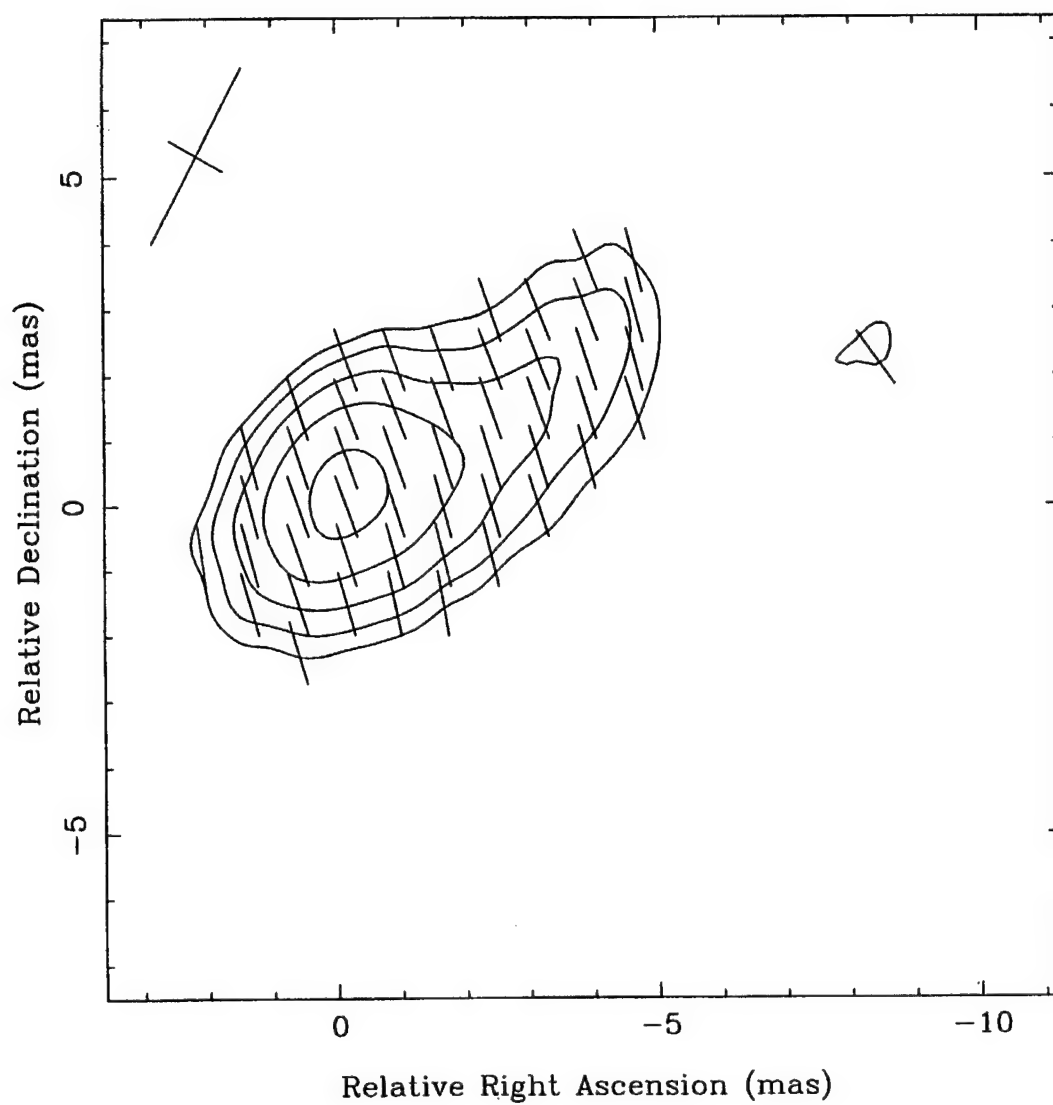


Figure 45: Complex Polarization Map of 3C 345 at 3.6 cm, Epoch 1990.4, made with natural weighting of the visibilities. Contours are at 23, 32.5, 46, 65.1, and 92% of the peak flux of 90.7 mJy/beam. The restoring beam is 3.4 by 1.1 milliarcseconds at a position angle of  $-28.8^\circ$ , which matches the 6 cm beam.

cm map at this epoch (see chapter 8). However, in both 3C 345 and 3C 273, the overall arrangement of components aligns well with the 6 cm map.

Figure 44 shows the complex polarization image of the same size made with the natural 3.6 cm resolution, which has higher resolution than the 6 cm map. The morphology of the jet is strikingly different in polarized flux than either the total intensity image at 3.6 cm or the polarized image at 6 cm. However, as noted in chapter 5, the jet in 3C 345 is edge-brightened, and in fact the total intensity clean components at 6 cm lie along the outer edges of the knots. They get resolved down by the restoring beam and the jets appear edge-brightened. Here in the polarized flux at the higher resolution, the edge-brightened structure of the jet is clear. Note the gradient between the top and bottom edges in the position angle, which can also be seen in the polarized CCs at 6 cm. By restoring the map with the beam from the 6 cm polarized image, a polarization map virtually indistinguishable from the 6 cm map results (figure 45).

Figure 46 shows the rotation measure map made with the assumption that the rotation measure is as low as possible. Alignment between the 6 cm and 3.6 cm maps was done by aligning the jets between C5 and C2. Except for some possible rotation near the core, the values in the center of the jet are practically zero. A problem in rotation measure mapping this source using the global VLBI array is the fine structure in the polarization images. A clear North-South gradient is present in the rotation measure. This results from the more successful separation of the polarized components by the higher resolution observations at 3.6 cm. As noted earlier, the clean components at 6 cm show some of this rotation as well.

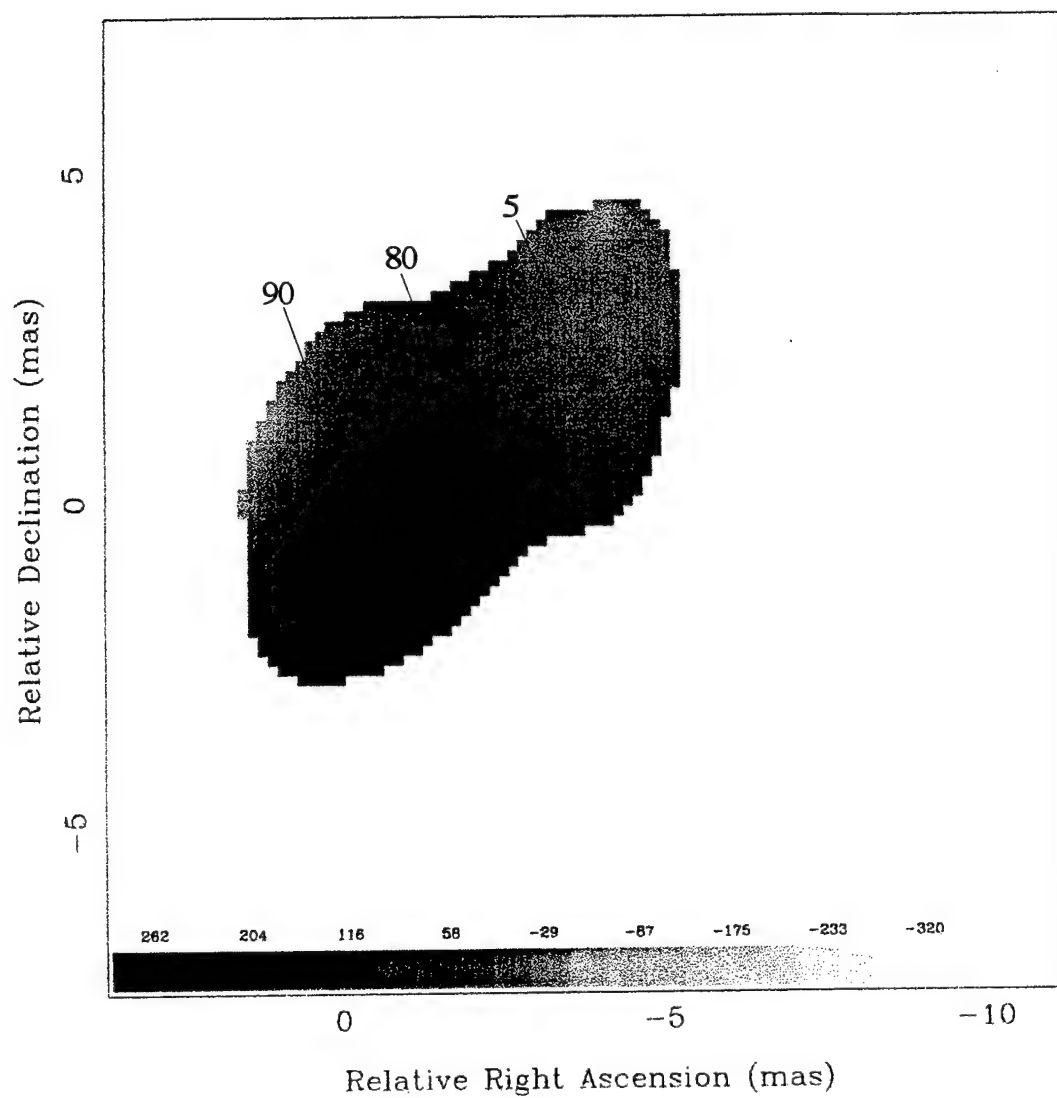


Figure 46: Faraday Rotation Measure Map of 3C 345, Epoch 1990.4, made from figures 42 and 45, with alignment of the maps made by visually aligning the jets in the total intensity images. Values are given in rad/m<sup>2</sup>.

## *2. Analysis*

As noted above, the 6 cm total intensity map shown in figure 41 agrees closely with the Mark II image produced using a more completely sampled UV data set from the same period. This suggests that the 6 cm data set is well calibrated, even if it is limited. The 3.6 cm total intensity map shown in figure 43 shows similarity to the 6 cm map, except for two points. First there is a shift of the core farther to the east relative to the brightest point associated with the knot C5.

Second there is the double structure out near the end of the jet which is not seen at 6 cm and which is brighter than the same point in the 6 cm map. Since the jet at this point should be optically thin, the 3.6 cm brightness should not be so great. The core at 3.6 cm could be shifted away from C5 by optical opacity effects, although it does appear farther than one might expect (see chapter 9). The outer region of the jet however seems to contain problems. The shifting of flux in the map probably indicates incorrect phases being assigned to the visibilities. These could occur in self-calibration, where some initial incorrectly determined phases would propagate through the data set.

Comparison of the complex polarization maps shown in figures 42 and 44 suggest that the polarization has been correctly determined within the inner part of the jet shown. The 6 cm map (figure 42) is expected to be correct, both for its agreement with previous epochs and for the apparent similarity between the total intensity map and higher dynamic range map cited earlier. The smoothed 3.6 cm map (figure 44) agrees so closely with the 6 cm map that it is probably correct despite the calibration errors which were present in the total intensity data set. This could occur for a number of reasons. First, the complex polarization map has almost all of the flux close to the bright core, where the total intensity map appeared correct. Second, the total intensity image is made from a far larger selection of visibilities, and the cross

### 3C345 Reconstructed B Field

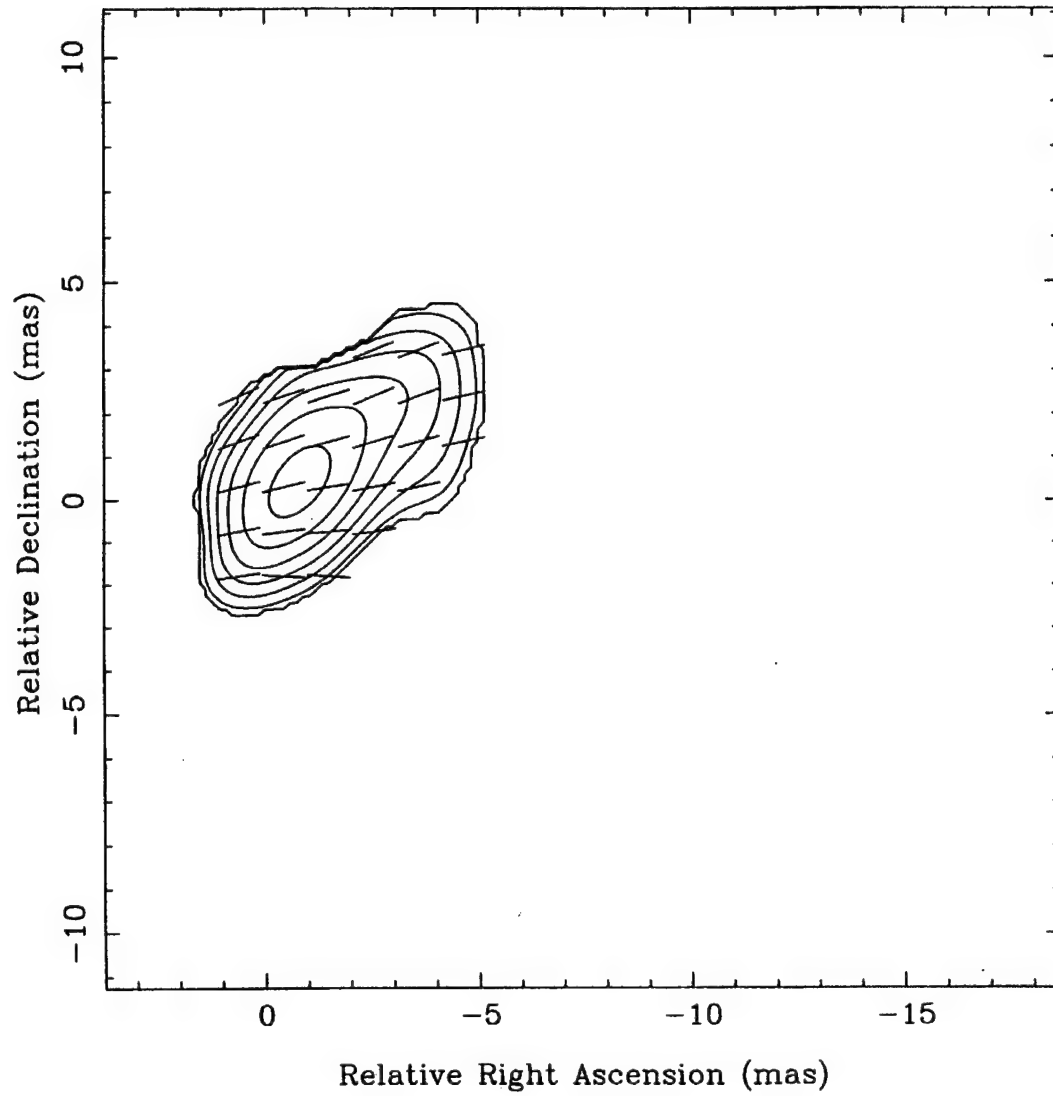


Figure 47: Map of the Reconstructed Magnetic Field in 3C 345, Epoch 1990.4, made from figure 45 corrected for Faraday Rotation using figure 46 and converting to magnetic field from electric field vectors.

hand visibilities corresponding to the troublesome parallel hand visibilities may be missing either due to failure during correlation or flagging during data editing.

The Faraday rotation map (figure 46) made from the complex polarization maps suggests that 3C 345 has little or no Faraday rotation on the parsec scale. The only significant measurement is near the bright point in the jet, where opacity effects may be playing a role. The outer part of the VLBI jet shows almost no rotation. Previously the magnetic movies made at 6 cm (see chapter 5) were interpreted to indicate alignment of the magnetic field with the jet axis in the outer VLBI jet, and this interpretation appears valid.

To reconstruct the magnetic field direction, the 3.6 cm complex polarization map is adjusted for Faraday rotation using figure 46 and then the vectors are rotated by  $90^\circ$  to convert from electric field emission direction from synchrotron radiation to the underlying magnetic field direction. The reconstructed magnetic field direction (see figure 47) from roughly 1 mas to 6 mas agrees closely with the jet axis determined from the total intensity image.

## *B. Epoch 1992.2*

### *1. Maps and Reduced Data*

The March-April, 1992, observations provided an excellent data set for the 6 cm mapping of 3C 345. After calibration and editing there were 3990 I visibilities and 1124 P visibilities. No CLEAN boxes or self-calibration limitations were needed to obtain convergence, although 22 iterations were used as flagging of cross hand data was done a number of times.

Figure 48 shows the final total intensity map for 3C 345 in epoch 1992.2 using natural weighting of the visibilities. There are no negative contours at the 1% level,

although there are small false features at 1% of the peak 2900 mJy/beam located north and south at roughly -10 mas relative RA. The core-jet morphology is clear, with the brightest component being the first knot in the jet lying to the west of the core. The jet then curves toward the northwest and the outer C1 component is seen and appears much more diffuse if clean components are limited to the inner jet (figure not shown). Further it appears that component C2 is beginning to break up at the end of the jet at relative RA  $\sim$  12 mas.

Figure 49 shows the corresponding complex polarization image made with natural weighting. The first false features are at roughly 5% of the peak 207 mJy/beam, and are scattered to the west of the jet. Because of the poor resolution (due to the dominance in the cross hand visibilities of the VLBA antennas), the core is not resolved away from the jet. The electric field vectors in the jet align with the 1990.4 epoch position angles in the outer ( $> 5$  mas) portion of the jet.

Figure 50 was produced from the same data set used to make figure 49. However, for figure 50, the data was weighted by  $\sqrt{r}$ , where  $r$  is the UV distance, and then Fourier transformed to produce a dirty map and dirty beam as described in chapter 2. The map was then deconvolved using CLEAN to produce this higher resolution map. The map has false features at 25% of the peak 63.2 mJy/beam scattered north and south of the jet. The jet is now seen as a series of four components showing a rotation of position angle along the jet, although the core is not seen in polarized flux.

At 3.6 cm, the data set is a vast improvement over the 1990.4 epoch observations. After calibration and editing, there are 1836 I visibilities and 559 P visibilities. Convergence was obtained without any restrictions on CLEAN or self-calibration.

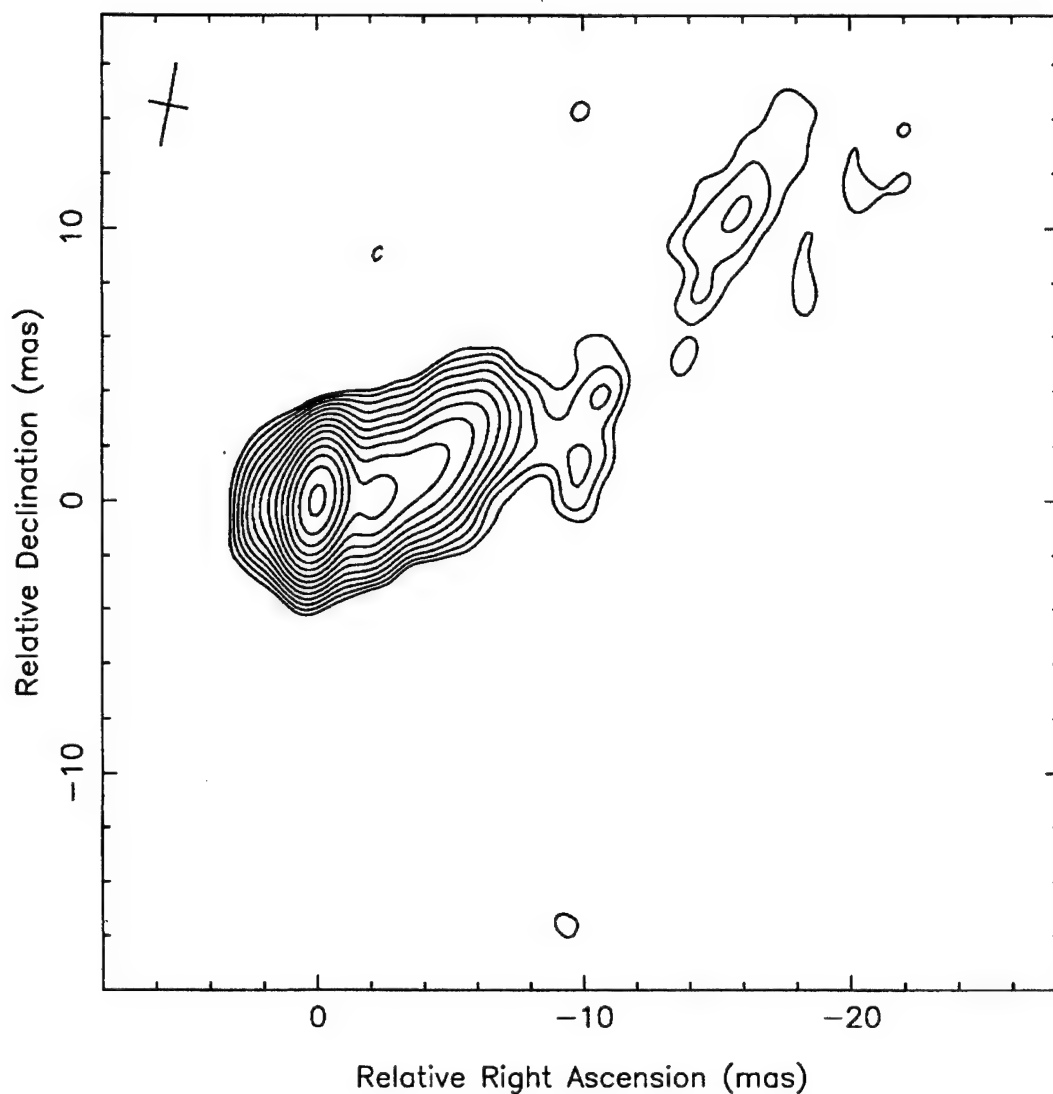


Figure 48: Total Intensity Map of 3C 345 at 6 cm, Epoch 1992.2, made with natural weighting of the visibilities. Contours are at -1, 1, 1.4, 2, 2.8, 4, 5.7, 8, 11.3, 16, 22.6, 32, 45.3, 64, and 90.5% of the peak flux of 2900 mJy/beam. The beam is 3.08 by 1.41 milliarcseconds at a position angle of  $-10.6^\circ$ .



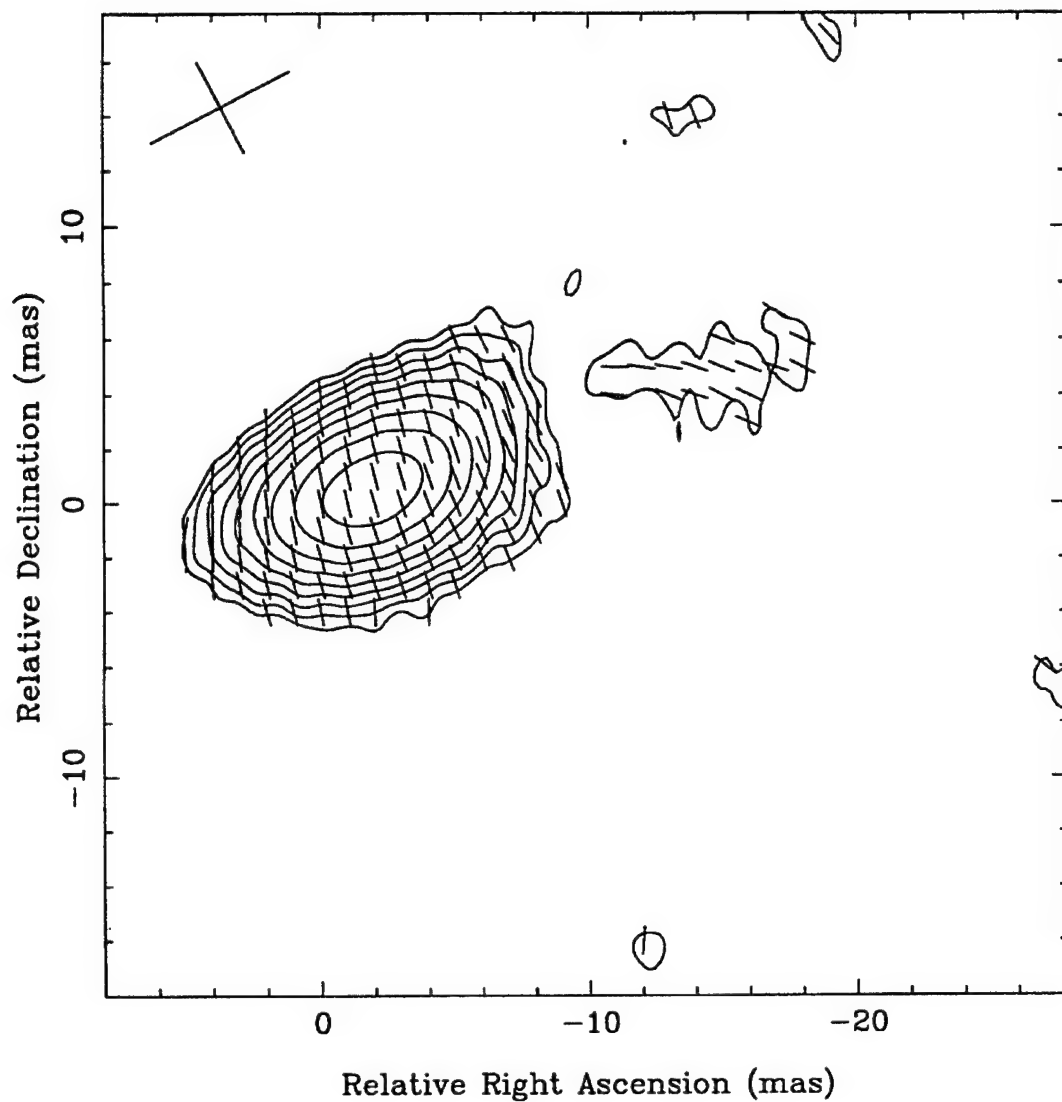


Figure 49: Complex Polarization Map of 3C 345 at 6 cm, Epoch 1992.2, made with natural weighting of the visibilities. Contours are at 5, 7.1, 10, 14.1, 20, 28.3, 40, 56.6, and 80% of the peak flux of 207 mJy/beam. The beam is 5.72 by 3.78 milliarcseconds at a position angle of  $-62.6^\circ$ .

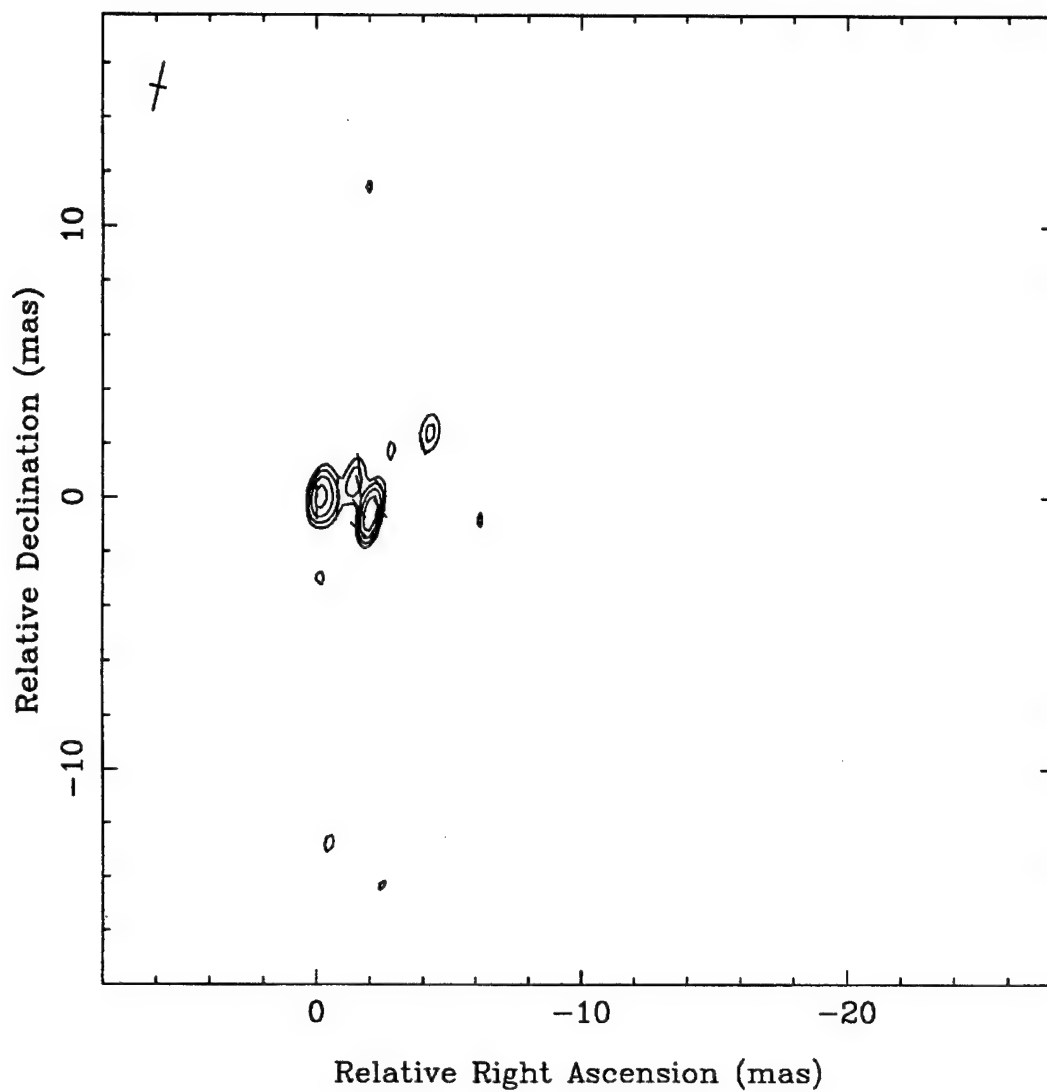


Figure 50: Complex Polarization Map of 3C 345 at 6 cm, Epoch 1992.2, made with  $\sqrt{r}$  weighting of the visibilities. Contours are at 22, 31.1, 44, 62.2, and 88% of the peak flux of 63.2 mJy/beam. The beam is 1.83 by 0.60 milliarcseconds at a position angle of  $-12.8^\circ$ .

The 3.6 cm total intensity map is shown in figure 51. False and negative features are apparent at 1% of the peak 5390 mJy/beam. The core-jet structure is clear, but the separation between the core and the first knot is significantly lower than expected. A check on the CLEAN components shows a very point-like, very strong (4.4 Jy in a single pixel) component within 0.6 mas of the expected core position. It appears therefore that a new component has emerged at 8.4 GHz, although not yet at 5 GHz. The flaring behavior noted in chapter 5 to have occurred in 1991 may be responsible for the birth of this component. The jet follows the usual behavior with the outer knots becoming progressively weaker at the higher observing frequency, and there is no unexpected brightening as seen in the epoch 1990.4 map.

Figure 52 shows the 3.6 cm complex polarization map of 3C 345 in epoch 1992.2. The morphology of the jet appears much like that in the earlier epoch with the polarized components sitting along the edges of the jet. The peak of the polarized image aligns exactly with the strong new component emerging from the core. The false features in the map occur at roughly 30% of the peak 45.9 mJy/beam and appear along the north edge and perhaps at roughly -13 mas relative RA.

In order to produce the Faraday rotation map 6 cm and 3.6 cm complex polarization maps need to have matching resolution. Although this cannot be done exactly without matching the interferometer spacings between the two frequencies, which is not possible in VLBI, an approximation can be made by weighting the data sets and smoothing the maps. In the following figures, the clean components are all restored with the same beam, while the residuals are convolved to this same resolution in the complex polarization maps

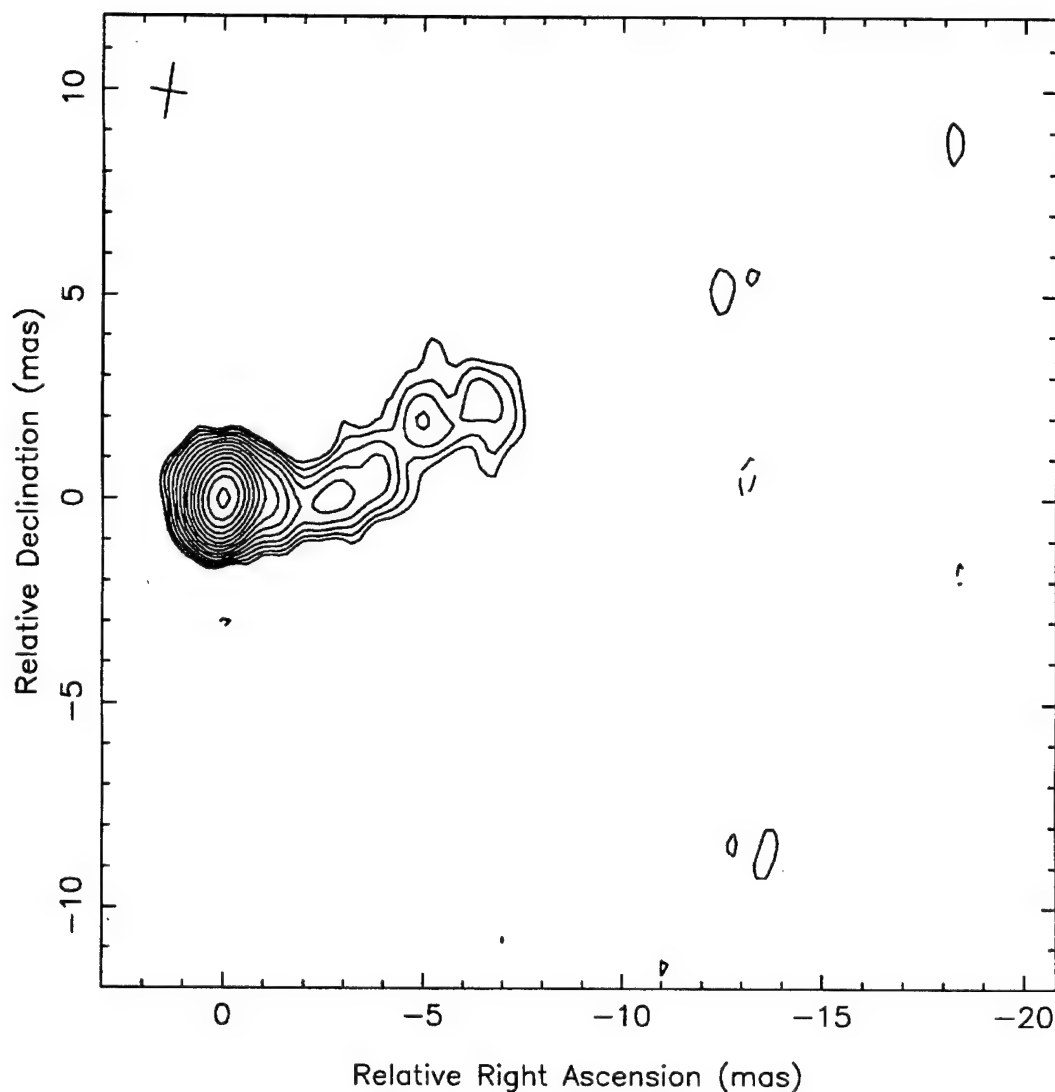


Figure 51: Total Intensity Map of 3C 345 at 3.6 cm, Epoch 1992.2, made with natural weighting of the visibilities. Contours are at -1, 1, 1.4, 2, 2.8, 4, 5.7, 8, 11.3, 16, 22.6, 32, 45.3, 64, and 90.5% of the peak flux of 5390 mJy/beam. The beam is 1.34 by 0.87 milliarcseconds at a position angle of  $-8.5^\circ$ .

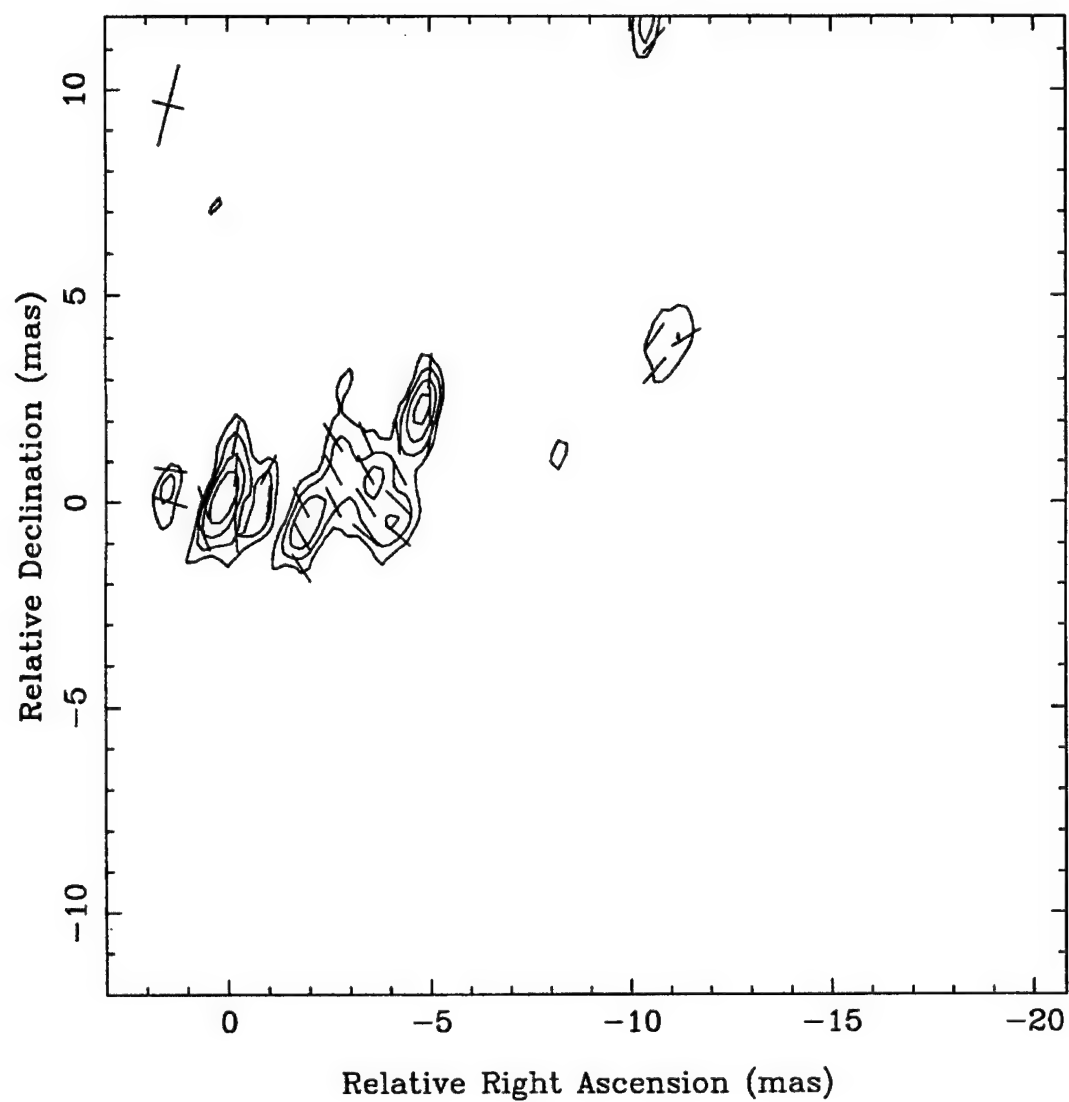


Figure 52: Complex Polarization Map of 3C 345 at 3.6 cm, Epoch 1992.2, made with natural weighting of the visibilities. Contours are at 25, 35.4, 50, and 70.7% of the peak flux of 45.9 mJy/beam. The beam is 2.04 by 0.75 milliarcseconds at a position angle of  $-14.5^\circ$ .

(where they are much more significant a fraction of the flux than in the total intensity maps).

In figure 53, the map shown in figure 48 is shown restored with a smaller beam to match that used in the following figures. There is not any significant change between the maps and there is no further information in this image. It is shown for completeness. Figure 54 shows the map resulting from restoring the weighted 6 cm complex polarization map, shown in figure 50, with the common beam. The four components seen in figure 50 are present here, with the first peak between 0 and -1 mas relative RA appearing broad since it contains two of the components. Figure 55 shows the 3.6 cm total intensity map, shown in figure 51, restored with the common beam. Again there is no new information in this map. Figure 56 shows the 3.6 cm complex polarization map, shown in figure 52, restored with the common beam. As in epoch 1990.4, this results in the components seen at the edges of the jet appearing in the form of sharp contours at the north and south edge of the jet.

Because of the high quality of the epoch 1992.2 images, an exact alignment between the 6 cm and 3.6 cm images is desirable, since there is more information in the maps than in those from epoch 1990.4, where there are clear calibration errors at 3.6 cm. Because the transition between optically thick and optically thin is frequency dependent, the alignment of the images at two frequencies is not automatic. Furthermore, in VLBI, self-calibration removes absolute position information from the data set, which means that the 6 cm and 3.6 cm images are not automatically registered. In order to investigate the robustness of the Faraday rotation map and of the reconstruction of the magnetic field, a number of possible alignments are presented here. Because of the inherent sampling at different resolutions between the two frequencies, false edge effects can be expected (such as the north to south gradients

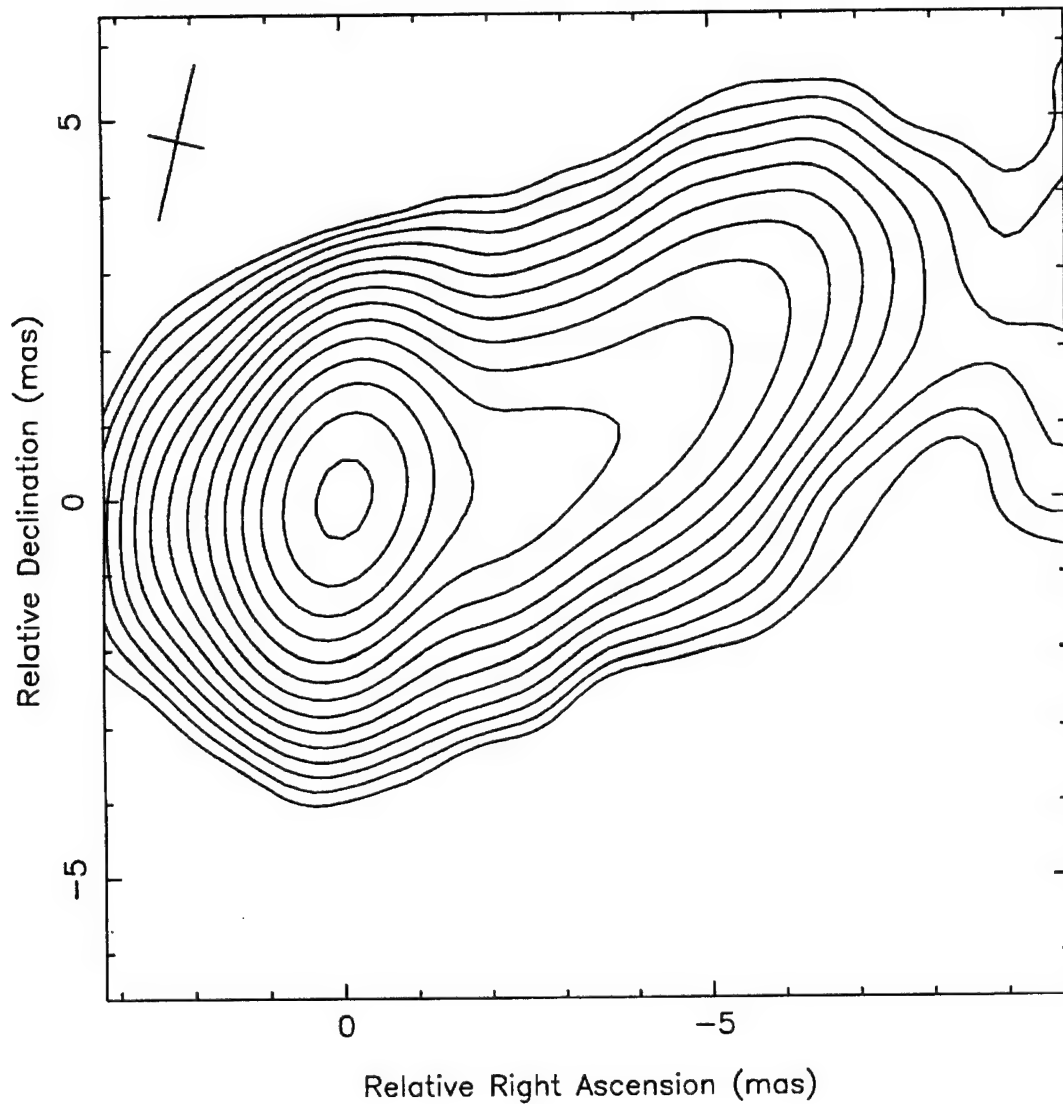


Figure 53: Total Intensity Map of 3C 345 at 6 cm, Epoch 1992.2, made with natural weighting of the visibilities and smoothed with an optional restoring beam. Contours are at -1, 1, 1.4, 2, 2.8, 4, 5.7, 8, 11.3, 16, 22.6, 32, 45.3, 64, and 90.5% of the peak flux of 3020 mJy/beam. The optional restoring beam is 2.10 by 0.75 milliarcseconds at a position angle of  $-13.5^\circ$ .

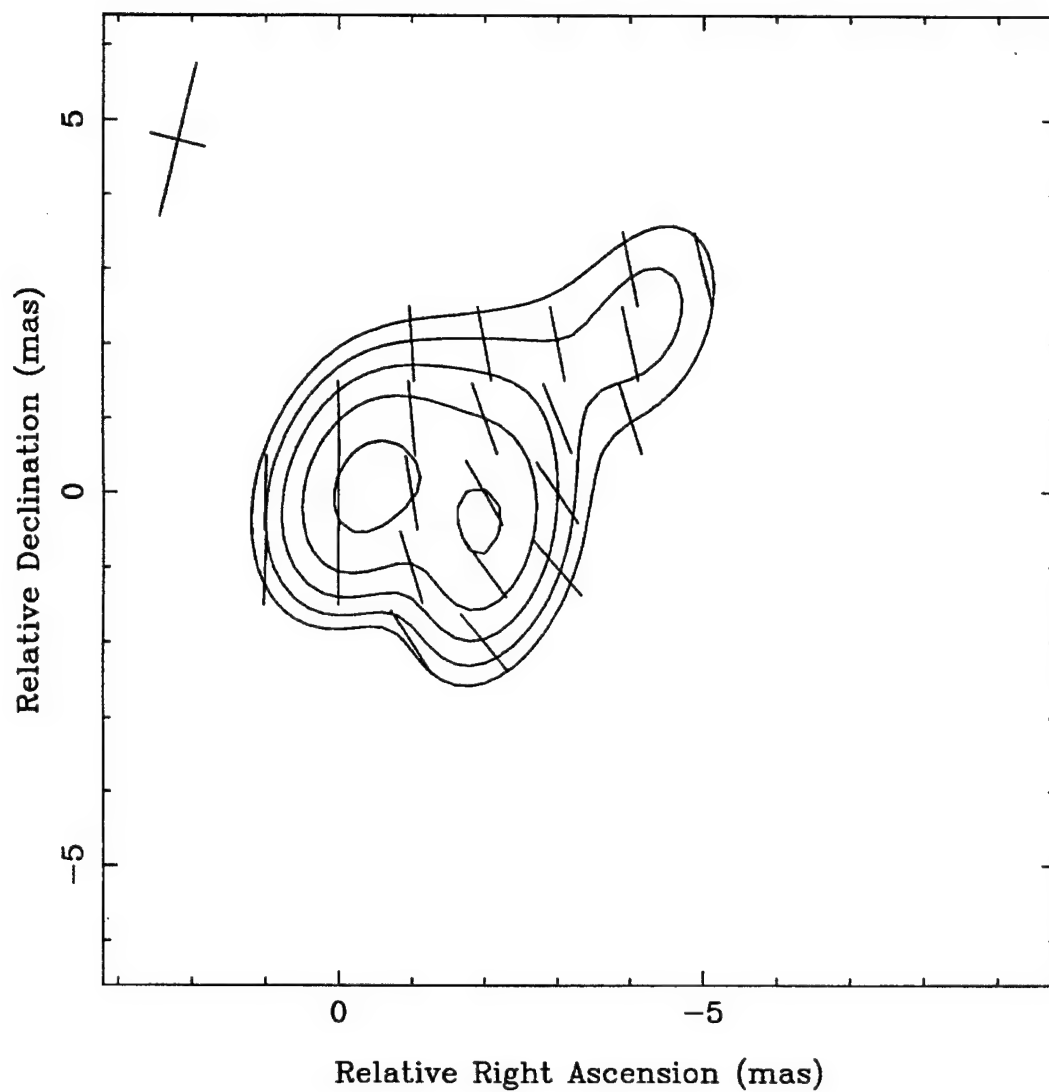


Figure 54: Complex Polarization Map of 3C 345 at 6 cm, Epoch 1992.2, made with  $\sqrt{r}$  weighting of the visibilities and smoothed with an optional restoring beam. Contours are at 22, 31.1, 44, 62.2, and 88% of the peak flux of 72.9 mJy/beam. The optional restoring beam is 2.10 by 0.75 milliarcseconds at a position angle of  $-13.5^\circ$ .



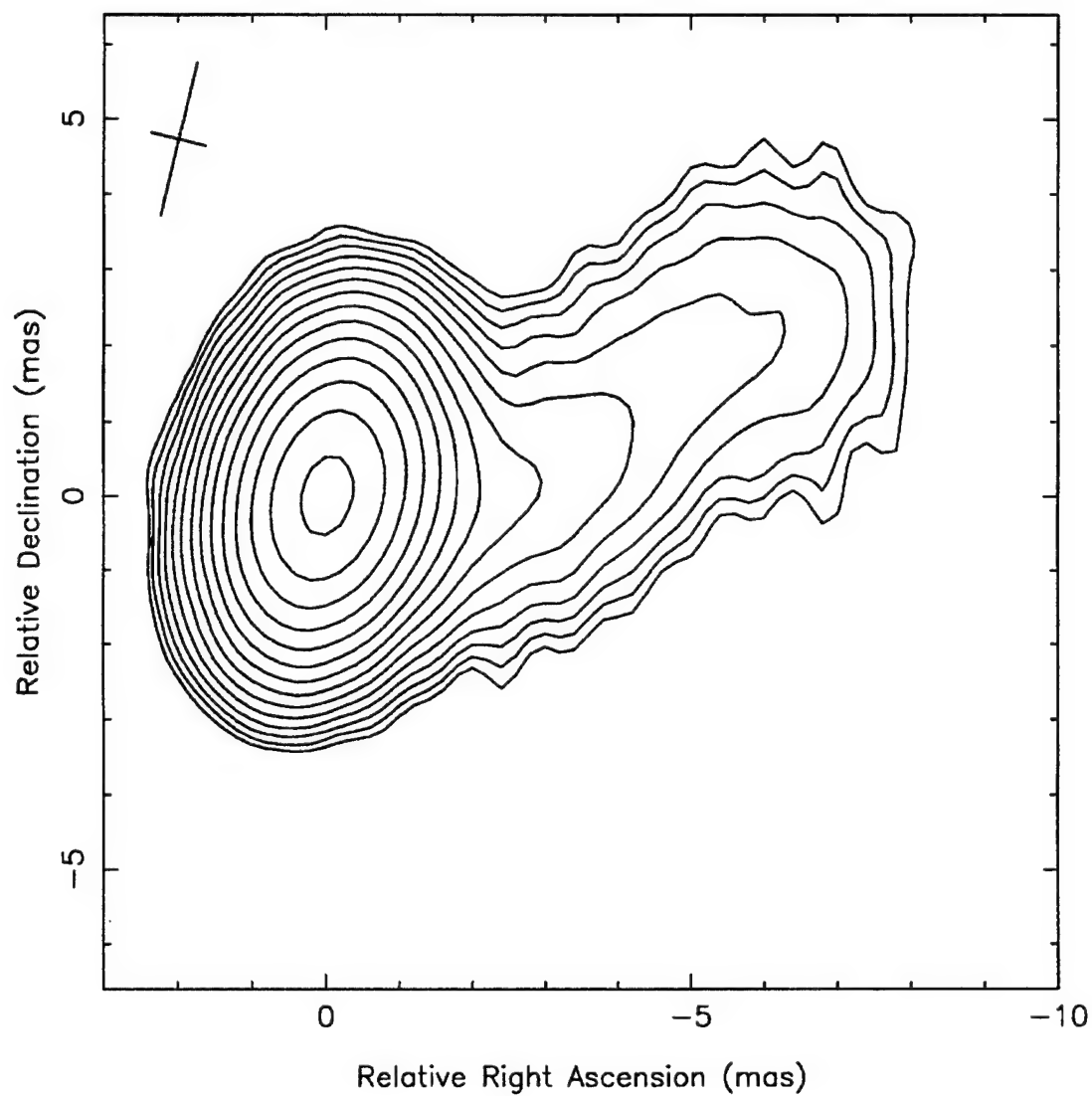


Figure 55: Total Intensity Map of 3C 345 at 3.6 cm, Epoch 1992.2, made with natural weighting of the visibilities and smoothed with an optional restoring beam. Contours are at -1, 1, 1.4, 2, 2.8, 4, 5.7, 8, 11.3, 16, 22.6, 32, 45.3, 64, and 90.5% of the peak flux of 5900 mJy/beam. The optional restoring beam is 2.10 by 0.75 milliarcseconds at a position angle of  $-13.5^\circ$ .

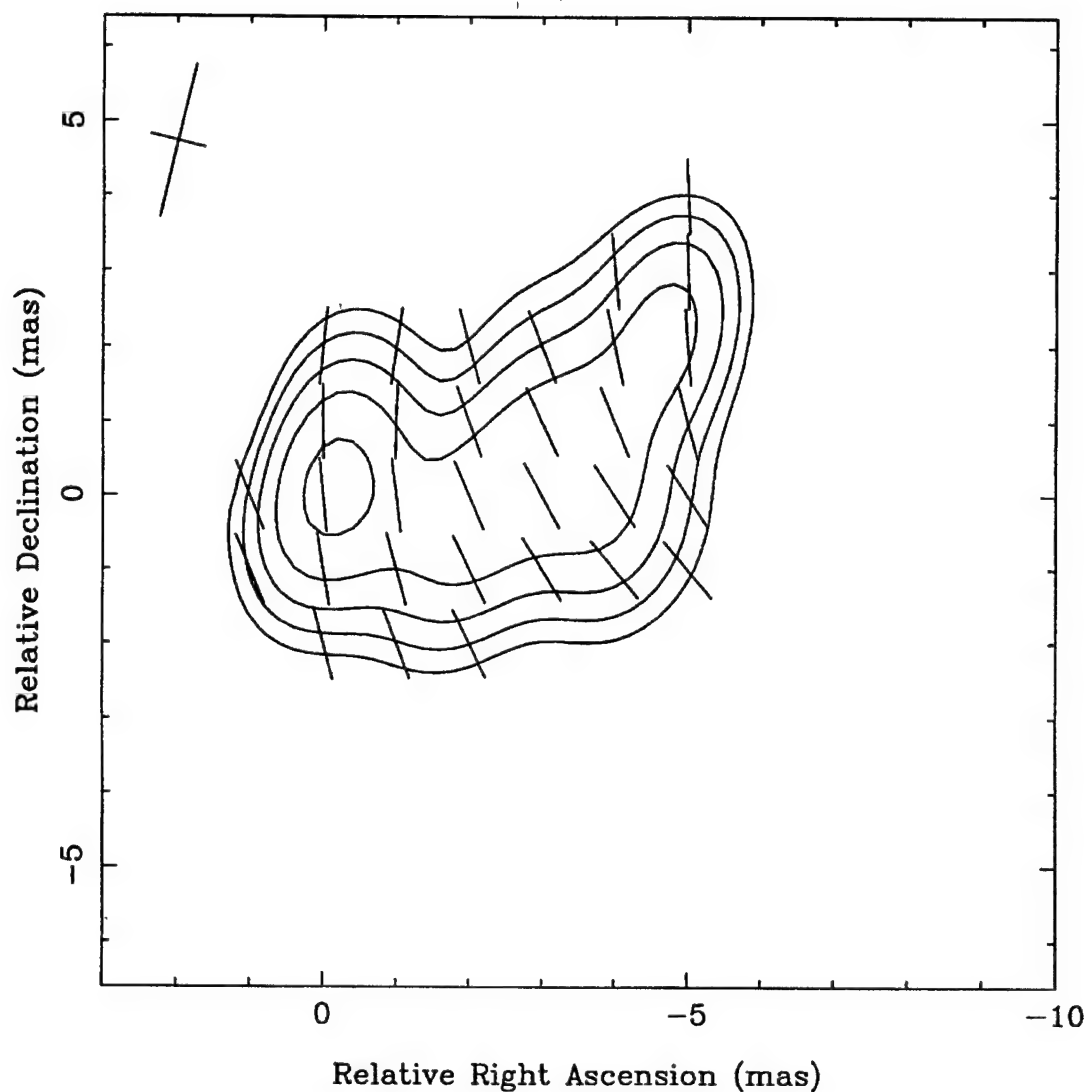


Figure 56: Complex Polarization Map of 3C 345 at 3.6 cm, Epoch 1992.2, made with natural weighting of the visibilities and smoothed with an optional restoring beam. Contours are at 22, 31.1, 44, 62.2, and 88% of the peak flux of 51.2 mJy/beam. The optional restoring beam is 2.10 by 0.75 milliarcseconds at a position angle of  $-13.5^\circ$ .

noted above). To minimize this problem, the interiors of the jets will be used to provide numbers on the maps.

All rotation measure maps are corrected for arcsecond scale Faraday rotation and represent the residual rotation measure. Since only two frequencies are used, there is inherent uncertainty about both the direction of rotation and the number of turns. In all cases presented here, the lowest possible rotation measure is given. Since the derived rotation measures for both 3C 345 and 3C 273 are low (less than 200  $\text{rad/m}^2$  throughout), other possible rotation measures are in excess of 1000  $\text{rad/m}^2$ , which is thought to be too large for inner regions of quasars from depolarization arguments (see chapter 4).

In figure 57, a Faraday rotation measure map made from figures 54 and 55 by aligning on the brightest points (0 mas relative RA and 0 mas relative Dec) is presented. Because the maps show a triple structure of polarized knots, three points in the Faraday rotation maps are labelled with their rotation measures in  $\text{rad/m}^2$ , corresponding to the middle of the polarized knots. In this map, the rotation measure is largest in the second knot and is always quite low ( $< 80 \text{ rad/m}^2$ ). The second knot is also much brighter in the 6 cm map than in the 3.6 cm map, and may indicate a region of changing optical opacity. At such a point an artificially high rotation measure might be expected.

In figure 58, the Faraday rotation map is made with the 6 cm map shifted one pixel (0.2 mas) west relative to the alignment used in figure 57. This decreases the measured rotation in the inner parts of the jet slightly ( $\sim 20 \text{ rad/m}^2$ ) while having almost no effect in the outer jet.

In figure 59, the Faraday rotation map is made with the 6 cm map shifted two pixels (0.4 mas) west relative to the alignment used in figure 57. This shift gives the best alignment of the bright points in the inner jet (components C4 and C3) between the two frequencies. If these components have become fully optically thin at 3.6 cm, then

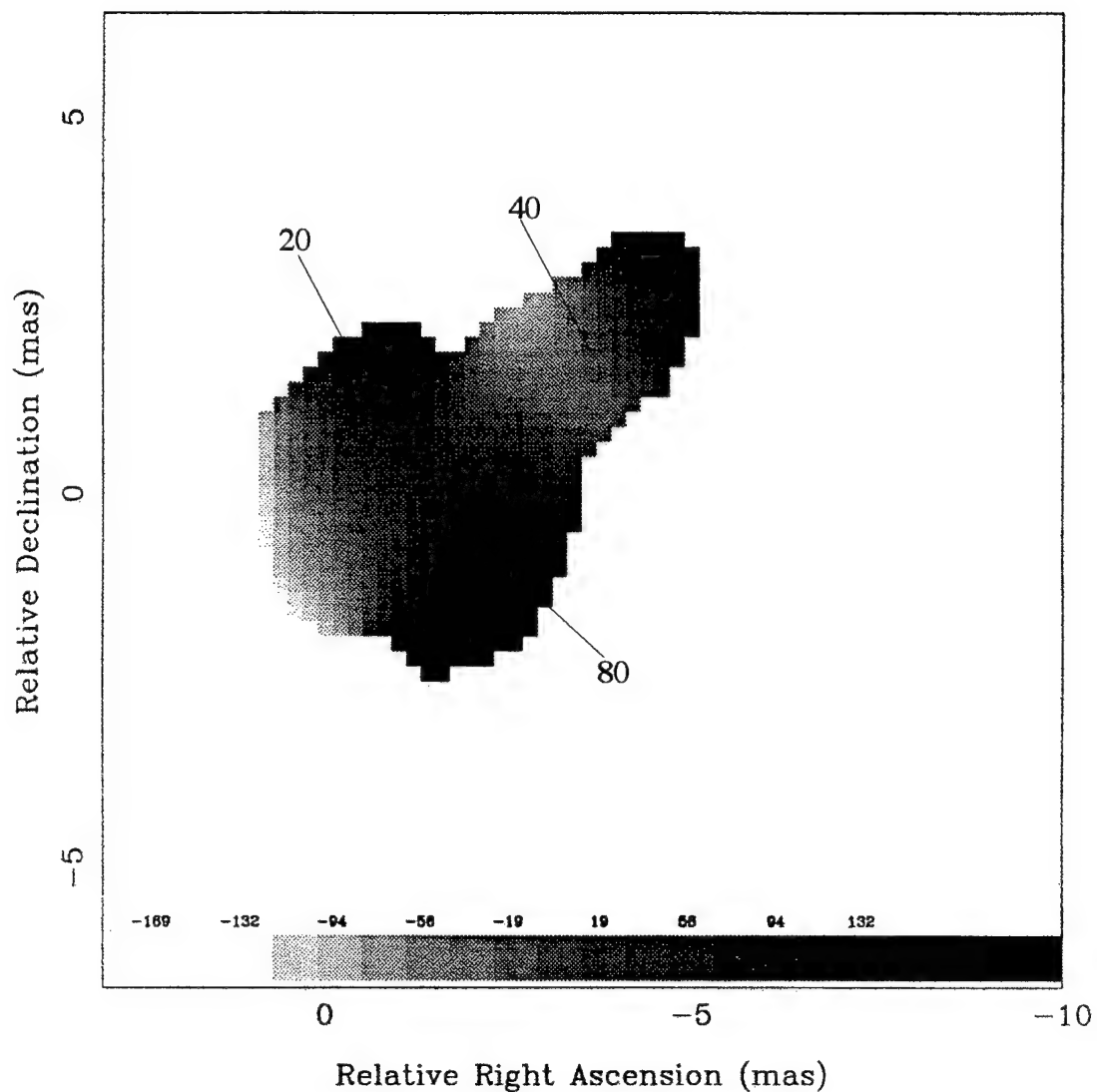


Figure 57: Faraday Rotation Measure Map of 3C 345, Epoch 1992.2, made from figures 54 and 56, with alignment of the 3.6 cm and 6 cm maps at the brightest total intensity peaks in each map. All values are in  $\text{rad/m}^2$ .

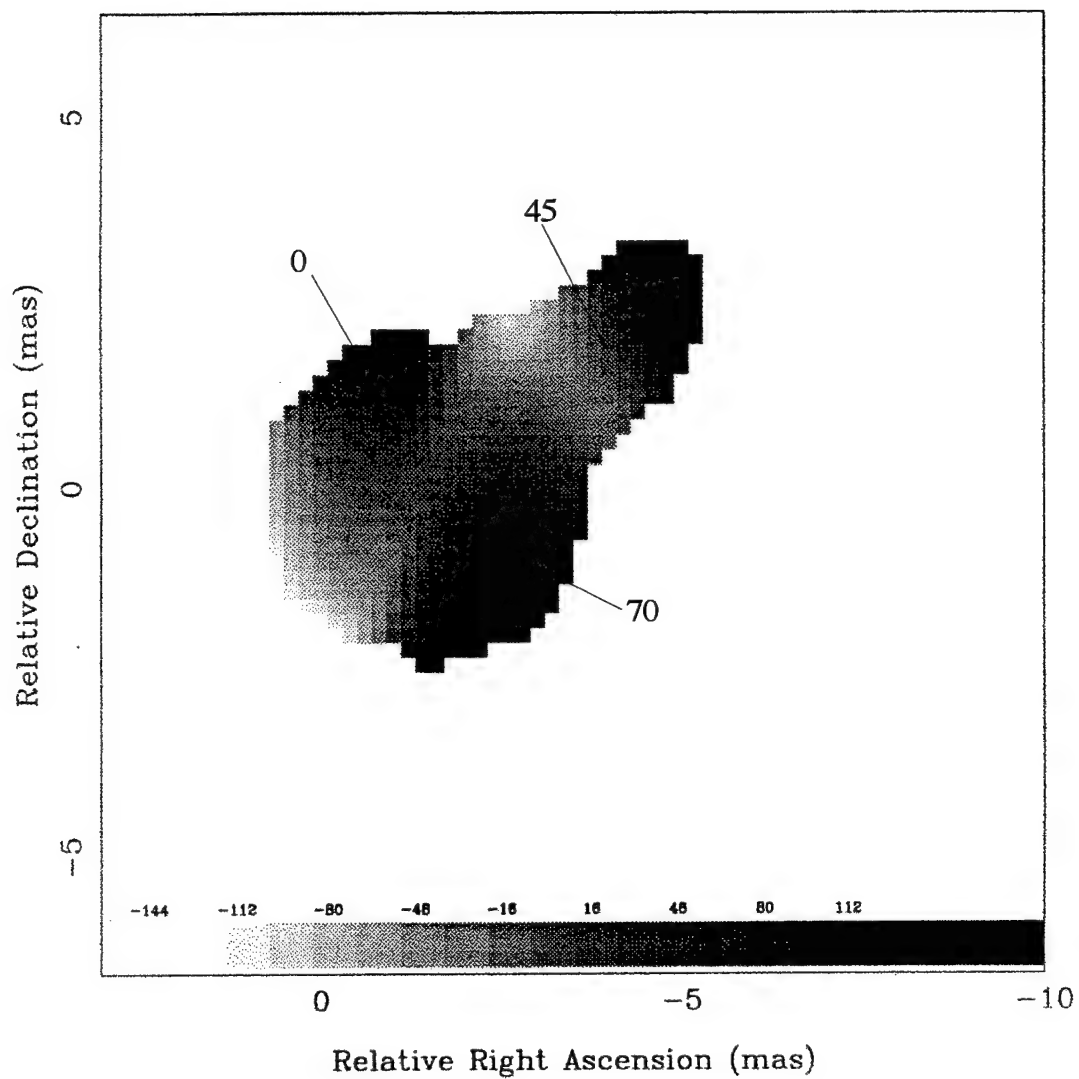


Figure 58: Faraday Rotation Measure Map of 3C 345, Epoch 1992.2, made from figures 54 and 56, with alignment of the 6 cm map shifted one pixel (0.2 milliarcsecond) right from the alignment used in figure 57. All values are in  $\text{rad/m}^2$ .

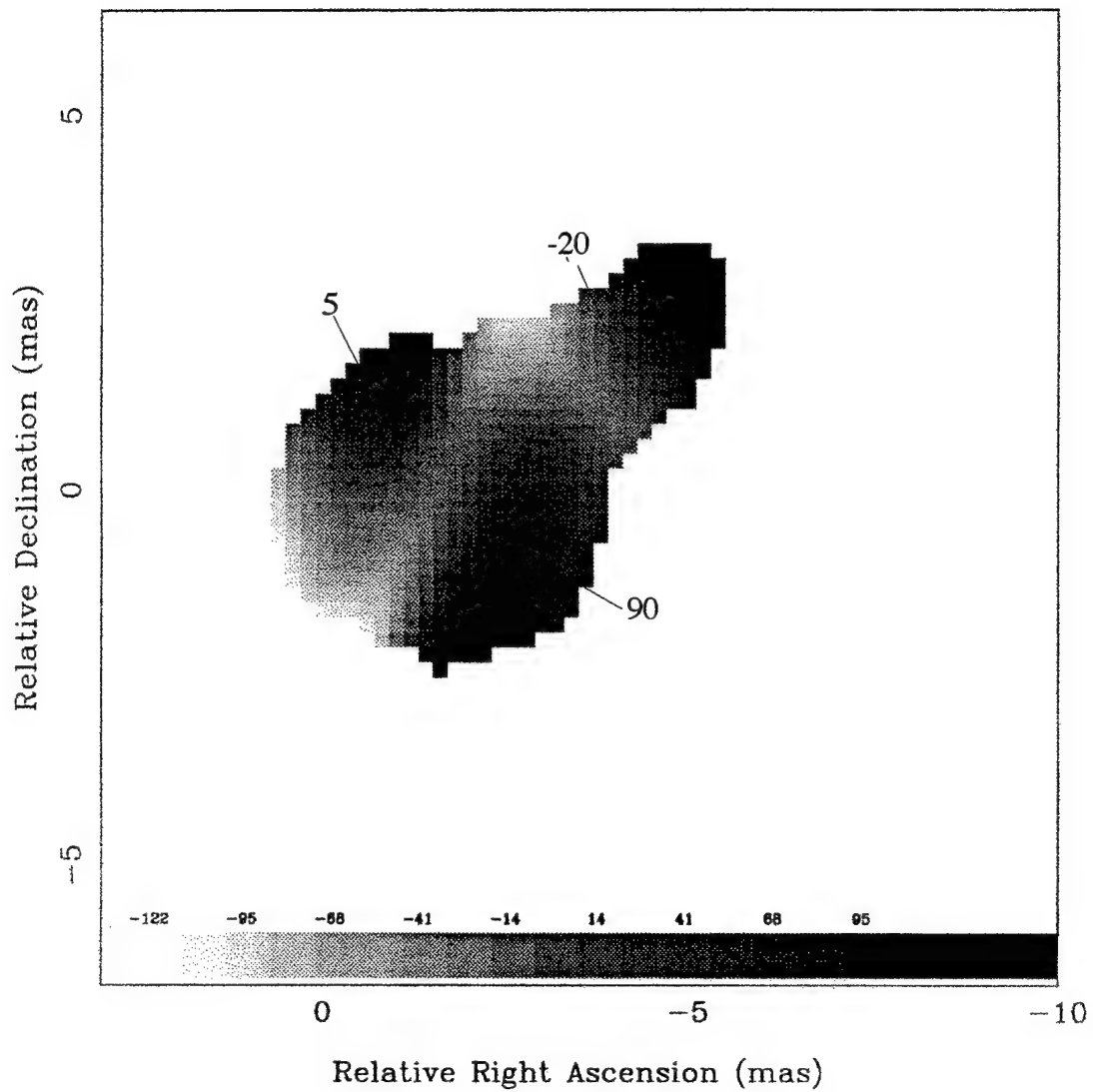


Figure 59: Faraday Rotation Measure Map of 3C 345, Epoch 1992.2, made from figures 54 and 56, with alignment of the 6 cm map shifted two pixels (0.4 milliarcsecond) right from the alignment used in figure 57. All values are in  $\text{rad/m}^2$ .

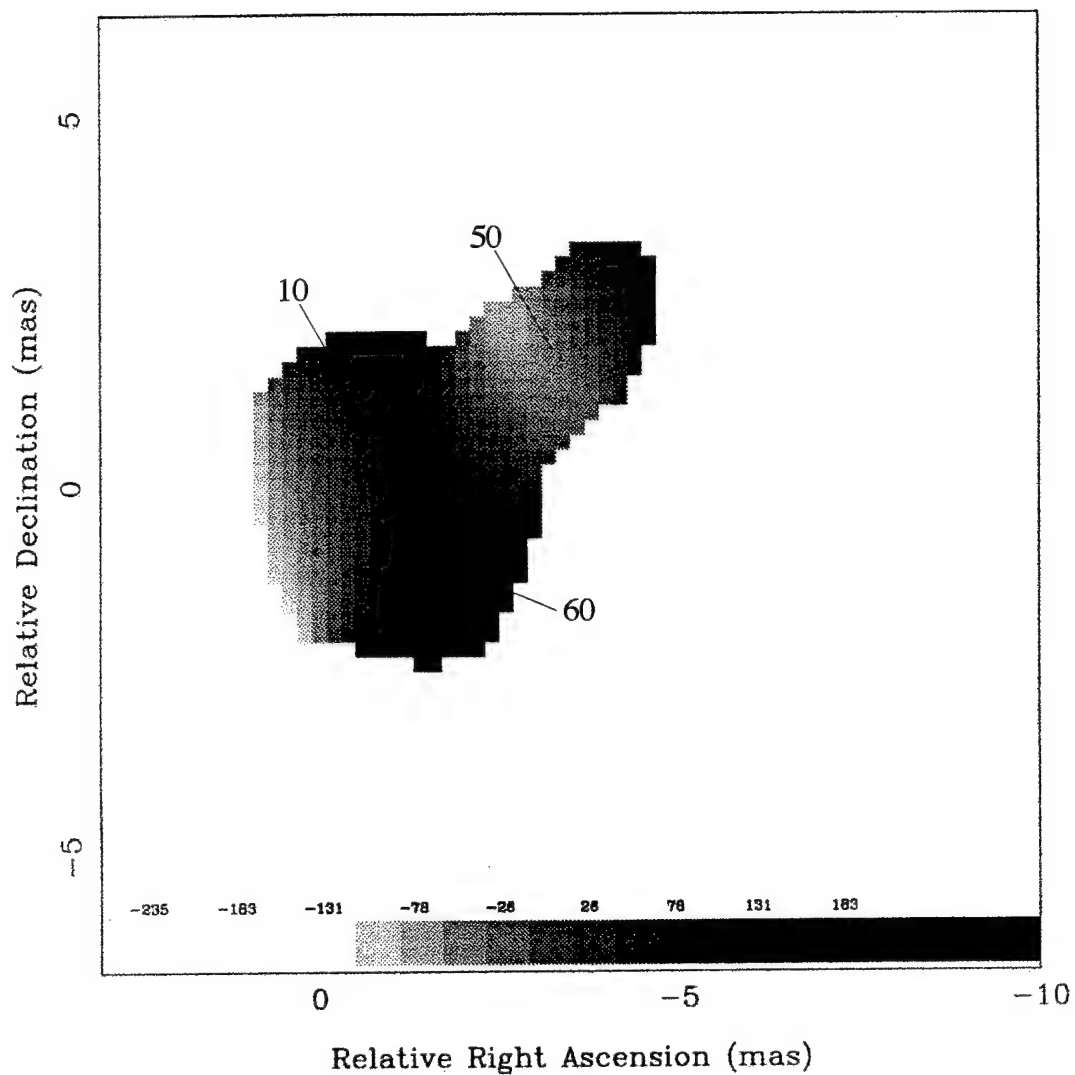


Figure 60: Faraday Rotation Measure Map of 3C 345, Epoch 1992.2, made from figures 54 and 56, with alignment of the 3.6 cm map shifted two pixels (0.4 milliarcsecond) right from the alignment used in figure 57. All values are in  $\text{rad/m}^2$ .

Comp.	1988.1 (LFB)		1990.2 (U&W)		1990.4		1992.2	
	distance	PA	distance	PA	distance	PA	distance	PA
D								
C6							< 1**	
C5	0.9	-104	1.5	-102	1.5†	-113	1.6†	-97
C4	2.8	-80	2.5		2.5††	-95	3.4*	-83
C3	5.5	-71	5.0		5.0††	-75	5.6*	-82
C2	8.2	-72	8.5		8.5††	-76	9.4††	-73
C1	--	--	~18	-54	--	--	~20*	~ -57

Table 17: 3C 345 component positions from Brown (LFB), Unwin and Wehrle (U&W), and this work (see text for references). The distance is given in milliarcseconds and the position angle (PA) is in degrees, both relative to the core. A \* indicates that the position was determined from the C band contour map, a \*\* that the component appears only in the X band map, a † that the position was determined from the C band clean components, and a †† that the RA was determined from U&W and the declination from the C band clean components.

this alignment would be the correct one. Here there is very little Faraday rotation present except in the knot which is bright at 6 cm but not at 3.6 cm. Except for this knot, the maximum absolute rotation measure is only 20 rad/m<sup>2</sup>.

In figure 60, the Faraday rotation map is made by shifting the 6 cm map two pixels (0.4 mas) east relative to the alignment used in figure 57 (*i.e.* in the opposite direction from the previous two maps). In this case the rotation measure increases only in the outer portion of the jet (to 50 rad/m<sup>2</sup>).

## 2. Analysis

The total intensity and complex polarization maps look quite reasonable. The lack of a need for self-calibration limits or CLEAN boxes suggests that the data sets are self-consistent and complete enough for the imaging requirements. The necessity of



Comp.	1988 LFB	1990 UW	CB 1990.4	XB	CB 1992.2	XB
D	1440	1050	770	1019	262	6469
C6	--	--	--	--	--	
C5	4280	2000	2075	1320	3065	
C4	670	400	869	433	989	548
C3	310	250	283	160	840	391
C2	200	130	202	--	267	52
C1	--	40	--	--	58†	--

Table 18: 3C 345 component fluxes from Brown (LFB), Unwin and Wehrle (UW), and this work (see text for references). The flux is given in mJy, except for UW which is mJy per mas along the jet. The † indicates that this reading is mJy/beam in the area of C1 determined using the clean map.

weighting the 6 cm cross hand data to improve resolution leads to the poor dynamic range seen in that complex polarization map, however the map is sufficient for producing the Faraday rotation maps.

In table 17, the determined component positions are presented together with those determined by Brown in epoch 1988.1 (Brown, 1992) and Unwin and Wehrle in epoch 1990.2 (Unwin and Wehrle, 1992). As can be seen by comparing the determination of component positions between the 1988.1 and 1990.2 epochs, it is difficult to determine the centers of components consistently. Overall the component positions determined appear within the variation shown earlier given the known component speeds.

The properties of the total intensity components are summarized in table 18. The most striking property seen is that the jet becomes progressively weaker at 3.6 cm relative to 6 cm in the high quality epoch 1992.2 observations, while increasing its 3.6 cm relative brightness at component C3 in the epoch 1990.4 observations. As noted

1990.4					1992.2				
Pos.	P Flux	PA	I ID	m (I)	Pos.	P Flux	PA	I ID	m (I)
0.6	26	5	D ?	3.4					
1.5	69	38	C5 bot	3.3	1.8	67	41	C5	2.2
2.6	28	29	C4 top	7.8	3.0	26	50	C4 top	8.9
2.8	40	32	C4 bot		3.6	60	83	C4 bot	
5.1	45	16	C3 top	20	5.6	22	54	C3 top	2
5.6	11	33	C3 bot						

Table 19: 3C 345 component polarization properties in C band for the two epochs presented here. Pos gives the position in milliarcseconds from the core, P Flux gives the linearly polarized flux in mJy, PA gives the electric field vector position angle corrected for arcsecond scale Faraday rotation, I ID gives the identification of the corresponding total intensity component, and m(I) gives the percentage polarization relative to that total intensity component.

earlier, this probably indicates a calibration error in the earlier data set. This could also explain the higher brightness of the C4 component in the earlier epoch map presented here, when compared to the epoch 1990.2 map from Unwin and Wehrle.

In table 19, the C band component polarization properties are summarized. As noted in the table, the polarized components lie along the north and south edges (top and bottom) of the total intensity components. In general, the percentage polarization appears to increase along jet, except in epoch 1992.2 where the C3 component has lost a substantial amount of polarized flux.

Table 20 summarizes the component polarization properties for the X band maps. The new C6 component is picked up with strongly in polarized flux, although it is so intense in total intensity that the percentage polarization is low. The polarized flux may also be mixed with polarized flux coming from the core. The polarized flux associated with knot C4 in epoch 1992.2 appears to give roughly the same percentage polarization as in the C band map. This is to be expected if the knot is optically thin at

1990.4					1992.2				
Pos.	P Flux	PA	I ID	m (I)	Pos.	P Flux	PA	I ID	m (I)
< 1	24	5	D?	2.4	< 1	44	42	C6	>1
1.4	46	23	C5 bot	5.5	1.2	16	54	C5	--
2.0	36	24	C5 top		2.2	27	68	C4 bot	10
2.8	36	13	C4	8.3	3.2	14	58	C4 top	
					4.0	16	69	C4 top	
4.5	16	20	C3 bot	29	4.6	11	84	C4/C3	
7.2	31	23	C3 top		5.8	23	44	C3 top	6

Table 20: 3C 345 component polarization properties in X band for the two epochs presented here. Pos gives the position in milliarcseconds from the core, P Flux gives the linearly polarized flux in mJy, PA gives the electric field vector position angle, I ID gives the identification of the corresponding total intensity component, and m(I) gives the percentage polarization relative to that total intensity component.

these frequencies. The polarized flux at C3 is slightly larger than expected from extrapolation from the C band.

The residual Faraday rotation maps all show similarities in the low values of Faraday rotation determined for the jet. It is interesting to note that the Faraday rotation map made using the best alignment of the total intensity images of the jets at 6 cm and 3.6 cm also gives the lowest rotation measures (excluding the knot which is much brighter at 6 cm than at 3.6 cm). Although there is no real reason to demand that the least Faraday rotation be the most reasonable solution, the strong alignment of the outer electric field vector position angle perpendicular to the jet axis over many epochs of polarization VLBI observations suggests a well maintained magnetic field. Such a field is easier to accept if a method is available to keep it aligned over time, which shearing could do for a field parallel to the jet axis. Since a low Faraday rotation measure would allow reconstruction of such a magnetic field orientation, there is some bias in favor of

such an interpretation. In any case, it appears that the maximum Faraday rotation measure on the parsec scale in 3C 345 is likely to be under  $100 \text{ rad/m}^2$ .

In figure 61 the first Faraday rotation map (figure 57) is used to adjust the electric field vector position angle in the 3.6 cm complex polarization map, and then the vector is rotated by  $90^\circ$  to shift to magnetic field orientation. The reconstructed magnetic field undergoes a rotation as it moves from the bright knot at C5 into the main part of the jet where it aligns with the jet axis. At the end it appears to undergo a second rotation, however this could be an edge effect arising in the Faraday rotation map construction and not a turn in the actual magnetic field, although such a turn is suggested in both the 6 cm and 3.6 cm complex polarization maps.

Figure 62 shows the reconstructed magnetic field using the Faraday rotation map in figure 58, while figure 63 shows the field reconstructed from figure 59 (the Faraday rotation map made from the best total intensity alignment). Both cases show the same basic behavior as seen in the reconstruction shown in figure 61. Throughout the sequence beginning in figure 61 and going through figure 63, the alignment of the magnetic field with the jet axis occurs earlier and earlier in the jet (*i.e.* closer to C5). All reconstructions do show the rotation near C5 and the rotation near the end of the jet.

In figure 64, the final reconstruction of the magnetic field is shown, which uses the Faraday rotation map shown in figure 60. This reconstruction is not quite as well aligned with the jet axis, although it is still reasonably well aligned. The reconstructed map appears slightly distorted because this shift reduces the overlap between the 6 cm and 3.6 cm complex polarization maps. It seems likely that minimizing the overlap is an indication that the maps are not properly aligned.

### 3C345 Reconstructed B Field

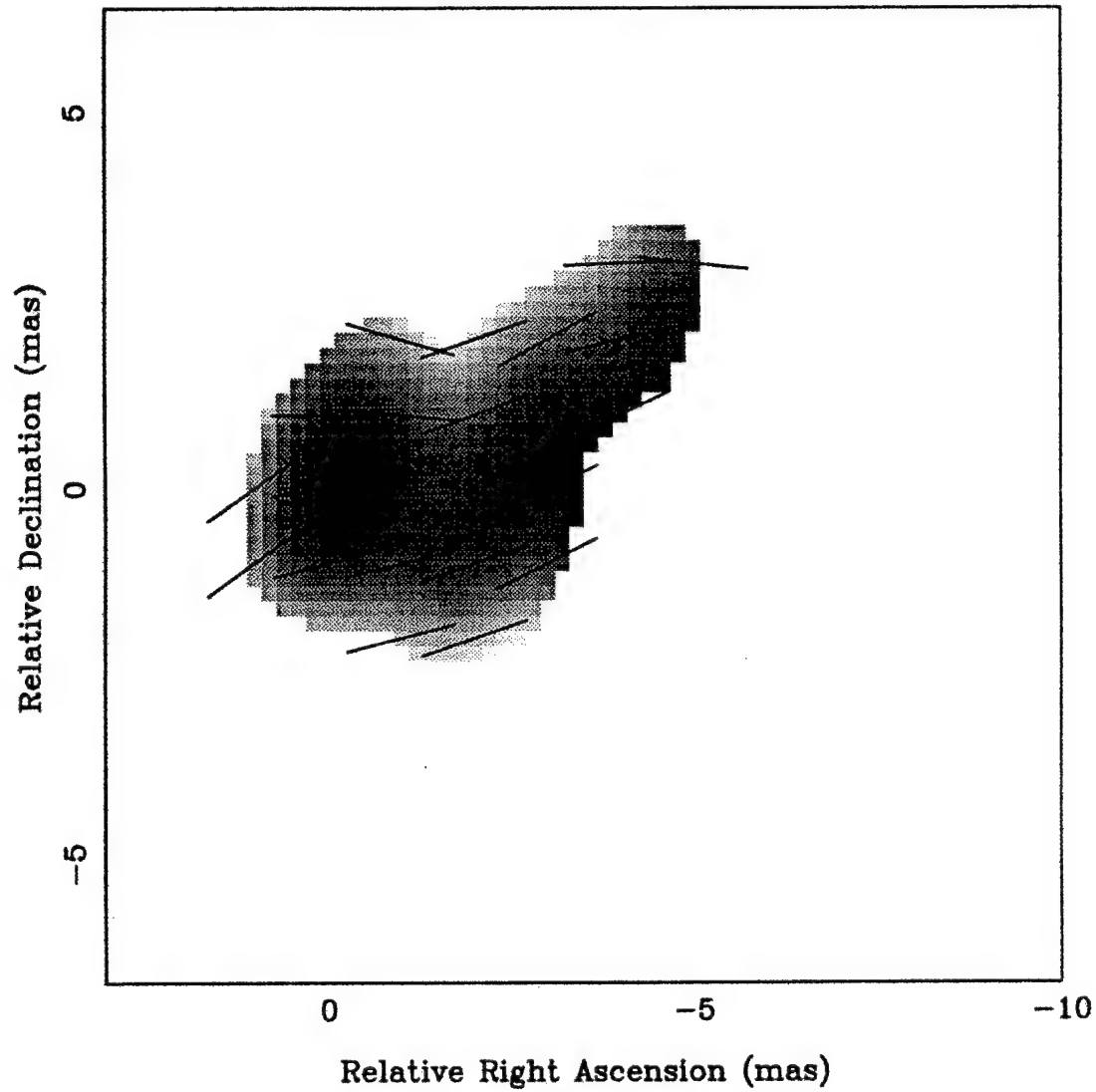


Figure 61: Map of the Reconstructed Magnetic Field in 3C 345, Epoch 1992.2, made from figure 56 corrected for Faraday Rotation using figure 57 and converting to magnetic field from electric field vectors.

### 3C345 Reconstructed B Field

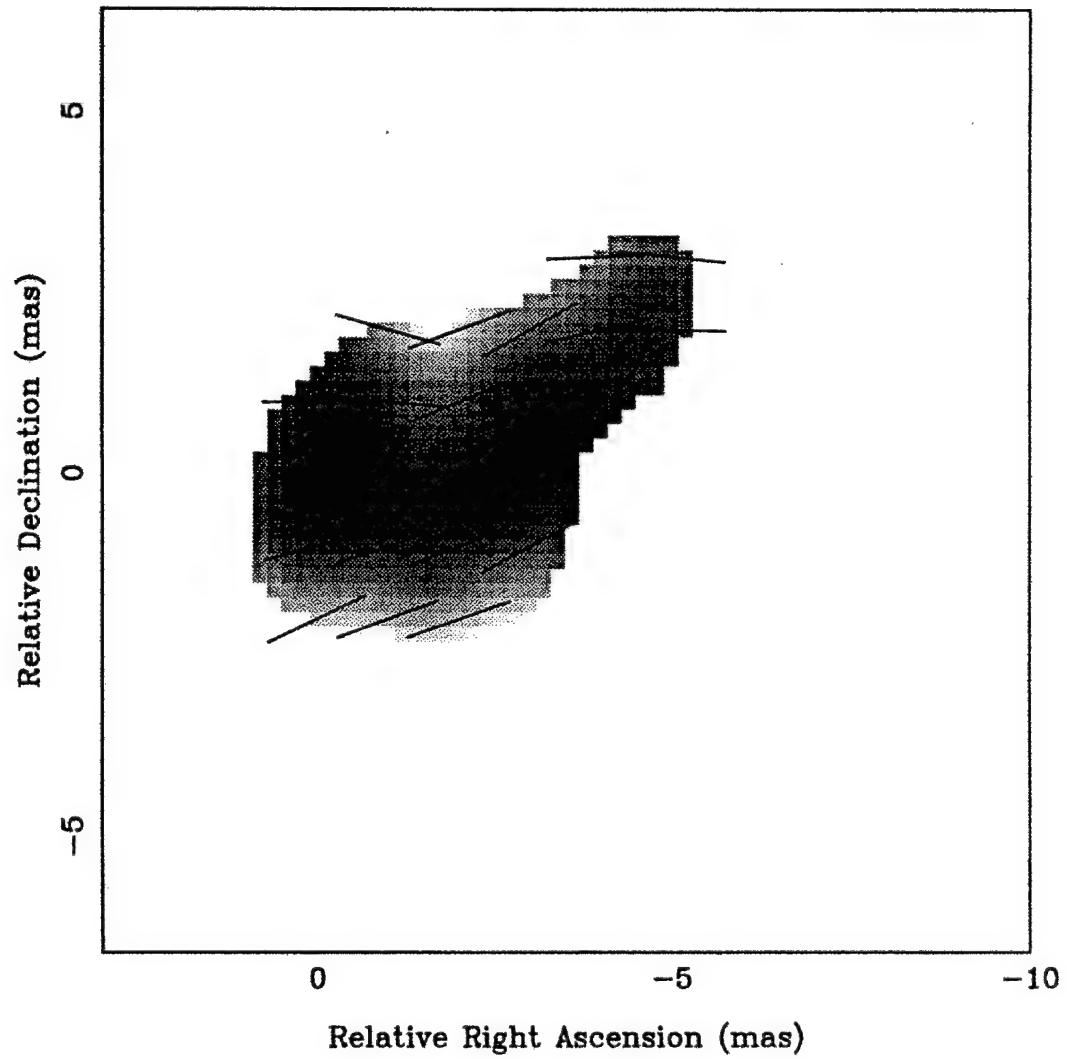


Figure 62: Map of the Reconstructed Magnetic Field in 3C 345, Epoch 1992.2, made from figure 56 corrected for Faraday Rotation using figure 58 and converting to magnetic field from electric field vectors.

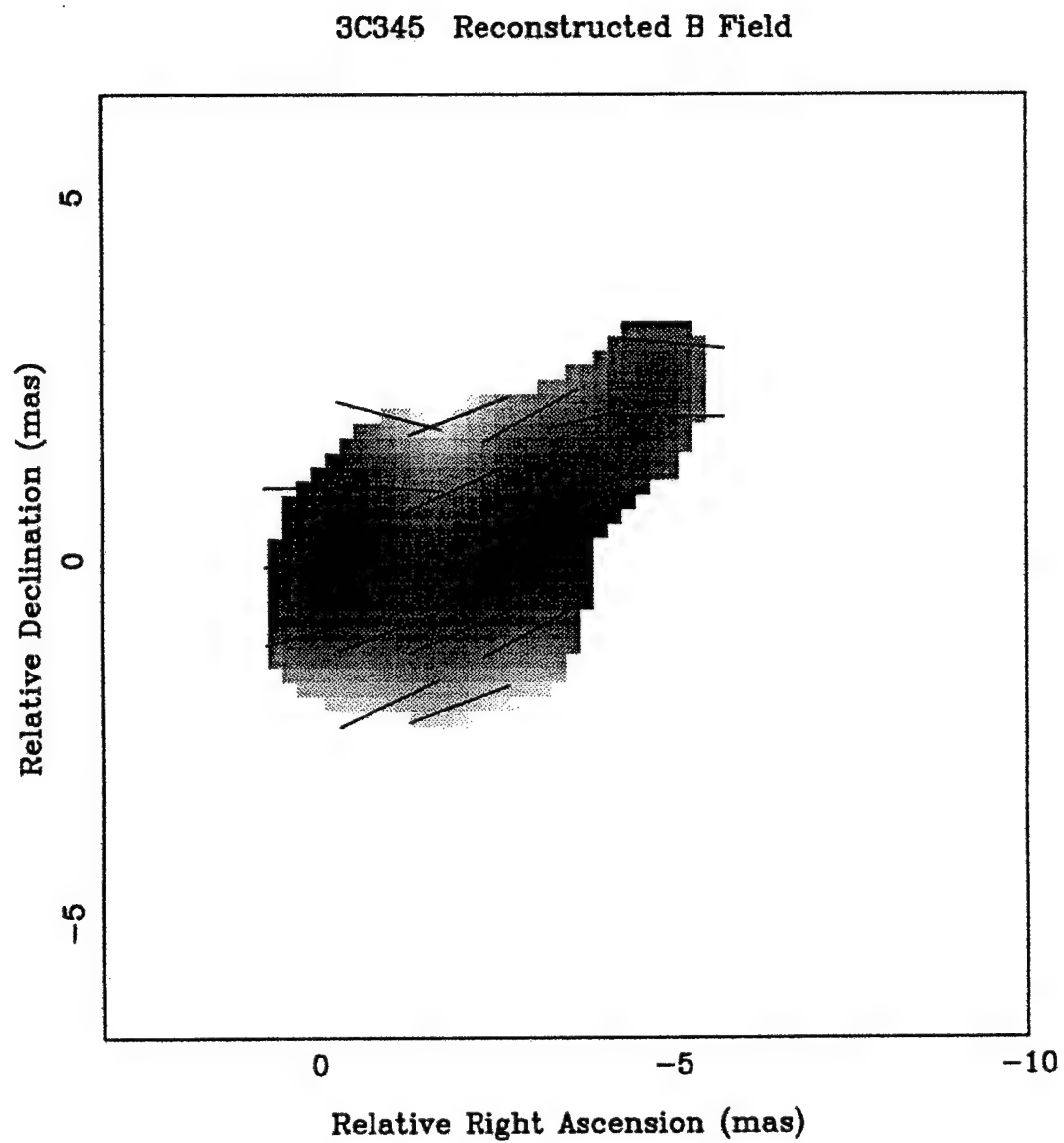


Figure 63: Map of the Reconstructed Magnetic Field in 3C 345, Epoch 1992.2, made from figure 56 corrected for Faraday Rotation using figure 59 and converting to magnetic field from electric field vectors.

# 3C345 Reconstructed B Field

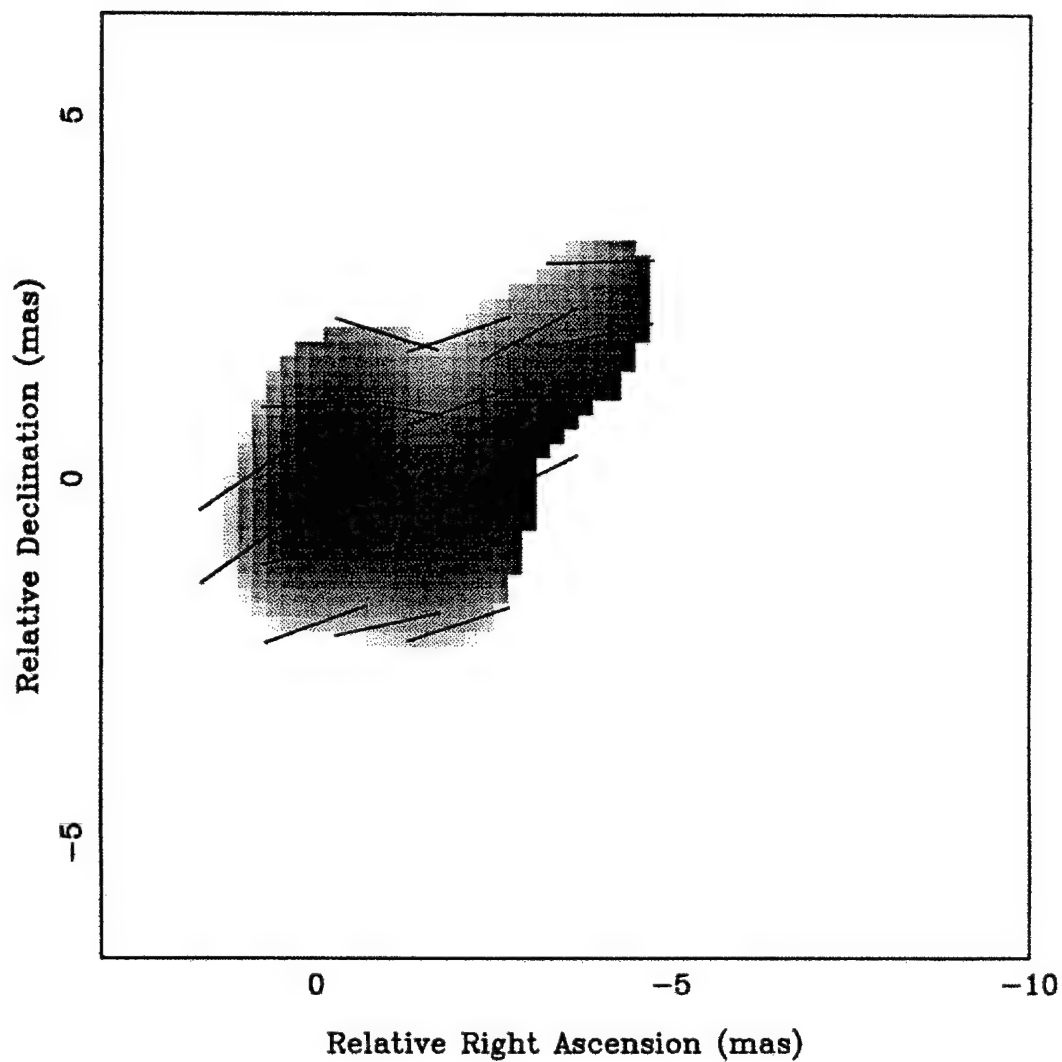


Figure 64: Map of the Reconstructed Magnetic Field in 3C 345, Epoch 1992.2, made from figure 56 corrected for Faraday Rotation using figure 60 and converting to magnetic field from electric field vectors.



### VIII. Results for 3C 273

In this chapter, the results from two epochs of dual frequency polarization VLBI observations of 3C 273 are presented. As with 3C 345, the epoch 1990.4 results are used primarily to support results from epoch 1992.2. The poor quality of the epoch 1990.4 observations are particularly damaging to 3C 273, since data sets are naturally smaller for this low declination source than for the high declination 3C 345.

Since 3C 273 lies close to the celestial equator, it is rarely visible to all the antennas in the VLBI array. As noted in chapter 7, the number of visibilities scales with the square of the number of antennas observing the source at one time, so that data sets for 3C 273 tend to be smaller than for other sources. Furthermore, the low declination results in large north-south beam sizes, so that there is very poor resolution along that axis of the beam. Luckily, as noted in chapter 5, 3C 273 is known to have an extremely straight jet which runs from east to west (at roughly  $40^\circ$  to the horizontal), so that the key resolution is the east-west resolution. Because the maps are roughly one dimensional, strip plots of intensity, polarized flux, electric field vector position angle, and percentage polarization provide a nicer summary of the jet properties than do component tables. In this chapter, strip plots replace the component tables used for 3C 345.

As with 3C 345 in chapter 7, the images presented here were produced by hybrid mapping, including phase self-calibration and deconvolution using CLEAN. In all cases, one global amplitude self-calibration was done. Polarization maps show polarized flux together with tick marks indicating electric field vector position angles. The arcsecond scale Faraday rotation effects are removed in all polarization maps, leaving the residual rotation to be measured in the Faraday rotation maps. All maps have roughly logarithmic contour levels. As with 3C 345, the epoch 1990.4 complex polarization maps were not heavily processed, as the data set did not justify it.

#### *A. Epoch 1990.4*

##### *1. Maps and Reduced Data*

Calibration and editing of the data for 3C 273 at 6 cm resulted in final maps being made from 768 parallel hand (I) visibilities and 487 cross hand (P) visibilities. The map was made by restricting self-calibration to use only clean components along the jet axis, west of the core. This resulted in a better fit to the data. The use of CLEAN boxes, which restrict the placement of CLEAN components during deconvolution, was not necessary. Nineteen iterations of hybrid mapping were required to obtain convergence.

Figure 65 shows the total intensity 6 cm map, which shows the standard core-jet morphology with a bright core at relative position 0, 0 mas east (E) and north (N), and a jet extending at a position angle of about -130 degrees for roughly 20 mas. The clean beam is pictured in the upper right on most maps of 3C 273. The poor north-south resolution resulting from the low declination of 3C 273 gives the components the large north-south spread. As noted in chapter 5, the jet is extremely straight after the first milliarcsecond, so that there are no worries about hidden components across the width of the jet.

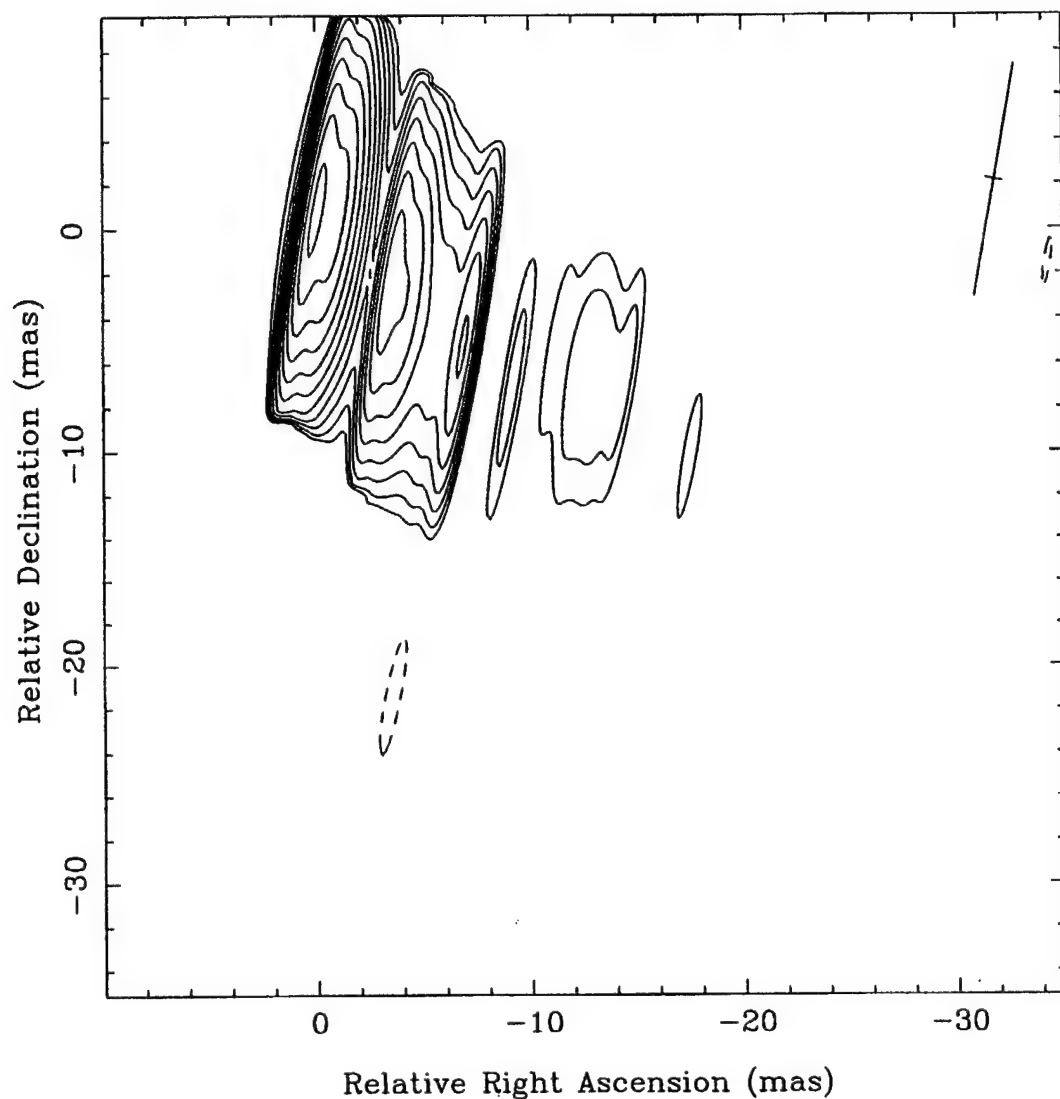


Figure 65: Total Intensity Map of 3C 273 at 6 cm, Epoch 1990.4, made with natural weighting of the visibilities. Contours are at -2.8, 2.8, 4, 5.6, 7.9, 11.2, 15.8, 22.4, 31.7, 44.8, 63.4, and 89.6% of the peak flux of 5420 mJy/beam. The beam is 10.6 by 0.8 milliarcseconds at a position angle of  $-10.3^\circ$ .

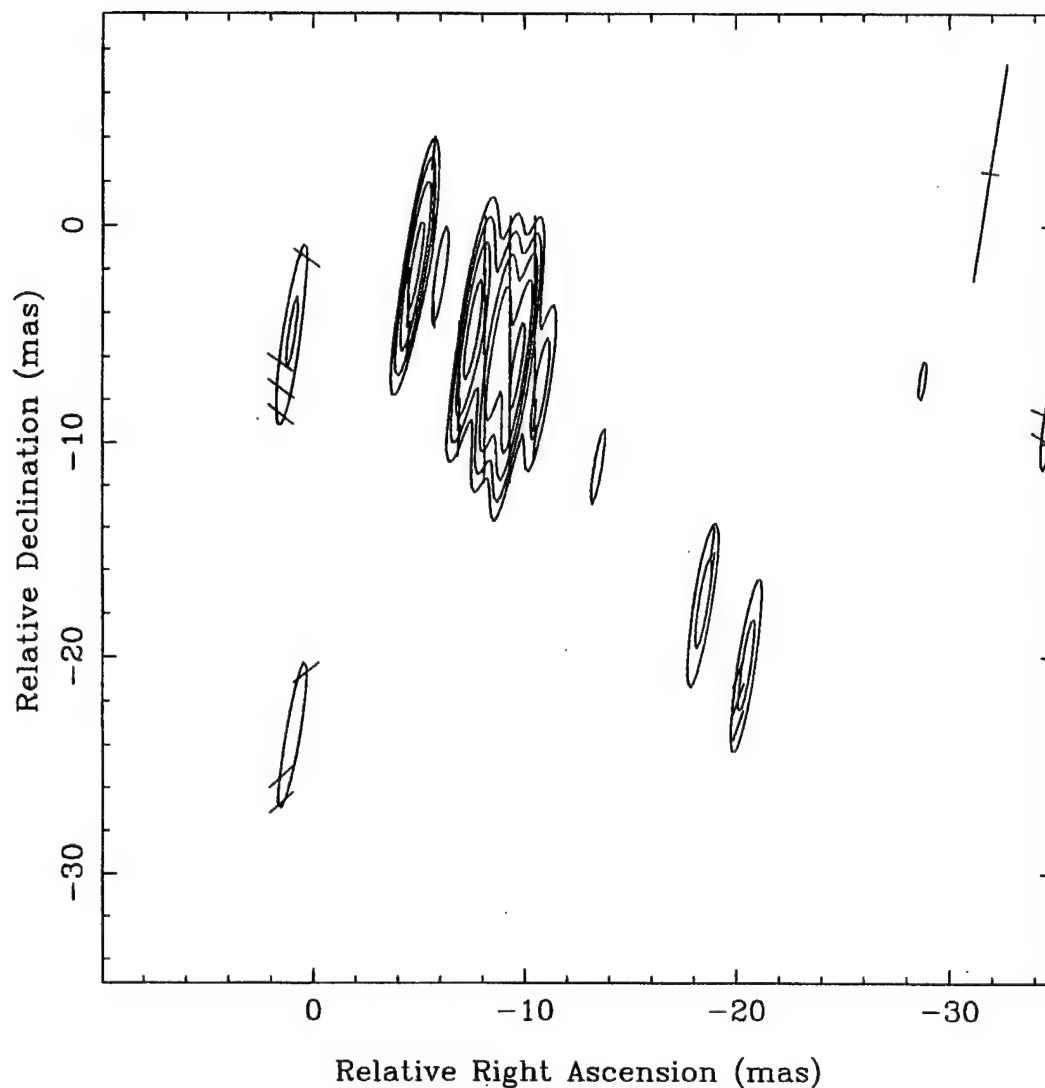


Figure 66: Complex Polarization Map of 3C 273 at 6 cm, Epoch 1990.4, made with natural weighting of the visibilities. Contours are at 22, 31.1, 44, 62.2, and 88% of the peak flux of 170 mJy/beam. The beam is 10.0 by 0.8 milliarcseconds at a position angle of  $-9.3^\circ$ .

Figure 66 shows the 6 cm complex polarization map which has substantial structure. The strongest clearly false feature is at 22% of the peak 170 mJy/beam, however the feature south of the core (~31% of peak) at roughly 1,-5 mas E and N is certainly questionable. The core is not observed in polarized flux, while the jet is highly polarized (up to 50%), with the peak fractional polarization occurring at the point of lowest total intensity in the jet (roughly 11 mas along the jet).

At 3.6 cm, the limited number of observations by dual polarization antennas, together with the large number of antenna failures resulted in very few visibilities for 3C 273. There were 343 I visibilities and only 167 P visibilities after calibration and editing. Convergence of the map was obtained after 25 iterations of hybrid mapping, but only by using increasingly tight CLEAN boxes around the jet.

Figure 66 gives the 3.6 cm total intensity map, which shows the expected core-jet morphology, although one feature in the jet, the component at about 11 - 12 mas, is much brighter than expected at this frequency. This feature may not be representative of the actual source, but may be a result of problems with self-calibration in the data set as noted in chapter 8. The overall features do align with those at 6 cm reasonably well, so that their rough positions are probably correct. The largest negative contour of -2.8% is shown.

Figure 68 shows the corresponding complex polarization map. It is unclear if the core polarization is recovered, since neither feature near the core aligns with the total intensity, although both appear stronger than the clearly false features outside the jet at 26% of the peak 172 mJy/beam. The feature south of the core does however align with the one seen south of the core at 6 cm. The two features in the jet do align with features in the 6 cm image, although they have different position angles for the electric field vectors. Figure 69 is the same image smoothed with a restoring beam which matches

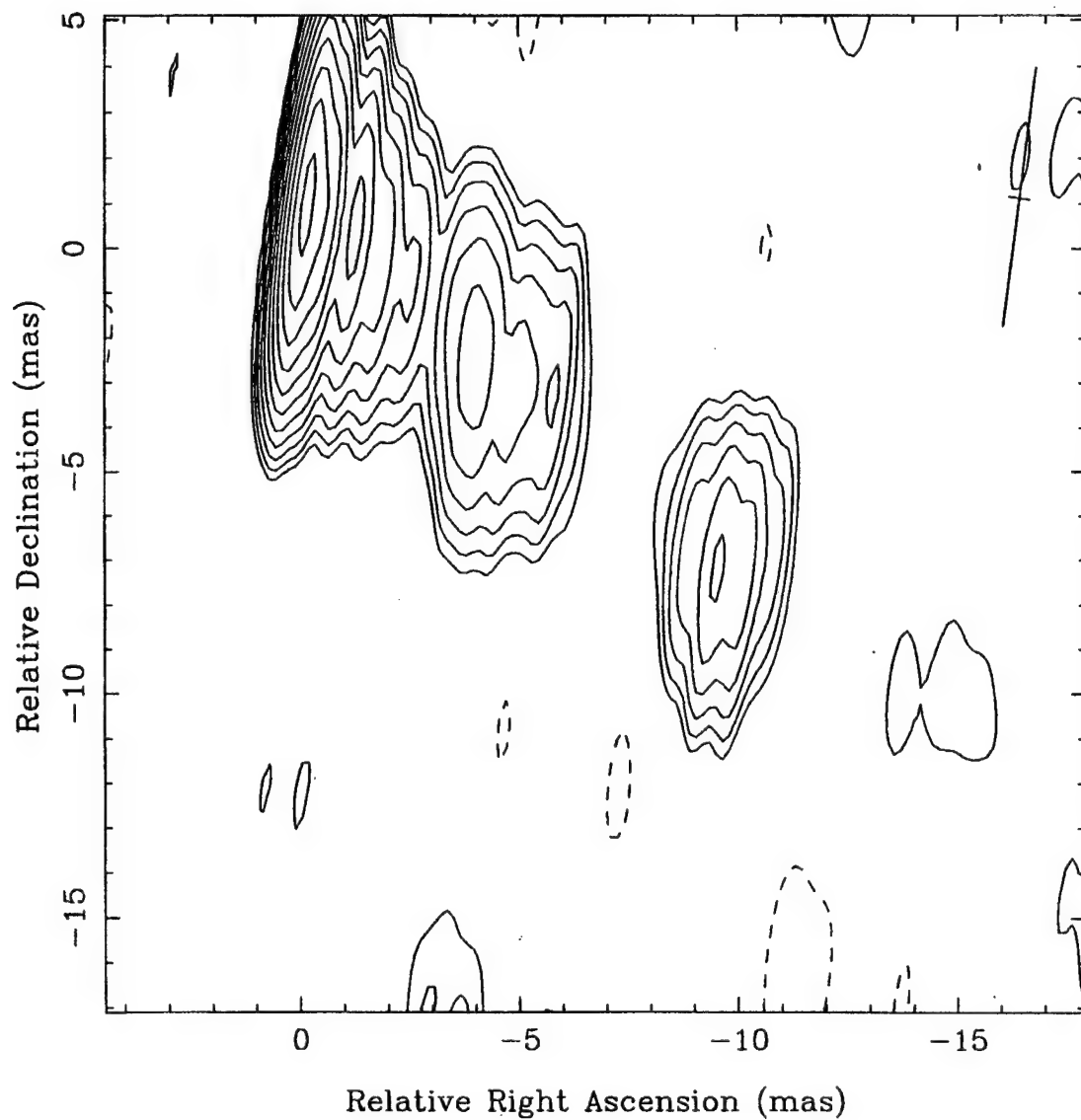


Figure 67: Total Intensity Map of 3C 273 at 3.6 cm, Epoch 1990.4, made with natural weighting of the visibilities. Contours are at -2.8, 2.8, 4, 5.6, 7.9, 11.2, 15.8, 22.4, 31.7, 44.8, 63.4, and 89.6% of the peak flux of 5230 mJy/beam. The beam is 5.8 by 0.5 milliarcseconds at a position angle of  $-7.7^\circ$ .

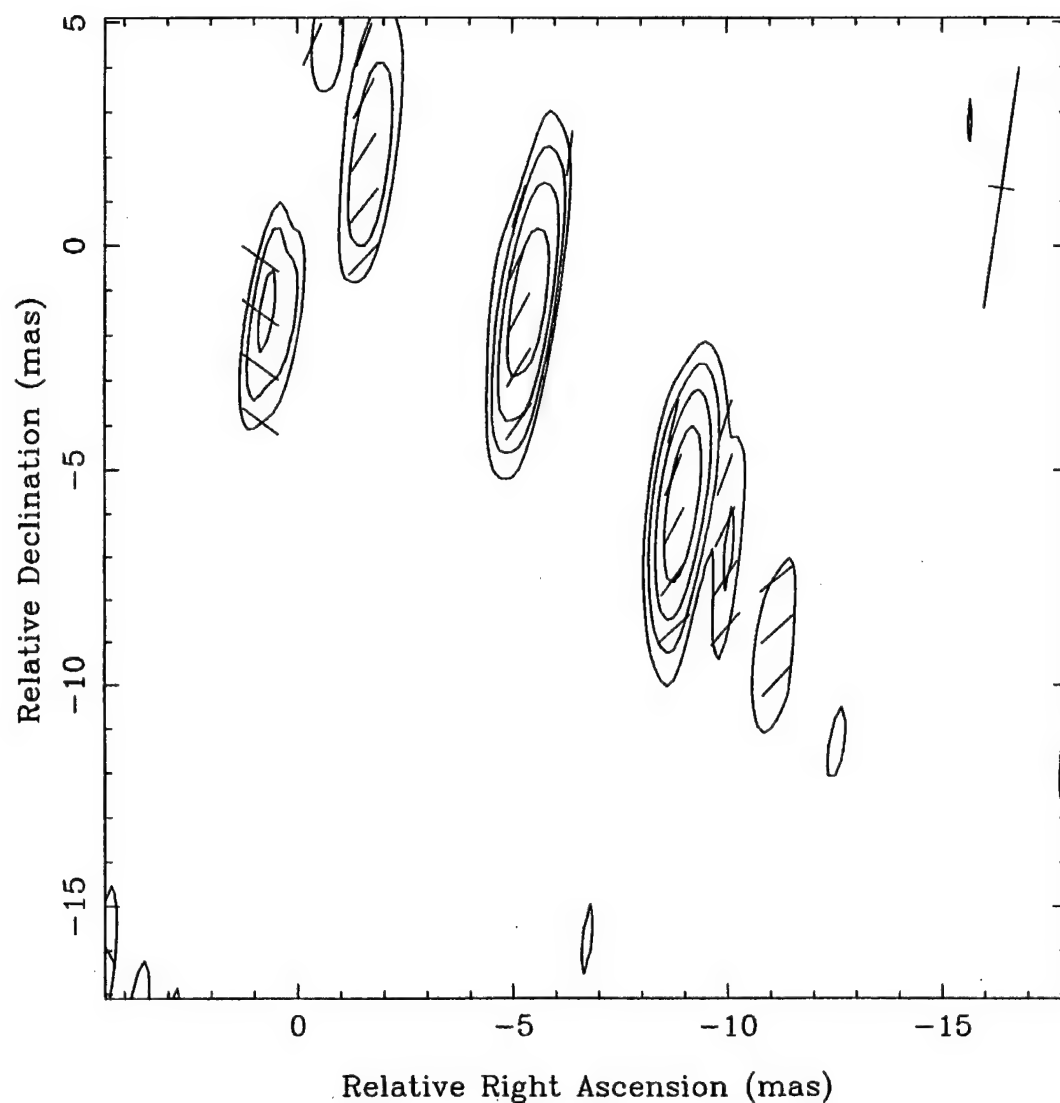


Figure 68: Complex Polarization Map of 3C 273 at 3.6 cm, Epoch 1990.4, made with natural weighting of the visibilities. Contours are at 26, 36.8, 52, and 73.5% of the peak flux of 172 mJy/beam. The beam is 5.4 by 0.6 milliarcseconds at a position angle of  $-12.2^\circ$ .

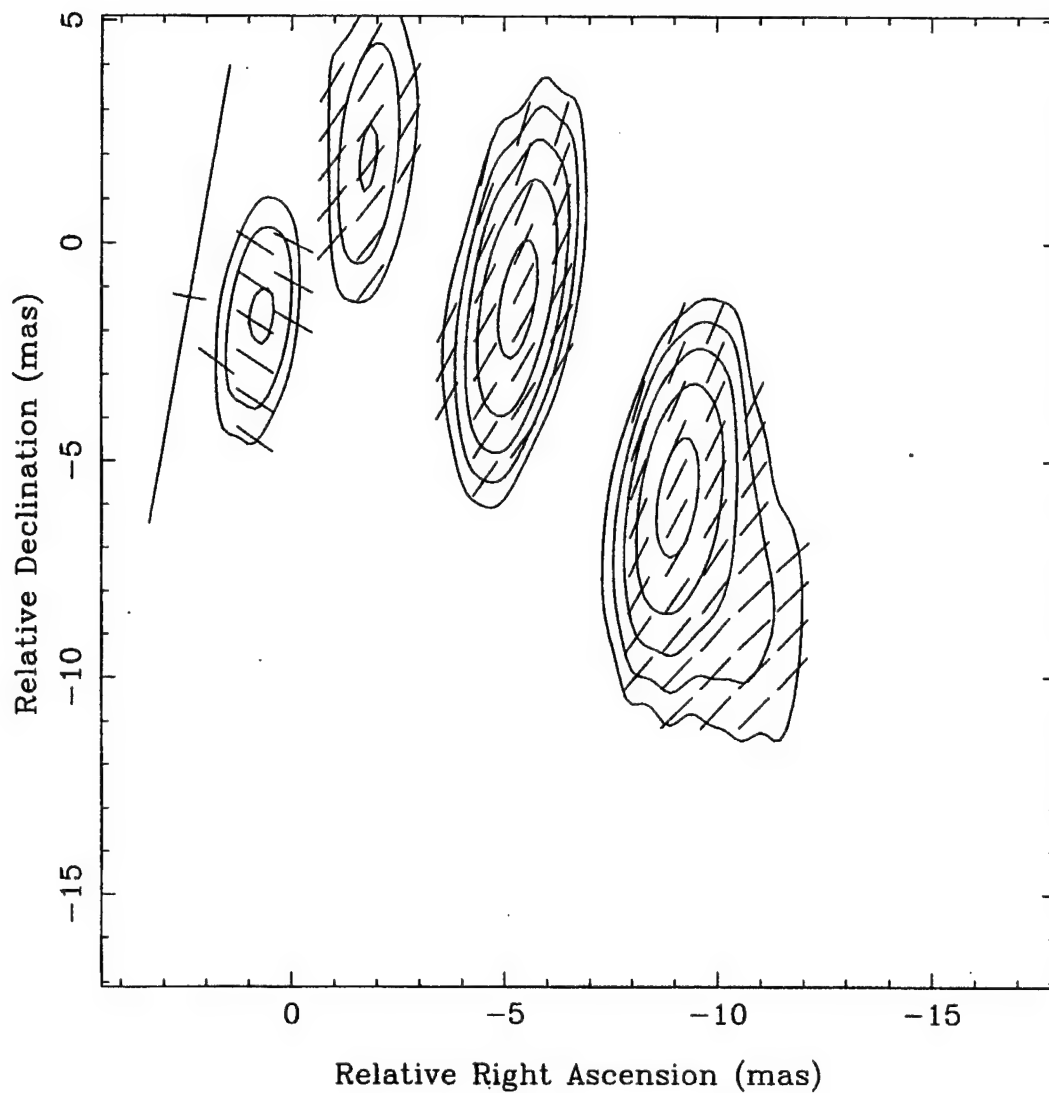


Figure 69: Complex Polarization Map of 3C 273 at 3.6 cm, Epoch 1990.4, made with natural weighting of the visibilities and smoothed with an optional restoring beam. Contours are at 22, 31.1, 44, 62.2, and 88% of the peak flux of 281 mJy/beam. The beam is 10.0 by 0.8 milliarcseconds at a position angle of  $-9.3^\circ$ .



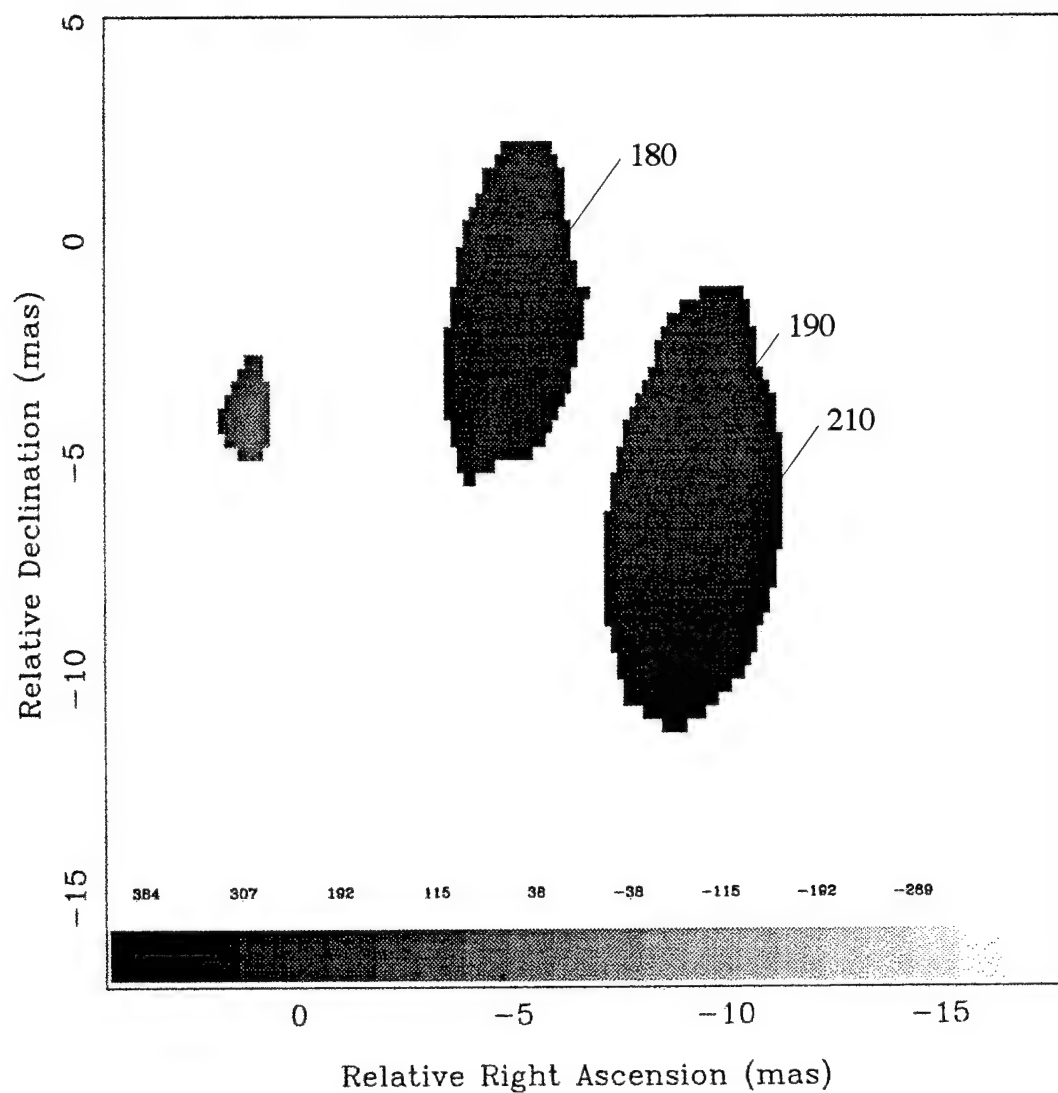


Figure 70: Faraday Rotation Measure Map of 3C 273, Epoch 1990.4, made from figures 66 and 69 with alignment of the 3.6 cm and 6 cm maps at the brightest total intensity peaks in each map. All values are in  $\text{rad/m}^2$ .

the one used at 6 cm, in order to facilitate the mapping of Faraday rotation measures. The increase in the peak flux to 281 mJy/beam reflects the fact that the beam now encompasses larger portions of the jet.

From the polarized images shown in figures 66 and 69, a Faraday rotation map can be made using the assumption, discussed in chapter 4, that the rotation measure is the smallest possible to explain the measurements. The rotation measure map is shown in figure 70. Alignment was done by aligning the core at 3.6 and 6 cm. Since intrinsically different resolutions are used to make the maps, edge effects should not be taken as real, and values are indicated for points well removed from the edges only. The slight gradient in rotation measure, which is apparent along the jet, is probably within the uncertainty in position angle for this observation, because of the poor calibration in the 3.6 cm map. The gradient arises solely from the variation in the 3.6 cm position angle along the jet, and calibration errors can feed back in the complex CLEAN needed to make a polarized image as movements in location or position angle, or in coordinated changes in both.

## 2. Analysis

The overall structure shown in the epoch 1990.4 maps for 3C 273 appears correct. The standard core-jet morphology is present and the position angle of the jet agrees with previous observations. At 6 cm the components grow less bright as they move away from the core, as expected. However, at 3.6 cm there is a brightening in the jet, most noticeably at roughly 11 milliarcseconds. This is likely to be the result of a calibration error, since the jet appears so bright that the spectrum would be inverted between 3.6 and 6 cm at that point. Since the conversion of a jet component from optically thin to optically thick has never been observed in 3C 273, this seems unlikely.

The complex polarization map at 6 cm shows many components. Its structure is similar in this way to earlier maps (Roberts *et al.*, 1990), although there is no rapid

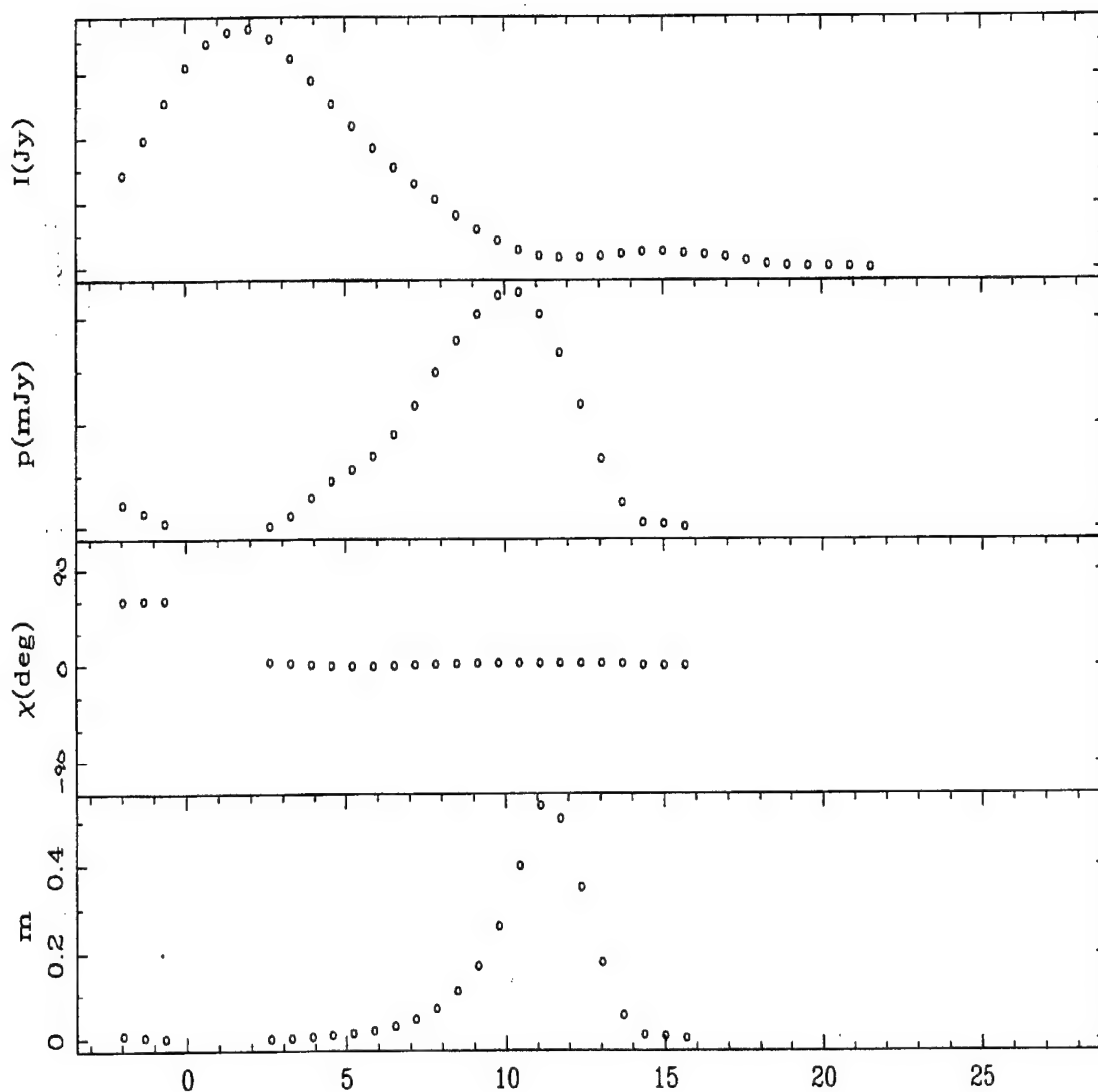


Figure 71: Strip plot of 3C 273 at 6 cm, Epoch 1990.4, made from figures 65 and 66, measured along the jet axis at a position angle of  $-140^\circ$ . The top box gives total intensity in arbitrary units, the second box gives linearly polarized intensity in arbitrary units, the third box gives the polarization position angle on the sky, and the fourth box gives the percentage polarization.

swing in position angle as seen earlier. The 3.6 cm complex polarization map has clear problems around the core, however the jet components do align with some of those seen at 6 cm.

Since 3C 273 appears quite straight at these resolutions and since the north-south resolution is so poor, it is convenient to sum the observed flux along the major axis of the clean beam. After this summing, the total intensity, polarized flux, position angle of the electric field vector, and the fractional polarization as a function of position along the jet can be plotted. Figure 71 gives the results for these observations at 6 cm, using normalized I and P fluxes (*i.e.* fraction of peak) and a linear scale. Note that the position angle is quite constant along the jet, and, as noted above, the fractional polarization peaks near the minimum in the total intensity. The feature seen to the east of the core in these plots is the polarized component which is south of the core in the maps, and which is probably not real.

Figure 72 gives the strip plots of the total intensity, polarized flux, electric field position angle, and fractional polarization along the jet at 3.6 cm. The double bump of polarized flux around the core total intensity flux comes from the components south and north of the core respectively, which are not reliable. Comparison with figure 71 reveals that the fractional polarization behaves very similarly to that at 6 cm, although it appears to peak somewhat lower and at an earlier point in the jet. This is primarily due to the strong total intensity outer component, which as noted earlier is probably overestimated.

Using the rotation measure map and a polarized image, a map of the magnetic field in the jet can be made by adjusting the electric field vector for Faraday rotation and adding  $90^\circ$ . This adjusts for rotation of the electric field vector and converts the recovered inherent electric field direction to the magnetic field direction by assuming

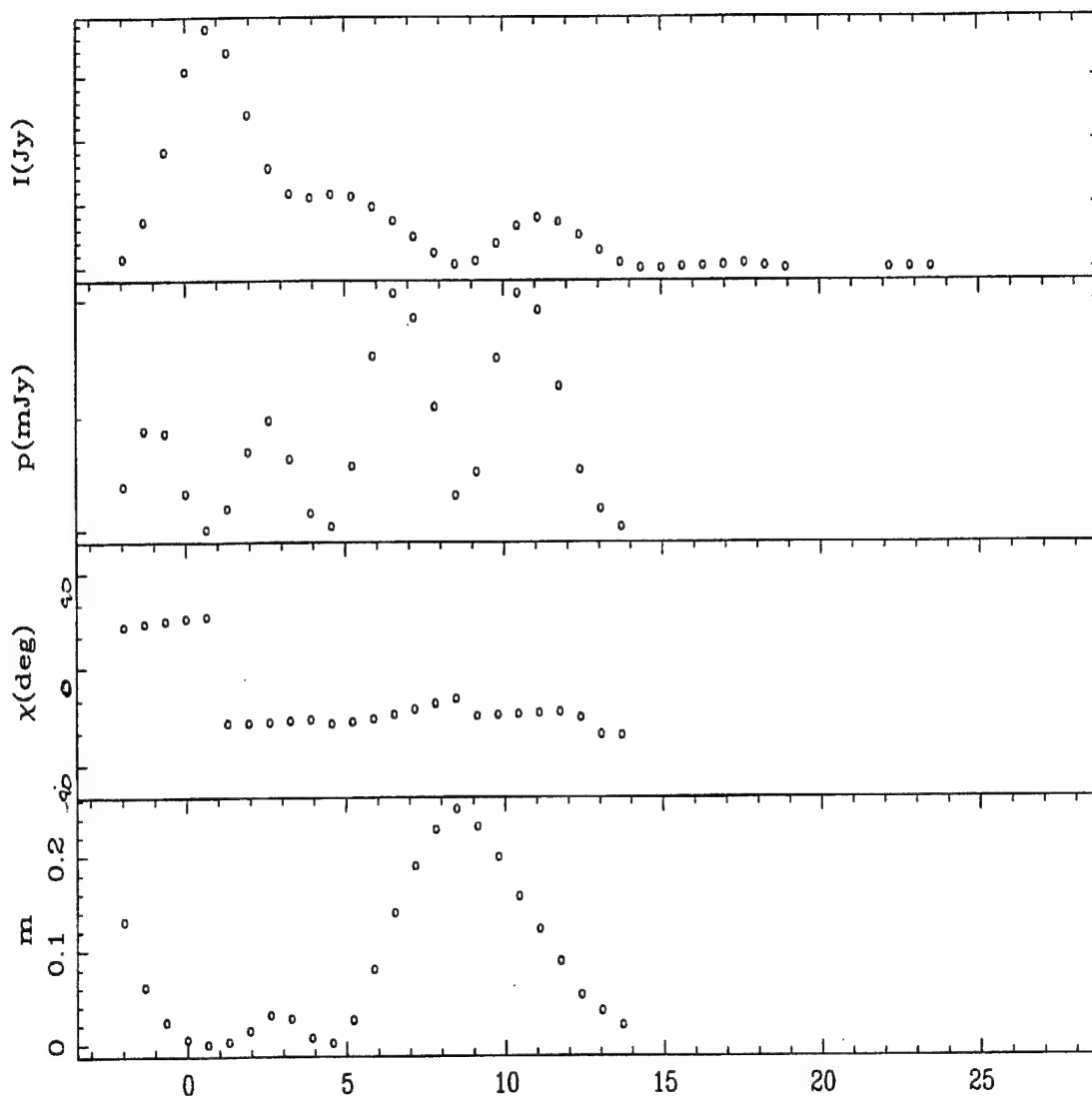


Figure 72: Strip plot of 3C 273 at 3.6 cm, Epoch 1990.4, made from figures 67 and 68, measured along the jet axis at a position angle of  $-140^\circ$ . The top box gives total intensity in arbitrary units, the second box gives linearly polarized intensity in arbitrary units, the third box gives the polarization position angle on the sky, and the fourth box gives the percentage polarization.

## Reconstructed B Field

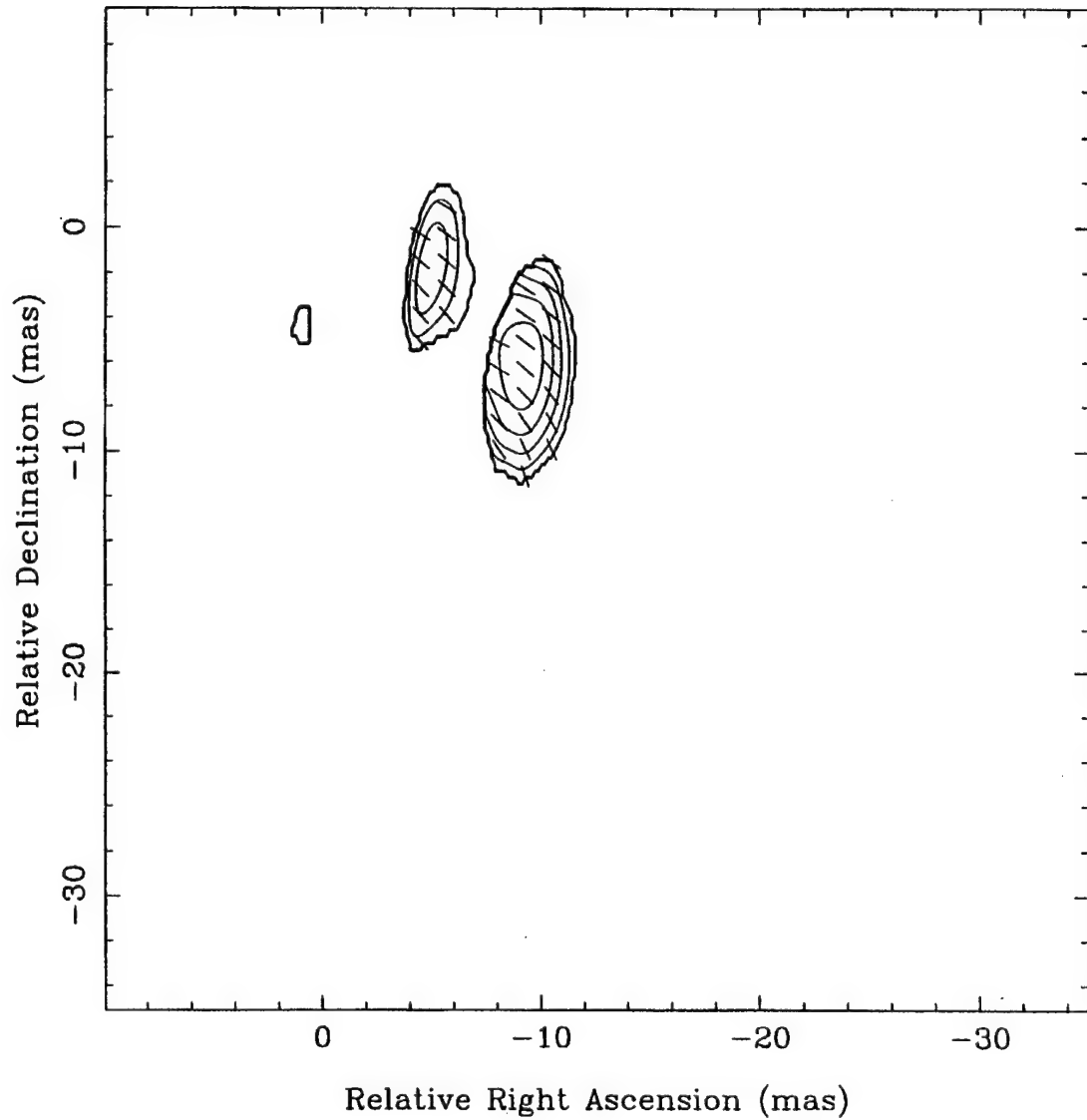


Figure 73: Map of the Reconstructed Magnetic Field in 3C 273, Epoch 1990.4, made from figure 69 corrected for Faraday Rotation using figure 70 and converting to magnetic field from electric field vectors.

synchrotron emission, where the emitted electric field is perpendicular to the magnetic field. The recovered magnetic field is shown in figure 72. It is strongly aligned with the jet axis determined from the total intensity image.

## *B. Epoch 1992.2*

### *1. Maps and Reduced Data*

The March, 1992, 6 cm observations were a vast improvement over the earlier 1990 observations. Calibration and editing of the 12 antenna data set left 2373 I visibilities and 1306 P visibilities. Mapping was done with minimal self-calibration restrictions, where self-calibration was not done using clean components east of the core. No CLEAN boxes were necessary. Only 13 iterations of hybrid mapping were needed to obtain convergence.

Figure 74 shows the 6 cm total intensity map made with natural weighting of the visibilities. The largest negative contour of -1.4% is shown as a broken line. The core-jet morphology is clear, with the bright core and a jet extending at a position angle of  $-130^\circ$  for roughly 25 mas. There is a minimum in the jet, as in the 1990.4 observations, which occurs between two sets of steep contours at roughly 11 milliarcseconds along the jet.

Figure 75 shows the corresponding complex polarization map, made with a weighting of  $(1 + r/50 \text{ M}\lambda)$  applied to the visibilities. This weighting was necessary to overcome the dominance of the western VLBA antennas in the cross hand visibilities, which gave extremely poor resolution using natural weighting. The first false features are at roughly 25% of the peak 201 mJy/beam. The position angle beyond roughly 11 mas along the jet (at the break seen in total intensity) agrees with that seen in the epoch 1990.4 observations. Up to that point, however, it shows some strong swings as in previous observations (see above).

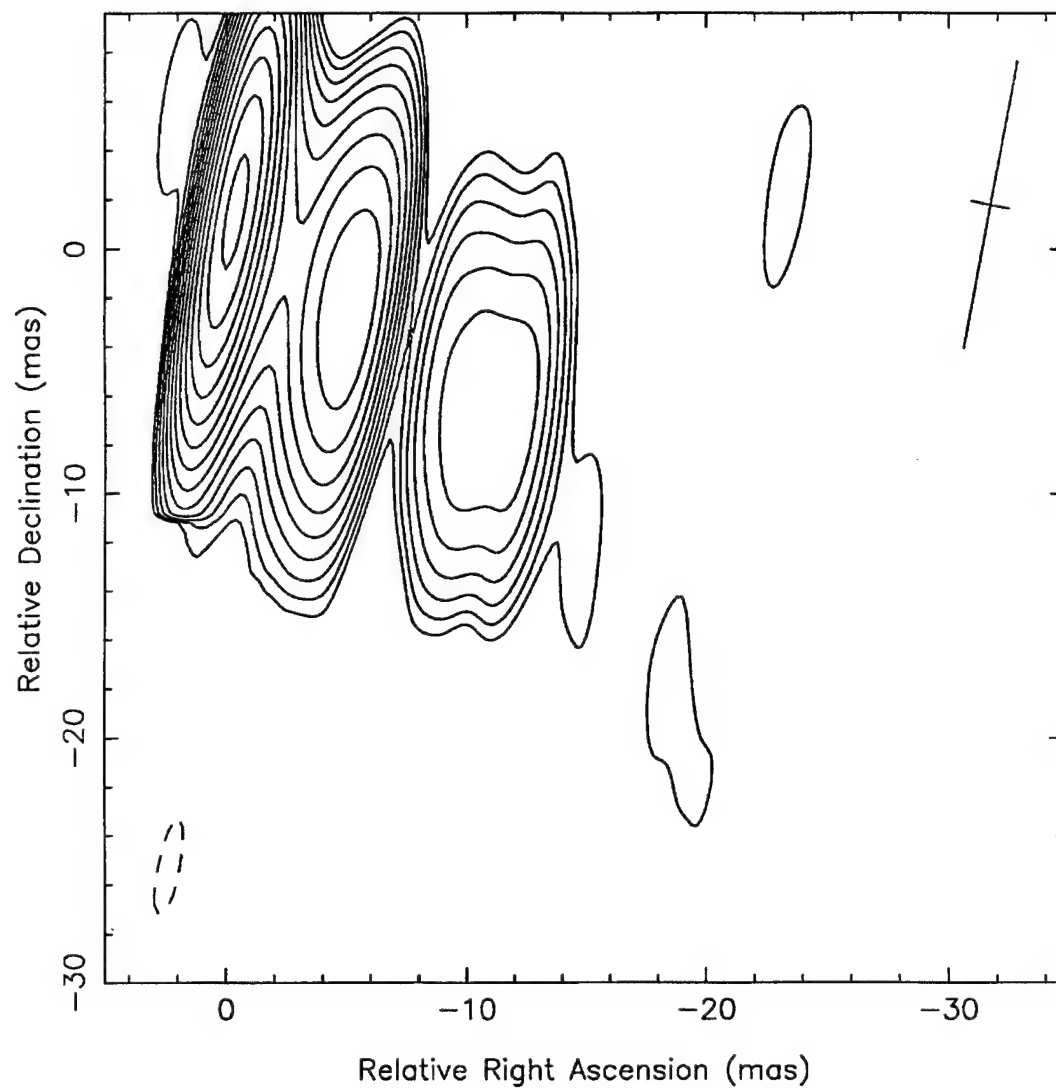


Figure 74: Total Intensity Map of 3C 273 at 6 cm, Epoch 1992.2, made with natural weighting of the visibilities. Contours are at -1.4, 1.4, 2, 2.8, 4, 5.6, 7.9, 11.2, 15.8, 22.4, 31.7, 44.8, 63.4, and 89.6% of the peak flux of 13,800 mJy/beam. The beam is 11.87 by 1.56 milliarcseconds at a position angle of  $-10.7^\circ$ .



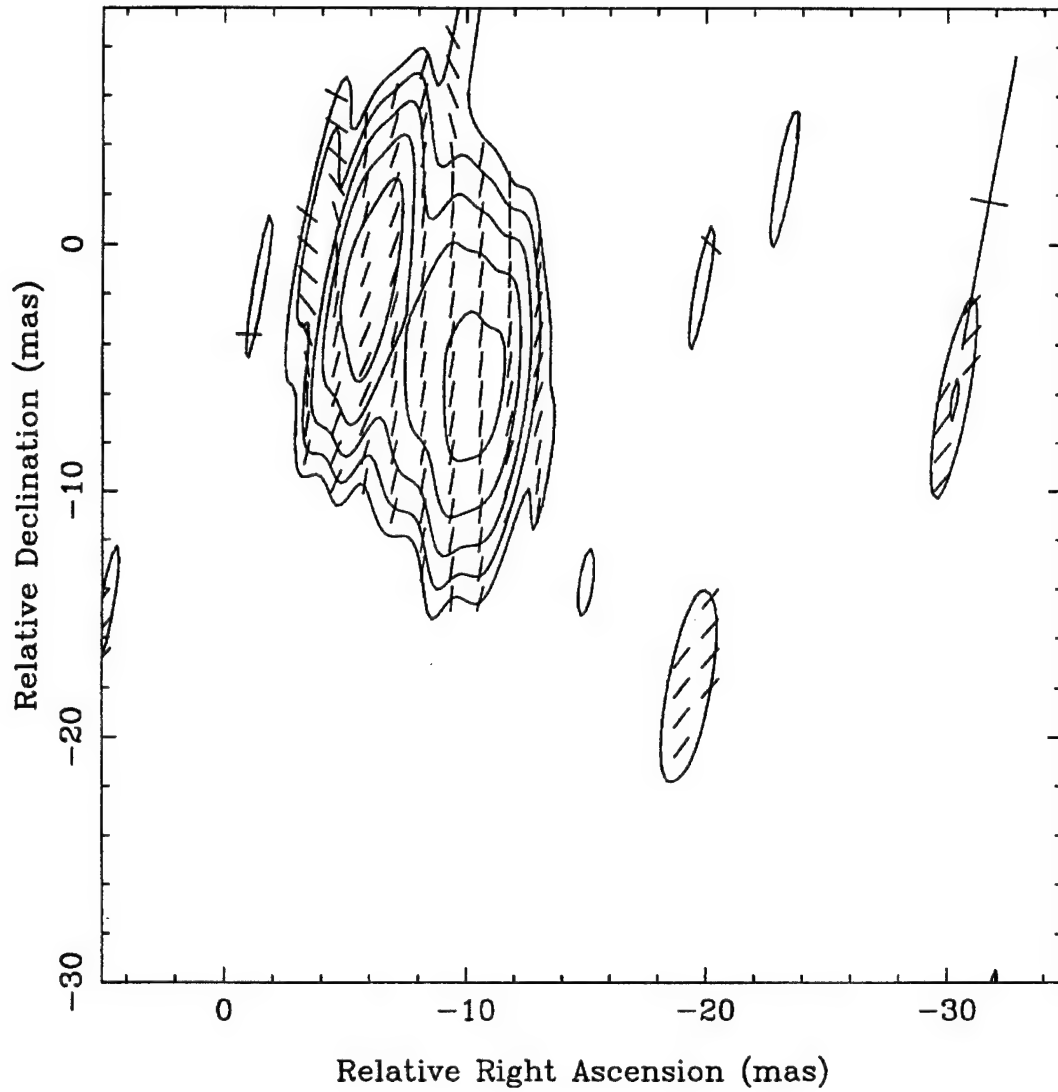


Figure 75: Complex Polarization Map of 3C 273 at 6 cm, Epoch 1992.2, made with  $(1 + r/50 M\lambda)$  weighting of the visibilities. Contours are at 18, 25.5, 36, 50.9, and 72% of the peak flux of 201 mJy/beam. The beam is 11.98 by 1.52 milliarcseconds at a position angle of  $-10.7^\circ$ .

At 3.6 cm there is good improvement over the 1990.4 observations, although the P visibilities are still limited by the lack of dual polarization stations in Europe and the eastern United States. After calibration and editing, there were 1114 I visibilities and 419 P visibilities. The low number of I visibilities, as compared with the 6 cm data, is due to the failure of a large number of RR correlations during processing at the Mark IIIA correlator at the Haystack observatory. Attempts to recover these data were not successful, and it is not clear why this occurred. Mapping required significant self-calibration restrictions, limiting CCs entering self-calibration to the jet area and removing all baselines below  $10 \text{ M}\lambda$  in the first few iterations. Later in the mapping process clean boxes were added restricting the components to lie within a few milliarcseconds of the jet axis. Convergence of the map was obtained in 25 iterations of hybrid mapping.

The 3.6 cm total intensity map made with natural weighting of the visibilities is shown in figure 76. The core-jet morphology is clear, however the jet is only followed in total intensity out to roughly  $10 \text{ mas}$ , because of the extremely bright core, limited dynamic range, and the steep spectrum in outer jet components. The jet does align well with the inner components of the 6 cm jet. The first negative contour is at the  $-1.4\%$  level.

Figure 77 shows the corresponding complex polarization image with visibilities weighted by  $(1 + r/80 \text{ M}\lambda)^{0.75}$ . As with the 6 cm map, this weighting was used to overcome the dominance of the VLBA antennas in the cross hand data. The core is not recovered in polarized flux, although there is a strong false feature (67% of peak) east of the core. Although the electric field vector position angles are quite different from those in the 6 cm map, they have similar behavior. They are roughly constant in the

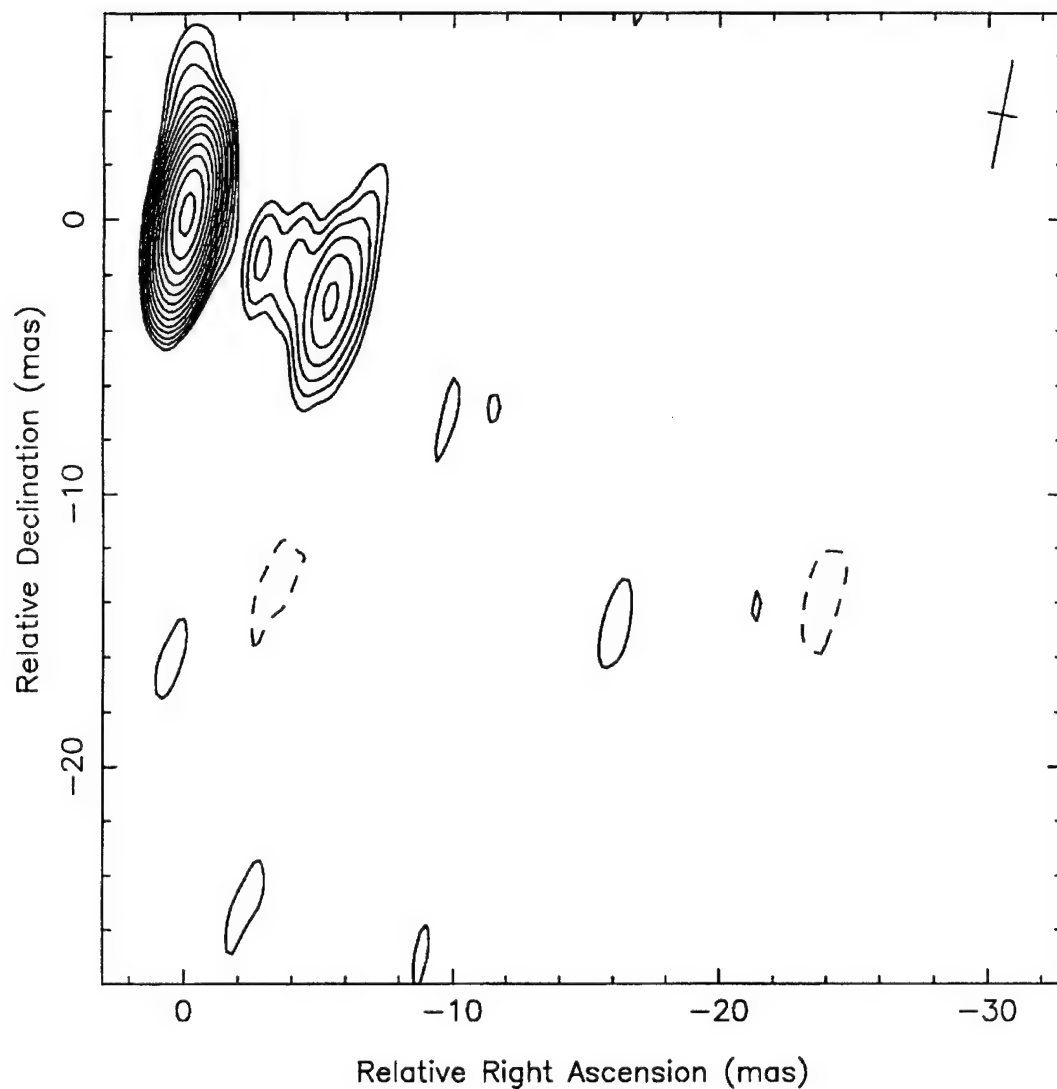


Figure 76: Total Intensity Map of 3C 273 at 3.6 cm, Epoch 1992.2, made with natural weighting of the visibilities. Contours are at -1.4, 1.4, 2, 2.8, 4, 5.6, 7.9, 11.2, 15.8, 22.4, 31.7, 44.8, 63.4, and 89.6% of the peak flux of 20,000 mJy/beam. The beam is 3.98 by 1.06 milliarcseconds at a position angle of  $-10.7^\circ$ .

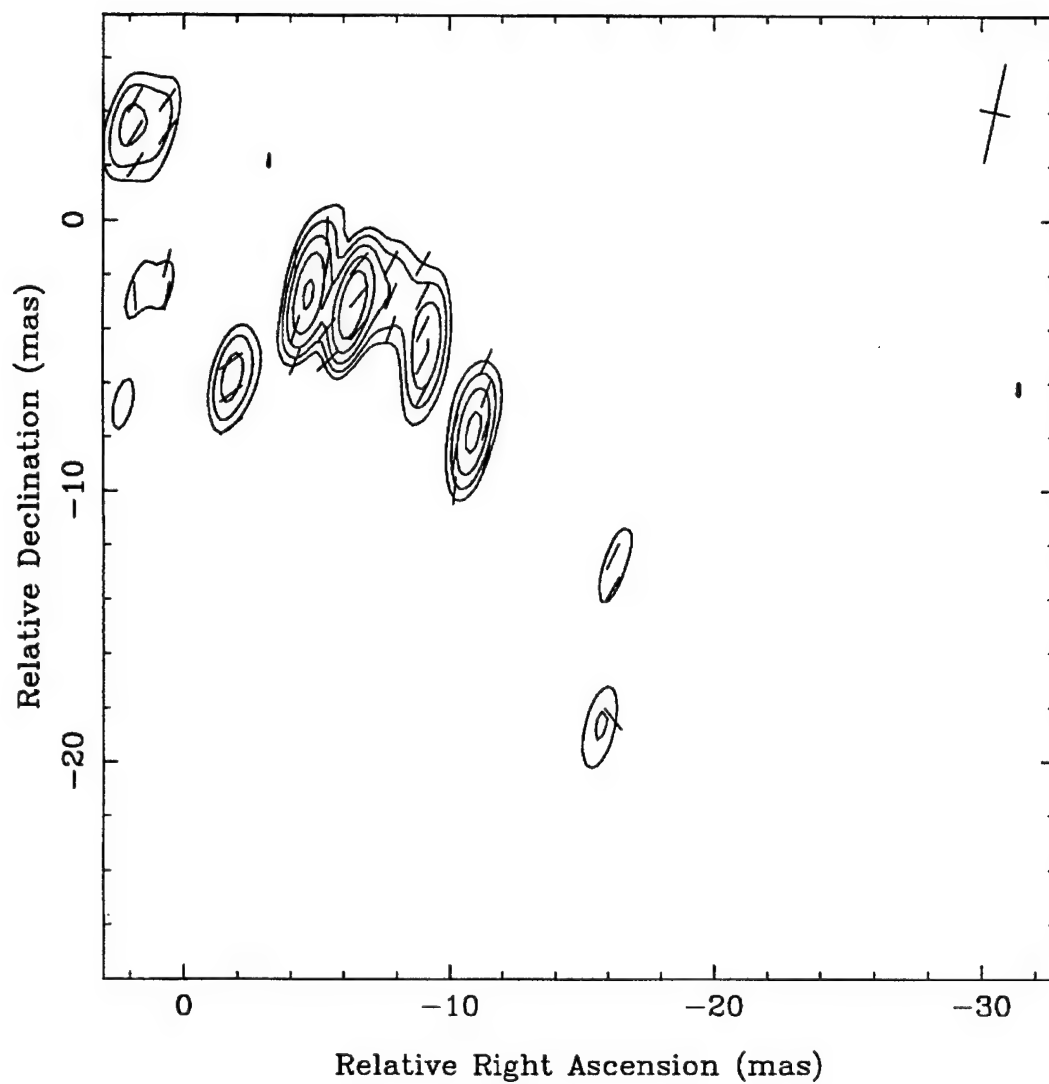


Figure 77: Complex Polarization Map of 3C 273 at 3.6 cm, Epoch 1992.2, made with  $(1 + r/80 \text{ M}\lambda)^{0.75}$  weighting of the visibilities. Contours are at 18, 25.5, 36, 50.9, and 72% of the peak flux of 201 mJy/beam. The beam is 3.72 by 1.09 milliarcseconds at a position angle of  $-12.2^\circ$ .

part of the jet greater than roughly 9 or 10 milliarcseconds from the core and show some rotation before that.

In order to make the Faraday rotation maps, the maps shown in figures 74 through 77 were smoothed with a common beam. As with 3C 345, the total intensity images have no new data in them and the residuals were not smoothed. The complex polarization maps have had their residuals smoothed to match the resolution of the restoring beam. In all maps, only the inner portion of the jet which has the polarization features common to both frequencies is shown. Figure 78 shows the 6 cm total intensity map. Figure 79 shows the 6 cm complex polarization map. The smoothing process has combined some of the features, however the rotation of the electric field vectors is still clear at the beginning of the mapped polarized flux out along the jet. Figure 80 shows the 3.6 cm total intensity map smoothed with the common beam. Figure 81 shows the 3.6 cm complex polarization map. As with the 6 cm map, the smoothing process has blurred some features, however the behavior seen in figure 77 is still evident.

In figure 82, the Faraday rotation map made from figures 79 and 81, aligning the maps on the cores (at 0 mas N, 0 mas E) of the total intensity maps, is shown. Ignoring edges, the map shows a gradient in rotation measure, starting around  $60 \text{ rad/m}^2$ , peaking at about  $150 \text{ rad/m}^2$ , and then dropping back to  $60 \text{ rad/m}^2$ . The peak occurs near the point in the total intensity images where the break occurs.

Figure 83 shows the Faraday rotation map made from figures 79 and 81, with the 6 cm map shifted two pixels (0.8 mas) north from the alignment used for figure 82. This was done because the 6 cm map shows its core shifted slightly to the north. The Faraday rotation map shows only minor changes with the gradient now running from  $50 \text{ rad/m}^2$ , peaking at  $160 \text{ rad/m}^2$ , and dropping back to  $60 \text{ rad/m}^2$ .

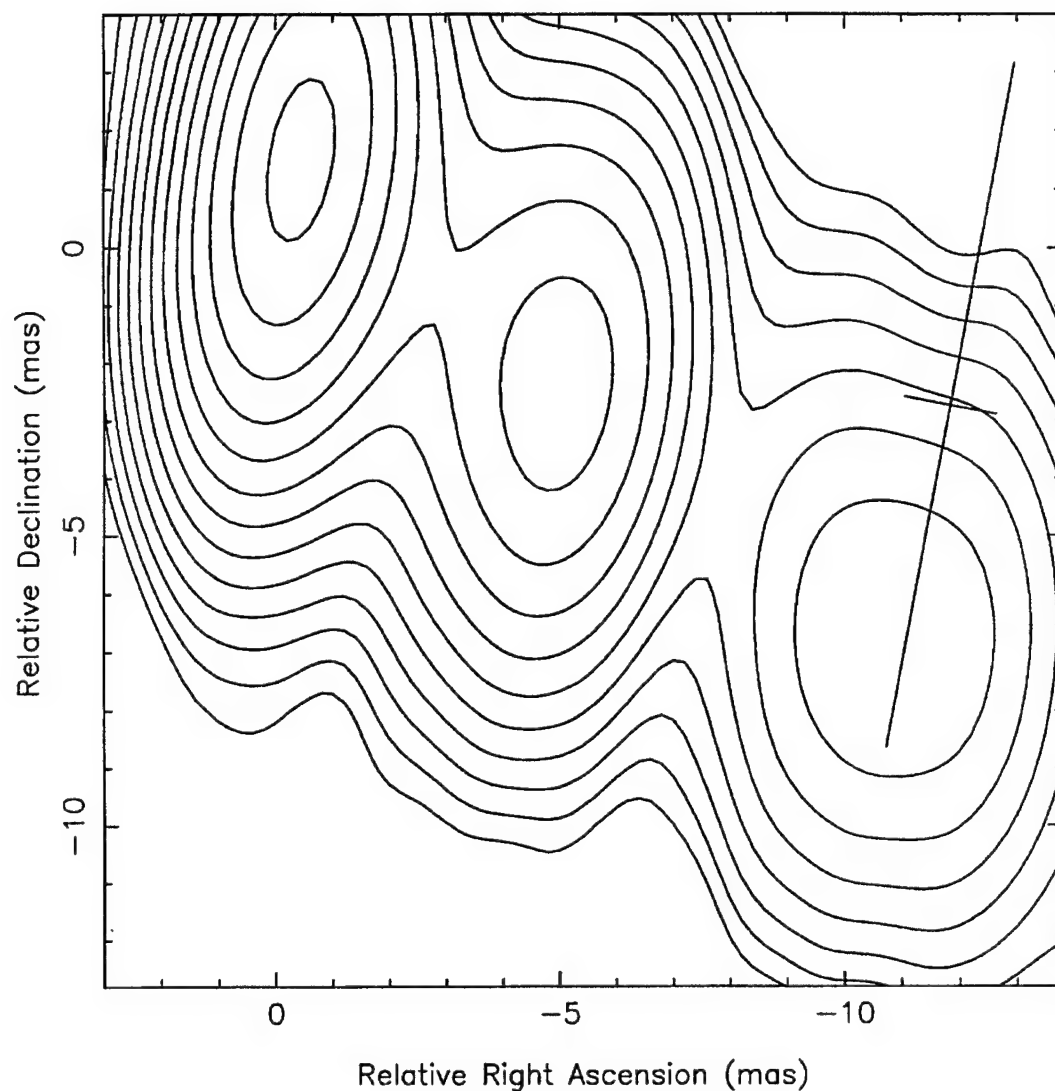


Figure 78: Total Intensity Map of 3C 273 at 6 cm, Epoch 1992.2, made with natural weighting of the visibilities and smoothed with an optional restoring beam. Contours are at -1.4, 1.4, 2, 2.8, 4, 5.6, 7.9, 11.2, 15.8, 22.4, 31.7, 44.8, 63.4, and 89.6% of the peak flux of 15,100 mJy/beam. The beam is 12.0 by 1.6 milliarcseconds at a position angle of  $-10.7^\circ$ .

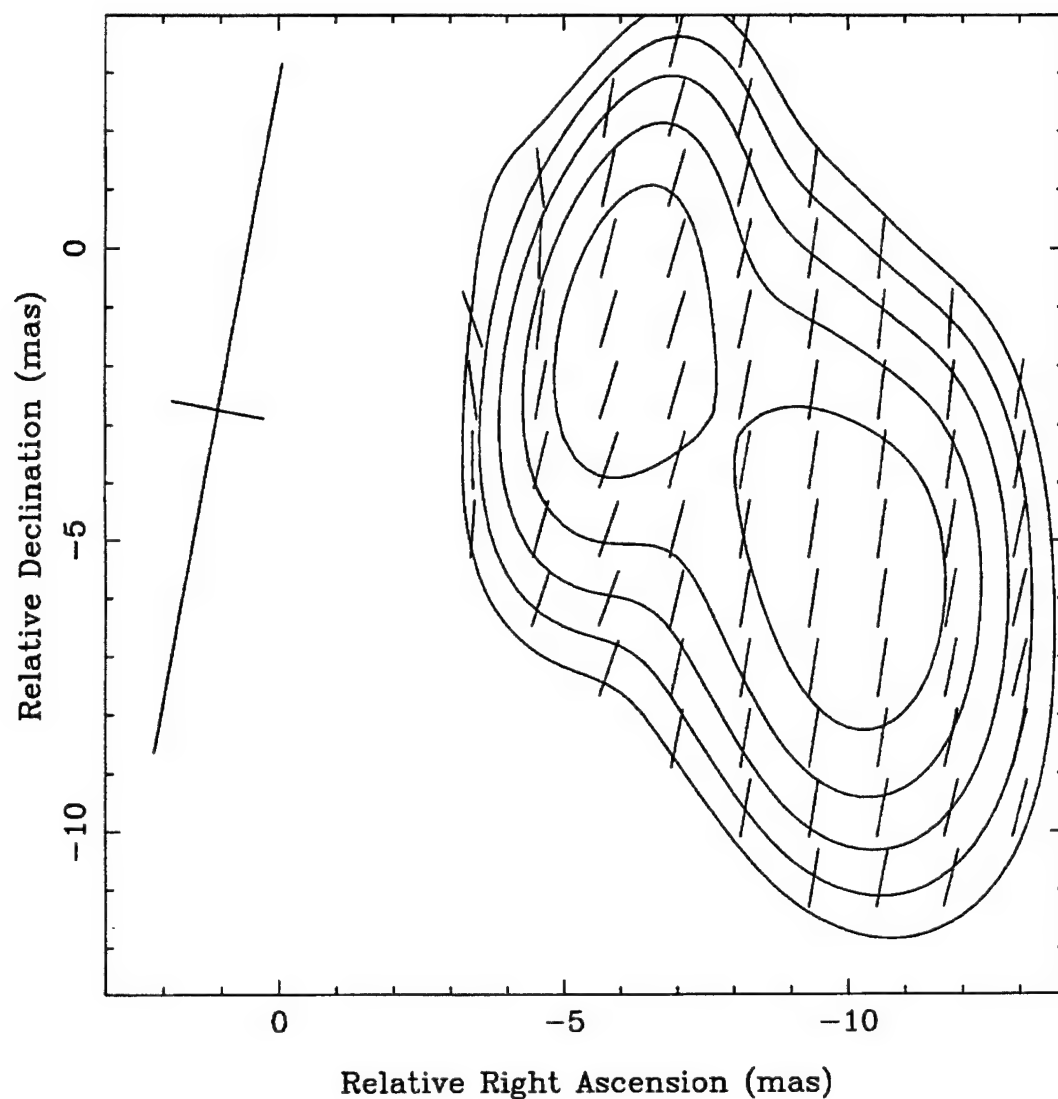


Figure 79: Complex Polarization Map of 3C 273 at 6 cm, Epoch 1992.2, made with  $(1 + r/50 M\lambda)$  weighting of the visibilities and smoothed with an optional restoring beam. Contours are at 18, 25.5, 36, 50.9, and 72% of the peak flux of 252 mJy/beam. The beam is 12.0 by 1.6 milliarcseconds at a position angle of  $-10.7^\circ$ .

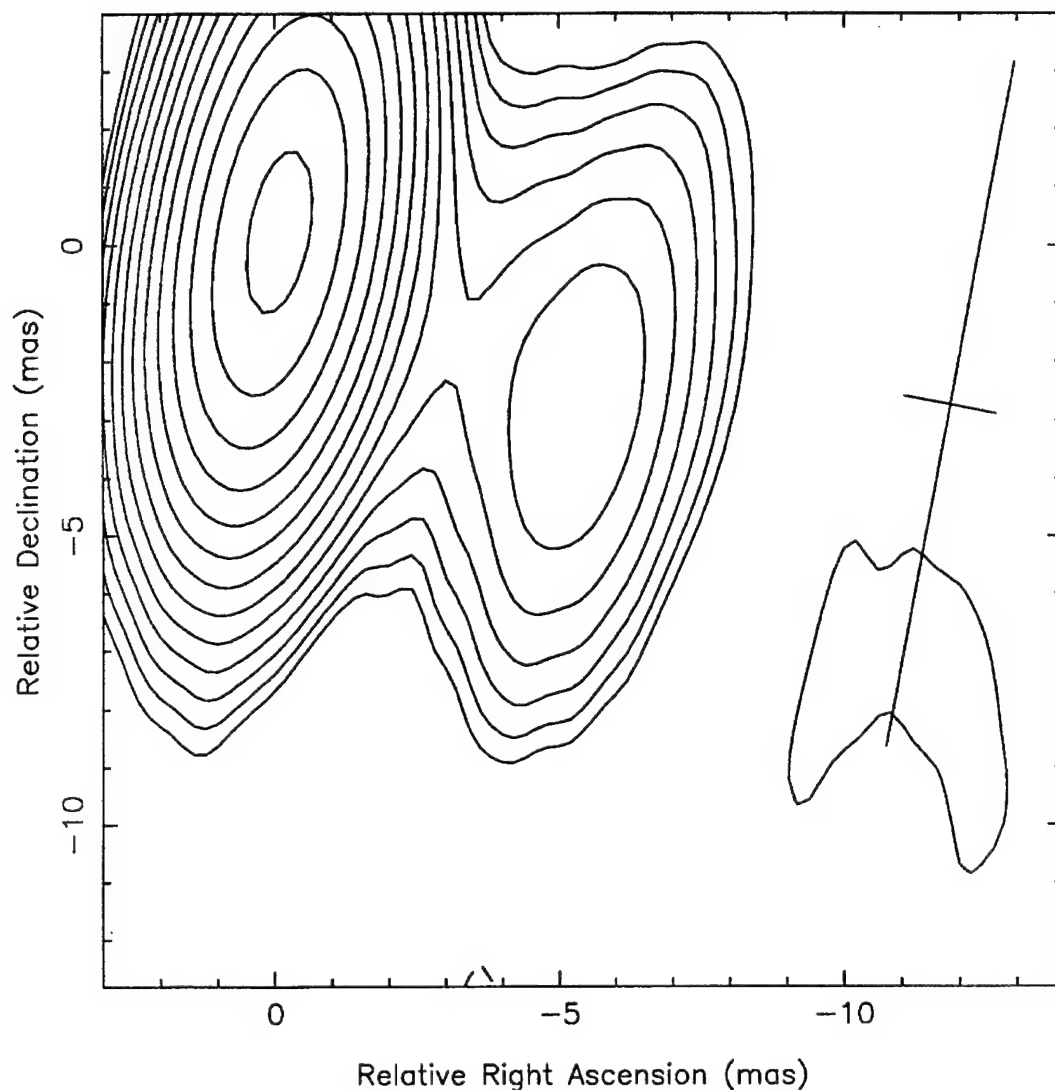


Figure 80: Total Intensity Map of 3C 273 at 3.6 cm, Epoch 1992.2, made with natural weighting of the visibilities and smoothed with an optional restoring beam. Contours are at -1.4, 1.4, 2, 2.8, 4, 5.6, 7.9, 11.2, 15.8, 22.4, 31.7, 44.8, 63.4, and 89.6% of the peak flux of 23,100 mJy/beam. The beam is 12.0 by 1.6 milliarcseconds at a position angle of  $-10.7^\circ$ .



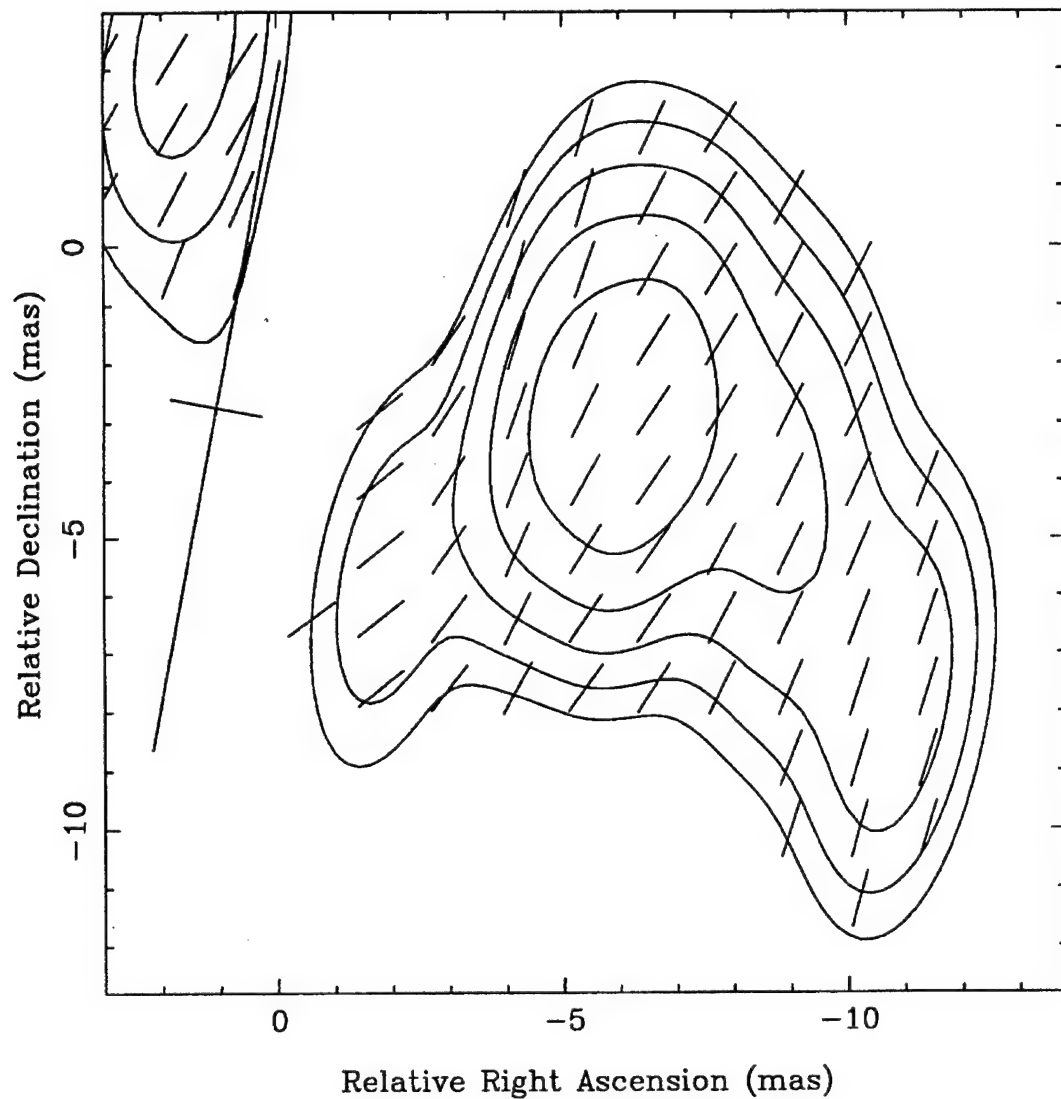


Figure 81: Complex Polarization Map of 3C 273 at 3.6 cm, Epoch 1992.2, made with  $(1 + r/80 M\lambda)^{0.75}$  weighting of the visibilities and smoothed with an optional restoring beam. Contours are at 18, 25.5, 36, 50.9, and 72% of the peak flux of 234 mJy/beam. The beam is 12.0 by 1.6 milliarcseconds at a position angle of  $-10.7^\circ$ .

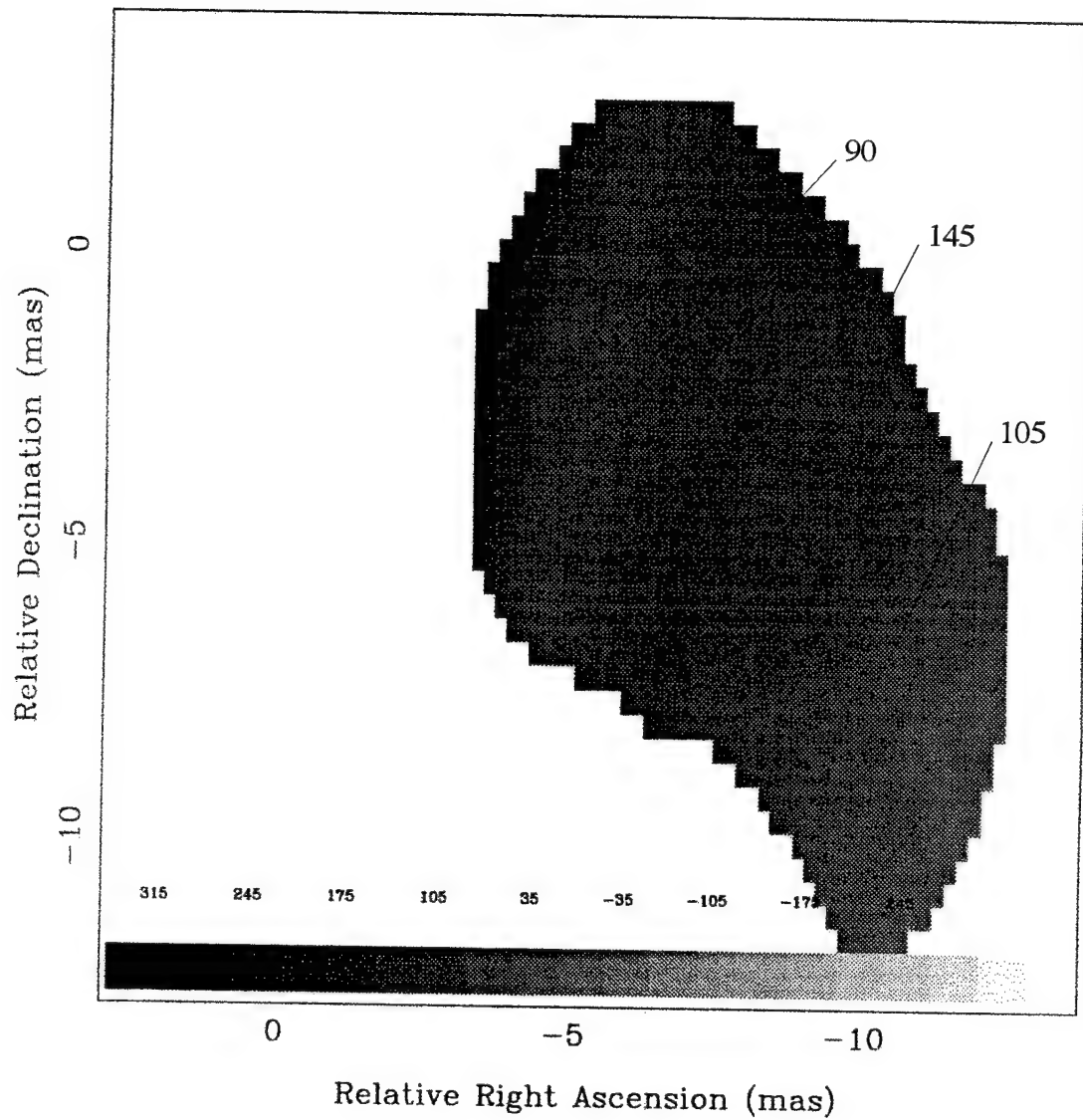


Figure 82: Faraday Rotation Measure Map of 3C 273, Epoch 1992.2, made from figures 79 and 81, with alignment of the 3.6 cm and 6 cm maps at the brightest total intensity peaks in each map. All values are given in rad/m<sup>2</sup>.

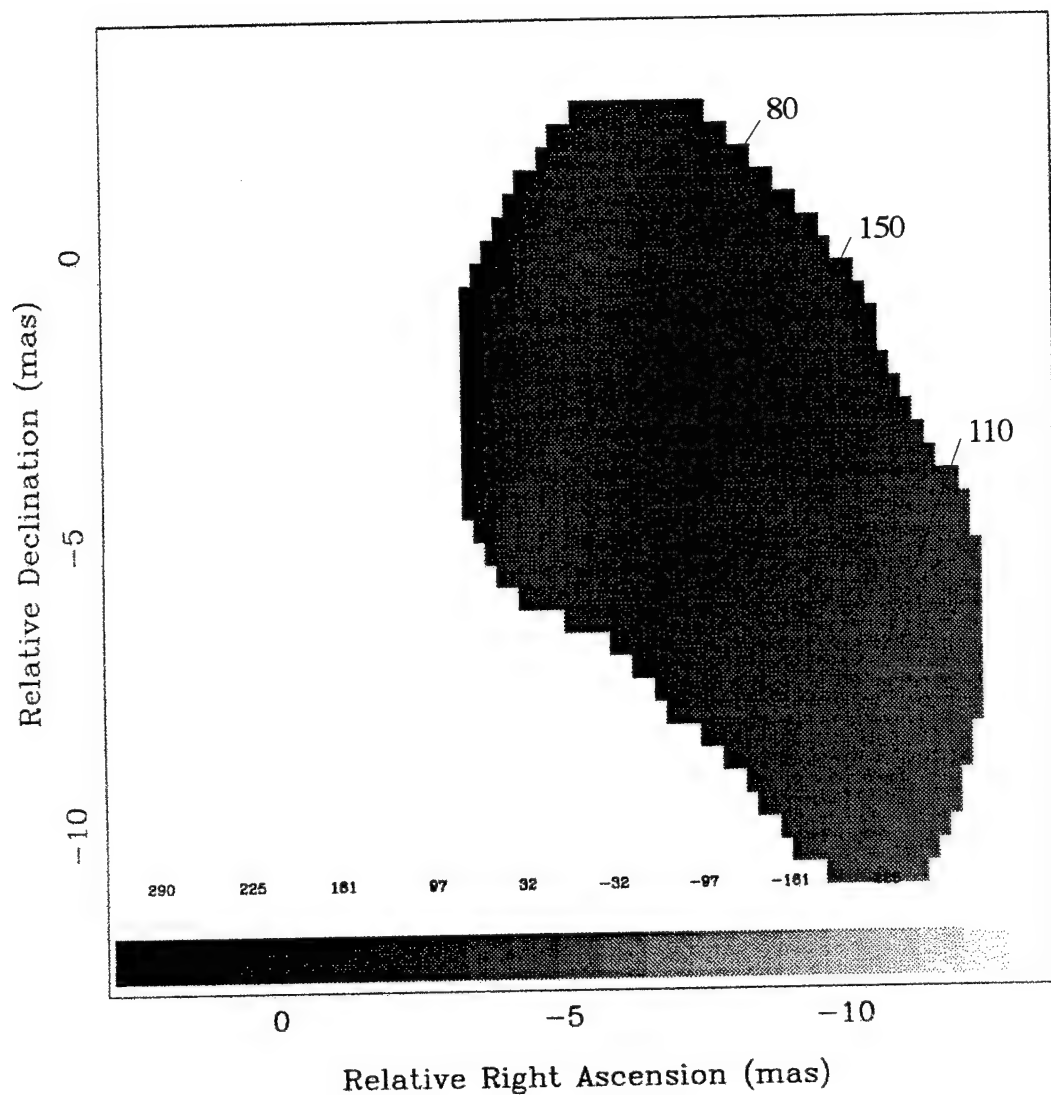


Figure 83: Faraday Rotation Measure Map of 3C 273, Epoch 1992.2, made from figures 79 and 81, with alignment of the 6 cm map shifted 2 pixels north (0.8 milliarcsecond) from that used in figure 82. All values are given in  $\text{rad/m}^2$ .

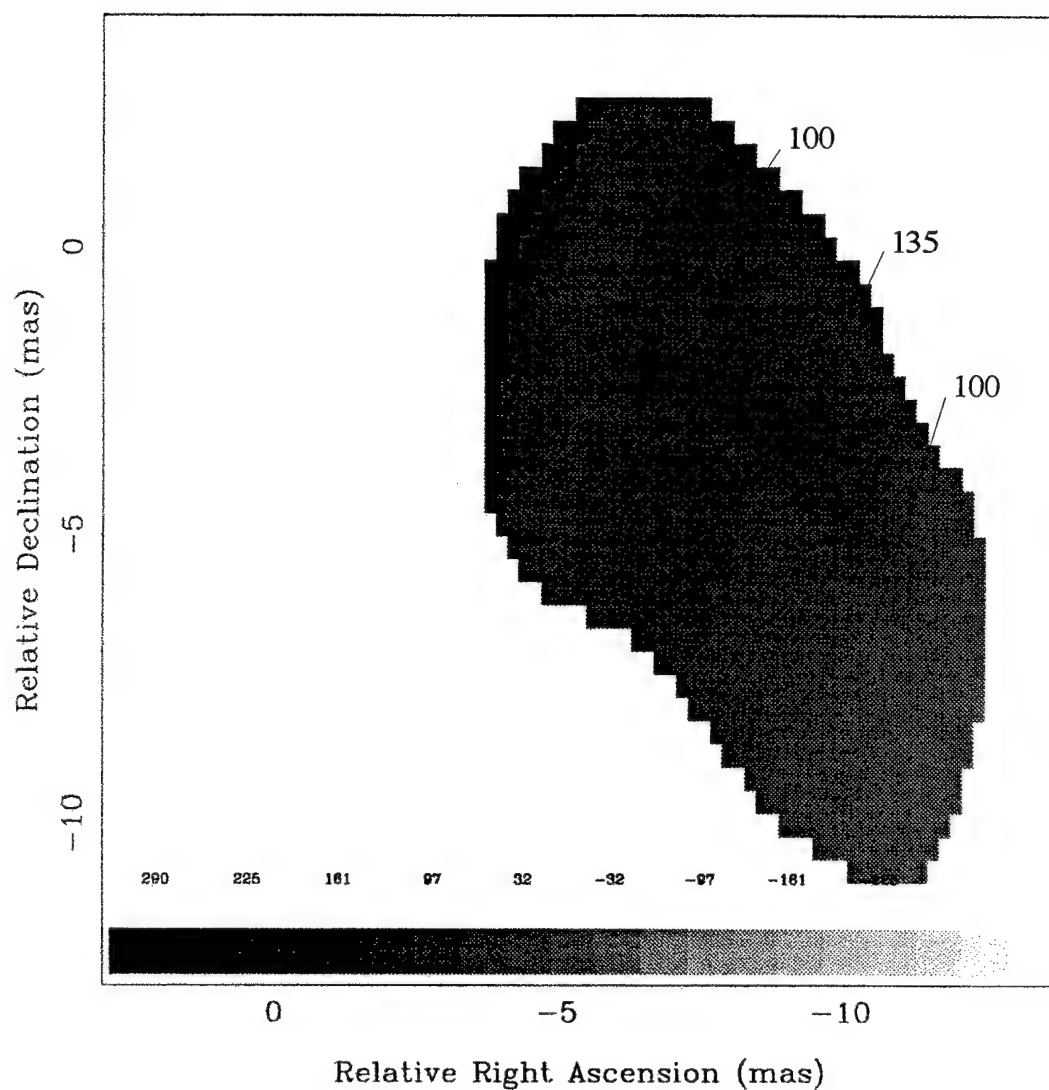


Figure 84: Faraday Rotation Measure Map of 3C 273, Epoch 1992.2, made from figures 79 and 81, with alignment of the 6 cm map shifted 2 pixels north (0.8 milliarcsecond) and 2 pixels right (0.4 milliarcsecond) from that used in figure 82. All values are given in  $\text{rad/m}^2$ .

In the Faraday rotation map shown in figure 84, the 6 cm map was shifted two pixels (0.8 mas) north and two pixels (0.4 mas) east relative to the alignment used for figure 82. This was done to test the robustness of the solution. This decreased the peak Faraday rotation slightly, but had little effect otherwise. In this map, the Faraday rotation gradient runs from roughly 80 rad/m<sup>2</sup>, peaks at 140 rad/m<sup>2</sup>, and drops back to 60 rad/m<sup>2</sup>.

## *2. Analysis*

Traditionally, mapping of 3C 273 is difficult because of its low declination, which leads both to a pseudo-one dimensional image and to gaps in the UV coverage. As noted earlier, such gaps tend to lead to problems in hybrid mapping (see chapter 6). The maps of 3C 273 in epoch 1992.2 appear to overcome these difficulties. The 6 cm total intensity map shows the core-jet morphology, with only a small westward extension from the core despite the use of only minimal self-calibration restrictions and no CLEAN restrictions. In complex polarization, the need to weight the data to limit the impact of the western VLBA antennas reduces the dynamic range, however the resulting map appears quite reasonable when compared with previous results (see above). At 3.6 cm, the data set is much more limited, so that CLEAN and self-calibration restrictions were needed. The final result of these limitations appears appropriate however, with no unusually bright components far from the core and with a sudden drop brightness at roughly 11 mas in total intensity, as is seen at 6 cm. The complex polarization map is a bit harder to interpret, however it shows similar behavior to the 6 cm map and is probably valid within the jet, although certainly over a smaller dynamic range.

As noted earlier, 3C 273 appears roughly one dimensional to the VLBI array, so that a strip plot is a convenient way of looking at the components in the jet. Figure

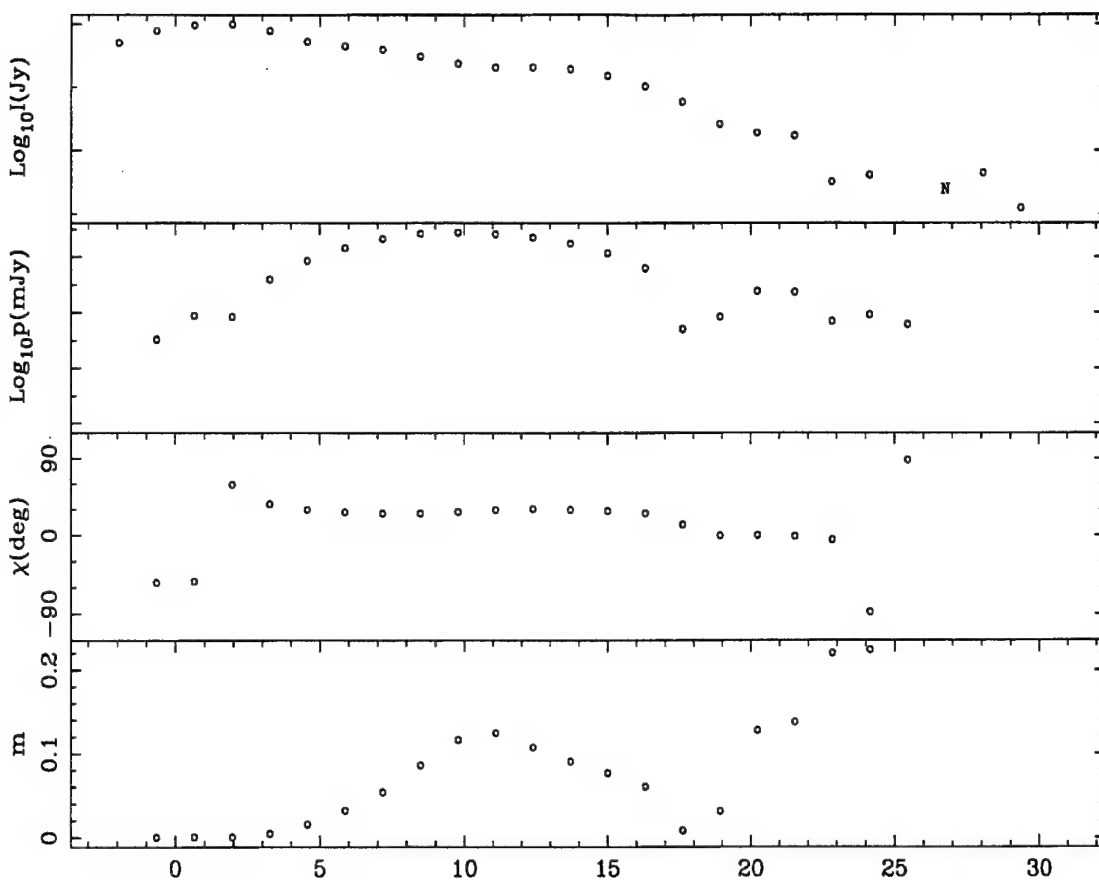


Figure 85: Strip plot of 3C 273 at 6 cm, Epoch 1992.2, made from figures 74 and 75, measured along the jet axis at a position angle of  $-140^\circ$ . The top box gives total intensity in arbitrary units, the second box gives linearly polarized intensity in arbitrary units, the third box gives the polarization position angle on the sky, and the fourth box gives the percentage polarization.

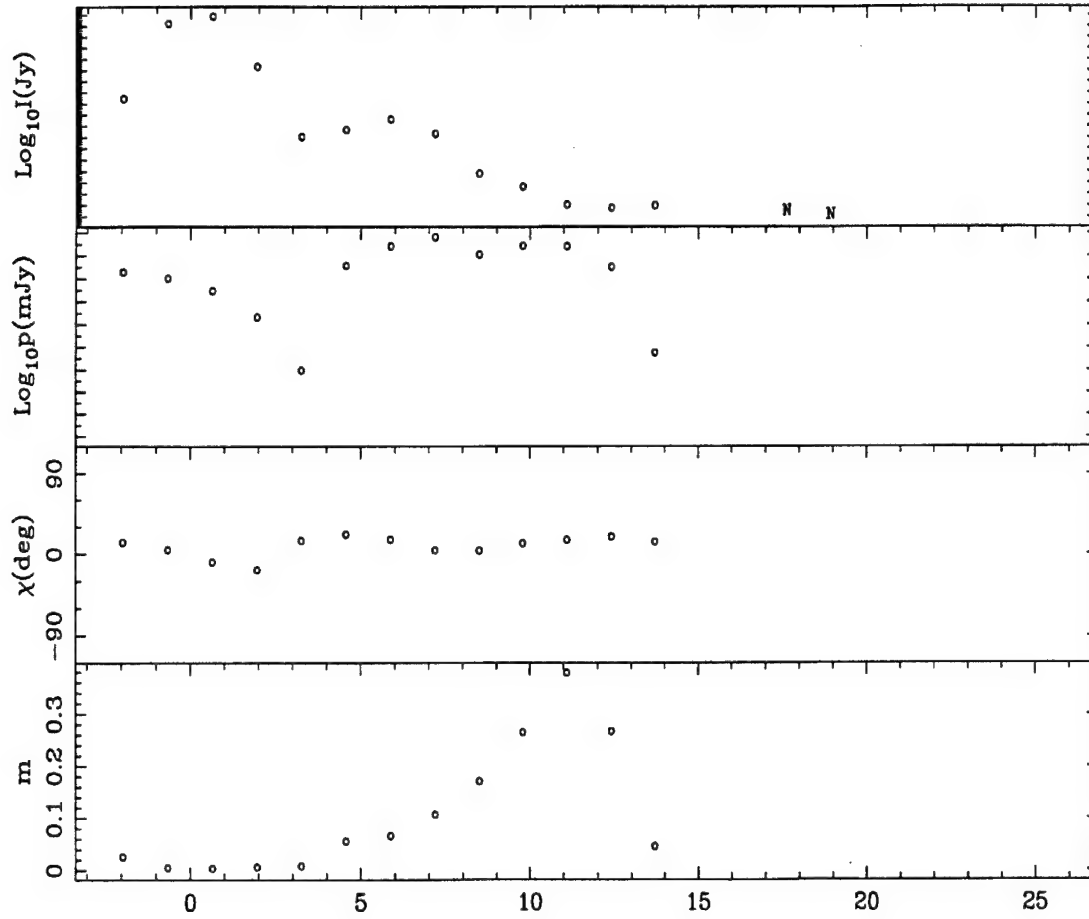


Figure 86: Strip plot of 3C 273 at 3.6 cm, Epoch 1992.2, made from figures 76 and 77, measured along the jet axis at a position angle of  $-140^\circ$ . The top box gives total intensity in arbitrary units, the second box gives linearly polarized intensity in arbitrary units, the third box gives the polarization position angle on the sky, and the fourth box gives the percentage polarization.

84 gives the strip plot along the jet of the total intensity, polarized flux, electric vector position angle, and fractional polarization at 6 cm. The highest fractional polarization occurs near the end of the jet, however this is at the level of the noise in the complex polarization map. Excluding this outer component, the fractional polarization peaks at the break in the total intensity map, as in epoch 1990.4.

Figure 86 gives the strip plot along the jet of the total intensity, polarized flux, electric vector position angle, and fractional polarization at 3.6 cm. Again the highest fractional polarization occurs at the break in total intensity map, although the limits on the dynamic range of the total intensity image limits interpreting the portions of the jet farther out from the break.

From the Faraday rotation maps, figures 82 to 85, the magnetic field direction can be reconstructed using the assumption that the emitted electric field vector position angle is perpendicular to the magnetic field (*i.e.* synchrotron radiation as noted earlier). Using the rotation map shown in figure 82 and the complex polarization map shown in figure 81, the magnetic field direction can be reconstructed as shown in figure 87. Except for the very end of the jet, the magnetic field direction appears extremely well aligned with the jet axis.

Reconstructing the magnetic field using the Faraday rotation map shown in figure 83 gives the reconstructed magnetic field shown in figure 88. Again the overall effect is to align the magnetic field with the jet axis, although now there is also a hint of a turn at the very start of the reconstructed field direction.

Using the Faraday rotation map shown in figure 84 gives a similar reconstructed magnetic field, as shown in figure 89. Once again there is good alignment between the reconstructed magnetic field direction and the jet axis, except at the very end of the jet.



The slight turns in the magnetic field directions at the ends of the recovered reconstruction are probably not valid. It is important to remember that these reconstructions are made from Faraday rotation measures determined using arrays with inherently different resolutions at different frequencies. As such, edge effects, like those seen here, are best ignored. Overall the effect of the determination of the Faraday rotation in 3C 273 is striking. A jet, which in polarization measurements at 6 cm (the only frequency previously available to VLBI polarization studies) appeared misaligned, has been shown to be aligned with the jet axis over the whole measurable length. This result appears consistent at both epochs studied as well.

3C273B Reconstructed B Field

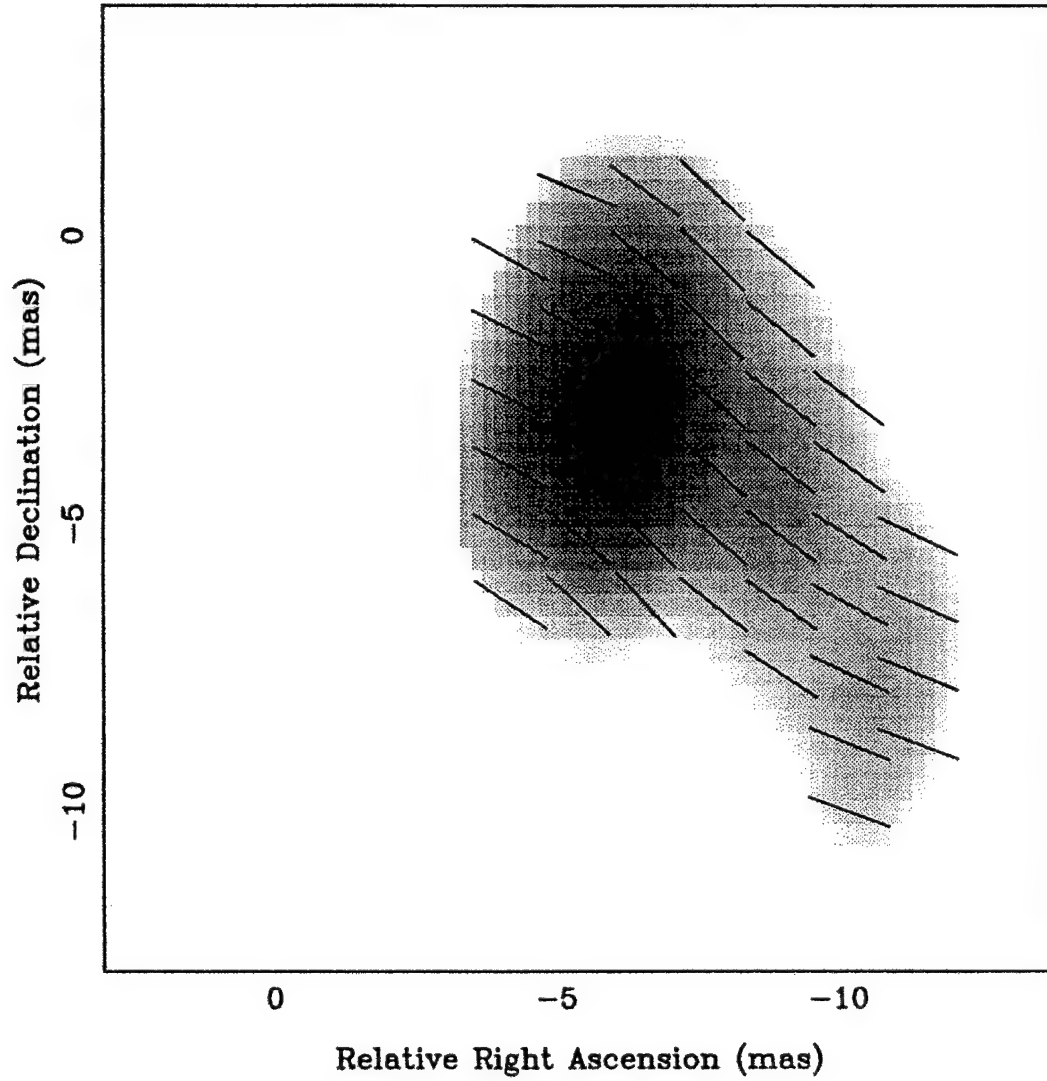


Figure 87: Map of the Reconstructed Magnetic Field in 3C 273, Epoch 1992.2, made from figure 81 corrected for Faraday Rotation using figure 82 and converting to magnetic field from electric field vectors.

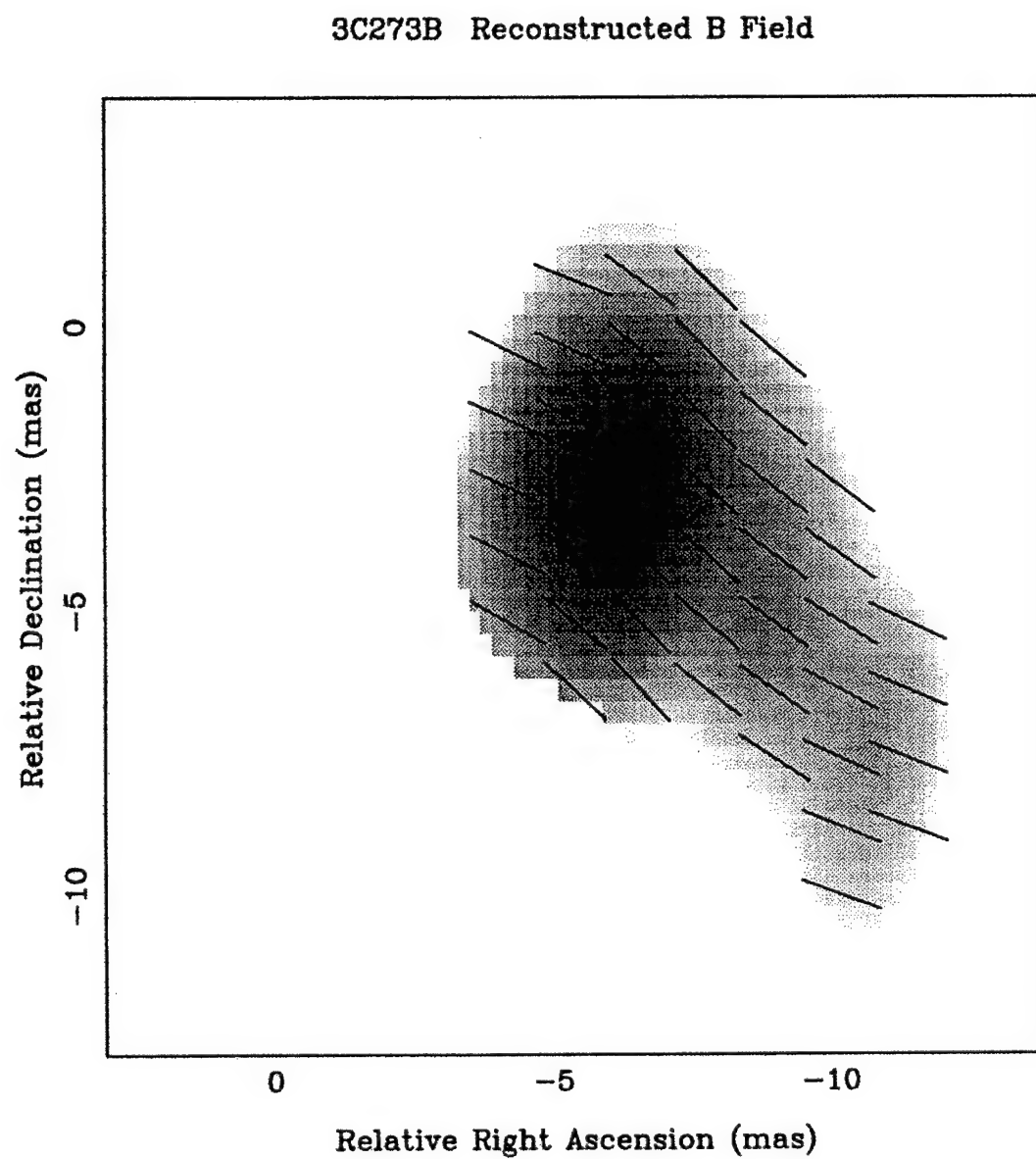


Figure 88: Map of the Reconstructed Magnetic Field in 3C 273, Epoch 1992.2, made from figure 81 corrected for Faraday Rotation using figure 83 and converting to magnetic field from electric field vectors.

### 3C273B Reconstructed B Field

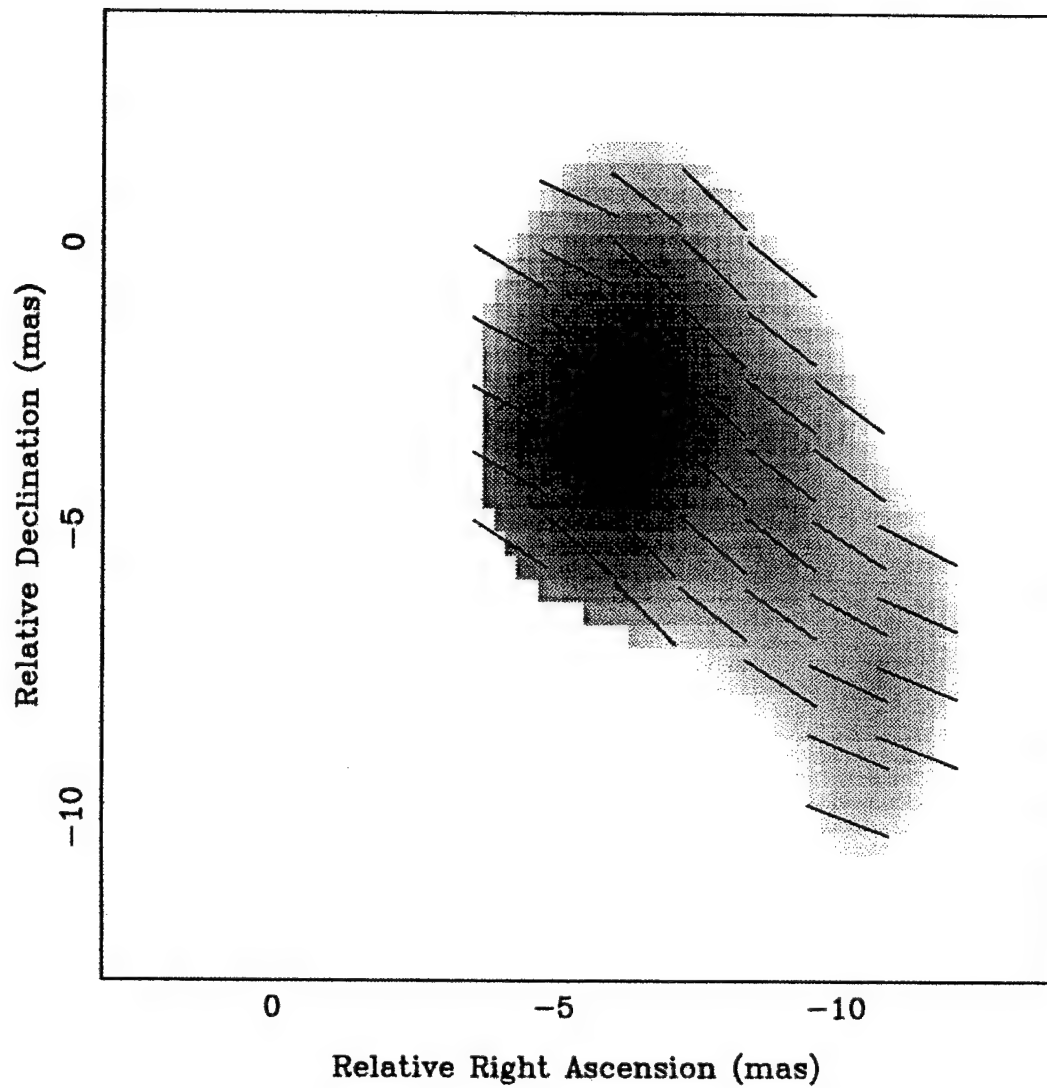


Figure 89: Map of the Reconstructed Magnetic Field in 3C 273, Epoch 1992.2, made from figure 81 corrected for Faraday Rotation using figure 84 and converting to magnetic field from electric field vectors.

## IX. Analysis and Discussion

In this chapter, the results presented in chapters 7 and 8 for the quasars 3C 345 and 3C 273 are investigated in more detail. In addition, the reliability of the maps, especially the complex polarization images, are discussed.

### *A. Reliability of the Maps*

#### *1. Errors in the Complex Polarization*

The interpretation of VLBI maps is complicated by the lack of a complete mathematical analysis of the errors introduced by iterations involving both self-calibration and deconvolution, which is non-linear (as discussed in chapter 2). Calculations of the noise in each visibility are made during correlation, however these measurements clearly overestimate the dynamic range seen in total intensity images. Generally total intensity maps are considered reliable to the lowest false contour or to the level where negative contours appear, since negative contours indicate negative flux, a physical impossibility. The dynamic ranges determined from the first false features are universally poorer than the calculated dynamic range based on noise levels. Simulations of VLBI data sets support these limits on total intensity images. The true dynamic range limits probably arise from uneven coverage in the uv plane and from errors introduced during the iteration process used to make the images.

For images of complex polarization in VLBI, no negative contours occur because the complex CLEAN algorithm is fitting two independent variables (both polarized flux and position angle) and therefore can be constrained to avoid negative flux. Although clearly false features still appear and can be helpful in interpreting the map, the reliability of the final image needs to be handled carefully. Unlike parallel hand visibilities used for total intensity mapping, cross hand visibilities used for complex polarization mapping have relatively low signal to noise ratios and include contamination from incompletely determined D terms, which could arise either from scatter in the data or from time variation in the D terms.

The dynamic range of the final complex polarization image can be limited by either the noise in the data or by the errors in the D terms. Because the larger error appears to be in the D terms, the analysis here concentrates on the errors in the D terms. In reality, noise in the data also enters the calculation as it scatters the data used to determine how well the D term is fixed, so that well-determined D terms still appear with a certain error due only to the scatter in the data. Since the D terms are determined using 3C 84, a source with polarization on all scales below 0.1%, well-determined D terms lead to residuals in the cross hand visibilities at the level of the noise and these enter the calculations below as errors in the D terms. Generally the D term errors are larger than this scatter, however for the new VLBA antennas this is not always the case (see below).

The errors in the final complex polarization map arising from errors in the D terms are derived for a point source by Roberts, Wardle, and Brown (Roberts, Wardle and Brown, 1994). The error on a D term is given by  $\Delta_{iX,S}$  where  $i$  is the antenna,  $X$  is the receiver polarization (R for RCP, L for LCP), and  $S$  is the scan number. The error in the final complex polarization image then depends on the errors in the D

terms multiplied by the total intensity term (which enters in determining the correct cross hand visibility as  $D^*I$ , see chapter 2):

$$\Delta M = \frac{\Delta P}{I} = \frac{1}{N_a N_s} \sum_{s=1}^{N_s} \sum_{a=1}^{N_a} (\Delta_{aR,s} + \Delta_{aL,s}^*) e^{2i\phi_{a,s}} \quad (9.1)$$

where  $\Delta M$  is the uncertainty in the fractional polarization,  $\Delta P$  is the uncertainty in the complex polarization,  $N_a$  is the number of antennas,  $N_s$  is the number of scans, and  $\phi_{a,s}$  is the parallactic angle of antenna  $a$  on scan  $S$ . For equatorial antennas, the parallactic angle term does not change, so that the exponential term is constant and the errors add coherently. For alt-azimuth antennas, the rotation of the parallactic angle tends to cause the errors to add incoherently, reduced by the number of independent parallactic angles used.

For error terms which have the same variance  $\sigma_\Delta^2$  and have random phases, the variance of the error in the fractional polarization reduces to

$$\text{var}(\Delta M) = \frac{2\sigma_\Delta^2}{N_a^2} \left( N_E + \frac{N_A}{N_s} \right) \quad (9.2)$$

where  $N_E$  is the number of equatorial antennas and  $N_A$  is the number of alt-azimuth antennas (Roberts, Wardle and Brown, 1994). The errors on the fractional polarization and position angle of the polarization can then be shown to be

$$\sigma_m = \frac{\sigma_\Delta}{N_a} \left( N_E + \frac{N_A}{N_s} \right)^{\frac{1}{2}} \quad (9.3)$$

$$\sigma_\chi \cong \frac{\sigma_m}{2m}$$

where  $\sigma_m$  is the error in the fractional polarization and  $\sigma_\chi$  is the error in the position angle.

The above result assumes that the source is at a reasonably high declination so that each separate scan involves an independent parallactic angle difference between

the antennas in the baseline, which results in the error term rotating and reducing its average size. For the low declination source 3C 273 this is not valid, since the parallactic angle differences tend to bunch. For that source it is more appropriate to assume there is no variation in the parallactic angle differences which gives

$$\Delta M = \frac{\Delta P}{I} = \frac{1}{N_A N_S} \sum_{s=1}^{N_S} \sum_{a=1}^{N_A} (\Delta_{aR,S} + \Delta_{aL,S}^*) \quad (9.4)$$

$$\text{var}(\Delta M) = \frac{2\sigma_\Delta^2}{N_a}$$

where the second line follows for the conditions used for equation 9.2. Equations 9.1 through 9.4 still contain a significant assumption concerning the observations. The number of scans for each antenna is assumed to be the same, which is generally not true for the edited cross hand data sets, although it may be valid in the future for observations involving only the VLBA. This assumption results in treating an antenna which appears in only a few visibilities as adding the same amount of error to the final image as an antenna which appears in many visibilities. Since antennas with more poorly determined D terms tend to have their visibilities edited out more frequently than good antennas do, this will lead to an overestimation of the uncertainty in the final image.

A more precise determination of the error in the final complex polarization image can be made from the final cross hand visibility data set. From this data set the exact occurrence of each visibility can be treated directly, providing that we look at the errors in the D terms on baselines instead of at each antenna. Although the D terms are antenna based, we determine the error on each D term from the visibility data in practice, so that treating each baseline as the source of error is valid. This will effectively overestimate the error, since the uncertainty in the D term for an individual



	L	B	W	J	K	G	I	X	Y	P	T	O
L		4.3	-	2.0	0.5	1.3	0.1	-	-	-	-	-
B	15†		-	1.0	1.9	2.8*	1.7	3.8*	3.6*	3.3*	2.2*	-
W	-	-		-	-	-	-	-	-	-	-	-
J	2.7†	0.5†	-		2.5	-	-	-	1.1	-	-	-
K	-	2.7	-	2.5		1.3	1.1	1.2	2.2	1.5	1.9	2.0
G	-	3.1*	-	-	1.4		1.4	1.1	2.3	1.4	0.8*	0.8*
I	-	3.1	-	-	1.1	1.6		1.0	1.9	1.1	0.4	0.5*
X	-	4.0*	-	-	1.4	1.3	1.2		1.9	1.2	0.3	0.3*
Y	-	5.0	-	-	1.6	1.1	1.0	1.1		1.0	0.2*	0.2*
P	-	3.3*	-	-	1.2	1.0	1.0	0.6	0.2		0.2*	0.3
T	-	4.2*	-	-	1.7	0.8*	0.4	0.2	0.2*	0.2*		0.3
O	-	-	-	-	-	0.6*	0.5*	0.3*	0.3*	0.4	0.3*	

Table 21: The residual errors in the cross hand visibilities for 3C 84 in the 1992.2 6 cm experiment. The upper right contains RL correlations, while the lower left contains LR correlations. The values are given in percent residual of the average cross hand magnitude over the average parallel hand magnitude. A \* indicates that the cross hand magnitude is extremely low and shows variation from zero only because of noise. A † indicates an isolated data point.

antenna is actually smaller than the error in an individual baseline measurement. The error is then given by

$$\Delta M = \frac{1}{N_{vis}} \sum_{i=1}^{N_{bl}} \sum_{X=1}^2 \frac{N_{vis,i,X} \Delta_{i,X}}{N_{PA,i,X}} \quad (9.5)$$

where  $N_{vis}$  is the number of visibilities,  $N_{vis,i,X}$  is the number of visibilities for correlation  $X$  on baseline  $i$ ,  $\Delta_{i,X}$  is the error in the overall polarization correction on baseline  $i$  with correlation  $X$  (LR or RL), and  $N_{PA,i,X}$  is the number of independent

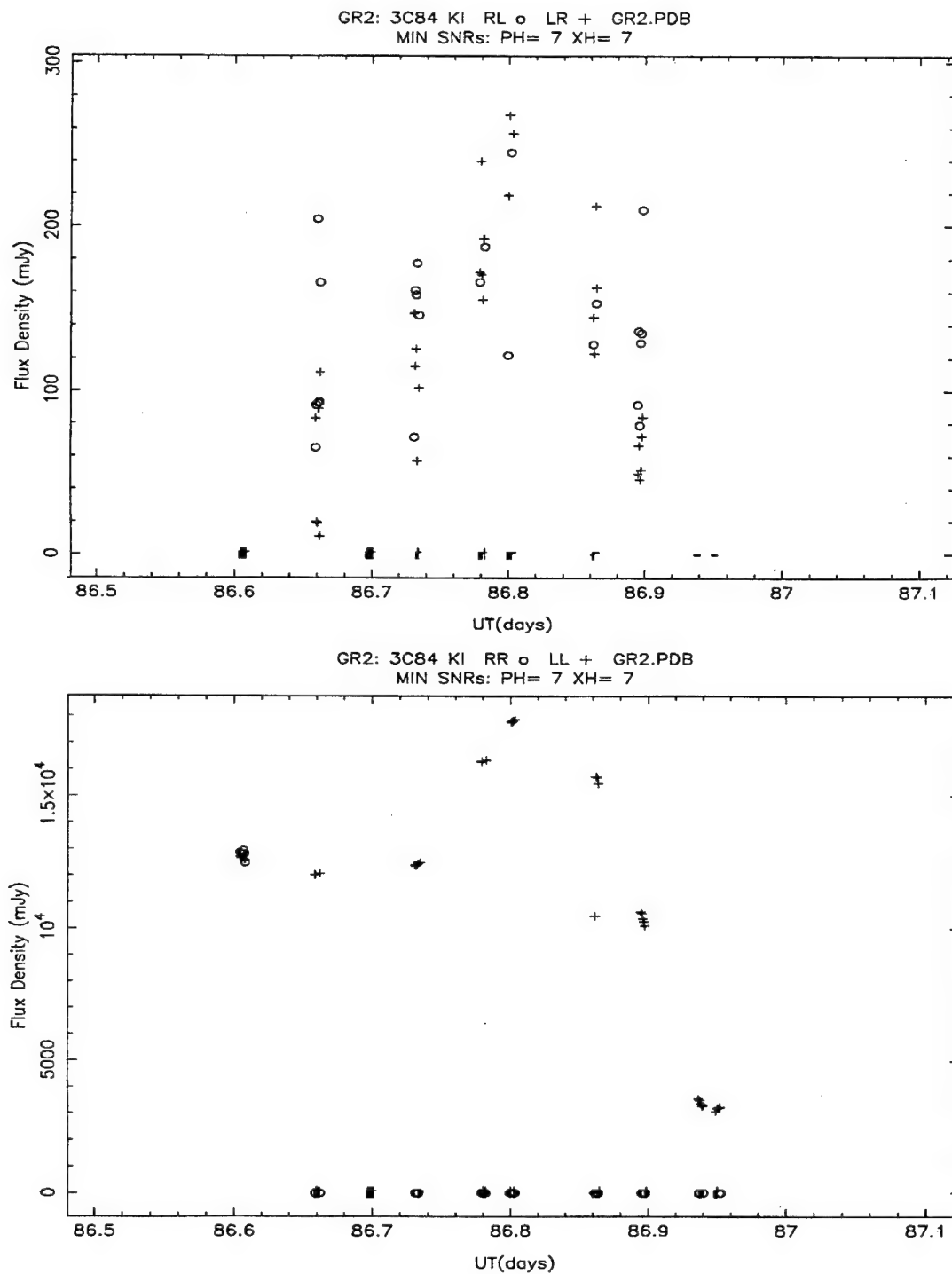


Figure 90: Plots of the cross hand (top) and parallel hand (bottom) visibilities for 3C 84 on a typical baseline in the epoch 1992.2 6 cm experiment.

parallactic angle differences on baseline  $i$  for correlation  $X$ . As seen in equation 9.5, the careful treatment of the visibilities directly also allows the direct treatment of the number of individual parallactic angle changes present in the data set.

In order to get a good measure of the errors in the  $D$  terms on each baseline, the cross hand and parallel hand visibilities from the fully calibrated database were plotted for 3C 84 (see figure 90 for a typical baseline). Comparing the cross hand and parallel hand visibilities allowed for an estimation of the residual errors in the  $D$  terms for each baseline and each correlation. The determined average errors for the baseline  $D$  term solutions in the 6 cm 1992.2 experiment are given in table 21. Using equation 9.5 and 9.3 together with the values in table 21 gives  $\Delta M = 0.63\%$ , so that  $\sigma_m \sim 0.0063$  and  $\sigma_\chi \sim 7^\circ$ .

For 3C 273, equation 9.5 is modified to remove the parallactic angle term, so that all errors add coherently. This is done to take into account the low declination of 3C 273, which causes parallactic angles to remain rather constant during the observations. The values in table 21 and equations 9.5 and 9.3 then give  $\Delta M = 0.90\%$ , so that  $\sigma_m \sim 0.0090$  and  $\sigma_\chi \sim 10^\circ$ . The error estimates for 3C 345 and 3C 273 represent clear overestimates, since the  $D$  terms have smaller errors than the baseline error estimates on 3C 84 and since 3C 345 and 3C 273 have strongly polarized visibilities. Further, it should be noted that the largest errors are expected at the core of complex polarization map (Roberts, Wardle and Brown, 1994), and the detected polarization lies primarily in the jet in both sources. For these reasons, the above errors should be viewed as true maximum limits.

It would be appealing to apply the same error analysis to the 3.6 cm observations. Unfortunately 3C 84 is so highly resolved at 3.6 cm that the parallel hand visibility amplitudes are quite low on all but the shortest baselines. Since there is always a residual signal in the cross hand visibilities ranging between 0 and 30 to

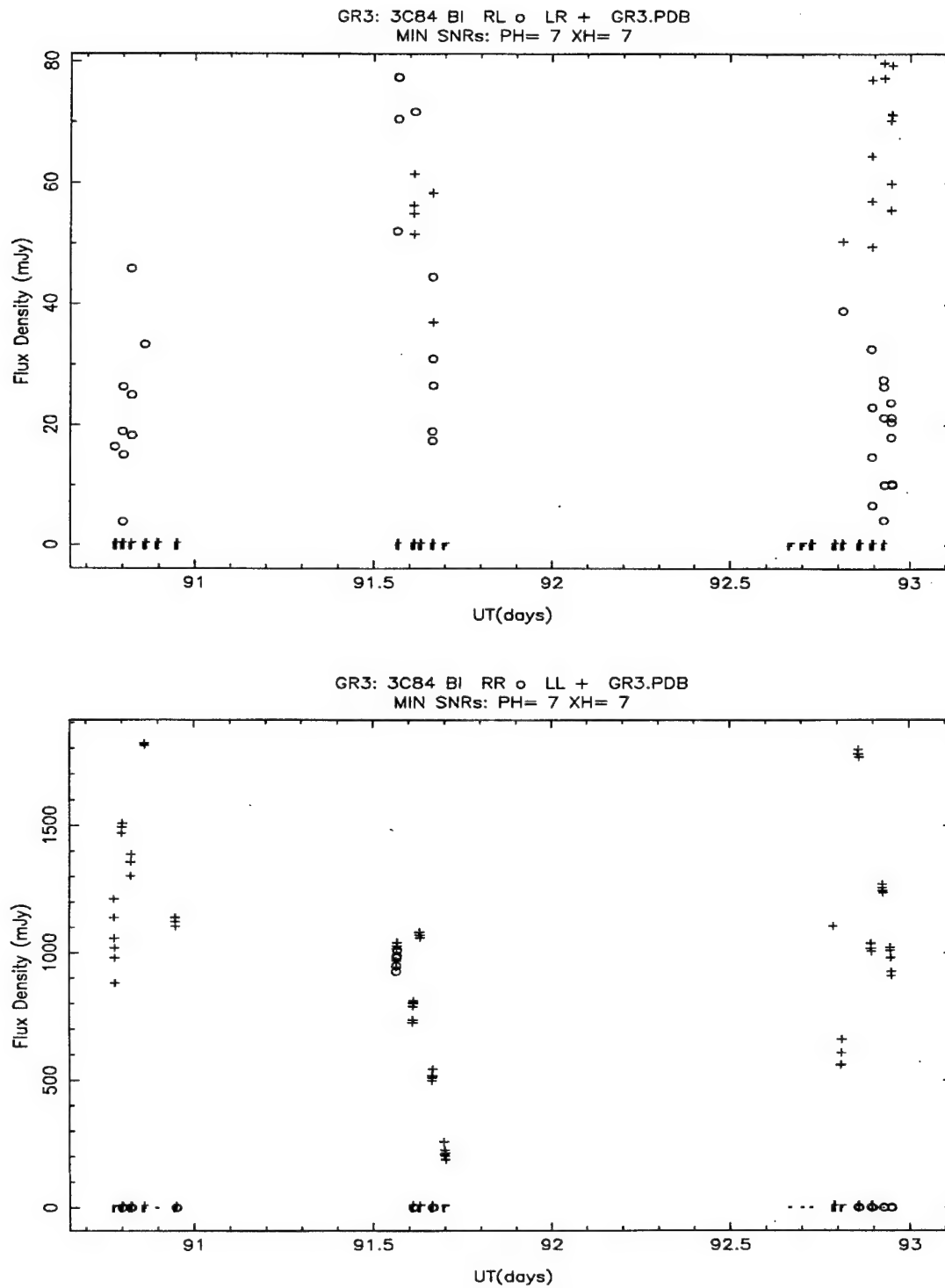


Figure 91: Plots of the cross hand (top) and parallel hand (bottom) visibilities for 3C 84 on a baseline which shows a low parallel hand visibility in the epoch 1992.2 3.6 cm experiment.

100 mJy, depending on the baseline (see figure 91), the error estimates using equation 9.5 would grossly overestimate the actual error. For the 3.6 cm observations, equations 9.2 and 9.4 are applied instead. The residual errors at each antenna are generally below 0.5% (and are even better for the VLBA antennas), so that a conservative treatment of 0.5% residual error is acceptable. Then following equation 9.2 and 9.3, the error in the D terms lead to  $\sigma_m \sim 0.00089$  and  $\sigma_\chi \sim 1^\circ$  for 3C 345, where we have estimated that roughly 5 independent parallactic angles are sampled by each antenna (a rough average of the data). For 3C 273, we must treat all antennas as equatorial and use equation 9.4 instead of equation 9.2. This yields  $\sigma_m \sim 0.0020$  and  $\sigma_\chi \sim 2^\circ$ .

The receivers on the VLBA antennas are a bit better at 3.6 cm than at 6 cm, but the five fold difference in these two error estimates is likely the result of the overestimation of the error in the first method. The first estimate for the 6 cm data was designed to obtain a maximum possible error, whereas the approach for the 3.6 cm data should have yielded a rough estimate of the actual expected error. From these two approaches, it appears a valid interpretation of the maps is to assume that the 3C 345 map shows a correct complex polarization image to roughly 0.2% in fractional polarization, with an upper limit of 0.6%, and a correct position angle to roughly  $2^\circ$ , with an absolute upper limit of  $7^\circ$ . For 3C 273, the complex polarization map is expected to be correct to roughly 0.4% in fractional polarization, with an upper limit of 0.9%, and to roughly  $4^\circ$  in polarization position angle, with an absolute upper limit of  $10^\circ$ . The final Faraday rotation maps could then be expected to show errors on the order of  $\Delta\chi \sim 3^\circ$  ( $\Delta RM \sim 20 \text{ rad/m}^2$ ) for 3C 345 and  $\Delta\chi \sim 6^\circ$  ( $\Delta RM \sim 45 \text{ rad/m}^2$ ) for 3C 273.

Epoch and Band	VLA  P  (mJy)	VLA $\chi$ (deg)	VLBI  P  (mJy)	VLBI $\chi$ (deg)	Sgl Dish  P  (mJy)	Sgl Dish $\chi$ (deg)
1990.4 C Band	279	33	161	30	314	36
1990.4 X Band	242	31	228	23	226	31
1992.2 C Band	295	23	100	22	297	27
1992.2 X Band	223	24	119	14	259	24

Table 22: The polarization characteristics of 3C 345 on three scales during the epoch 1990.4 and epoch 1992.2 observations. Single dish measurements were provided by Margo Aller of the University of Michigan and epoch 1992.2 VLA measurements were provided by Scott Aaron of Brandeis University.

## 2. Intermediate Scale Polarization

From the measurements of the unresolved VLA core made during the observations and the sum of the polarized clean components in the VLBI map, a measure of the complex polarization on intermediate scales between the VLA core and VLBI map can be made. Table 22 shows the VLA measurements of the core polarization, the sum of the VLBI polarized components, and the single dish observations of 3C 345 during the two observations. Many previous epochs of observations of the VLBI polarized structure of 3C 345 at 6 cm have given consistent position angle measurements of the intermediate scale polarization of 3C 345 (Brown, 1992). The rough position angle measured has been between  $33^\circ$  and  $50^\circ$ .

The measured value of the intermediate scale polarization in the epoch 1990.4 observations at 6 cm is 119 mJy at  $37^\circ$ , consistent with previous results. However, the epoch 1992.2 intermediate scale polarization is 195 mJy at  $24^\circ$ , roughly  $10^\circ$  lower than any previous observation. Although this seems to indicate a problem with the data set, there are a number of reasons to believe that this result is actually correct and indicates a change in the intermediate scale polarization in this source.

Epoch and Band	VLA  P  (mJy)	VLA $\chi$ (deg)	VLBI  P  (mJy)	VLBI $\chi$ (deg)	Sgl Dish  P  (mJy)	Sgl Dish $\chi$ (deg)
1990.4 C Band	1150	-10	640	-37	1220	-10
1990.4 X Band	1170	-26	722	-31	1460	-26
1992.2 C Band	1150	-24	821	-13	1170	-20
1992.2 X Band	1250	-31	727	-30	1350	-31

Table 23: The polarization characteristics of 3C 273 on three scales during the epoch 1990.4 and epoch 1992.2 observations. Single dish measurements were provided by Margo Aller of the University of Michigan and epoch 1992.2 VLA measurements were provided by Scott Aaron of Brandeis University.

The possibility of the position angle calibration being in error in the experiment as a whole can be ruled out. The VLA data was reduced twice independently and gave the same results (within  $4^\circ$  in phase) for OJ 287, the position angle calibrator. A fully calibrated VLBI database was recreated and OJ 287 was remapped, giving the same results as before. Any error in the adjustment of the R - L phase differences at the antennas would show up during the determination of the D terms. The D term fits were extremely good and the residual polarization detected on 3C 84 was extremely low (especially on VLBA baselines where it was routinely in the noise, see figure 91).

In addition, the same type of analysis can be applied to the intermediate scale polarization in 3C 273 (table 23 gives the VLA polarization, sum of the VLBI polarized components, and the single dish measurements for 3C 273). For the epoch 1990.4 observations, an intermediate scale polarization of 650 mJy at  $16^\circ$  results. This is probably incorrect as it would indicate a substantial misalignment with the well-known jet which has been mapped in the region. This result is probably an indicator of the problems in mapping 3C 273 from the poor data set of that epoch, as discussed in chapter 8. The 1992.2 results for the intermediate scale polarization are

Epoch and Band	VLA - VLBI  P  (mJy)	VLA - VLBI $\chi$ (deg)	Sgl Dish - VLA  P  (mJy)	Sgl Dish - VLA $\chi$ (deg)
1990.4 C Band	119	37	39	59
1990.4 X Band	35	-86	~0	-
1992.2 C Band	195	24	~0	-
1992.2 X Band	108	35	36	24

Table 24: Polarization on Intermediate Scales in 3C 345.

378 mJy at  $-48^\circ$ , which is within  $2^\circ$  of previous polarization VLBI observations and suggests that the intermediate scale jet which extends at  $-138^\circ$  from the core contains a magnetic field well aligned with the jet axis (Roberts *et al.*, 1990). This result also suggests that the calibration is better than the worst case calculation above, as expected. One caveat to this result is that the intermediate scale polarization seen in the X band is 523 mJy at  $-33^\circ$ , which suggests that Faraday effects may play a role on the intermediate scale.

Finally, if the intermediate scale polarization position angle in 3C 345 were to be taken as constant, it would require that either the magnitude of the intermediate scale polarization underwent a massive increase to over 300 mJy, or that the magnitude of the VLBI complex polarization for 3C 345 at 6 cm in epoch 1992.2 is incorrect by a large amount. The hybrid mapping of 3C 345 at 6 cm in epoch went extremely smoothly and involved a very large, and as discussed above, very well calibrated data set. If the magnitude of the intermediate scale polarization did undergo an increase, then there seems little reason to expect that the position angle would remain the same, since a shock of unknown geometry would likely be involved. It seems more plausible to assume that there has been a change in the



Epoch and Band	VLA - VLBI	VLA - VLBI	Sgl Dish - VLA	Sgl Dish - VLA
	lPl (mJy)	$\chi$ (deg)	lPl (mJy)	$\chi$ (deg)
1990.4 C Band	650	16	70	-10
1990.4 X Band	455	-18	290	-26
1992.2 C Band	378	-48	83	54
1992.2 X Band	523	-33	100	-31

Table 25: Polarization on Intermediate Scales in 3C 273.

intermediate scale polarization, involving a mild increase in flux and a change in position angle. This is also plausible because of the migration of the relatively strong C2 component into the intermediate structure.

Nevertheless, the appearance of a change in the position angle of the intermediate scale structure should not be ignored. In the X band the intermediate scale polarization is 108 mJy at  $35^\circ$ , giving a position angle more consistent with the earlier measurements. However, the spectral indices of jet components will lead to their having a smaller effect at higher frequencies in the intermediate scale structure. Nevertheless the results presented here for 3C 345 should be taken as tentative until confirmation can be made in future polarization VLBI observations.

Table 24 summarizes the intermediate scale polarization results for 3C 345, while table 25 summarizes them for 3C 273. Care should be used in interpreting the position angle on the measurements between single dish and VLA scales, since the measurements from the VLA and a single dish may give roughly the same results. A small difference in position angle will give the difference a position angle very different from either of the two measurements. It is more likely that there is a small error in the position angle measurement instead.

### *3. Alignment of Total Intensity and Complex Polarization Maps*

The measurement of a number of important physical properties in quasars relies upon the alignment of the complex polarization image with the total intensity image (*e.g.* fractional polarization which helps to constrain magnetic field properties). For Faraday rotation mapping, where alignment is most conveniently made by aligning the total intensity images independent of the more sparse polarization images, alignment plays a vital role. A substantial misalignment would shift the polarization image at one frequency relative to that at another. The result would be to compare different regions of the source. (The concern over this issue led to the inclusion of a number of possible alignments in chapters 7 and 8.)

The question of the reliability of the alignment of the images is treated by Roberts, Wardle and Brown (Roberts, Wardle and Brown, 1994). Their results indicate that the alignment is generally good to within a few tenths of the beamwidths in the CLEAN beam. The Faraday rotation maps presented in chapters 7 and 8 include shifts which cover a larger area than this.

### *4. Alignment of Maps made at Different Frequencies*

Because VLBI maps do not retain absolute phase information, the absolute position of the source on the sky is lost during mapping. The problem of frequency dependent shifts in the positions of VLBI components has been discussed for both 3C 345 and 3C 273 by observers in measuring the spectral indices of the components. For 3C 345, the curvature in the jet has been used to align maps made at frequencies from 1.7 GHz to 22.2 GHz by a number of authors (Cohen *et al.*, 1983; Biretta, Moore and Cohen, 1986; Rantakyrö *et al.*, 1992; Unwin and Wehrle, 1992). The most detailed study of possible component shifts was done by Biretta, Moore, and Cohen, and a frequency dependent shift of 0.05 to 0.30 mas was found for components between 5.0 GHz and 10.7 GHz, with the higher frequency components

shifted farther from the core (Biretta, Moore and Cohen, 1986). Since the observing frequencies used here are more closely spaced than this, an upper limit in a component shift of roughly 0.20 mas (or one pixel) is reasonable. The shift which gave the best alignment of the jet components and curvature (figure 59) results in a component shift between the two frequencies of this amount.

For 3C 273, the slight curvature in the inner jet has been used by most authors to establish alignment at multiple frequencies from 2.3 GHz to 43 GHz (Cohen *et al.*, 1983; Unwin *et al.*, 1985; Krichbaum *et al.*, 1990). The results indicate no frequency dependent shift of component positions in this source, which is the result used to produce the Faraday rotation map in figure 82.

It appears from previous work on alignment of multiple frequency VLBI images and from this work, that the frequency dependent shifts in component positions should be rather small. The use of multiple possible shifts in chapters 7 and 8 should cover the possibility of misalignment of the maps used in making the Faraday rotation measure maps.

##### *5. Possible Errors from Resolution Effects in Faraday Rotation Maps*

In addition to the sources of error dealt with above, a further problem must be discussed for the Faraday rotation maps. Since at least two frequencies must be used to produce a Faraday rotation map, the intrinsic resolution of the interferometer arrays used to produce the maps is presently different in VLBI. Unlike the VLA which has the capacity to use separate arrays to match UV spacings between different frequencies, the VLBI network is a fixed array. This introduces a scaling of the array of  $6/3.6 = 1.7$  in the present observations. In order to counteract the different resolutions (which also arise from the removal of data which changes the UV coverage), weighting of the data set is used to match resolutions between the two

frequencies. However, there remains the question of the intrinsic resolution of the interferometers.

The primary place that effects due to different resolutions are likely to appear is at points where the flux or position angle is undergoing a rapid change. In these observations, where the position angle varies gradually most of the time, the primary effect should be seen on the edges of polarized components. For this reason, the numbers cited throughout this work are for the central regions of the polarized components, where resolution effects should be minimal.

## *B. Quasar and BL Lac Magnetic Field Structure*

### *1. Faraday Rotation and Magnetic Field Direction in OJ 287*

Not surprisingly, OJ 287 shows virtually no Faraday rotation in these observations. Since the source is unresolved, and since the VLA observations align the electric field position angle of the core, there could be no other result. Nevertheless, in terms of the overall possible results for an object, the lack of Faraday rotation in OJ 287, a BL Lac object, should not be ignored. Since BL Lacs are believed to have weak NLRs and since the Faraday rotation observed on parsec scales should occur in the NLR (see chapter 4), the lack of Faraday rotation in OJ 287 makes sense.

The reconstructed magnetic field in OJ 287 has been observed for a number of years (Roberts, Gabuzda and Wardle 1987; Cawthorne and Wardle 1988; Roberts, Wardle and Brown 1990; Cawthorne *et al*, 1993a; Cawthorne *et al*, 1993b). It lies perpendicular to the known parsec scale jet axis, as do the magnetic fields in the other BL Lac objects presented in the works cited here. The lack of Faraday rotation in OJ 287 confirms the magnetic field direction for this BL Lac.

## *2. Magnetic Field Direction in 3C 345 and 3C 273*

The reconstructed magnetic field maps presented in chapters 7 and 8 show remarkable consistency. Although the results from the epoch 1990.4 observations should not be treated as reliable, they agree with the overall results of the high quality epoch 1992.2 observations. In each quasar, the results of Faraday rotation measurements are to align the magnetic field in the parsec scale jet with the jet axis.

For 3C 345 this result follows from the virtual lack of Faraday rotation beyond two milliarcseconds from the core in the jet. The results of previous observations, presented in chapter 5, suggested a well aligned magnetic field which has been maintained for a number of years. The measurement of minimal Faraday rotation in this source confirms this alignment.

For 3C 273 the results are much more dramatic. The previous polarization VLBI observations of this source have shown a position angle which varies along the jet and which does not lead to a reconstructed magnetic field perpendicular to the jet axis (see chapter 5). The results presented in chapter 8 suggest that the misalignment of the reconstructed magnetic field is not indicative of an actual misalignment, but instead results from the presence of a Faraday rotation. Taking the measured Faraday rotation into account leads to the reconstruction of a magnetic field which is extremely well aligned with the jet axis.

The typical errors expected in the Faraday rotation maps are on the order of a few tens of  $\text{rad/m}^2$  and this would change the inferred magnetic field directions by a few degrees. These possible errors do not change the overall alignment of the magnetic fields in the reconstructed field directions.

## *3. Magnetic Fields in Quasars and BL Lacs*

Previous polarization VLBI observations showed a distinct difference between quasars and BL Lacs on the parsec scale. BL Lacs tend to have short jets with

reconstructed magnetic fields lying perpendicular to the jet axis, while quasars have longer jets with reconstructed magnetic fields lying within roughly 45 degrees of the jet axis, but with most quasars tending to better alignment (Roberts, Wardle and Brown, 1990; Cawthorne *et al.*, 1993a; Cawthorne *et al.*, 1993b). The scatter in the alignment data is much smaller for BL Lacs (strongly bunched reconstructed fields lying near 90° to the jet axis) than for quasars.

The results presented here support a possible explanation for these results presented in the works cited above. BL Lacs, with their weak NLRs, should show little Faraday rotation on the parsec scale. If magnetic fields in BL Lacs do align perpendicular to the jet axis, then the lack of Faraday rotation would lead to observations showing reconstructed magnetic field directions perpendicular to the jet axis. For quasars, with their stronger and more varied NLRs, there should be cases of strong Faraday rotation and cases of weaker rotation. If the magnetic fields are truly aligned with the jet axis, then the reconstructed magnetic fields would tend to bunch near alignment but with a large scatter, due to the large number of possible Faraday rotation measures on the parsec scale. Measurement of the Faraday rotation on parsec scales should then lead to reconstruction of the true, aligned magnetic field direction as it did here for 3C 273.

#### *4. Implications for Unified Schemes*

The results for the parsec scale magnetic fields of quasars and BL Lacs noted above strengthen the case against the unification of BL Lacs and quasars discussed in chapter 1. In such a unification, BL Lacs would be quasars with highly beamed cores (beaming within the critical angle) and therefore should show the same properties as quasars in respects not affected by this beaming. Since this requires that the reconstructed magnetic field direction be the same in both types of objects, this unification can be ruled out more forcefully because of this work.

The unification scheme linking CDQs, LDQs, and FR II radio galaxies is not directly affected by this work. The intermediate scale polarization measured for 3C 273 agrees with previous results, as noted above, and together with the results for 3C 345 is consistent with such a unification.

### *C. Properties for External Faraday Screens*

#### *1. 3C 273 Integrated LOS Magnetic Field and Electron Density*

If the Faraday rotation observed is external and if it obeys a  $\lambda^2$  law, then the integrated electron density and line of sight magnetic field is determined by these measurements. Unfortunately, it is unclear if the rotation is external or even if the  $\lambda^2$  law is valid, since only two frequencies were used. However, the calculation for 3C 273 is straightforward and gives measures of roughly  $10^{15}$  G-cm<sup>-2</sup>, which is quite small considering the expected pathlength through the NLR. Naturally, VLA scale measurements have already shown that the large Faraday rotation expected from the NLR is not seen (see chapter 4).

The gradient seen in the Faraday rotation is probably real, although the problems in interpreting the Faraday rotation maps because of unmatched intrinsic resolutions should not be ignored. If the rotation arises in the NLR and if the gradient is confirmed, then the NLR must show changes in magnetic field structure or electron density on the scale of parsecs. Since the NLR emission is known to arise in clouds, this result is not surprising, if the Faraday rotation arises in clouds and not in the intercloud medium.

Information which might prove that the Faraday rotation arises in the NLR must await the introduction of Faraday rotation mapping using at least three observing frequencies. Unfortunately, the present measurements simply do not allow

key points to be understood about the Faraday rotation, which are necessary to interpretation of exactly what the maps indicate about the NLR.

### *2. Limits on 3C 345 Integrated LOS Magnetic Field and Electron Density*

The quasar 3C 345 shows virtually no Faraday rotation. The highest rotation is seen right at the point where the jet might be undergoing rapid changes in opacity, which introduces an uncertainty in the overall electric field direction of the radiation, since the beam is sampling many emission points which might have different emitted directions between 3.6 and 6 cm. If this knot is excluded, then the peak of the Faraday rotation is under  $50 \text{ rad-m}^{-2}$ , and is likely to be much lower (*i.e.* figure 59 in chapter 7). In the most believable Faraday rotation map, the maximum reliable measurement was only  $20 \text{ rad-m}^{-2}$ , and the jet had a measure of roughly zero. Since the core is deeper within the NLR than the jet components, it would be more likely to be covered if NLR clouds were responsible for the Faraday rotation, so that this result makes the most sense in these terms as well as the best matching of the maps. The maximum Faraday rotation appears to be down roughly an order of magnitude from that seen in 3C 273, so that the integrated line of sight magnetic field and electron density also drop an order of magnitude. It is also likely that there is no intervening Faraday screen between us and the jet.

### *3. Overall Implications for Faraday Screens*

Although the above results do not let us say much about the material giving rise to the observed Faraday rotation, it is consistent with the results of VLA observations presented in chapter 4. For 3C 345 there is virtually no rotation and very little indication of depolarization. This leads to requirements on the cell size in the NLR which are less stringent (*i.e.* larger) than those given in chapter 4 from VLA scale measurements.



### Percentage Polarization in Jet of 3C 273

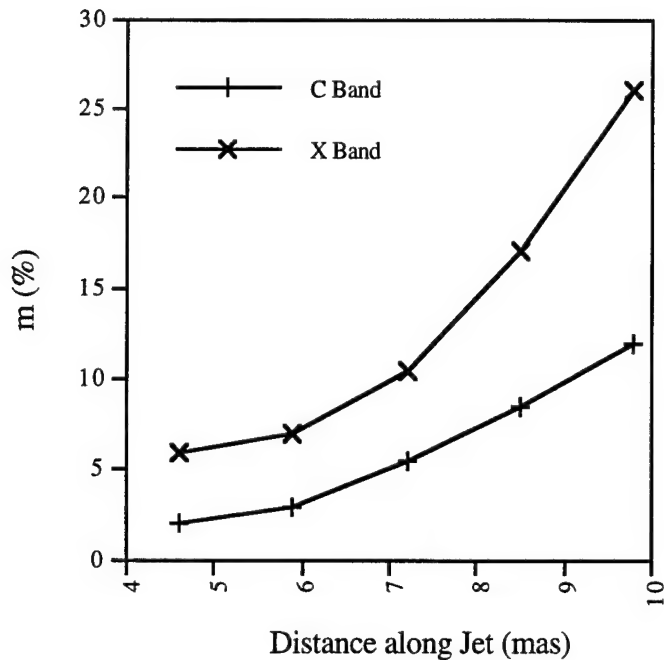


Figure 92: The fractional polarization along the jet in 3C 273 at X band and C band.

In 3C 273 the situation is very different. Figure 92 gives the fractional polarization along the jet at 3.6 and 6 cm. Only the first two points are reliable at 3.6 cm, since the dynamic range of the total intensity image does not allow reliable determination of the total intensity farther out in the jet. However all the data is consistent with a depolarization of roughly 50% between the two frequencies.

In figure 93, the geometry of an external Faraday screen lying in the NLR of 3C 273 is shown. The radio waves emitted by the jet pass through the NLR with a pathlength of  $L$ . The beam of the interferometer determines the width of the volume sampled for each point in the jet. For linearly polarized radiation passing through a

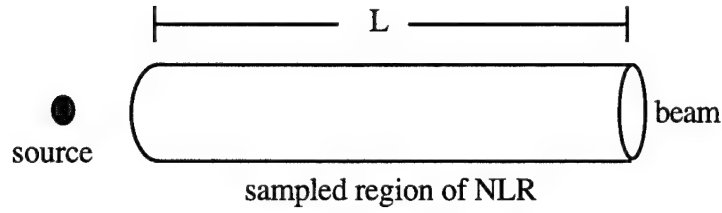


Figure 93: The region of the NLR responsible for the Faraday rotation observed in parsec scale maps. The object on the left emits the radiation and is unresolved or just resolved by the beam of the telescope.

medium with a Gaussian distribution of fluctuations, the magnitude of the polarization observed at a wavelength  $\lambda$  is (Burn, 1966)

$$P(\lambda) = P_0 e^{-2K^2 (n_e B_{\parallel})^2 d_f L \lambda^4} \quad (9.6)$$

where  $P_0$  is the emitted magnitude of polarization,  $K$  is  $2.62 \times 10^{-17}$  in c.g.s. units,  $n_e$  is the electron density in a fluctuation,  $B_{\parallel}$  is the parallel component of the magnetic field in a fluctuation,  $d_f$  is the scale size of the fluctuations, and  $L$  is the pathlength through the medium. Using the measurements at the two frequencies, the ratio of  $P(\lambda)$  between 3.6 cm and 6 cm can be formed. Inserting the values in this ratio and solving for  $d_f$  gives

$$d_f = 4.48 \times 10^{29} n_e^{-2} B_{\parallel}^{-2} L^{-1} \quad (9.7)$$

where all quantities are in c.g.s. units. For the geometry shown in figure 93, the number of cells is given by the volume of the sampled cylinder divided by the volume of a single element, or

$$N = \frac{\pi a^2 L}{d_f^3} \quad (9.8)$$

where  $a$  is half the size of the beam, or roughly 1 pc. If the magnetic field is assumed to be random, then the parallel component is given by  $B_{\parallel} = (3N)^{-1/2} B$ . Inserting these

values into equation 9.7 and assuming a field of roughly 1 mG, an electron density of  $10 \text{ cm}^{-3}$  in the NLR (from arguments for cloud confinement, see chapter 4), and a pathlength of 100 pc gives  $d_f = 0.3 \text{ pc}$ . But in chapter 4, it was shown that detectable polarization at 20 cm leads to a requirement that  $d_f$  be less than 0.00001 pc. Allowing Faraday depolarization to arise only in the NLR clouds does not alleviate this problem, but instead requires estimates of more than  $10^{22}$  cells when combined with cloud sizes suggested by VLA measurements based on  $3 \times 10^5$  cells.

The lack of a strong drop off in polarization with wavelength has led to an analysis of Faraday depolarization which modifies the model from Burns to allow intermediate scale sizes in the Faraday screen (Tribble, 1991). For a linear source at long wavelengths of observation, the polarization is given by

$$P(\lambda) = P_0 \frac{\sqrt{\ln 2} d_f / w}{\sqrt{2 d_f L K n_e B_{\parallel} \lambda^2}} \quad (9.9)$$

where  $w$  is the FWHM of the beam and the other values are as given before. In this situation, the polarization drops much more slowly with wavelength than in the model from Burns. Unfortunately, to fully analyze the situation, the value of  $P_0$  is needed, since it is possible in this model to get a 50% drop in polarized flux far out along the curve (as opposed to Burn, where the curve quickly reaches zero polarized flux). It is likely however, that the strong disagreement between the VLA results and the results presented here will remain, since the discrepancy using Burn is greater than four orders of magnitude.

These results can only be explained if the media lying in front of the emission points of the 6 cm and the 20 cm radiation are unbelievably different. This is unlikely to be the case, since the 20 cm radiation also arises in the jet and since it is unlikely

that the NLR medium is so finely structured. As such, it is necessary to also consider the more complicated case of internal Faraday depolarization and rotation.

#### *D. Internal Faraday Rotation*

The case of internal Faraday rotation in a synchrotron emitting plasma is much more complicated. Previous studies have shown that the presence of any detectable linearly polarized emission in quasars requires that there be a substantial difference in the populations of the relativistic and non-relativistic electrons in the plasma (Wardle, 1977; Jones and O'Dell, 1977). Naturally this means that we have no reliable way of estimating the density of cold electrons (which give rise to Faraday rotation) in the synchrotron emitting medium.

If the magnetic field in the quasar jet is composed of both a random and an ordered component, which appears to be required by observations and by the best models of these jets (Brown, Roberts, and Wardle, 1994; Wardle *et al.*, 1994), then the polarization observed at wavelength  $\lambda$  is (Burn, 1966)

$$P(\lambda) = P_0 \int_0^{\infty} f(x) e^{-2sx} dx \quad (9.10)$$

$$\text{with } s = \frac{(Kn_e B_r)^2 d}{2} \lambda^4 - iKn_e B_z \lambda^2$$

where  $f(x)$  is the fraction of the source radiation transversing the pathlength  $x$  to  $x + dx$ ,  $K$  is the constant given above,  $n_e$  is the cold electron density,  $B_r$  is the random component of the magnetic field,  $B_z$  is the uniform component of the magnetic field along the line of sight, and  $d$  is the scale size of the fluctuations.  $P_0$  is the intrinsic polarization of the source given by

$$P_0 = P_\gamma \frac{H_0^2}{H_0^2 + H_r^2} \quad (9.11)$$

where  $P_\gamma$  is the polarization for a power law distribution of electrons in a totally uniform magnetic field.

Since very little is known about the structure of the jets in terms of both the magnetic fields and cold electron densities, the simplest approach to equation 9.10 is to assume that the uniform field component is aligned with the jet axis and that the radiation is emitted perpendicular to this axis in the rest frame the jet. This maximizes the superluminal motion observed and reduces the second component in s in equation 9.10 to zero. It is unclear if this assumption is valid, although it is clear that the emission in the rest frame must be somewhat perpendicular to the jet in order to obtain the necessary conditions for superluminal motion and beaming, so that the assumption is the most reasonable simplifying assumption to make.

Equation 9.10 is solved by Burn for two geometries, the uniformly emitting sphere and the uniformly emitting slab (Burn, 1966). In the case of the slab, the observed polarization reduces to

$$P(\lambda) = P_0 \frac{1 - e^{-s}}{s} \quad (9.12)$$

while for the sphere it reduces to

$$P(\lambda) = P_0 \frac{3 \left[ (s+1)e^{-s} + \frac{1}{2}s^2 - 1 \right]}{s^3} \quad (9.13)$$

which can both be solved numerically for the depolarization observed in 3C 273. For the situation discussed above, where the emission in the rest frame is depolarized only by the random component of the magnetic field, s becomes

$$s = C\lambda^4 = (Kn_e B_r)^2 dL\lambda^4 \quad (9.14)$$

and the numerical solution determines C. For the slab geometry, C is found to be  $1.48 \times 10^{-3}$  in c.g.s. units, while for the sphere geometry, C is  $1.33 \times 10^{-3}$  in c.g.s.

units. While the solution for the sphere is fairly robust, changing only in the fourth significant figure for ratios of the polarization between the two frequencies of 0.4 to 0.6, the solution for the slab varies between  $1.03 \times 10^{-3}$  and  $2.15 \times 10^{-3}$  in the same range. Using the solution for the sphere and taking  $L$  to be 1 parsec, the scale size of fluctuations of the random component of the magnetic field is

$$d = 6.1 \times 10^{11} n_e^{-2} B_r^{-2} \quad (9.15)$$

which yields a cell size that permits a random field component in the jet. The factor of two introduced from the sensitivity of the slab model to the ratio of the polarization at the two wavelengths does not substantially change this result.

The observed Faraday rotation indicates that the simple model given above cannot be fully correct. A totally random field would naturally lead to no overall Faraday rotation, so some component of the uniform field would have to be involved. It is not useful to introduce such a field in determining  $d$ , since its effect should be small, however it is necessary for a discussion of the observed Faraday rotation. The addition of a uniform field leads to a  $\lambda^2$  law of rotation when the depolarization is small (Burn, 1966, figure 2). The range following the  $\lambda^2$  law is larger in the more realistic spherical model, however for the ~50% depolarization observed in 3C 273 the rotation should go roughly as  $\lambda^2$  in both models.

The models of internal Faraday rotation shown above are unrealistic and more work needs to be done on the topic in light of the results of the parsec scale Faraday rotation and depolarization observed in 3C 273. The results of the depolarization measurements on the jet of 3C 273 suggest that the Faraday depolarization is not arising in an external screen. Then the depolarization must be arising within the source itself, and the direct measurement of the depolarization given here is consistent with a cell size for the magnetic field fluctuations which could appear in the jet.

Further, the rotation measure correlates with the total intensity of the jet, which indicates that there is a link between the jet and the Faraday rotation, suggesting internal Faraday rotation in addition to depolarization.

## X. Conclusion

This work presents the first extension of polarization VLBI measurements to 8.4 GHz and the first multiple frequency polarization VLBI observations. The dual frequency observations allow the mapping of the Faraday rotation in quasars on the parsec scale, although the assumption of a  $\lambda^2$  dependence of the rotation on wavelength must be made, since only two wavelengths were used. The well-known  $n\pi$  ambiguity is unlikely to be a problem, since an additional turn in position angle would lead to unreasonably high rotation measures.

The measurements of the Faraday rotation in the quasars 3C 345 and 3C 273 give roughly zero and roughly 150 rad-m<sup>-2</sup> respectively and allow the reconstruction of the intrinsic magnetic field direction within the parsec scale jets in these sources. In both cases, the magnetic field is inferred to align closely with the jet axis after a few parsecs from the radio core, even though previous single frequency observations suggested a very strong misalignment in 3C 273. The reconstruction of the magnetic field relies upon the  $\lambda^2$  dependence of the rotation, but this is reasonable for these sources given the limited depolarization found and the possible sources for the depolarization. For the BL Lacertae object OJ 287, there is no detectable Faraday rotation and the reconstructed magnetic field lies perpendicular to the jet axis.

Previous polarization VLBI observations suggested a sharp division between quasars and BL Lacertae objects in the alignment of the parsec scale magnetic fields.



This work confirms this division for the three sources cited above. The measurement is most critical for the quasar 3C 273, which showed substantial misalignment between the magnetic field and the jet axis in 6 cm observations, indicating a source that possibly did not conform with the sharp division. The reconstruction of an intrinsic magnetic field aligned strongly with the jet through the application of the Faraday rotation correction supports the BL Lac/quasar dichotomy and suggests that BL Lacs and quasars are indeed two different types of AGN. Any unified scheme which attempts to link quasars and BL Lacs must take into account their differences at parsec scales.

The measurements also place stringent limits on any Faraday screen in the NLR of these quasars. For 3C 345, this limit is no more stringent than those derived from VLA measurements, however for 3C 273 the situation is rather dramatic. Because 3C 273 shows resolved Faraday rotation structure with a depolarization of roughly 50% between 3.6 and 6 cm, a direct measure of the size of the fluctuations of the magnetic field in the NLR is possible. Using the standard model of Faraday depolarization applied to previous VLA measurements, a scale size for the fluctuations of 0.3 pc results. Previous VLA measurements at 20 cm require a scale size at least four orders of magnitude smaller, indicating that the depolarization cannot arise in the NLR of 3C 273.

The failure of the model of an external Faraday screen to account for the observed depolarization, together with the correlation between total intensity and rotation measure in 3C 273, suggest that internal Faraday rotation could be occurring. Application of the standard model for internal Faraday rotation in geometries for both a slab and a sphere yield scale sizes for fluctuations which are consistent with the widths of the parsec scale jets. Such models also result in a  $\lambda^2$  dependence for rotation at limited depolarizations, such as those measured in 3C 273. However such models are

primitive and rest upon unreal assumptions about the source geometry. More realistic models should be developed in order to test the ability of internal Faraday rotation to account for the observed depolarization and Faraday rotation.

In the future, the VLBA will provide high quality polarization measurements routinely. Further, sections of the VLBA can be chosen to match spatial resolutions at multiple frequencies, providing more reliable Faraday rotation measurements on the parsec scale. From these measurements, the magnetic field structure of many quasars can be determined to see if they match the alignment seen here for 3C 345 and 3C 273, confirming predictions from previous polarization VLBI measurements.

It is especially important to extend polarization VLBI measurements to longer wavelengths in order to search for deviations from a  $\lambda^2$  rotation law. The lack of such a deviation over a significant degree of rotation ( $\geq 90^\circ$ ) can establish that the Faraday rotation is occurring externally to the source. In 3C 273, the rotation encompasses roughly  $50^\circ$  already, if the reconstruction of the magnetic field is accepted. The mapping of the milliarcsecond linearly polarized structure at a wavelength above 10 cm (simultaneously with polarization mapping at 3.6 cm and 6 cm) could settle the issue of where the Faraday rotation is occurring. If it truly is internal, then a deviation from the  $\lambda^2$  law would be expected. A lack of such a deviation would indicate external Faraday rotation and prove conclusively that either our models of the NLR or our models of Faraday depolarization have major errors.

This work proves the feasibility of using multiple frequency VLBI observations to create Faraday rotation maps on parsec scales. Such maps provide excellent probes of the NLR and jet Faraday structure, and these maps allow reconstruction of the intrinsic magnetic field directions in quasar jets from VLBI complex polarization maps. Completion of the VLBA provides the instrument which can significantly improve the results presented here by adding additional frequencies for VLBI complex polarization

mapping and by providing an instrument dedicated to routine VLBI observing. The increase in the number of sources observed and the frequency of observations on some sources should provide a relatively vast amount of data to confirm the results presented here.

In the end, the VLBA and future VLBI networks should provide answers to many of the questions regarding the inner regions of quasars. Through direct observations, the parsec scale jets can be studied to constrain the models of energy generation in the cores of these AGN. Through use of the polarized jets as a background source whose radiation passes through the NLR, characteristics of this region which gives rise to the characteristic line emission seen in AGN can be determined. If internal Faraday rotation and depolarization are shown to be present, measurements can constrain the cold electron densities and magnetic field structures in the jet.<sup>x</sup> Finally, if these techniques can be extended to higher frequencies, the BLR might also be probed in this way.

## **Appendix A: An Interactive Macintosh System for Modelling Relativistic Astrophysical Jets**

### *A. Introduction*

#### *1. Radio Sources and Jets*

With the rise of radio astronomy in the 1950's and 1960's, a new class of extragalactic object was discovered. These sources were characterized by powerful radio emission while their optical properties could not be explained. Generally the radio sources were coincident on the sky with giant elliptical galaxies, although the most interesting sources were identified with optical objects of stellar appearance (QSO's). With Schmidt's identification of the optical spectrum of the QSO coincident with the radio source 3C273, a quasar, as redshifted emission lines from gases (Schmidt, 1963), the power output of QSO's was realized to be prodigious. The quasars (the term originally referred only to the radio source, but now is generally used in place of QSO as well) showed rapid variability in a substantial fraction of their energy output on time scales of the order of days or weeks, which suggested that a remarkably small region was responsible for a large portion of the total energy output. If the variability is extreme, the quasar is referred to as a blazar.

The completion of the Very Large Array (VLA) in the early 1980's, developed after the success of earlier, less capable radio interferometers designed by Ryle and others, allowed imaging of quasars at radio wavelengths with arcsecond resolution. This led to the detailed images of radio-loud quasars which generally showed two lobes and often a jet leading from the core to the lobe on one side.

In order to obtain even higher resolution than that available from the VLA, interferometry between antennas spanning the diameter of the earth was developed. The output from the telescopes is mixed with lower frequency local oscillators and the lower frequency signal is recorded together with accurate timing marks on video tape. The correlation is then done using these tapes at a later time. This has become known as Very Long Baseline Interferometry (VLBI). The resulting milliarcsecond resolution far exceeds any other observational technique for detailed mapping of the core regions of quasars, and allows imaging of the regions within a few parsecs of the central engine driving the quasar.

## *2. Observations of Blazars*

Blazars show a number of remarkable properties in observations at all accessible wavelengths (this paragraph follows Impey, 1987). Optical observations show variabilities in the luminosity of the continuum component by factors up to 500 in time scales as short as one day. The percentage polarization of the continuum radiation is also variable, reaching as high as 46% but also falling below 3% during quiescent phases. These observations indicate the existence of a compact highly variable source, which, because of high linear polarization and a power law spectrum over several decades of frequency, is assumed to be a synchrotron source. The infrared power radiated, if isotropic, would exceed the Eddington limit for the compact core size resulting from restrictions imposed by the variability. However, X-ray observations show lower luminosity by several orders of magnitude than that expected from a

synchrotron source limited by self-Compton effects. These IR and X-ray luminosities require either new physics in the emission mechanism or relativistic beaming to avoid the inconsistencies between observations at different wavelengths.

VLBI observations, which have resolutions 1000 times greater than optical observations, have strengthened the case for relativistic beaming in blazars. Blazars, including BL Lacertae objects (BL Lacs) and optically violent variable quasars (OVVs), show a one-sided optically thin jet emerging from an optically thick core. These jets are not always aligned with the VLA jets. The components of the jets, points of increased surface brightness generally referred to as knots, appear to move at speeds substantially greater than the speed of light, so that the sources are called superluminal. Superluminal sources are core dominated radio sources (the core of the VLA images is brighter than the lobes) and many are blazars.

The apparent superluminal motion shown in some quasars is believed to be a result of relativistic effects, where the jet is moving close to our line of sight to the quasar. The emitting knots are moving relativistically towards the observer and therefore time compression increases the knot's transverse velocity in the observer's frame. This relativistic motion also allows an explanation of the rapid variability observed, since beaming effects greatly enhance the flux received from a source as long as the observer is in the beamed light cone, as well as compressing observed time scales by the Doppler factor. In addition a slight bend in the jet which moved the observer into the light cone would increase the flux rapidly, although in the rest frame of emission there would be no change in the luminosity. Since the IR emission appears to arise in a region smaller than the milliarcsecond jet imaged by VLBI, the IR continuum is also beamed, which avoids the problem of the luminosity exceeding the Eddington limit. The synchrotron source would then not be as luminous as determined assuming the received flux derives from isotropic emission in the observer's frame of

reference, so that the self-Compton limit is not exceeded eliminating the requirement for greater X-ray flux.

### *3. VLBI Polarization Observations*

Since synchrotron radiation appears to be the most likely emission source for the radio continuum observed in superluminal sources, the structure of the magnetic field within the VLBI jet can be determined by polarization measurements, because synchrotron radiation results in the electric vector of the electromagnetic wave being perpendicular to both the magnetic field of the source and the direction of propagation of the wave. The Brandeis Radioastronomy Group has developed the capability to make linear polarization measurements and maps on VLBI scales (*e.g.* Roberts, Wardle and Brown, 1994). These maps resolve many jets observed in superluminal sources and show the complex polarization of the radiation (percentage polarization and field direction). From measurements of the polarization, models of blazar jets can be constrained, sometimes with dramatic results (*e.g.* Cawthorne and Wardle, 1988). However, models which deal with relativistically beamed synchrotron sources show strong interactions between the variables which lead to beaming effects, so that it is not always clear how changes in the variables will affect the appearance of a source.

### *4. The Goal of the Macintosh Modelling System*

In order to explore the parameter space presented by even the simplest of relativistic jet models, an interactive system was developed to allow rapid variation in input parameters, such as fluid speed and jet angles, with immediate generation of the resulting image and observable properties. In general, initial parameters including the type of physical model (plane parallel shock or a partially parallel magnetic field with a random component), velocities, angles, and the number of knots are put into the system and a choice is made of any two applicable parameters to vary. The variations are then made using the mouse on an on-screen tablet with both the picture of the source model

(three-dimensional distribution of the knots) and the plane-of-the-sky image (the brightness distribution) being updated in real time. It is hoped that this easy-to-use system will allow a rapid investigation of parameter space to discover simple geometries and velocities which might give rise to flux distributions observed in blazars.

### *B. The Physical Models*

The emission of electromagnetic waves by synchrotron emission from a power law distribution of electrons with random pitch angles in realistically distributed magnetic fields has been studied in detail by a number of groups. In general, the problem is extremely difficult due to the expected complexity of real magnetic fields generated in quasar jets. Two basic models have emerged which allow simple modelling with the Macintosh system. The first involves a magnetic field which has both random and parallel (to the axis of the jet) components, which could be created by shear (although exactly how this process would work is unclear, see Scheuer, 1987). The second, a more refined model developed by Hughes, Aller, and Aller and modified by Cawthorne and Wardle, stipulates the compression of an initially random magnetic field in a relativistic shock, leading to a partially ordered field which in this case is perpendicular to the jet axis (Hughes, Aller and Aller, 1985; Cawthorne and Wardle, 1988).

#### *1. The Blandford and Königl Model*

In order to deal with problems presented by rapid variability in blazars, Blandford and Königl developed the initial relativistic jet model based on an original argument from Rees (Blandford and Königl, 1979; Rees, 1966). This model proposes a relativistically moving jet making a small angle to the line of sight of the observer, so that small bends in the rest frame of the jet cause large changes in received flux and



measured electric vector direction. These features match observations of variable quasar flux in the optical and radio regime, as well as explaining the apparent superluminal motion observed in VLBI radio maps. The Blandford and Königl model uses a completely ordered magnetic field and presents the aberration effects on the synchrotron emission. Since an astrophysical jet probably cannot generate a totally ordered field, the model used in the Macintosh system has been modified to use a partially ordered magnetic field with a random component as might result from shearing in the jet.

The Blandford and Königl model assumes a quasi-steady relativistic supersonic jet with emission arising from both the underlying jet and from shocks either propagating in the fluid or arising behind relativistically moving blobs which are accelerated by the jet. The stationary component seen in VLBI maps at multiple epochs is assumed to be an optically thick core with the superluminal components being the shocks. The shocks are a necessary addition to the model, since the observed synchrotron emission requires either unrealistically high total energy requirements to overcome expansion losses or local acceleration of the electrons, such as shocks would provide. Since the emitting fluid is moving relativistically, Doppler beaming greatly enhances the flux and a small bend in the jet can result in large changes in observed brightness. The observed electric vector direction of the radiation also varies with jet axis to line of sight angle and fluid speed, since these factors will change the angle at which the light that reaches the observer is emitted in the frame of reference of the emitting fluid, *i.e.* aberration of angles.

If we assume that the emitting region of the source, *i.e.* the knots or core, are spherical or optically thick, then the observed flux varies simply with Doppler factor as

$$S_{ob}(\nu) = S_{em}(\nu) D^{3+\alpha} \quad (\text{A.1})$$

where  $S_{ob}$  is the observed flux,  $S_{em}$  is the emitted flux,  $\alpha$  is the spectral index using the

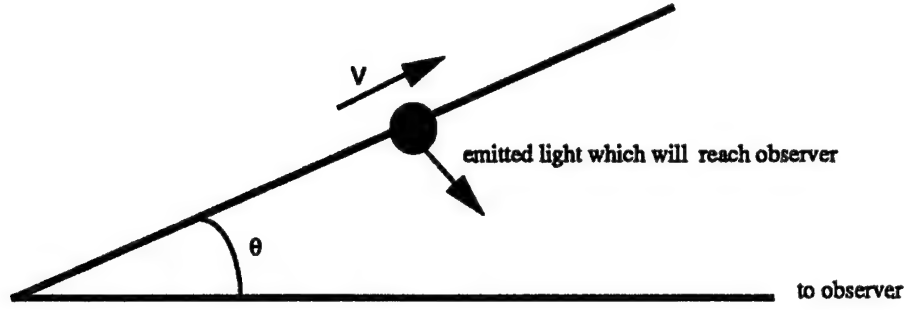


Figure A1: The geometry for beaming in a relativistic jet.

convention  $S \propto \nu^{-\alpha}$ ,  $\nu$  is the frequency of the light, and  $D$  is the Doppler factor given by

$$D = [\gamma(1 - \beta \cos \theta)]^{-1} \quad (\text{A.2})$$

with  $\gamma = (1 - \beta^2)^{-1/2}$ ,  $\beta = v/c$ , and  $\theta$  the angle between the line of sight and the direction of motion of the knot (the jet axis) in the observer's frame. Equation A.1 takes into account the redshifting of the light as well as geometrical and kinematical effects. It applies only to the individual knots and must be modified in cases where the knots are not resolved in order to take into account the apparent lifetimes of the knots.

The electric field vector angle will also be affected by the beaming. This is a result of the fact that the light received by a telescope has undergone aberration, so that the emitted angle in relation to the jet axis is not the received angle (see figure A1). In the extreme case where the jet axis to line of sight angle is very small but the velocity is near that of light, the photons received by the telescope are actually emitted perpendicular to the jet axis. The polarization properties therefore represent those seen by a comoving observer along side the jet, and not those seen by a comoving observer in front of the jet. From the requirement in synchrotron emission that the electric vector direction be perpendicular to the magnetic field direction, and using the geometry and

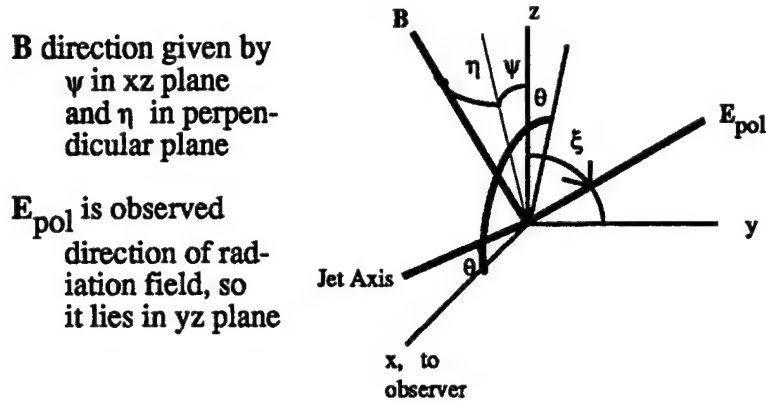


Figure A2: Coordinates and definitions used in equation A.3.

angles defined in figure A2, the direction of the electric vector on the plane-of-the-sky,  $\xi$ , can be shown to be given by

$$\tan \xi = \frac{\gamma^{-1} \sin \theta \sin \psi' + (\cos \theta - \beta) \cos \psi'}{\tan \eta' (1 - \beta \cos \theta)} \quad (A.3)$$

which differs from the Blandford and Königl formula only by the use of the primed angles (indicating measurement in the fluid frame) for the definition of the magnetic field directions and by the definition of the angle  $\theta$  in order to handle bends in the jet more easily;  $\theta$  here equals  $-\theta$  in the Blandford and Königl coordinates.

The magnetic field in the model is assumed to be a random field with a component parallel to the jet enhanced by some mechanism. This modification allows images generated from the model to be directly compared to VLBI polarization maps. Additionally the Macintosh incorporates the simplifying assumption that all emission comes from the knots, so that the equivalent of the Blandford and Königl emission from the underlying jet is emission from the random component of the magnetic field within the knot. The random component can be varied from 0 to 100% of the total field. Since particle acceleration is believed to occur in the knots, which are thought to be

shocks, eliminating the emission from an underlying jet may not result in changes significant at the level of the modelling.

## *2. The Cawthorne and Wardle Model*

The most detailed models for relativistic jets have been worked out for systems with plane parallel shocks within the jet. In these models an initially random field is compressed at the shock resulting in a field which has a preferred direction perpendicular to the jet axis. This is in opposition to the shear model, in which the preferred field direction is parallel to the jet axis. The basic concepts for such a shock were presented by Laing in 1980 as an explanation for extended synchrotron sources such as the Crab Nebula and radio lobes in galaxies (Laing, 1980). Such shocks are generally referred to as Laing sheets.

Hughes, Aller, and Aller used Laing sheets as the basis of a model for the outbursts observed by themselves in BL Lac at 4.8, 8.0, and 14.5 GHz (Aller, Aller and Hughes, 1985). These observations used a single dish and measured the total flux from BL Lac and did not resolve the individual shocks which the model predicted. Nevertheless their model gave good agreement with their observations. The knots observed in BL Lacs by VLBI are assumed to be points where a shock is compressing the fluid with an initially random magnetic field into a smaller volume (Laing sheet) with a partially ordered field. Observations using polarization VLBI by Gabuzda, Wardle, and Roberts on BL Lac object 0735+178 verified that the knots, where the Laing sheets are assumed to be present, do indeed show the high polarization with electric vectors parallel to the jet direction (*i.e.* magnetic field direction perpendicular to the jet axis)(Gabuzda, Wardle and Roberts, 1989). VLBI polarization studies of 0735+178 and VLBI polarization maps of other BL Lacs certainly support the Hughes, Aller, and Aller model (Gabuzda, 1988).

In studying the milliarcsecond polarization properties of BL Lac object OJ287 mapped by Roberts, Gabuzda, and Wardle, Cawthorne and Wardle discovered that the standard Hughes, Aller, and Aller model was inadequate to explain the extremely high polarization of a knot given its low superluminal apparent velocity (Roberts, Gabuzda and Wardle, 1987; Cawthorne and Wardle, 1988). However, the structure of the magnetic field in the knot suggests that a Laing sheet is indeed present, so they modified the Hughes, Aller, and Aller model so that the shock moves relative to the emitting fluid as expected from fluid dynamics. Then the speed of the pattern (*i.e.* the shock) is different from the fluid speed giving rise to the Doppler boosting of the flux.

The beaming of flux from the emitting fluid depends on the velocity of the fluid in relation to the observer. However the observable superluminal motion depends only on the velocity of the shock, so that the logical way to structure the fluid and shock velocities is by making the observable shock velocity the primary velocity. Then the fluid velocity in relation to the shock gives the second component of the fluid velocity in relation to the observer. Using the convention that a positive fluid velocity represents flow from the shock towards the nucleus of the quasar in the shock's frame of reference, the Doppler factor becomes

$$D_f = D_s D_{fs} = [\gamma(1 - \beta \cos \theta)]^{-1} [\gamma_f(1 - \beta_f \cos \theta_f)]^{-1} \quad (\text{A.4})$$

where  $D_f$  is the overall Doppler shift for the emitting fluid,  $D_s$  is the Doppler shift of the shock with its  $\beta$  and  $\theta$  measured in the observer's frame of reference and is given by the first term on the right hand side of the equation,  $D_{fs}$  is the Doppler shift of the fluid with  $\beta_f$  and  $\theta_f$  measured in the shock's frame of reference and is given by the second term on the right hand side of the equation,  $\gamma$  is for the shock's  $\beta$  and  $\gamma_f$  is for the fluid's  $\beta_f$  in relation to the shock. The beaming of flux from this emitting fluid is

$$S_{ob}(\nu) = S_{em}(\nu) D_s^{3+\alpha} D_{fs}^{2+\alpha} \quad (\text{A.5})$$

for an individual knot.

In this model of a Laing sheet within the jet, the magnetic field is always compressed in the plane perpendicular to the jet direction. The synchrotron emission then has an electric vector direction always parallel to the jet regardless of the angle of observation in relation to the jet axis. The observed linear polarization vector is therefore always parallel to the observed (projected) jet axis.

### *3. Common Considerations*

Although the Blandford and Königl and Cawthorne and Wardle models are quite different, they possess a number of similar features which must be taken into account when calculating the plane-of-the-sky brightness distribution which they would generate. The common considerations fall into four basic categories involving the observed superluminal motion and the observed positions of the knots and their polarization.

All of the observed properties of a jet undergo dramatic changes when even a small bend is introduced, since at highly relativistic velocities the aberration effects depend heavily on the angle between the velocity of the emitting fluid and the line of sight to the observer. As noted above, the light seen by the observer may even be emitted perpendicular to the jet and then beamed by relativistic effects at the observer. The exact angle of emission depends on the angle between the jet axis and the line of sight.

The introduction of a random bend to a jet can be parameterized by using two angles as shown in figure A3. The new jet axis forms a new angle to the line of sight to the observer as well as defining a new coordinate system, which is obtained from the old system by a rotation about the  $x$  axis. The angle  $\phi$  is in the  $xz$  plane, while the plane of  $\chi$  is perpendicular to this plane. The angle between the line of sight and the new jet axis,  $\epsilon$ , can be determined from spherical trigonometry and is given by

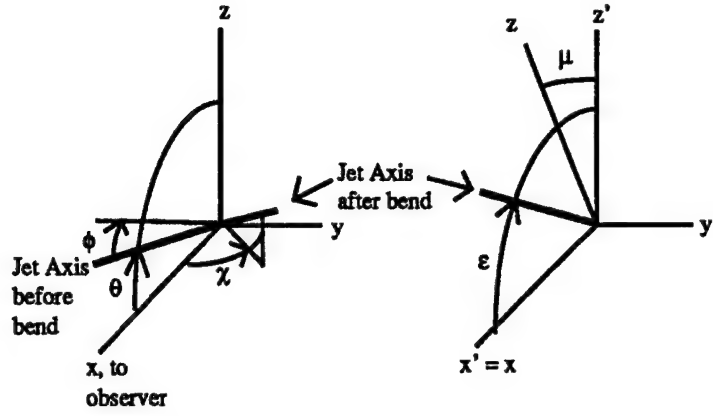


Figure A3: Jet geometry with a bend in the jet.

$$\cos \varepsilon = \cos(\phi + \theta) \cos \chi \quad (\text{A.6})$$

and  $\varepsilon$  must be used in place of  $\theta$  for all beaming considerations after the bend.

Since the Blandford and Königl model derives the electric vector direction in terms of the coordinate system formed by the line of sight axis, here the  $x$  axis, and the jet axis, the derived angle  $\xi$  will need to be rotated back into the  $xyz$  coordinate system from the  $x'y'z'$  system for knots which lie beyond the bend in the jet. This can be done by finding the angle between the  $z$  and  $z'$  axes,  $\mu$ , from the formulas of spherical trigonometry. The result is

$$\cos \mu = \frac{\cos \chi \sin(\theta + \phi)}{\sin \varepsilon} \quad (\text{A.7})$$

so that rotating  $\xi$  by  $\mu$  (with the sign of  $\mu$  given by the sign of  $\chi$ ) after calculating it from equation A.3 gives the correct electric vector direction.

For the Cawthorne and Wardle model the adjustment is simpler since the electric vector direction is always parallel to the jet axis. In this case the local jet axis after the bend is used instead of the axis before the bend to determine the electric vector direction.

From VLBI observations at different epochs, it has been determined that the knots in blazars show superluminal apparent motion across the plane-of-the-sky. The relativistic beaming model explains these observations, since the emitting regions are moving relativistically towards the observer and are therefore catching up with their own emission. Simple geometry gives an apparent velocity of

$$\beta_{app} = \frac{\beta \sin \theta}{1 - \beta \cos \theta} \quad (A.8)$$

where  $\beta_{app}$  is the apparent velocity determined from multiple epoch observations assuming a straight line motion of the knot between observations,  $\beta$  is the actual velocity of the knot relative to the observer, and  $\theta$  is the angle between the actual velocity and the line of sight measured in the observer's frame of reference.

The three dimensional position of the knots is calculated from the values of the angles defined for the bend in the jet using spherical trigonometry and the assumption that the knots are equally spaced along the jet length. Using the coordinate system defined in figure A2, the position of each knot before the bend is given by

$$\begin{aligned} x_n &= n \cos \theta \\ y_n &= 0 \\ z_n &= n \sin \theta \end{aligned} \quad (A.9)$$

where  $n$  is the number of the knot counting out from the core and the interknot spacing is the unit length with the zero of the coordinate system at the core. After the bend, which occurs halfway between the middle two knots, the locations are

$$\begin{aligned} x_n &= L_1 \cos \theta + L_2 \cos \chi \cos \phi \cos \theta - L_2 \sin \phi \sin \theta \\ y_n &= L_2 \sin \chi \cos \phi \\ z_n &= L_1 \sin \theta + L_2 \cos \chi \cos \phi \sin \theta + L_2 \sin \phi \cos \theta \end{aligned} \quad (A.10)$$



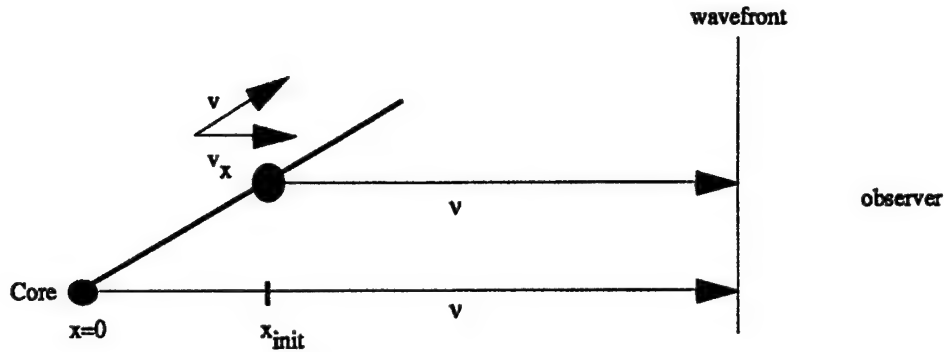


Figure A4: Propagation of a wavefront from a relativistic jet.

where  $n$  is the number of the knot,  $N$  is the total number of knots in the jet,  $L_1 = (N+1)/2$  is the distance to the bend, and  $L_2 = (2n-N-1)/2$  is the distance from the bend to the knot.

The light which arrives at a telescope from the knots of a jet with relativistic velocity and a jet axis making a small angle to the line of sight shows each knot at a different time in the jet's frame of reference (this is technically valid only for a straight jet with a constant velocity since otherwise it is impossible to synchronize clocks at each knot, however the arguments for taking into account such effects apply generally).

Figure A4 shows the general situation with the wavefront which will strike the telescope containing light from each knot at a different delay. Since the source is assumed to be constituted of knots along a jet, some knots are closer to us than others, so that the position of the knots must be adjusted to take into account how they were positioned when the light was actually emitted. The light from the knots farther from the observer must catch up with the nearer knot, but during that time the nearer knot will have advanced along the jet axis. The time delay,  $t$ , between the times of emission of light which forms the wavefront from a knot and from the core is

$$t = \frac{x_{init}}{c(1 - \beta \cos \theta)} \quad (\text{A.11})$$

where  $x_{init}$  is the distance along the line of sight axis between the knot and the core without delay effects (as in equation A.9),  $\beta$  is the speed of the knot, and  $\theta$  is the angle between the line of sight and the jet axis. Since the distance travelled by the knot during this time is  $\beta ct$ , the coordinates of the knot when the wavefront reaches it (*i.e.* when the light is emitted which hits the telescope coincident with the light from the core) are

$$\begin{aligned} x &= x_{init} \left( 1 + \frac{\beta \cos \theta}{1 - \beta \cos \theta} \right) \\ y &= 0 \\ z &= z_{init} + x_{init} \left( 1 + \frac{\beta \sin \theta}{1 - \beta \cos \theta} \right) \end{aligned} \quad (\text{A.12})$$

assuming that the knot does not reach the bend in the jet in that time and where  $x_{init}$  and  $z_{init}$  give its position before taking into account the time delay effect.

If the knot has a high velocity in the  $x$  direction, it might reach the bend before the light wavefront reaches it. In this case, the time delay given by equation A.11 is greater than the time it takes a knot to reach the bend,  $t_{bend}$ , which is given by

$$t_{bend} = \frac{x_{bend} - x_{init}}{v \cos \theta} \quad (\text{A.13})$$

where  $x_{bend}$  is the  $x$  coordinate of the bend given by  $L_1$  in equation A.10 and  $v$  is the velocity of the knot. At this point the knot is still nearer the observer than the wavefront, so there is an additional time delay given by

$$t_{diff} = \frac{x_{bend} - ct_{bend}}{c[1 - \beta(\cos \chi \cos \phi \cos \theta - \sin \phi \sin \theta)]} \quad (\text{A.14})$$

where the angles are those defined for the bend in the jet in figure A3. The position of the knot at the point where the wavefront reaches it is then given by

$$\begin{aligned}
x &= x_{bend} + vt_{diff}(\cos \chi \cos \phi \cos \theta - \sin \phi \sin \theta) \\
y &= vt_{diff} \sin \chi \cos \phi \\
z &= z_{bend} + vt_{diff}(\cos \chi \cos \phi \sin \theta - \sin \phi \cos \theta)
\end{aligned} \tag{A.15}$$

where  $t_{diff}$  is given in equation A.14.

The final possibility in taking into account the time delay effects is that the knot is initially beyond the bend of the jet. Then the situation is exactly like a knot which does not reach the bend, except that the more complex relations incorporating the bend angles must be used in place of  $\theta$ . Equation A.11 can be directly modified to give

$$t = \frac{x_{init}}{c[1 - \beta(\cos \chi \cos \phi \cos \theta - \sin \phi \sin \theta)]} \tag{A.16}$$

where  $t$  is again the time delay for the wavefront to reach the knot. The adjusted positions are then calculated as in equation A.15 substituting  $t$  for  $t_{diff}$ , except that the initial positions for the knot in  $x$ ,  $y$ , and  $z$  must be added while the coordinates of the bend in  $x$  and  $z$  are eliminated.

In the modified Blandford and Königl model, the percentage polarization varies with the assumption of a parallel to random field ratio and the angle between the jet axis and the emission direction of the light received by the observer. For example, if the light was emitted perpendicularly to the jet and beamed to the observer, the percentage polarization would just equal the percentage of the parallel component of the field. In contrast, if the light was emitted along the jet axis, the light emitted by electrons spiraling around the parallel component would not be visible so that the percentage polarization would be zero. In between these extremes, the percentage polarization varies with angle by

$$m = m_0 \frac{B_p^2 \cos^2 \epsilon}{B_p^2 \cos^2 \epsilon + B_r^2} \tag{A.17}$$

where  $m$  is the percentage polarization,  $B_p$  is the percentage of the field which is parallel,  $B_r$  is the percentage of the field which is random,  $m_0$  is the maximum polarization for the given power law distribution of electrons in a completely parallel field,  $\epsilon$  is the angle at which the light leaves the jet with 0 degrees being perpendicular to the jet axis and should not be confused with the angle between the line of sight and the jet axis. The angle  $\epsilon$  is related to the jet axis to line of sight angle by aberration so that

$$\sin \epsilon = \frac{\cos \theta - \beta}{1 - \beta \cos \theta} \quad (\text{A.18})$$

gives the transformation from the jet axis to line of sight angle to the emission angle.

In the Cawthorne and Wardle model, the percentage polarization varies with the assumed compression factor of the shock,  $k$ , as well as the angle between the shock plane and the direction of emission. Then the percentage polarization is given by

$$m = m_0 \frac{(1 - k^2) \cos^2 \epsilon}{2 - (1 - k^2) \cos^2 \epsilon} \quad (\text{A.19})$$

where  $k$  gives the size of a unit length after compression and the other variables are the same as above, so that  $\epsilon$  is measured perpendicular to the jet in the plane of the shock.

Using relativistic fluid dynamics within the limits where the fluid speed lies between  $1/3$  and  $1/\sqrt{3}$ , this equation can be rewritten as

$$m = m_0 \frac{\left[ \sin^2 \theta'_s (1 - \beta_f^2) / (1 + \beta_f \cos \theta'_s)^2 \right]}{\left[ 2(1 - \beta_f^2) / (1 - 9\beta_f^4) \right] - \left[ \sin^2 \theta'_s (1 - \beta_f^2) / (1 + \beta_f \cos \theta'_s)^2 \right]} \quad (\text{A.20})$$

where  $B_f$  is the speed of the emitting (shocked) fluid and  $\theta'_s$  is the angle between the jet axis and the line of sight, both measured in the reference frame of the shock. This angle must be calculated from the observed angle by the aberration formula.

### *C. VLBI and Mapping*

Very Long Baseline Interferometry offers the highest resolution tool available to astronomers. However, the fact that the resolution obtained is equivalent to a single antenna of the diameter of the longest baseline indicates that there is a substantial amount of information lost, which would be present if the aperture were filled, *i.e.* if the antenna really were the size of the longest baseline. The process of forming VLBI images is not as straightforward therefore as forming images in single mirror systems, and a certain amount of data processing must take place before an image, a "map", is made.

#### *1. Observations*

Presently a VLBI observation generally involves 8 to 14 telescopes worldwide, which observe a number of sources over a given amount of time, usually 24 hours to obtain a full rotation of the earth. During this period of observation, it is assumed that the source undergoes no dramatic and substantial changes, so that all the data gathered may be combined into a single data set for the making of a map. Since the earth is rotating during this time, the baseline formed by two antennas appears to rotate when viewed from the source, so that any two antennas form a number of different apparent interferometers during the observation (see figure A5 where  $u$  and  $v$  represent components along two orthogonal directions on a plane perpendicular to the line of sight to the source).

The telescopes used are a worldwide network of radio antennas of various sizes and sensitivities. The variations between the antennas result in the necessity of doing careful calibration of the amplitude (the relation of the received power to the actual flux coming from a source) and the phase (the relation of the measured phase of an interference pattern to the true phase once instrumental phase contamination has been

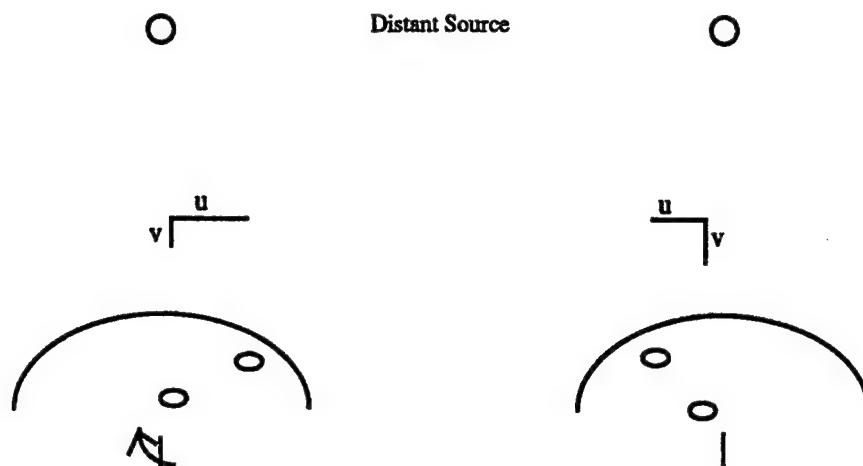


Figure A5: Rotation of the earth and aperture synthesis.

removed). For VLBI polarization studies there is an additional complication introduced by the necessity of obtaining cross-hand data, *i.e.* data which measures the right circular polarization at one antenna interfering with the left circular polarization at the second antenna. Since the receivers for circular polarization are not ideal, there is a certain amount of left hand flux received by the right hand receiver and *vice versa*. The development by the Brandeis Radioastronomy Group of calibration procedures to handle this "cross-talk" resulted in the ability to make polarization maps at milliarcsecond resolution for the mapping of magnetic fields in the jets of radio-loud quasars and BL Lacs.

Once the interferometer baselines are calibrated, there is still a physical limit on the information as stated above. Since there is not a filled aperture, only certain Fourier components of the actual brightness distribution on the sky are measured during an observation. The distribution of the Fourier components can be plotted on a plane

perpendicular to the line to the quasar nucleus which is called the uv plane. The plotting is done in units of the wavelength of the observation and directly measures the fullness or lack of the available data to be used for image formation.

## *2. Modelling and Image Formation*

Since, in general, there are substantial gaps in the uv coverage of an observation, the process of forming an image of the brightness distribution is not a straightforward inverse Fourier transform from the Fourier components to the image. Instead a series of models must be constructed, each progressively more closely related to the actual brightness distribution, in order to obtain an "image" of the source.

The process of creating and modifying the model brightness distributions involves a process of self calibration and a system known as CLEAN (Cornwell and Wilkinson, 1981; Högbom, 1974). Since most blazars have strong cores with weaker diffuse emission forming the knots of the jet, an initial model with a strong point source and a weaker second source will give a fair starting point. By generating the Fourier components which would be seen by the interferometer baselines if this model were the actual brightness distribution of the source, and by comparing these model Fourier components to the actual Fourier components, a second generation model can be developed. By repeating this process until the generated models are not changing significantly, a good approximation to the real brightness distribution is achieved.

The interferometer baselines create a non-spherical uv coverage for most sources, so that the resolution obtained is dependent on the direction from the core of the source. Generally therefore the final model components are convolved with a Gaussian ellipse which models the resolution of the interferometer system and removes the sidelobes. This ellipse is known as the clean beam.

The final maps produced by the observations are generally contour maps with contours of constant brightness. The final model from CLEAN convolved with the

Gaussian beam is gridded and a series of programs called PG Plot are used to generate these maps from the gridded brightness distribution (the PGPlot Libraries were provided by T. J. Pearson, the California Institute of Technology).

#### *D. The Macintosh System*

The Macintosh modelling system divides conveniently into two parts. The first part involves the construction of the three dimensional distribution of sources, called the model, which consists of the core and jet and is made up of 2 to 10 knots. Although the knots are displayed as balls to make their visual placement easier, in actuality they are treated as point sources of emission. Since a real interferometer, system does not have infinite resolution, each point will appear as a Gaussian distribution of brightness. This is the equivalent of the beam of the interferometer so that the second part of the system involves the formation of the image based on convolution of the Gaussian beam with the point sources and subsequent contouring of the gridded brightness distribution.

Unfortunately "model" has many meanings in physics. In this chapter model refers to the created three dimensional distribution of sources unless it is used in conjunction with the word physical or with the names of the physical models. Generally when it is unclear from the context, the created distribution will be referred to as the source model, while the "physical" models described in chapter 2, the Blandford and Königl and Cawthorne and Wardle models, will be referred to as the physical model.

##### *1. The User Interface*

The interface between the program and the user allows the construction of the source model, both graphically, by the changing of values on an on-screen tablet by movement of the mouse, and through Macintosh dialogue boxes brought up by



pressing icon buttons or from menu driven commands. The qualities of the image, resolution in relation to interknot spacing and gridding of brightness points, are modified through menu driven dialogue boxes. The interface is designed to Macintosh standards, so that anyone familiar with the Macintosh system will find it easy to generate models and images.

The shell of the program, including the main window, dialogue windows, menus, and links between icons and dialogues, was established using the Prototyper development system (trademark and copyright by SmethersBarnes Publishing). Although Prototyper generates C code for the placement and design of windows, it does not perform any actual tasks normally ascribed to a programmer, *i.e.* there is no construction of input/output routines or even routines to pass information from dialogues to the main program. However by providing handling of window structures and the main program loop which is common to Macintosh programs, it provides the first time programmer with the basic structure on which to build a working system and saves a great deal of time by providing the details of handling the low level interrupts common in the Macintosh system.

Prototyper generates the equivalent of an outline of window and mouse handling routines in a form mostly compatible with the Think C development system (trademark and copyright of Symantec Corporation). Minor changes in some headers and the method of calling up dialogues are necessary in order to successfully handle string copying and the passing of values between the dialogues and the main window in which all drawing is done. The Think C system, a subset of ANSI C, is used for all program code. The ANSI mathematical libraries provided with Think C are used, as well as most internal string handling routines, to handle calculations and input/output between the user and program.

The Macintosh system software includes a wide variety of routines for handling the low level functions involved with drawing and writing on the screen or reading from and writing to disk. The collection of routines, mostly in internal ROM, is known as the Toolbox. The Toolbox is heavily used in Macintosh programming as it contains the drawing primitives, the routines handling the writing alphanumerics onto the screen, and the routines handling mouse driven events such as menu selection or pressing of on-screen buttons. In general the Toolbox routines are called almost continually during program execution as the user is either driving the program with the mouse or the program is writing information onto the screen.

The internal information in the Macintosh is kept in Pascal numbers and strings, since the Macintosh was originally programmed in this language. For numbers there are no differences, except the need to watch definitions such as double and float, between Think C and Pascal. However, the structure of strings is very different between the two languages. C treats strings as a series of characters terminated with an EOF character, while Pascal begins a string with a length byte followed by the string itself. In order to communicate with the Macintosh Toolbox, it is necessary to convert C strings into Pascal strings using the routine CtoPstr provided by Think C. The strings returned by the Toolbox to the program must then be converted back into C using PtoCstr.

The careful use of these procedures is vital to the operation of any C program on the Macintosh, since the Macintosh treats all keyboard input as alphanumerics. This means that entered values for variables must be converted from strings into numerical values using C procedures, which naturally require C strings to work. Unfortunately the failure to use one of the conversion procedures does not cause the system to crash. Instead the program continues but with the odd results which are to be expected when nonsense variables have been entered. As an example, if a number were entered into a dialogue when called for, and the string was not converted into a C string, the first

character would be a length byte which would not be a numeric character. The routines to convert strings into numeric values will not work on nonnumeric characters so that a meaningless variable will have entered the program and calculations with it will generate meaningless though not nonnumeric results.

Once the conversion of strings has taken place, the calling of the Toolbox routines is straightforward. Although problems can still occur due to the failure to successfully maintain the distinction between handles and their data, *e.g.* one must lock the position of the data referred to by a handle when acting on the handle, these problems are no different than those faced in programming any language which relies heavily on pointers. The only minor distinction between C and Pascal that enters is the need to always pass an argument to a C function, while Pascal uses procedures when no value is passed, *e.g.* C uses DoThis(void) when Pascal calls DoThis.

## *2. The Model Picture*

The model created by the user is stored internally as a series of numbers and characters representing the features of the model. From this information a rough three dimensional picture, called the model picture, is generated, so that the user has an immediate feeling for the characteristics of the model. On screen there is also a display of the primary parameters of the model in numerical form for reference.

The model is modified in two ways. When the user starts up the system, a set of common values representing a small angle to the line of sight and moderately relativistic speeds is stored into the model parameters. These values can then be modified either interactively on the on-screen tablet, if the values represent angles or velocities, or through the use of menus and dialogues, if the values represent the number of knots or characteristics of the magnetic field, *i.e.* the Blandford-Königl model or the Cawthorne-Wardle model. As changes are made the screen is updated so

that there is immediate feedback on how the changes affect both the knot distribution and the image seen on the plane-of-the-sky.

In order to get a feeling for the exact angles involved, the system allows the model to be viewed along any of the three orthogonal axes defining the coordinates of the model. This menu driven procedure changes only the appearance of the model as the observer is always assumed to be along the x axis. Since any perspective drawing, such as is used to view the model, creates an uncertainty in the angles being viewed, this feature allows the user to get a better intuitive feel for the angles being used by allowing those angles to be drawn more in the plane of the screen, where there is little or no distortion due to perspective projection.

The model is drawn to the screen using a simple perspective algorithm developed by trial and error. The algorithm first draws a coordinate axis which is labelled so that the axis pointing at the observer is clear, in case the model has been rotated by the user. With the three dimensional positions calculated by equations A.9 and A.10, the knots are projected onto the screen (after taking into account any rotation of the model picture) using

$$\begin{aligned}y' &= y + (0.118y - 0.167z - 0.7)x \\z' &= z + (-0.167y + 0.0367z - 0.7)x\end{aligned}\tag{A.21}$$

where  $y'$  gives the horizontal coordinate from the origin of the coordinate system with positive going to the right,  $z'$  gives the vertical component from the origin with positive going upwards, and the origin of the  $xyz$  and  $y'z'$  coordinates are the same. These coordinates are then transformed into screen coordinates by adding an offset moving  $y' = z' = 0$  to the center of the model picture and multiplying the results of equation A.21 by a scaling factor which fits the points to the screen. The offset is added to  $y'$  to

get the horizontal coordinate as the Macintosh coordinate system increases to the right, but  $z'$  is subtracted from the offset as the Macintosh coordinates increase downwards.

At the origin of the coordinate system a black ball is drawn indicating the core. Then at the  $y'z'$  coordinate obtained for each knot, a shaded ball is drawn which results in a picture of the core and jet being formed on the screen. Since the jet makes a bend, there is no single valid coordinate system in which clocks can be synchronized for a relativistically moving jet. As such the drawing does not represent any physically seeable object, but merely presents a helpful diagram of the structure of the jet. The time delay effects are not taken into account in drawing the model picture.

The variations allowed in the angles will keep all jets in the front half volume of the xyz coordinate system (*i.e.*  $x$  is always positive and increasing with knot number), as such each knot is drawn after the previous one, which automatically handles overlapping knots. This is not the case for drawings where the  $y$  or  $z$  axis is pictured outward because the user has rotated the coordinates to get a better view of a bend. Therefore some care must be used in interpreting a model picture when the  $x$  axis is pictured in the plane of the screen. In general, the models of interest make reasonably small angles to the line of sight, *i.e.* the  $x$  axis, so that the separation of knots on the screen is adequate to eliminate possibly confusing overlaps when the  $x$  axis is in the plane of the screen.

Once the model has been established, changes will need to be made to all variables involved to study the changes in the image caused by variations in the parameters. The Macintosh screen is diagrammed in figure A6. The model picture in the upper left contains the three dimensional distribution of the knots assuming that they are stationary, *i.e.* ignoring relativistic effects. The model values associated with the model picture are listed in the lower right and include the speeds, gamma factors, angles, and apparent velocities (in relation to the core) for the jet both before and after the bend. The

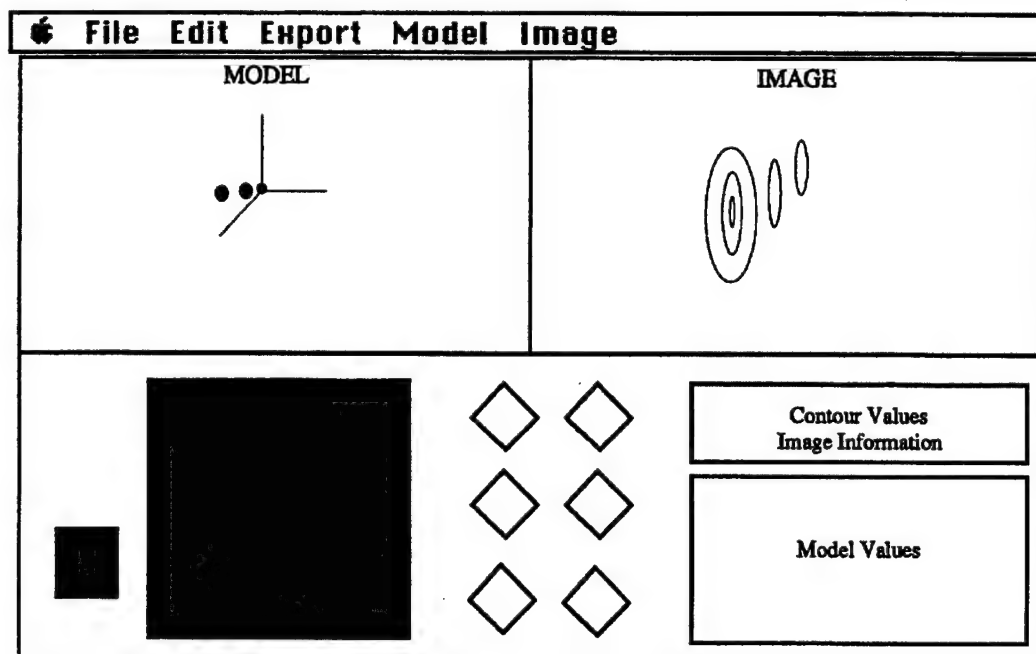


Figure A6: The Macintosh screen layout for the modelling program.

icons at the bottom center are buttons which when pushed with the mouse have two possible outcomes. For variables which are changed interactively, *i.e.* speeds and angles, the first icon pushed lists that item on the horizontal axis of the large pad at the lower left, while the second icon pushed lists the item on the vertical axis. For variables which are changed through dialogues, *i.e.* B field distribution and number of knots, pushing the icon brings up the appropriate dialogue.

Once two variables are listed beside the tablet, the values of these variables can be changed by using the mouse. The mouse is moved onto the tablet and pressed. As long as the button is held down the variables will be constantly updated and the position of the mouse will be given by the cross cursor. The model picture and image picture are updated constantly as well. When the mouse is released, the position on the tablet is shown with a black dot and updating of the model and image halts. In order to get finer

variation in the variables changed by the tablet, the button left of the tablet can be pressed which will result in the quadrant in which the black dot lies becoming the new tablet. By repeated use of this feature, the tablet can be made as sensitive as desired in order to make fine changes in the value of a variable. In order to return to a coarser tablet, the two icons must be repushed which resets the endpoints of the tablet to the maximum values. The endpoints of the present tablet are always displayed along the ends of the tablet.

There are further model parameters which are set by use of the Model menu. The menu allows choice between the Blandford-Königl and Cawthorne-Wardle models and records the choice by placing a check next to it. The axis directed outward for viewing the source model is chosen in the same way again with a check indicating the choice presently in use. Finally there is a choice to Set the Core Flux level. This brings up a dialogue box in which any flux level up to 10.0 can be entered for the unpolarized core flux which is placed at the center of the coordinate system. Each knot in the jet has one unit of flux.

### *3. The Image Picture*

In the region in the upper right of the Macintosh screen the image picture is drawn. This is a contour map of the plane-of-the-sky brightness distribution taking into account a number of factors, both from the model and image parameters. Each knot of the model beams an amount of total flux and an amount of polarized flux, depending on the relativistic factors, into the plane of the image. The image plane is gridded, and the fluxes from each knot convolved with the Gaussian beam are added into grid points. The contours are then drawn based on these flux points and ticks are added for the electric vector directions with their length depending on the percentage polarization.

In the lower right hand corner just above the model parameter values, the image

characteristics are listed. These include the contouring levels in terms of flux units with each knot having one unit before beaming, the level of zoom into the image picture, and the maximum percentage polarization in the image. The number of contour levels is set by a dialogue box brought up by choosing the Contour item in the Image menu. The value of the maximum contour can be set automatically by the program or by the user through this dialogue. The number of grid points can also be set to either a 32x32 grid or a 64x64 grid by choosing these items in the Image menu. A check indicates the grid in use. The Image menu also allows the user to zoom in on the image picture up to a level 16 times greater than a one to one correspondence between the model and image pictures. This is useful since many models are close to the line of sight and zooming imitates a finer resolution which separates the knots more effectively.

The plotting of the contours is performed in direct analogy to PG Plot. The code from PG Plot was adapted from its original Fortran form used on the VAX minicomputer into Think C. The gridded data from the image brightness distribution is used and the contours are scaled in two ways. First they are scaled to fit the screen, with a zoom factor of one matching the Image size to the Model size as shown on the screen, and higher zoom levels indicating that the Image picture corresponds to a smaller region around the Model center. Second the contour lines are offset between grid points following the PG Plot algorithm, so that the line is drawn as close as possible to the point where the flux matches the contour level, assuming that the flux is dropping linearly between the points.

Once the contours have been drawn, tick marks are added to the contour lines indicating the electric vector direction and magnitude of the polarized radiation. Both memory constraints internally in the Macintosh and ease of reading the final image picture require that the polarization be measured only at certain points on the grid. The percentage polarization and direction is kept track of during the generation of the image



brightness grid by calculating at the appropriate points the additional polarized flux from the knot emission convolved with the Gaussian beam. Since this polarized flux and electric field direction is a vector quantity, vector addition is performed for each appropriate point in the map.

#### *4. Real World Considerations*

Ideally the generation of the models and images could take place without regard for the difficulty of generating the data necessary for the pictures. However, the limited speed of any computer, especially a personal computer such as the Macintosh II, requires a trade-off between the best possible image pictures and the time required to draw them. A number of modifications in the program were made to deal with these problems.

The computing time required to generate the image brightness grid is directly proportional to the number of knots in the jet. Since each knot is beamed and convolved with a Gaussian beam, there is a good deal of overhead in generating the appropriate fluxes which are added for each knot to the image brightness distribution. In addition, there are the requirements of keeping the polarized flux data for each point, and each point of the flux added to the polarization information requires a vector addition. The program limits the user to 10 knots to avoid excessive time being spent on this part of the computation, but for most sources even fewer knots can probably be used.

A more serious constraint is the number of points in the image brightness distribution. The 64x64 grid requires four times the processing time of a 32x32 grid, so that although it gives a much nicer, more rounded contour plot, it can slow the program so significantly that it effectively becomes non-interactive. In order to avoid this problem, the 32x32 grid was established so that the initial development of a model can be done using the smaller number of image brightness grid points, and then the final image can be generated with the finer 64x64 grid. The Gaussian beam forms are

automatically adjusted so that the effective beam size is the same in both grids, which insures that the image does not change significantly (percentage polarization, contouring line placement) between the two grid sizes.

For each contour drawn, the line drawing routine of PG Plot must be called. This routine is very time consuming, so that drawing a large number of contour lines slows the program execution significantly. The levels of the contours are set automatically with only the most significant contour levels being drawn for any choice of the number of contour levels. By trying the maximum number of levels on the machine executing the program, the number of levels which gives adequate performance can be found. Again when a final map is made, the number of levels can be increased to the maximum of 10 and together with the finer 64x64 grid, good maps can be generated.

## *E. Conclusions*

### *1. The Simple Physical Model*

The physical models used in the Macintosh system generally rely on kinematic factors generated from the relationships of special relativity. For the modified Blandford and Königl model, this is virtually the entire modelling involved. In this model the generation of the magnetic field is assumed to be some kind of shear process, but there is no requirement on the generation involved in the program. The maximum percentage polarization is also an assumed factor, so that the radiating particle distribution must basically be written into the program as a number which is not derived from any physical considerations. For the Cawthorne and Wardle modification of the Hughes, Aller, and Aller model, the situation is different. The generation of the magnetic field structure is based on dynamic considerations and therefore comes with limits on the speeds involved in the generation of this structure, which must be

considered when working with the program. Particle energy distribution is again assumed.

The physical models used are simple and certainly do not attempt to explain the generation of the particle energies or any features of the underlying power source in the quasars and BL Lacs. Nevertheless they provide strong constraints upon the characteristics of the jets which are used in the modelling of the distribution of sources. Since the program allows rapid searching of a broad range of the parameter space of the source models, possible configurations which can give rise to the superluminal motion and brightness distribution seen in blazars can be identified. These configurations are not subject to change based on detailed physical modelling of the sources, unless such models somehow violate apparently obvious constraints provided by special relativity. As such the source models generated on the Macintosh with this program should provide a framework for discussion of the distribution and velocities of the emitting regions in the jets of quasars and BL Lacs.

The primary goal in the development of this system is its applicability to the milliarcsecond scale jets in superluminal radio sources. As stated above, the source models generated provide kinematical constraints on a jet and therefore provide a framework for analysis of the jet. The actual sources observed in VLBI studies, however, appear to be quite complex. Although there are some simple sources, these generally have only one or two knots in addition to the core, and the question of whether the simplicity results from the inability to see enough of the structure at present dynamic ranges or from an inherent simplicity cannot be answered. The source models generated by the system must therefore be considered to be a starting point for analysis and not an end in themselves. Future developments of the system should add some features, such as a precessing source, which will be of interest to actual sources, but at all times the simplicity of the models will require caution in the application of the results.

Despite these worries, the simplicity of the source models should not be looked on as a failing. The more complex the model, the more independent parameters exist which can be modified to give a good fit to the observations. However the danger of having so many parameters that any conceivable observation can be successfully matched is quite real in radio interferometry. Many VLBI maps are generated from sparse uv plane coverage, so that the details in an image need not show up in a map at a given epoch. Therefore a modelling system with a large number of parameters can successfully match any source. However a simple model, such as the Macintosh program, basically attempts to match only some very reliable features of a VLBI map, specifically the apparent superluminal velocity, polarization features, and flux changes. As such the Macintosh system can successfully discover some information about the source which should be true, since pure kinematics require it.

## *2. The Macintosh System*

The Macintosh interface has many advantages for an interactive system. Since the interface is graphically based, the construction of the methods of changing variables by onscreen tablet is simplified. Since the routines to handle mouse location and pressing, as well as the drawing of pictures, are ROM based and optimized for an interrupt driven system, the speed of the interface is excellent. Also the interface, including menus, buttons, and mouse driven events such as the tablet, is standardized between Macintosh programs, which makes the modelling system simple to use for anyone familiar with any Macintosh application.

Since the Macintosh is graphically oriented, the generation of images which convey information about the source model is fast. Most astrophysical data is presented in such images, and the comparison of an image generated from a model and data gathered by a VLBI experiment is simplified by the use of a graphical system. The main problem with such a system is the speed of the actual computation required to go from

the model to the image. As personal computers and workstations merge and become faster, this problem for simple kinematical models such as this program generates will disappear.

### *3. Applications of the System*

As long as the cautions stated above are not overlooked, the application of the modelling system to actual sources is straightforward. Most superluminal sources show a polarization structure suggesting either a parallel or perpendicular magnetic field structure (to the jet axis), so that an initial choice between the modified Blandford and Königl model and the Cawthorne and Wardle model can be made. Since the superluminal speed is generally known for the more studied sources, this provides an initial variable to match to observations through variations of the speed of the pattern (shock) and the angle between the line of sight and the jet axis. After this it is a matter of exploring the other variables until satisfactory matching to the source brightness distribution is obtained and until it is clear that all other likely arrangements which give similar results have been ruled out or discovered.

The source model at this point has provided a distribution of knots based on some kinematical constraints together with some information about their possible velocities and magnetic fields. The distribution can be used as a starting point for more detailed analysis of the source. Such an analysis includes information on multiple epochs, since a speed and direction implies the ability to predict the location of a knot in the future, and information from other parts of the electromagnetic spectrum. The comparison of expected results predicted by the simple source model for future epochs with actual VLBI observations provides some feedback as to whether the generated model is reasonable. Information about the magnetic field and velocities provides information of use to observations at other wavelengths, although such application requires significant extrapolation as most other parts of the spectrum are believed to

arise in regions even smaller than the VLBI core. But the fact that a jet of material forms the VLBI structure, including the core which appears to be relativistically beamed, suggests that a jet may be involved in the emission in other regions as well, although emission would occur from a point closer to the base of the jet of material. The determined velocity and angles from the source model can be used to explore this possibility.

Although the modelling system cannot provide the answers to the most interesting questions of blazar phenomenon, such as the generation of the fantastic energy output, it can provide some strong constraints on angles and velocities involved, as well as suggesting magnetic field distributions within those constraints. Since these constraints arise from the requirements of special relativity, they are quite robust in the face of changes in the underlying physical models for energy generation and emission in other parts of the electromagnetic spectrum. As such they can provide constraints on models which provide the basic mechanisms for quasar emission and structure.

## Appendix B: The Source Code Control System

The Brandeis package of programs comprises two main sets of routines, CALIB for calibration and HMAP for hybrid mapping (as described in chapter 3). Both systems are maintained in a control system, which monitors when they are being edited and keeps track of all changes made to the source code. The control system used is the Source Code Control System (SCCS) of the Digital Equipment Corporation.

The SCCS places the source codes into files and allows access only through *sccs* commands. The primary commands include *sccs edit*, *sccs get*, *sccs info*, and *sccs delta*. The *edit* command retrieves a file for modification. After modification the *delta* command writes the new file together with an editing record so that all previous versions can be recovered. For compilation, only a copy of the file is needed, and the *get* command retrieves a copy while leaving the original unalterable. The *info* command tells the programmer whether a file is already out for editing (by another programmer) and also gives information about the files editing history.

This system interacts with the UNIX make utility, so that the updating of tasks is automatically handled. When a task is updated, make automatically retrieves a copy of each source file needed and compiles them in turn. This removes the need to maintain libraries of subroutines, which often turned out to cause major problems as old versions of subroutines were often left in active libraries.

## Appendix C: Manuals for the Brandeis Package

### Amplitude Calibration

The experiment name is assumed to be GXX below. Programs are listed in **bold** typeface. The programs are presently case sensitive so use all capitals for file names.

#### *A. Creating the Initial Files*

1. Certain files should be available from the correlator which has processed the data.

At this time correlation occurs on the MarkIII correlator at Haystack and the files are the Schedule File (#S----:49 where ---- is the four digit number which Haystack assigns to your experiment) and the segmented data file. In the near future correlation will be done at the VLBA correlator in Socorro and programs will need to be written to handle the data format from the correlator.

2. Copy the schedule file into GXX.SKD and remove any header lines so that the first lines are

\*CODING

\$INDEX-\$EXPER...



Run **wrtexp** to create the experiment file, GXX.EXP. Compare the Bonn and VLA fluxes for the sources in the experiment (to obtain the VLA fluxes you must calibrate the VLA data, see the Note *Calibrating VLA Data with AIPS*). In general these fluxes should be almost identical although Bonn might be slightly higher for some large extended sources. If there are significant differences use the VLA fluxes, otherwise use the Bonn fluxes as these are closer to the actual flux seen by single antennas in the VLBA and EVN. If the VLA data is not yet calibrated, you can continue using the Bonn fluxes or continue by entering 1.0 for fluxes until you need to calculate a T(sys) file or run **edtcals**. Make sure to check the fluxes later if you use Bonn fluxes. If there are errors you will need to return to the **edtcals** step to make corrections. Any information which you do not have at this point can be hand edited into the file at a later time.

3. Gather together all the logs from the stations in the experiment. These are now mostly electronic logs which can be retrieved via FTP from `uvax1.aoc.nrao.edu` and from `astbo1.bo.cnr.it`. There might also be some electronic logs with handwritten notes or with gain information. Move the appropriate logs into your working directory. Appropriate logs are those with calibration information (for the VLBA these have all VLBA stations with system temperature measurements for all base band converters, for MarkIII stations these have lines of the form `time/T(SYS)1/xx.x,xx.x,...` where `xx.x` is some real value, while for the VLA these are files with the correlation coefficients for all times).
4. For the VLBA, edit the file to create a series of files, one for each station, with the name `GXX.%MON` where `%` is the station one letter designation code (as in the schedule file from the correlator and the experiment file. For the VLA rename the RCP and LCP files `GXX.YRCAL` and `GXX.YLCAL`. All other stations should have the files named `GXX.%LG`. Bonn generally sends an electronic summary of

T(sys) measurements which must be entered by hand, so print this file instead of renaming it.

5. Look in the GXX.%LG files for the lines

/CALTEMP1=xxx.xx

/CALTEMP2=xxx.xx

and record this information temporarily. Also look in the VLA calibration files for the IAT-UTC clock offset and record this (**wrtexp** asks for this value, if you did not have it then hand edit it into the experiment file).

6. Create the GXX.PAR and GXX.CAL files by running **wrtparcal**. The par file contains station pointing information for all scans. The cal file has locations for all T(sys) and T(ant) measurements in an unformatted form. Initially all values are zero.
7. For log files in the form GXX.%LG, run the program **extract** to create the extracted log files GXX.%LE. The extracted log file contains only the lines necessary to calculate the T(sys) values. Then run **wrtts** which creates the GXX.%TS files. This program interactively leads you to creating the T(sys) file.
8. For VLBA stations, remove or comment out any bad data lines in the T(sys) measurements and then run the program **vlbacal** which creates GXX.%TS files from the GXX.%MON files from the VLBA calibration file.
9. For the VLA, remove or comment out any bad data lines in the .YRCAL and .YLCAL files and then run the program **wrtycal** which creates the files GXX.YRR and GXX.YLL from the GXX.YRCAL and GXX.YLCAL files. The created files are the equivalent to the T(sys) files.
10. For stations which send paper logs, run **handtsta**. Choose the option of hand entering the T(sys) measurements and enter them as the program prompts you.
11. For stations which send no calibration data, run **handtsta** choosing the option of calculating the T(sys) measurements. From previous experiments or from the EVN

or VLBA handbooks, estimate the system temperature (lowest possible  $T(\text{sys})$  value) and the variation of  $T(\text{sys})$  with elevation. The program will ask for these two values and use them to calculate a TS file. For strong sources (3C84 and 3C273 and their like), you should also enter the response of the antenna to the source. This is estimated by multiplying the first term of the gain curve in ANTGAINS.MST by the source flux and adding this temperature to the previously calculated temperature. If the value to be added is insignificant, you need not do this step.

12. Modify the ANTGAINS.MST file by adding a segment for your experiment. Each antenna needs to have a gain formula entered as used by the subroutine kperjy (see appendix for formulas). This information is available in the EVN handbook (retrievable from astbo1), the VLBA handbook (retrievable from uvax1), or is sent by the stations after the experiment.

#### *B. Generating the VIS and calibration files*

1. Copy the segmented data file onto the VAX in the VLBI account in its output area as GXX.SEG (space limitations on most accounts cause the sorting programs to fail).

Run **dupscansort** by typing

dupscansort GXX.SEG

which will sort the data into the Brandeis order as a batch job. Then modify the file PAR:DUPSCANS.PAR to reflect your experiment and run **dupscans** as a batch job by typing

batch dupscans

which will remove any duplicate scans. Finally run the program **flagdata** and flag out data for poor quality codes (0 1 2 3 A B C D E F) and for too little data (generally less than 52 seconds). Copy the data file back to the Decstation.

2. Run **wrtvis** on the segmented data file. This will create the file GXX.VIS which has the segmented data information in the Brandeis format.
3. Run **edtc** to add the TS data into the CAL file created by **wrtparcal**. Choose the option to insert the data from the TS files into the CAL file for each station, except the VLA which uses the option for inserting VLA data. You do not need to insert TA data as that will be calculated.
4. Run **wrtgai** which takes the TS data in the CAL file, the pointing information in the PAR file, and the gain curve from ANTGAINS.MST and creates the file GXX.GAI, which contains the necessary terms to convert the uncalibrated VIS file into a calibrated database. Choose to use calculated TA values for all antennas when asked.

*C. Creating the CDB file and making corrections*

1. Run **wrtcd** to create the amplitude calibrated database file (GXX.CDB) from the VIS and GAI files. Look at the log file to make sure calibration was accomplished correctly.
2. Since some antennas send no calibration data and since some calibration data is generally in error, the CDB file must be checked for inconsistencies. Run **pltv** on the CDB file (use the file PLTVIS.PAR to set switches and inputs) in the mode which plots each baseline against UT for the parallel hands. Look at the plot outputs to make sure that the RR and LL visibilities are aligned (i.e. circles and pluses lie roughly on top of each other). If the data is not aligned on some baseline, try to check other baselines to each antenna to see if one antenna is responsible. Scale the data from that antenna using **scaletsta** on the TS file with the new RCP caltemp given by

$$T_{\text{CAL}}^{\text{RCP}(\text{new})} = (\text{Ampl}_{\text{LL}} / \text{Ampl}_{\text{RR}})^2 T_{\text{CAL}}^{\text{RCP}(\text{old})}$$

where the adjustment is squared since the gain enters into the CDB visibility as a square root. Run **edtc** to insert the new TS data into the CAL file for all antennas adjusted (this overwrites the old data so antennas which are not adjusted need not be reentered). Run **wrtgai** to create a new GAI file, then run **wrtcdb** to create a new CDB file.

3. Run **pltvis** on the new CDB file using the baseline against UT mode and verify that the changes aligned the data. The RR and LL visibilities should be aligned to within a few percent if possible. Very fine adjustments will be made later in **rlcal**.
4. Run **pltvis** again in the mode which plots all visibilities from all baselines against UV distance. Look for points which are out of line with the neighboring points. If a set of discrepant points are all do to a single antenna (check this by plotting visibilities against UV distance for individual baselines that are suspected), then adjust both the RCP and LCP TS data by using **scaletsta** with new caltemps given by

$$T_{CAL}(new) = (Amp_{expected}/Amp_{CDB})^2 T_{CAL}(old)$$

where the  $Amp_{expected}$  is the amplitude which would fit the visibility curve and  $Amp_{CDB}$  is the amplitude plotted. Run **edtc** and insert the new TS data into the CAL file, then run **wrtgai** and **wrtcdb** to create the new CDB file.

5. Run **pltvis** on the new CDB file in the mode which plots add data against UV distance and verify that the changes have aligned the data.
6. Once **pltvis** indicates that no further improvements in data alignment can be made, the CDB file is considered complete.
7. The quality of the data in the experiment can be checked by using **pltvis** to plot closure phases (which do not depend on instrumental terms) for all possible triangles on the source 3C84. Plotting closure phase against UT should show roughly smooth variation, with the longest baselines showing the most rapid changes in phase. Since

instrumental terms do not enter closure phases, this is useful for flagging out bad data and for checking the overall quality of the data in the experiment.

#### *D. File Formats and Gain Curve Formulae*

##### The Experiment (GXX.EXP) File:

The experiment file has two lines of header information which includes the reference frequency and UT-IAT time difference. Line three contains the number of stations and the source of data for the EXP file. Next all stations are listed one per line with the information (in order of appearance), the station code, the three geodetic coordinates, the latitude and longitude, the type of mount (0=alt-az, 1=equatorial), and the polarizations recorded (R L). The next line gives the number of sources then each source follows one per line. Each source line contains the source name, its coordinates, the epoch of the coordinates, the adjusted coordinates, the coordinates in decimal form, the date of the adjusted coordinates, and the flux in Janskys. The next line gives the number of scans followed by the one line for each scan which has the time of the start of the scan, the source name, the length of the scan in seconds, the number of antennas in the scan, and the station code of the antennas in the scan. The old format includes the baseline codes following the station codes.

##### The System Temperature (TS) Files:

These files are created by **wrtts**, **handtsta**, and **vlbacal**. The format has three header lines with information on the program which created the file, the date of creation, and the cal temperatures. The rest of the file is a listing, one line per scan, with the time of the scan, the source, a comment on how the entry was put in, the RCP receiver temperature, the LCP receiver temperature, and a comment field.

##### The VLA Calibration (YRR, YLL) Files:

These files, created by **wrtycal**, are similar in form to the TS files except that there is one for each hand. The first number on each line is the real part of the correlation coefficient (x256 actually) and the second number is the number of baselines in the scan.

The ANTGAINS.MST File:

This file contains the parameterized gain curves for all antennas in the all experiments. Each experiment's data begins with a header line containing the date, the experiment designation (GXX), the frequency, the number of antennas, and the station codes. Then follows a line for each antenna containing the gain curve parameterization for that antenna. Each line begins with the station code followed by the code for the form of gain curve used (1, 2, 3, or 4, see below). Then there are seven floating point numbers which are the coefficients C1 through C7 used the the gain curve formulae. The next two numbers are the RCP and LCP cal temperatures and each line ends with a comment field.

The formulae used (ZA = zenith angle, HA = hour angle)

$$1) K/Jy = C_1(1 + C_3Y + C_4Y^2 + C_5Y^3 + C_6Y^4)$$

$$\text{with } Y = ZA - C_2$$

$$2) K/Jy = C_1(1 + C_3Y + C_4Y^2 + C_5Y^3 + C_6Y^4)$$

$$\text{with } Y = HA - C_2$$

$$3) K/Jy = C_1(C_2Y_{00}+C_3Y_{10}+C_4Y_{11E}+C_5Y_{20}+C_6Y_{21E}+C_7Y_{22E})$$

where the Y's are spherical harmonics, C<sub>1</sub> is a conversion factor

$$4) K/Jy = C_1\exp\{-C_2[(Y-C_3)C_4]^2\}$$

$$\text{with } Y = \text{elevation}$$

### The Segmented Data (SEG) File:

The segmented data file is transferred from Haystack by ftp. If you should record the file onto tape for storage before any processing. The file has one visibility point on each line (a 60 second integration) with the format:

- 1) File name (Haystack internal)
- 2) Extent type (2 for visibility)
- 3) Extent number
- 4) Number of seconds in segment
- 5) Experiment number (Haystack)
- 6) Processing time with decimal point form encoding phase residual type
- 7) Segment time
- 8) Source name
- 9) Baseline code, made up of two station codes plus the quality code
- 10) Decimal seconds of segment center (now 0.0)
- 11) Hour and minute of scan start encoded to 3 characters
- 12) Frequency
- 13) Correlation code (R=RR, L=LL, r=RL, l=LR)
- 14) Number of channels of data
- 15) Correlation amplitude
- 16) Signal to noise ratio
- 17) Residual phase (VLBI phase, geometric phase removed)
- 18) Incoherent (noise-corrected) amplitude
- 19) Incoherent (noise-corrected) signal to noise ratio
- 20) Varies by type of segmenting
- 21) Allan variation
- 22) Coherent integration time in seconds



## The Visibility (VIS) and Related Files:

Most of the data kept on disk is recorded in an unformatted (binary) file in order to save space. The program wrtvis takes the formatted SEG file and extracts the appropriate information to create the VIS file. Data is written into the VIS file in the following way. For each scan a header is created with the scan time (a8), source (a8), year (int), day (int), hour (int), minute (int), decimal second (real) of the visibility, GST (real), data type (a4), central frequency (real), source flux (real), and  $N_S$  copies of [index (int), station ID (a1), U, V, W (all real) geodetic coordinates of the station, hour angle, elevation, parallactic angle (all real) of the source as seen from the station] where  $N_S$  is the number of stations in the experiment. Then the number of baselines  $N_{BL}$  (int) is written. Finally, for each baseline, i.e.  $N_{BL}$  copies of, the data is written. The data is of the form baseline ID (a2), four copies (one for each correlation) of [correlation ID (a2), amplitude (real), phase (real), signal to noise ratio (int), duration in seconds (int)], then the u, v, w (all real) point of the baseline and 4 copies of the quality code (a1), one for each correlation.

This format is used for all visibility files, such as the calibrated database (CDB) and polarization calibrated database (PDB) files. Programs which read visfiles, such as **pltvis** or **prtvis**, can be run on any file with this format.

## Polarization Calibration

The experiment name is assumed to be GXX below. Programs are listed in **bold** typeface. The programs are presently case sensitive so use all capitals for file names. Both **rlcal** and **ipcal** are menu driven programs, so you choose options when running them.

### *A. RCP and LCP Gain Alignment*

1. Create a flagfile for your experiment with at least one line (usually called GXX\_FLAGFILE.LST) and create a Dterms file generally called GXX\_DTERMS.LST with initial values set equal to zero.
2. Modify the parameter files RLCAL.PAR and IPCAL.PAR to reflect your experiment and input the GXX.CDB file as the database.
3. Run **ipcal** and choose the option to do a blockcheck on the data for the source which will be used for calibration of the D terms (generally 3C84, however if there is limited data then both 3C84 and OQ208). Flag the appropriate data in the flagfile.
4. Run **rlcal** and choose the option to print the RR/LL amplitudes. Quit the program and look over the output file. Flag bad data points (i.e. R/L amplitudes which are out of line with the data) by entering the scans into the flagfile.
5. Run **rlcal** and choose the option to find R/L amplitudes. Quit the program and look over the output file and verify that the R/L adjustments are consistent. Again flag bad data points.
6. Run **rlcal** and choose the option to plot R-L phases using the raw data. Quit the program and look over the output data. Compare all the plots (each antenna is plotted against the other antennas in the experiment) and find the best antennas (in

order) to use for adjustment of the R-L phases. The criteria for selection are stable or slowly varying phase differences with other good antennas. Phase jumps should only occur in antennas near the end of the order of phase referencing antennas. The best antenna becomes your reference antenna and should be entered on the appropriate line in your Dterms file. Record the order of antennas for referencing (note that only dual polarization antennas can be used as there is no R-L phase at single polarization antennas).

7. Run **rlcal** to create the real rlc file (generally GXX\_RLCAL.CAL). Choose the option to solve for the R/L antenna gains then choose the option to find R-L phases. Then begin a loop. After finding the phases for the first antenna, choose the option to change to a new reference antenna. Choose the antenna and then choose to interpolate over all scans with a two point interpolation. Then again choose to solve for the R/L antenna phases. Repeat the sequence of choosing a new reference antenna, interpolating, and solving for antenna phases until all dual polarization antennas have been used (following the order you determined in step 6). Then repeat the choice of choosing a new reference antenna and interpolating without the solving step for all single polarization antennas (this fills in the codes section of the rlc file). Quit and write out an rlc file when prompted. Note that if you have an existing rlc file the program will bomb at this point, so be sure to delete or rename the file before beginning this program or you will have to repeat this step!

#### *B. Determining D Terms*

1. Run **ipcal**. Enter the source or sources to be used (see step 3 above) and then begin by choosing the option to look at closure phases. Quit the program and look over the data for inconsistencies. Flag bad data points.

2. Run **ipcal** and choose the source to work on. Choose the option to apply the rlcsl file. Then choose to solve for all D terms in sequence setting source polarization to zero and referencing to both RR and LL hands. Quit the program and look at the output. Find the best first estimates for the D terms by looking over the output data for clearly discrepant calculations and averaging the good data for each D term. Enter these initial estimates into the Dterms file.
3. Run **ipcal** and choose the source to work on. Choose the option to apply the rlcsl file. Then choose to iterate on the D terms referencing to both RR and LL hands and setting the source polarization to zero, but do not set the D terms to new or they will be zeroed. Quit the program and look over the output concentrating on each calculation of the D term. Flag discrepant points. Note that for small amplitude D terms, it is not unusual for phases to be poorly determined on any given data point, so do not automatically flag out small amplitude data with an odd phase.
4. Run **ipcal** and choose the source to work on. Choose the option to apply the rlcsl file. Then choose to iterate on the D terms referencing to both RR and LL hands and setting the source polarization to zero, but do not set D terms to new or they will be zeroed. If the new estimates seem reasonable, iterate again on the D terms choosing to set the D terms equal to the new estimates. Continue this process until the Dterms converge. If at any point the estimates of the D terms seem inconsistent or to be poorly handled, quit the program and hand enter the new estimates into the Dterms file.
5. Once the estimates of the D terms have converged, quit the program and write the D term estimates into the Dterms file. Run **ipcal** again, choosing the source to work on and to apply the rlcsl file. Now choose the option to compare the calculated and predicted fringes. This option will create a data file (presently output:ip\_dcomp\_SOURCE.GXX, but that should be changed soon).

6. Run **ip\_dplot** with the output file set as the input file in the parameter file **IP\_DPLOT.PAR**. Set the switches in the parameter file to plot the whole experiment and to plot the D term vectors. Look over the output plots to make sure that the D term fits are good. Modify the Dterm file and repeat steps 4 and 5 as necessary to get the best estimates of the D terms.

### *C. Writing out the PDB File*

1. Once the best D term estimates are entered into the Dterms file, run **wrtpdb2**. This has a parameter file **WRTPDB2.PAR** which specified the files needed for the program. This will create the polarized database file, **GXX.PDB**, which will be used as the input for the hmap package.
2. At this point the data is calibrated fully except for the R-L phase offset of the primary reference antenna. Use hmap to map OJ287 and determine the sum of the polarized clean components. Use AIPS to calibrate the VLA interferometer mode scans (see the note, *Calibrating VLA Data with AIPS*) and to determine the polarization of OJ287. Compare the sum of the VLBI clean components and the VLA data. The recovered flux density should be roughly the same, but there will generally be an offset between the calculated phases. Enter the phase needed to rotate the VLBI data to match the VLA data in the Dterms file on the line for PA calibration.
3. Run **wrtpdb2** again (remember to rename the old PDB file). Remap OJ287 using hmap and make sure the sum of the polarized clean components agrees with the VLA data. Once they agree, the calibration is complete.

#### *D. File Formats*

##### The Flag File:

The flagfile is a list of the points to be removed from the data set when making calculations as they have been found to be bad. The format is once flag record per line with 3 spaces (at position 2 a 'D' will disable the flag), the source name (a8), a space, a scan number for the source (i3), a space, a second scan number for the source (i3), a space, the correlator to be flagged (a4), a space and then a comment field.

The flagged data is from the first scan number to the second scan number inclusive with the correlator to be flagged removed. The correlator to be flagged can include:

- ALL - flag all data for this scan
- X - any antenna code, flag all data for that antenna
- XY - any baseline code, flag all data for that baseline
- XYRL - flag that baseline for that correlation

All programs expect a flagfile to be present, so you must create a file for the programs to read. You can disable the first flag entered to begin with.

##### The Dterms File:

The Dterms file has the primary reference antenna listed, the position angle calibration listed, and the D terms for each antenna. It also has additional antenna gains after the D terms, although these are not generally used anymore they are needed as the programs look to read them. Enter them as all ones. The format is a totally dependent on numbers as the programs read this file by looking for antenna numbers rather than the station code. The order is as in the experiment file (GXX.EXP) with each D term line giving one hand (RCP then LCP) with the antenna number, the amplitude of the D term, and the phase of the D term.

#### The RLCAL File:

The file GXX\_RLCAL.CAL is an unformatted file which contains the antenna R/L amplitude and phase corrections for aligning the two polarizations. It is written by **rlcal**, read and used internally by **ipcal**, but only applied to the database by **wrtpdb2**.

## Bibliography

- Abraham, Z., E. A. Carrara, J. A. Zensus and S. C. Unwin (1994): "The ejection rates of superluminal components in 3C 273," in J. A. Zensus and K. I. Kellerman (ed.): *Compact Extragalactic Radio Sources*. NRAO, Greenbank, 87 - 90.
- Aldcroft, T. L., M. Elvis and J. Bechtold (1993): "A sample of lobe-dominated quasars with Mg II absorption lines." *The Astronomical Journal*, **105**, 2054-2063.
- Aller, H. D., M. F. Aller and P. A. Hughes (1985): "Polarized radio outbursts in BL Lacertae. I. Polarized emission from a compact jet." *The Astrophysical Journal*, **298**, 296-300.
- Aller, M. F., H. D. Aller and P. A. Hughes (1992): "Pearson-Readhead survey sources: properties of the centimeter-wavelength flux and polarization of a complete radio sample." *The Astrophysical Journal*, **399**, 16-28.
- Angel, J. R. P. and H. S. Stockman (1980): "Optical and infrared polarization of active extragalactic objects," in G. Burbidge, D. Layzer, *et al.* (ed.): *Annual Review of Astronomy and Astrophysics. Volume 18*. Annual Reviews Inc., Palo Alto, 321-361.
- Bare, C., B. G. Clark, K. I. Kellermann, M. H. Cohen and D. L. Jauncey (1967): "Interferometer experiment with independent local oscillators." *Science*, **157**, 189-191.
- Barthel, P. D. (1989): "Is every quasar beamed?" *The Astrophysical Journal*, **336**, 606-611.
- Barthel, P. D., J. R. Hooimeyer, R. T. Schilizzi, G. K. Miley and E. Preuss (1989): "Superluminal motion in the giant quasar 4C 34.47." *The Astrophysical Journal*, **336**, 601-605.
- Barthel, P. D., D. R. Tytler and B. Thomson (1990): "Optical spectra of distant radio loud quasars. I. Data: spectra of 67 quasars." *Astronomy and Astrophysics Supplement Series*, **82**, 339-389.
- Bassani, L., *et al.* (1992): "SIGMA observation of two quasars: 3C 273 and 0241+62." *The Astrophysical Journal*, **396**, 504-509.
- Begelman, M. C. (1989): "Physics of the central engine," in D. E. Osterbrock and J. S. Miller (ed.): *Active Galactic Nuclei*. Kluwer Academic, Dordrecht, 141-153.
- Biretta, J. A., R. L. Moore and M. H. Cohen (1986): "The evolution of the compact radio source in 3C 345. I. VLBI observations." *The Astrophysical Journal*, **308**, 93-109.
- Blandford, R. D. and A. Königl (1979): "Relativistic jets as compact radio sources." *The Astrophysical Journal*, **232**, 34-48.



- Blandford, R. D. and M. J. Rees (1974): "A 'twin-exhaust' model for double radio sources." *Monthly Notices of the Royal Astronomical Society*, **169**, 395-415.
- Boroson, T. A. and K. A. Meyers (1992): "The optical properties of IR-selected and MgII broad absorption line quasars." *The Astrophysical Journal*, **397**, 442-451.
- Bregman, J. N. (1988): "Continuum properties and rapid variability in BL Lac objects and violently variable quasars," in M. Kafatos (ed.): *Supermassive Black Holes*. Cambridge University Press, Cambridge, 43-54.
- Bregman, J. N., *et al.* (1986): "Multifrequency observations of the superluminal quasar 3C 345." *The Astrophysical Journal*, **301**, 708-726.
- Bregman, J. N. and B. R. Hufnagel (1989): "Radio and optical variability in blazars," in L. Maraschi, T. Maccacaro, *et al.* (ed.): *BL Lac Objects*. Springer-Verlag, Berlin, 159-170.
- Broten, N. W., *et al.* (1967): "Observations of quasars using interferometer baselines up to 3,074 km." *Nature*, **215**, 38.
- Brown, L. F. (1992). *The Evolution of the VLBI Polarization of Superluminal Radio Source 3C 345*. Brandeis University, Ph. D. Thesis, Physics.
- Brown, L. F., D. H. Roberts, and J. F. C. Wardle (1994): "Evolution of the parsec-scale linear polarization structure of the superluminal quasar 3C 345." To be published in *The Astrophysical Journal*, December, 1994.
- Browne, I. W. A. (1989): "BL Lac objects, OVV/HPQs and unified models," in L. Maraschi, T. Maccacaro, *et al.* (ed.): *BL Lac Objects*. Springer-Verlag, Berlin, 401-411.
- Burn, B. J. (1966): "On the depolarization of discrete radio sources by Faraday dispersion." *Monthly Notices of the Royal Astronomical Society*, **210**, 67-83.
- Carswell, R. F. (1988): "Properties of the Ly-alpha clouds," in J. C. Blades, D. Turnshek, *et al.* (ed.): *QSO Absorption Lines: Probing the Universe*. Cambridge University Press, Cambridge, 91-105.
- Cawthorne, T. V. and J. F. C. Wardle (1988): "Kinematic constraints of models of BL Lacertae object OJ 287 from VLBI polarization observations." *The Astrophysical Journal*, **332**, 696-701.
- Cawthorne, T. V., J. F. C. Wardle, D. H. Roberts, L. F. Brown and D. Gabuzda (1993a): "Milliarcsecond polarization structure of 24 objects from the Pearson-Readhead sample of bright extragalactic radio sources. I. The images." *The Astrophysical Journal*, **416**, 496-518.
- Cawthorne, T. V., J. F. C. Wardle, D. H. Roberts and D. Gabuzda (1993b): "Milliarcsecond polarization structure of 24 objects from the Pearson-Readhead sample of bright extragalactic radio sources. I. Discussion." *The Astrophysical Journal*, **426**, 519-535.

- Clavel, J., *et al.* (1991): "Steps toward determination of the size and structure of the broad-line region in active galactic nuclei. I. An 8 month campaign of monitoring NGC 5548 with IUE." *The Astrophysical Journal*, **366**, 64-81.
- Clegg, P. E., *et al.* (1983): "Millimeter and submillimeter observations of 3C 273." *The Astrophysical Journal*, **273**, 58-63.
- Cohen, M. H., W. Cannon, G. H. Purcell, D. B. Shaffer, J. J. Broderick, K. I. Kellermann and D. L. Jauncey (1971): "The small-scale structure of radio galaxies and quasi-stellar sources at 3.8 centimeters." *The Astrophysical Journal*, **170**, 207-217.
- Cohen, M. H., *et al.* (1983): "VLBI maps of 3C 273 and 3C 345 at 2.3 GHz." *The Astrophysical Journal*, **272**, 383-389.
- Cohen, M. H. and S. C. Unwin (1982): "Superluminal Radio Sources," in D. S. Heesch and C. M. Wade (ed.): *Extragalactic Radio Sources*. Reidel, Dordrecht, 345-354.
- Cohen, M. H., J. A. Zensus, J. A. Biretta, G. Comoretto, P. Kaufmann and Z. Abraham (1987): "Evolution of 3C 273 at 10.7 GHz." *The Astrophysical Journal, Letters*, **315**, L89-L92.
- Cornwell, T. J. and K. F. Evans (1985): "A simple maximum entropy deconvolution algorithm." *Astronomy and Astrophysics*, **143**, 77-83.
- Cornwell, T. J. and P. N. Wilkinson (1981): "A new method for making maps with unstable radio interferometers." *Monthly Notices of the Royal Astronomical Society*, **196**, 1067-1068.
- Courvoisier, T. J.-L., *et al.* (1987): "The radio to X-ray continuum emission of the quasar 3C 273 and its temporal variations." *Astronomy and Astrophysics*, **176**, 197-209.
- Courvoisier, T. J.-L., *et al.* (1990): "Multi-wavelength observations of 3C 273. II. 1986-1988." *Astronomy and Astrophysics*, **234**, 73-83.
- Courvoisier, T. J.-L., E. I. Robson, A. Blecha, P. Bouchet, D. H. Hughes, K. Krisciunas and H. E. Schwarz (1988): "Rapid infrared and optical variability in the bright quasar 3C 273." *Nature*, **335**, 330-333.
- Davis, R. J., T. W. B. Muxlow and R. G. Conway (1985): "Radio emission from the jet and lobe of 3C 273." *Nature*, **318**, 343-345.
- Dent, W. A. (1965): "Quasi-stellar sources: Variation in the radio emission of 3C 273." *Science*, **148**, 1458-1460.
- Dietrich, M., *et al.* (1993): "Steps toward determination of the size and structure of the broad-line region in active galactic nuclei. IV. Intensity variations of the optical emission lines of NGC 5548." *The Astrophysical Journal*, **408**, 416-427.

- Eracleous, M. and J. P. Halpern (1993): "A search for rapid variability in the broad Ha profiles of Seyfert and radio galaxies." *The Astrophysical Journal*, **409**, 584-591.
- Evans, I. N., H. C. Ford and X. Hui (1989): "Maximum entropy deconvolution of the optical jet of 3C 273." *The Astrophysical Journal*, **347**, 68-73.
- Fanaroff, B. L. and J. M. Riley (1974): "The morphology of extragalactic radio sources of high and low luminosity." *Monthly Notices of the Royal Astronomical Society*, **167**, 31P-35P.
- Foltz, C. B., J. Chaffee Frederic H., R. J. Weymann and S. F. Anderson (1988): "QSO absorption systems with  $z_{\text{ABS}} \approx z_{\text{EM}}$ ," in J. C. Blades, D. Turnshek, *et al.* (ed.): *QSO Absorption Lines: Probing the Universe*. Cambridge University Press, Cambridge, 53-69.
- Gabuzda, D. C. (1988). *VLBI Polarization Measurements of BL Lacertae Objects*. Brandeis University, Ph. D. Thesis, Physics.
- Gabuzda, D. C., D. H. Roberts, J. F. C. Wardle (1989): "Linear polarization structure of the BL Lacertae object 0735+178 at milliarcsecond resolution." *The Astrophysical Journal*, **338**, 743-751.
- Gabuzda, D. C., T. V. Cawthorne, D. H. Roberts and J. F. C. Wardle (1992): "A survey of the milliarcsecond polarization properties of BL Lacertae objects at 5 GHz." *The Astrophysical Journal*, **388**, 40-54.
- Garilli, B. and D. Maccagni (1990): "X-ray spectra of three BL Lac objects." *Astronomy and Astrophysics*, **229**, 88-92.
- Gubbay, J., A. J. Legg, D. S. Robertson, A. T. Moffet, R. D. Ekers and B. Seidel (1969): "Variations of small quasar components at 2,300 MHz." *Nature*, **224**, 1094-1095.
- Gull, S. F. and G. J. Daniell (1978): "Image reconstruction from incomplete and noisy data." *Nature*, **272**, 686-690.
- Hartman, R. C., *et al.* (1993): "EGRET detection of high-energy gamma radiation from the OVV quasar 3C 454.3." *The Astrophysical Journal*, **407**, L41-L44.
- Högbom, J. A. (1974): "Aperture synthesis with a non-regular distribution of interferometer baselines." *Astronomy and Astrophysics Supplement Series*, **15**, 417-426.
- Holdaway, M. A. (1990). *Maximum Entropy Imaging of Radio Astrophysical Data*. Brandeis University, Ph. D. Thesis, Physics.
- Hough, D. H. and A. C. S. Readhead (1987): "Relativistic beaming and the nuclei of double-lobed quasars," in J. A. Zensus and T. J. Pearson (ed.): *Superluminal Radio Sources*. Cambridge University Press, Cambridge, 114-128.

- Hu, E. M., A. Songaila, L. L. Cowie and A. Stockton (1991): "Lyman-alpha companions to high-z quasars." *The Astrophysical Journal*, **368**, 28-39.
- Hufnagel, B. R. and J. N. Bregman (1992): "Optical and radio variability in blazars." *The Astrophysical Journal*, **386**, 473-484.
- Hughes, P. A., H. D. Aller and M. F. Aller (1985): "Polarized radio outbursts in BL Lacertae. II. The flux and polarization of a piston-driven shock." *The Astrophysical Journal*, **298**, 301-315.
- Hutchings, J. B. (1992): "[O II] and continuum structure in radio-loud QSOs to  $z=0.9$ ." *The Astronomical Journal*, **104**, 1311-1319.
- Impey, C. (1987): "Infrared, optical, UV, and X-ray properties of superluminal radio sources," in J. A. Zensus and T. J. Pearson (ed.): *Superluminal Radio Sources*. Cambridge University Press, Cambridge, 233-250.
- Impey, C. (1989): "Energy distribution of blazars," in L. Maraschi, T. Maccacaro, et al. (ed.): *BL Lac Objects*. Springer-Verlag, Berlin, 149-158.
- Impey, C. and L. Gregorini (1993): "Energy distributions of radio galaxies." *The Astronomical Journal*, **105**, 853-863.
- Impey, C. D., M. A. Malkan and S. Tapia (1989): "The miniblazar in 3C 273." *The Astrophysical Journal*, **347**, 96-111.
- Impey, C. D. and S. Tapia (1990): "The optical polarization properties of quasars." *The Astrophysical Journal*, **354**, 124-139.
- Jennison, R. C. (1958): "A phase sensitive interferometer technique for the measurement of the fourier transforms of spatial brightness distributions of small angular extent." *Monthly Notices of the Royal Astronomical Society*, **118**, 276-284.
- Jennison, R. C. and M. K. Das Gupta (1953): "Fine structure of the extra-terrestrial radio source Cygnus I." *Nature*, **172**, 996-997.
- Jones, T. W. and S. L. O'Dell (1977): "Physical conditions in polarized compact radio sources." *Astronomy and Astrophysics*, **61**, 291-293.
- Kellermann, K. I. and F. N. Owen (1988): "Radio galaxies and quasars," in G. L. Verschuur and K. I. Kellermann (ed.): *Galactic and Extragalactic Radio Astronomy*. Springer-Verlag, Berlin, 561-602.
- Kidger, M. and L. Takalo (1990): "A large anti-flare in the light curve of 3C 345." *Astronomy and Astrophysics*, **239**, L9-L11.
- Kidger, M. R. (1989): "The optical variability of 3C 345." *Astronomy and Astrophysics*, **226**, 9-22.

- Kidger, M. R., J. A. de Diego, L. O. Takalo, A. Sillanpää and M. Okyudo (1993): "Optical photometry and polarimetry and infrared photometry of 3C 345 in outburst." *The Astrophysical Journal*, **407**, L1-L4.
- Kollgaard, R. I., J. F. C. Wardle and D. H. Roberts (1989): "High-dynamic range VLA observations of the quasar 3C 345." *The Astronomical Journal*, **97**, 1550-1555.
- Kollgaard, R. I., J. F. C. Wardle and D. H. Roberts (1990): "High dynamic range VLA observations of eight core-dominated quasars." *The Astronomical Journal*, **100**, 1057-1072.
- Kollgaard, R. I., J. F. C. Wardle, D. H. Roberts and D. C. Gabuzda (1992): "Radio constraints on the nature of BL Lacertae objects and their parent population." *The Astronomical Journal*, **104**, 1687-1705.
- Krichbaum, T. P., *et al.* (1990): "43 GHz-VLBI observations of 3C 273 after a flux density outburst in 1988." *Astronomy and Astrophysics*, **237**, 3-11.
- Kronberg, P. P. and J. J. Perry (1982): "Absorption lines, Faraday rotation, and magnetic field estimates for QSO absorption-line clouds." *The Astrophysical Journal*, **263**, 518-532.
- Laing, R. A. (1980): "A model for the magnetic-field structure in extended radio sources." *Monthly Notices of the Royal Astronomical Society*, **193**, 439-449.
- Laing, R. A. (1984): "Interpretation of radio polarization data," in A. H. Bridle and J. A. Eilek (ed.): *Physics of Energy Transport in Extragalactic Radio Sources*. NRAO, Socorro, 90-98.
- Levy, G. S., *et al.* (1989): "VLBI using a telescope in earth orbit. I. The observations." *The Astrophysical Journal*, **336**, 1098-1104.
- Linfield, R. P., *et al.* (1989): "VLBI using a telescope in earth orbit. II. Brightness temperatures exceeding the inverse Compton limit." *The Astrophysical Journal*, **336**, 1105-1112.
- McCready, L. L., J. L. Pawsey and R. Payne-Scott (1947): "Solar radiation at radio frequencies and its relation to sunspots." *Proceedings of the Royal Society of London, Series A*, **190**, 357-375.
- Mead, A. R. G., P. W. J. L. Brand, J. H. Hough and J. A. Bailey (1988): "Polarimetric observations of the quasar 3C 345." *Monthly Notices of the Royal Astronomical Society*, **233**, 503-509.
- Miller, J. S. (1988): "Spectropolarimetry and the structure of active galactic nuclei," in H. R. Miller and P. J. Wiita (ed.): *Active Galactic Nuclei*. Springer-Verlag, Berlin, 112-120.

- Moore, R. L. and H. S. Stockman (1984): "A comparison of the properties of highly polarized QSOs versus low polarization QSOs." *The Astrophysical Journal*, **279**, 465-484.
- Moore, R. L. and H. S. Stockman (1984): "A comparison of the properties of highly polarized QSOs versus low-polarization QSOs." *The Astrophysical Journal*, **279**, 465-484.
- Mushotzky, R. F. (1988): "X-Ray spectra of active galaxies," in H. R. Miller and P. J. Wiita (ed.): *Active Galactic Nuclei*. Springer-Verlag, Berlin, 239-247.
- Netzer, H. (1989): "Structure and nature of AGNs," in D. E. Osterbrock and J. S. Miller (ed.): *Active Galactic Nuclei*. Kluwer Academic, Dordrecht, 69-84.
- O'Dea, C. P. (1989): "Constraints on integrated nuclear rotation measures in core-dominated active galactic nuclei." *Astronomy and Astrophysics*, **210**, 35-41.
- O'Dea, C. P. (1989): "Constraints on the hotspot advance speed in the core-dominated quasar 1510-089," in K. Meisenheimer and H.-J. Röser (ed.): *Hot Spots in Extragalactic Radio Sources*. Springer-Verlag, Berlin, 69-73, (O89).
- O'Dea, C. P., R. Barvainis and P. M. Challis (1988): "Subarcsecond-resolution radio observations of sixteen core-dominated quasars and active galactic nuclei." *The Astronomical Journal*, **96**, 435-454.
- Orr, M. J. L. and I. W. A. Browne (1982): "Relativistic beaming and quasar statistics." *Monthly Notices of the Royal Astronomical Society*, **200**, 1067-1080.
- Osterbrock, D. E. (1993): "The nature and structure of active galactic nuclei." *The Astrophysical Journal*, **404**, 551-562.
- Padovani, P. and C. M. Urry (1991): "Fanaroff-Riley I galaxies as the parent population of BL Lacertae objects. II. Optical constraints." *The Astrophysical Journal*, **368**, 373-379.
- Padovani, P. and C. M. Urry (1992): "Luminosity functions, relativistic beaming, and unified theories of high-luminosity radio sources." *The Astrophysical Journal*, **387**, 449-457.
- Pearson, T. J. and J. A. Zensus (1987): "Superluminal radio sources: Introduction," in J. A. Zensus and T. J. Pearson (ed.): *Superluminal Radio Sources*. Cambridge University Press, Cambridge, 1-11.
- Perley, R. A. (1989): "Hot spot radio galaxies - An introduction," in K. Meisenheimer and H.-J. Röser (ed.): *Hot Spots in Extragalactic Radio Sources*. Springer-Verlag, Berlin, 1-26.
- Perry, J. J., A. M. Watson and P. P. Kronberg (1993): "Magnetic field strengths in high-redshift galaxies: Can the galactic dynamo be tested?" *The Astrophysical Journal*, **406**, 407-419.

- Peterson, B. M., B. Ali, K. Horne, R. Bertram, N. J. Lane, R. W. Pogge and R. M. Wagner (1993): "The structure of the broad-line region in the Seyfert galaxy Markarian 590." *The Astrophysical Journal*, **402**, 469-478.
- Peterson, B. M., *et al.* (1991): "Steps toward determination of the size and structure of the broad-line region in active galactic nuclei. II. An intensive study of NGC 5548 at optical wavelengths." *The Astrophysical Journal*, **368**, 119-137.
- Peterson, B. M. and C. M. Gaskell (1991): "On the size of the broad-line region in Arakelian 120." *The Astrophysical Journal*, **368**, 152-157.
- Porcas, R. W. (1987): "Summary of known superluminal sources," in J. A. Zensus and T. J. Pearson (ed.): *Superluminal Radio Sources*. Cambridge University Press, Cambridge, 12-25.
- Price, R., A. C. Gower, J. B. Hutchings, S. Talon, D. Duncan and G. Ross (1993): "VLA observations of 91 quasars at  $0.35 < z < 1$ ." *The Astrophysical Journal Supplement Series*, **86**, 365-387.
- Rantakyrö, F. T., L. B. Bååth, I. I. K. Pauliny-Toth, L. I. Matveyenko and S. C. Unwin (1992): "High dynamic range VLBI observations of 3C 345 at 18 cm wavelength." *Astronomy and Astrophysics*, **259**, 8-16.
- Readhead, A. C. S., D. H. Hough, M. S. Ewing, R. C. Walker and J. D. Romney (1983): "Asymmetric structure in the nuclei of NGC 1275 and 3C 345." *The Astrophysical Journal*, **265**, 107-131.
- Readhead, A. C. S. and P. N. Wilkinson (1978): "The mapping of compact radio sources from VLBI data." *The Astrophysical Journal*, **223**, 25-36.
- Rees, M. J. (1966): "Appearance of relativistically expanding radio sources." *Nature*, **211**, 468-470.
- Rees, M. J. (1971): "New interpretation of extragalactic radio sources." *Nature*, **229**, 312-317.
- Roberts, D. H., D. C. Gabuzda and J. F. C. Wardle (1987): "Linear polarization structure of the BL Lacertae object OJ 287 at milliarcsecond resolution." *The Astrophysical Journal*, **323**, 536-542.
- Roberts, D. H., R. I. Kollgaard, L. F. Brown, G. C. Gabuzda and J. F. Wardle (1990): "Milliarcsecond polarization structure of the superluminal quasar 3C 273." *The Astrophysical Journal*, **360**, 408-416.
- Roberts, D. H., J. F. C. Wardle and L. F. Brown (1990): "Parsec scale linear polarization properties of quasars, galaxies, and BL Lacertae objects," in J. A. Zensus and T. J. Pearson (ed.): *Parsec-Scale Radio Jets*. Cambridge University Press, Cambridge.

- Roberts, D. H., J. F. C. Wardle and L. F. Brown (1994): "Linear polarization radio imaging at milliarcsecond resolution." *The Astrophysical Journal*, **427**, 718-744 (RWB).
- Robson, E. I., *et al.* (1993): "The infrared-millimetre-centimetre flaring behavior of the quasar 3C 273." *Monthly Notices of the Royal Astronomical Society*, **262**, 249-272.
- Robson, E. I., W. K. Gear, L. M. J. Brown, T. J.-L. Courvoisier, M. G. Smith, M. J. Griffin and A. Blecha (1986): "A new infrared spectral component of the quasar 3C 273." *Nature*, **323**, 134-136.
- Robson, E. I., *et al.* (1983): "A flare in the millimetre to IR spectrum of 3C 273." *Nature*, **305**, 194-196.
- Rudnick, L. and T. W. Jones (1983): "Rotation measures for compact variable radio sources." *The Astronomical Journal*, **88**, 518-526, (RJ).
- Rybicki, G. B. and A. P. Lightman (1979): *Radiative Processes in Astrophysics*. John Wiley & Sons, New York.
- Ryle, M. (1952): "A new radio interferometer and its application to the observation of weak radio stars." *Proceedings of the Royal Society of London, Series A*, **211**, 351-375.
- Ryle, M. (1962): "The new Cambridge radio telescope." *Nature*, **194**, 517-518.
- Ryle, M. and A. Hewish (1960): "The synthesis of large radio telescopes." *Monthly Notices of the Royal Astronomical Society*, **120**, 220-230.
- Sargent, W. L. W. (1988): "QSO absorption lines: Introduction," in J. C. Blades, D. Turnshek, *et al.* (ed.): *QSO Absorption Lines: Probing the Universe*. Cambridge University Press, Cambridge, 1-15.
- Scarrott, S. M. and C. D. Rolph (1989): "Further studies of the optical polarization in the jet of 3C 273." *Monthly Notices of the Royal Astronomical Society*, **238**, 349-355.
- Scheuer, P. A. G. and A. C. S. Readhead (1979): "Superluminally expanding radio sources and the radio-quiet QSOs." *Nature*, **277**, 182-185.
- Schmidt, M. (1963): "3C 273: a starlike object with large red-shift." *Nature*, **197**, 1040.
- Schwarz, U. J. (1978): "Mathematical-statistical description of the iterative beam removing technique (method CLEAN)." *Astronomy and Astrophysics*, **65**, 345-356.
- Seyfert, C. K. (1943): "Nuclear emission in spiral nebulae." *The Astrophysical Journal*, **97**, 28-40.
- Seymour, P. A. H. (1984): "Faraday rotation and the galactic magnetic field - a review." *Quarterly Journal of the Royal Astronomical Society*, **25**, 293-300.



- Shastri, P., B. J. Wilkes, M. Elvis and J. McDowell (1993): "Quasar X-ray spectra revisited." *The Astrophysical Journal*, **410**, 29-38.
- Stickel, M., J. W. Fried and H. Kühr (1993): "The complete sample of 1 Jy BL Lac objects. II. Observational data." *Astronomy and Astrophysics Supplement Series*, **98**, 393-442.
- Stoeke, J. T., S. L. Morris, R. J. Weymann and C. B. Foltz (1992): "The radio properties of the broad-absorption-line QSOs." *The Astrophysical Journal*, **396**, 487-503.
- Takalo, L. O., M. R. Kidger, J. A. de Diego, A. Sillanpää and K. Nilsson (1992): "Near infrared monitoring of a sample of blazars with the Carlos Sanchez telescope. I." *The Astronomical Journal*, **104**, 40-52.
- Thompson, A. R., J. A. Moran and G. W. Swenson (1986): *Interferometry and Synthesis in Radio Astronomy*. John Wiley & Sons, Inc., New York, (TMS).
- Tran, H. D., J. S. Miller and L. E. Kay (1992): "Detection of obscured broad-line regions in four Seyfert 2 galaxies." *The Astrophysical Journal*, **397**, 452-456.
- Tribble, P. C. (1991): "Depolarization of extended radio sources by a foreground Faraday Screen." *Monthly Notices of the Royal Astronomical Society*, **250**, 726-736.
- Turner, M. J. L., *et al.* (1990): "The X-ray emission of 3C 273." *Monthly Notices of the Royal Astronomical Society*, **244**, 310-321.
- Unwin, S. C., M. H. Cohen, J. A. Biretta, T. J. Pearson, G. A. Seielstad, R. C. Walker, R. S. Simon and R. P. Linfield (1985): "VLBI monitoring of the superluminal quasar 3C 273, 1977-1982." *The Astrophysical Journal*, **289**, 109-119.
- Unwin, S. C., M. H. Cohen, T. J. Pearson, G. A. Seielstad, R. S. Simon, R. P. Linfield and R. C. Walker (1983): "Superluminal motion in the quasar 3C 345." *The Astrophysical Journal*, **271**, 536-550.
- Unwin, S. C. and A. E. Wehrle (1992): "Kinematics of the parsec-scale relativistic jet in 3C 345." *The Astrophysical Journal*, **398**, 74-86.
- Valtaoja, L., *et al.* (1991): "The connection between the low polarization quasar 3C 273 and blazars." *The Astronomical Journal*, **102**, 1946-1955.
- Wardle, J. F. C. (1977): "Upper limits on the Faraday rotation in variable radio sources." *Nature*, **269**, 563-566.
- Wardle, J. F. C., R. L. Moore and J. R. P. Angel (1984): "The radio morphology of blazars and relationships to optical polarization and to normal radio galaxies." *The Astrophysical Journal*, **279**, 93-111.

- Wardle, J. F. C., T. V. Cawthorne, D. H. Roberts, L. F. Brown (1994): "Interpretation of VLBI Kinematic and Polarization Data: Application to 3C 345." To be published in *The Astrophysical Journal*, December, 1994.
- Weedman, D. W. (1986): *Quasar Astronomy*. Cambridge University Press, Cambridge.
- Welter, G. L., J. J. Perry and P. P. Kronberg (1984): "The rotation measure distribution of QSOs and of intervening clouds: Magnetic fields and column densities." *The Astrophysical Journal*, **279**, 19-39.
- Weymann, R. J., S. L. Morris and S. F. Anderson (1988): "Some spectroscopic properties of mass-ejecting and radio-loud quasars," in H. R. Miller and P. J. Wiita (ed.): *Active Galactic Nuclei*. Springer-Verlag, Berlin, 92-105.
- Whitney, A. R., *et al.* (1971): "Quasars revisited: Rapid time variations observed via very-long-baseline interferometry." *Science*, **173**, 225-230.
- Wills, B. J. and I. W. A. Browne (1986): "Relativistic beaming and quasar emission lines." *The Astrophysical Journal*, **302**, 56-63.
- Wills, B. J., H. Netzer, M. S. Brotherton, M. Han, D. Wills, J. A. Baldwin, G. J. Ferland and I. W. A. Browne (1993): "The narrow-line region of high-luminosity active galactic nuclei." *The Astrophysical Journal*, **410**, 534-542.
- Wills, B. J., D. Wills, M. Breger, R. R. J. Antonucci and R. Barvainis (1992): "A survey for high optical polarization in quasars with core-dominant radio structure: is there a beamed optical continuum?" *The Astrophysical Journal*, **398**, 454-475.
- Wills, D., B. J. Wills, R. R. J. Antonucci, R. Barvainis, M. Breger, J. A. Bailey, J. H. Hough and K. Ballard (1989): "High optical polarization in flat-spectrum radio sources," in D. E. Osterbrock and J. S. Miller (ed.): *Active Galactic Nuclei*. Kluwer Academic, Dordrecht, 323-324.
- Worrall, D. M. and B. J. Wilkes (1989): "A comparison of the X-ray spectra of quasars and BL Lac objects," in D. E. Osterbrock and J. S. Miller (ed.): *Active Galactic Nuclei*. Kluwer Academic, Dordrecht, 197-198.
- Zensus, J. A., L. B. Bååth, M. H. Cohen and G. D. Nicolson (1988): "The inner radio jet of 3C 273." *Nature*, **334**, 410-412.
- Zensus, J. A., S. C. Unwin, M. H. Cohen and J. A. Biretta (1990): "The milliarcsecond structure of 3C 273 at 22 GHz." *The Astronomical Journal*, **100**, 1777-1784.